MARTIN MARIETTA ENERGY SYSTEMS LIBRARIES
3 4456 0350609 8

CENTRAL RESEARCH LIBRARY
DOCUMENT COLLECTION

ORNL-2500
Part 2 cy 2
Plant Design

THE ORNL GAS-COOLED REACTOR

OAK RIDGE NATIONAL LABORATORY

operated by

UNION CARBIDE CORPORATION

for the

U.S. ATOMIC ENERGY COMMISSION

CENTRAL RESEARCH LIBRARY
DOCUMENT COLLECTION
LIBRARY LOAN COPY
DO NOT TRANSFER TO ANOTHER PERSON
If you wish someone else to see this document, send in name with document and the library will arrange a loan.

ORNL-2500
Part 2
Plant Design

Contract No. W-7405-eng-26

THE ORNL GAS-COOLED REACTOR

By

The Staff

of the

Oak Ridge National Laboratory

DATE ISSUED

April 1, 1958

OAK RIDGE NATIONAL LABORATORY
Oak Ridge, Tennessee
operated by
UNION CARBIDE CORPORATION
for the
U.S. ATOMIC ENERGY COMMISSION

MARTIN MARIETTA ENERGY SYSTEMS LIBRARIES

3 4456 0350609 8

CONTENTS

SECTION 1. Introduction and Summary

SECTION 2. Gas-Cooled Reactor Physics

SECTION 3. Materials

SECTION 4. Fuel Elements

SECTION 5. Reactor

SECTION 1

INTRODUCTION AND SUMMARY

1. INTRODUCTION AND SUMMARY

Contents

1.1 Introduction to Study..... 1.1

1.2 GCR-2..... 1.3

1.3 Comparison of GCR-2 with Fossil Fuel Plants..... 1.8

1.4 Future of Gas-Cooled Reactors in the United States..... 1.10

1.5 Conclusions..... 1.11

1. INTRODUCTION AND SUMMARY

1.1 Introduction to Study

In late September 1957, the Atomic Energy Commission undertook two separate studies at Kaiser Engineers and Oak Ridge National Laboratory to ascertain whether or not gas-cooled reactors should be given serious consideration as part of the reactor development program of the United States. The ORNL portion of this program was to consist of a design study of a graphite-moderated, enriched gas-cooled reactor, together with the research and development work on both natural and enriched gas-cooled reactors. The AEC requested that a detailed design report of an enriched gas-cooled reactor be submitted by ORNL on March 3, 1958. This is the required report (ORNL-2500, Pt. 2).

Because of the very tight time schedule it was necessary from the beginning of the study to restrict the purview of the design work so as to insure completion of an adequately detailed design on a specific reactor plant for the purpose of comparing the performance of that plant with a natural-uranium, gas-cooled plant designed simultaneously by Kaiser Engineers. In order to make the comparison as direct as possible, ORNL and Kaiser agreed upon a set of common assumptions and "ground rules" for evaluating both designs. It is recognized that differences of opinion and technique still exist, but it is certain that the liaison effort has made comparisons of the designs both easier and more valid.

In order to insure the development for the GCR-2 of a well integrated steam power plant and cost estimates based on the best currently available data, the assistance of the Tennessee Valley Authority (TVA) was enlisted by the Oak Ridge National Laboratory. Their cooperation in every phase of this program and their important contributions to the study are gratefully acknowledged by the Laboratory.

The AEC specified that the ORNL enriched gas-cooled reactor design, GCR-2, must be based on existing technology in order that it could be constructed immediately if a decision were taken to do so. It should be recognized that this restriction places the enriched system in an unfavorable light in comparison with the natural system, since all of the British and

French experience with natural-uranium reactors serves to strengthen the natural-uranium design and permit a high degree of optimization. Even with this restriction, the conservative version of an enriched system is a better choice for construction than a highly rationalized version of the natural system. Accordingly, it would seem wise, if a gas-cooled reactor is built in the United States, to concentrate our technology in the area of slightly enriched systems.

It was not possible in the limited time available to investigate the effects of all possible parameter variations on the plant design before selecting a set of design parameters for detailed work. It is, therefore, not surprising that the design reported herein is not completely optimized. Only after the entire design was finished was it possible to see wherein the system was off optimum.

The first phase of the study was an investigation of the available information on gas-cooled reactor plants in the United States and in the United Kingdom. To this end, specific attention was drawn to Calder Hall, the designs for the Central Electrical Authority plants in Britain, the recent work of American-Standard and Atomics International in the United States, and the preliminary design proposals prepared prior to the original reactor construction at Hanford. Although this list is by no means exhaustive, it serves to indicate the range and depth of the background work on which the study is based.

The ultimate performance of such a reactor plant is determined by three types of limitations:

1. The reactivity and radiation damage lifetimes of the fuel elements.
2. The performance limitations of the structural materials.
3. The pressure and temperature levels at which the system can be operated.

The standard technique for designing a gas-cooled-reactor system is first to select the coolant and the materials which will comprise the core, then to design the best possible pressure vessel to contain the reactor, and finally, to design the rest of the system. It is necessary at every stage of the design to keep in mind the final optimization with respect to net electric power cost and the effects of each portion of the system on

that optimized cost. A continuing optimization analysis was carried out in which the interplay between various components in the system against each other was gauged.

1.2 GCR-2

A perspective section through the proposed plant is shown in Fig. 1.1.

The site selected for the study is one which is typical for United States power plants, and which meets the nuclear requirement for remoteness, as well as the practical requirements of water transportation, a supporting power network, good construction conditions and an adequate labor force. The most important deviations from standard gas-cooled reactor practice, represented by the GCR-2 design, are as follows:

1. Utilization of stainless steel capsules as the cladding for the fuel.
2. Utilization of enriched UO_2 as the fuel material.
3. Utilization of helium as the cooling gas.

There are, in addition, a large number of engineering novelties introduced into the design, none of which markedly changes the comparison between the GCR-2 and any other gas-cooled reactor. It is worthwhile, however, to draw specific attention to the effects of the three important changes in design.

1. The principal virtues of stainless steel as a structural material are two in number.
   a. Because of the excellent high-temperature strength of stainless steel, it is possible to raise the temperature of the reactor exit gas, thus improving the over-all heat-transfer and thermodynamic performance of the system.
   b. There is no catastrophic oxidation between stainless steel and the important coolants which could initiate a graphite fire.
2. The utilization of enriched fuel is not merely a matter of counteracting the nuclear poisoning effect of stainless steel. Rather, the use of enriched fuel has several other important consequences:
   a. The enriched fuel design permits the utilization of UO_2 which is definitely a superior fuel material to natural uranium. UO_2 does not suffer the mechanical deformation characteristic

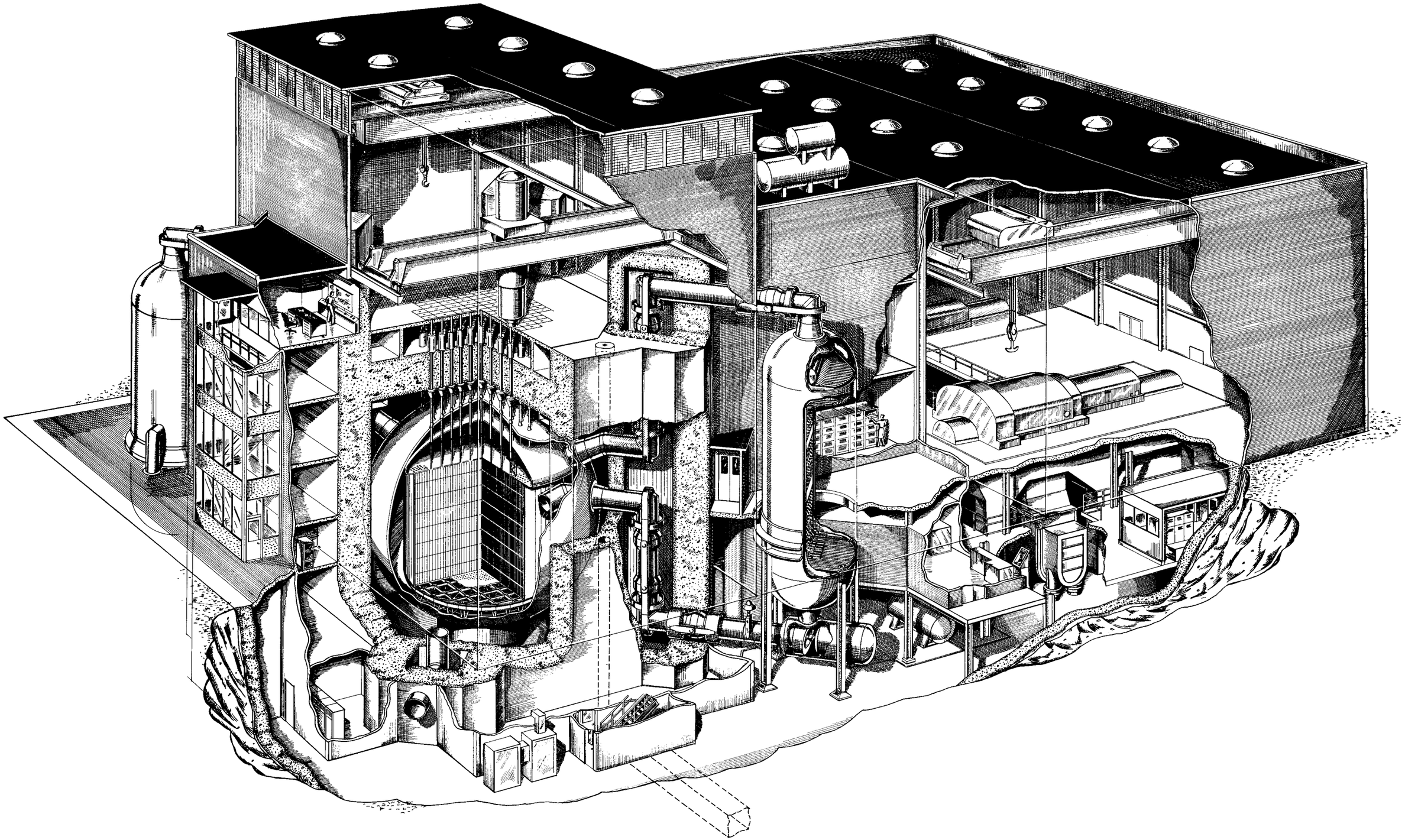

Fig. 1.1. Cutaway Perspective of ORNL Gas-Cooled Reactor Plant (GCR-2).

of uranium metal in the low temperature range. At higher temperatures UO_2 retains most of the fission product gasses which are produced without undergoing severe distortion, as does the metal.

b. By enriching beyond the level required for simple criticality, it is possible to obtain enough excess reactivity so that the nuclear poisoning effect of the Pu^{240} which is produced can be overcome to the point where Pu^{240} begins to behave as a fertile material through the production of fissionable Pu^{241}. The effect of this over-enrichment is to increase the reactivity lifetime to such an extent that the over-all fuel costs of the enriched gas-cooled reactor become comparable to those of a natural-uranium gas-cooled reactor. In the past the principal argument for building enriched gas-cooled reactors has been to achieve reductions in capital cost. It has always been presumed that the fuel costs associated with enriched systems would be considerably higher than in natural systems. The GCR-2 study indicates that there is no substantial fuel cost penalty associated with a properly designed enriched reactor system.

c. The principal economic effect of enrichment is to reduce the over-all capital cost by permitting operation at higher specific power levels. The investment costs/kw fall substantially as the power density of a given sized system is increased, since the capital cost of a rather large fraction of the over-all power plant is independent of power level.

d. Graphite-moderated, gas-cooled reactors in which the fuel is either natural uranium or only very slightly enriched uranium exhibit a positive moderator temperature coefficient of reactivity for exposure in excess of roughly 1000 Mwd/Tonne. This is a very important design consideration in both the British and French power plants. By enriching the fuel so that the absorption competition between plutonium and U^{235} is shifted, it is possible to maintain a slightly negative moderator temperature coefficient over the entire range of reactivity lifetime.

3. It is recognized that the use of stainless steel imposes a severe nuclear penalty on the system which can best be offset by raising the exit gas temperature of the system. Once the design temperature is substantially higher than the levels in use at Calder Hall and Marcoule, the whole materials system based on CO_2 is suspect, in virtue of the chemical reactions between CO_2 and graphite. In order to circumvent this problem, helium was selected for the coolant in GCR-2. It was recognized ab initio that helium is severely handicapped since it is not available on the world market. If helium were universally available, it would undoubtedly be the standard coolant for such reactors. The chemical inertness of helium makes catastrophic oxidation of the clad material, as well as the graphite almost impossible since only impurities enter into such reactions. Thus, the character of the principal maintenance problem, location and replacement of leaking fuel elements, is greatly simplified.

   The high cost of helium imposes an engineering requirement on the design for much-improved leak-tightness over the Calder Hall performance. It is the opinion of ORNL that adequate leak-tightness can be assured by proper design. An over-all system helium-leakage loss of 1% per day, which is more than ten times higher than is achieved in present practice in large gas systems, would result in an increase in net power cost of 0.05 mills/kwh.

1.3 Comparison of GCR-2 with Fossil Fuel Plants

It is of interest to compare the GCR-2 design with recently constructed fossil fuel plants of approximately the same thermal rating. A relative analysis of the GCR-2 and three such plants is presented in Table 1.1. Table 1.1 lists an escalated cost column for each of the fossil fuel plants which takes account of the increase in construction costs since the date of construction of these plants. Although the GCR-2 is not competitive with these modern steam plants, it should be noted that the GCR-2 is at least as competitive as recent studies have shown the best pressurized-water reactors to be.

TABLE 1.1

COMPARISON OF COST AND PERFORMANCE DATA FOR TYPICAL COAL-FIRED POWER PLANTS[1] WITH CORRESPONDING DATA FOR THE ORNL GCR-2

Plant Designation (ORNL or Electrical World)	GCR-2	303(218)		304		305	
GENERAL DATA							
Total Generator Rating - Mw	252	262		275		230	
Date of Construction	1958	1954		1955		1954	
Thermal Efficiency Over-all	32.8	32.48		37.22		33.98	
Steam Pressure psia	950	900 and 1450		2050		1475 and 1825	
Steam Temperature, Initial Superheater °F	950	950 and 1000		1050		1010	
(Reheat) °F	--	1000		1000		1010	
Plant Factor, %	80	80.85		87.7		89.4	
INVESTMENT DATA ($/kw)	(Base)	(Base)	(Escalated)[2]	(Base)	(Escalated)[2]	(Base)	(Escalated)[2]
(310) Land	1.83	0.43	0.43	4.93	4.93	0.49	0.49
(311) Structures and Improvements	42.24	35.27	44.70	40.02	47.70	33.56	41.20
(312) Boiler or Reactor Plant	147.61	60.62	76.70	52.82	63.00	64.72	81.90
(314) Turbine-Generator Plant	66.20	39.24	49.70	38.07	45.40	42.20	53.40
(315) Accessory Elect. System	22.48	7.51	9.51	9.75	11.64	12.88	16.31
(316) Miscellaneous Plant Equipment	4.81	1.53	1.94	1.97	2.35	2.00	2.53
TOTAL	285.17	144.60	182.98	147.56	175.02	155.85	195.83
Total Less Reactor or Boiler	137.56	83.98	106.28	94.74	112.02	91.13	113.93
COST OF ENERGY (mills/net kwh)							
Fixed Charges							
A. Plant Costs	6.38	2.93	3.86	3.353	4.43	3.319	4.48
B. Computed at (%)	14.0	13.6	14.0	12.61	14.0	15.0	14.0
C. Fuel Inventory at 4%	0.76						
D. Fuel Element Fab. at 14%	0.38						
TOTAL Fixed	7.52	2.93	3.86	3.35	4.43	3.32	4.48
OPERATING COSTS (mills/net kwh)							
Wages (including supervision)	0.38	0.25		0.38		0.18	
Water, lubrication, supplies	0.25	0.03		0.15		0.004	
Maintenance	0.26	0.15		0.21		0.066	
Total, operating and maintenance (excluding fuel)	0.89	0.43		0.74		0.25	
Fuel	1.73	2.78		2.73		2.97	
Total Operation (including fuel)	2.62	3.21		3.47		3.22	
Total Cost of Energy	10.14	6.14	7.07	6.82	7.90	6.54	7.70

[1] Base data for coal-fired plants from "Electrical World," (October 7, 1957).

[2] All costs except land and operating costs were escalated to a 1958 base at 6% per year compounded semiannually and fixed charges were computed at 14% for an 80% load factor.

During the course of the GCR-2 design study it became apparent that it would be possible to improve the plant performance by changing certain important parameters. Unfortunately, the press of time did not allow for incorporating these changes into the present design. Three improvements which would probably be included in a future plant optimization are:

1. Increase the steam pressure to 1,400 psia.
2. Increase the power density, and hence the over-all thermal rating, by boosting the pumping power per channel.
3. Increase the maximum fuel capsule surface temperature to 1300°F.

These changes would increase the thermal power of the system from 687 Mw to more than 1100 Mw and produce an over-all savings in net power cost of approximately 2 mills/kwh.

1.4 Future of Gas-Cooled Reactors in the United States

It is only natural to inquire into the possible future of gas-cooled reactors in the United States power reactor economy. It is too early to predict how rapidly gas-cooled reactor technology would improve in attempting to achieve competitive costs with the best fossil fuel plants. Nevertheless, there are important variations on the gas-cooled-reactor theme which remain to be investigated before a complete appraisal is possible. Some of these possibilities which are discussed in Part 4 of this report will be investigated by ORNL during the next several months. The most important variations are the utilization of beryllium as the cladding material for the UO_2 fuel elements, and the replacement of graphite with heavy water as the moderator. It is impossible to judge at this time how the introduction of either beryllium cladding or heavy-water moderator would alter the economics of the power plant.

An important distinction needs to be made in comparing gas-cooled reactors of the GCR-2 type and those which the British and French are building at the present time. It is not certain that it is possible to establish a free-world market in helium and enriched uranium, even at the two per cent level. Accordingly, if the United States decides to underwrite the development of a gas-cooled reactor technology, at least some portion of the effort should probably be expended in the design and

construction of reactors which are suitable for the export market. The major variations of the GCR-2 design mentioned above could develop into systems utilizing CO_2 and perhaps even into systems in which the enriched-uranium inventory is limited to the first core with the recycle being based completely on plutonium produced in the reactor, plus natural-uranium feed. As such they would be prime candidates for export.

1.5 Conclusions

The Oak Ridge National Laboratory offers the following conclusions which represent the opinion of the Laboratory on the basis of the work done through March 1, 1958 on the gas-cooled reactor program.

1. Adequate technology exists to build gas-cooled reactors in the United States, either of the natural-uranium or the enriched-uranium variety, in the very near future.
2. An enriched gas-cooled reactor of the GCR-2 type will produce cheaper power than a natural-uranium plant. This follows from the large reduction in capital costs achieved by enriching the fuel combined with the fact that no serious penalty is paid in rising fuel costs as a result of fuel enrichment.
3. Gas-cooled reactors are at the present time technologically competitive with the best available pressurized-water reactors.
4. On the basis of recent paper studies, it appears that gas-cooled reactors are also competitive with pressurized-water reactors on an economic basis in the United States.
5. Both gas-cooled reactors and pressurized-water reactors have substantial developmental potential to be realized in the future. There does not seem to be any fundamental reason for selecting one type for development to the exclusion of the other.

SECTION 2

GAS-COOLED REACTOR PHYSICS

2. GAS-COOLED REACTOR PHYSICS

CONTENTS

2.1 Multiplication Factor 2.1

2.1.2 Neutron Yield 2.2

2.1.2 Fast Effect 2.2

2.1.3 Resonance Escape Probability 2.7

2.1.4 Thermal Utilization 2.12

2.1.5 Cross Sections 2.14

2.1.6 Check Calculations 2.19

2.2 Results of Lattice Calculations 2.29

2.2.1 Uranium Metal Lattices - Fig. 2.8 . . . . . 2.32

2.2.2 Lattices with Single UO_2 Rods - Figs. 2.9 – 2.16 . . . . . 2.32

2.2.3 Lattices with Clusters of UO_2 Rods - Figs. 2.17 – 2.27 . . 2.41

2.2.4 General Conclusions. 2.52

2.3 Loss of Neutrons by Leakage 2.66

2.4 Reactivity Limitations on Fuel Exposure 2.73

2.5 Temperature Coefficient of Reactivity 2.86

2.6 Control Rods 2.93

2.7 Power Flattening 2.97

2.8 Shielding 2.106

2.8.1 Gamma-Ray Dose Rate 2.106

2.8.2 Fast and Thermal Neutron Dose Rate 2.109

2.8.3 Heating in the Concrete 2.110

2. GAS-COOLED REACTOR PHYSICS

The optimization of a gas-cooled reactor plant with respect to the cost of producing electricity reduces to the selection of a proper balance between capital costs and fuel cycle costs. Once the heat-transfer characteristics of various fuel element configurations are established, it becomes a question of determining how much fuel, or heat-transfer surface, can be put into the reactor, and how much energy can be extracted from the fuel elements before they must be removed from the reactor. The main questions, then, from the nuclear analysis point of view, have to do with the multiplication factor and the reactivity lifetime of the core as a function of fuel element size, spacing, and enrichment. Other parameters whose effect must also be evaluated are cladding thickness, cooling channel diameter, moderator quality and density, etc. In addition to these major problems, design of the plant requires information on the temperature coefficient of reactivity, requirements for control rods and the effectiveness of possible control rod configurations, radiation shielding requirements, radiation heating in various reactor components, and finally the possible means for obtaining a reasonably uniform power density distribution. These topics are discussed in the paragraphs that follow.

2.1 Multiplication Factor

The multiplication factor, or reproduction factor, of the fuel lattice is expressed by the classical four factor formula

$$k = \eta \, \epsilon \, p \, f. \tag{2.1}$$

Here

η = direct yield of fission neutrons per neutron absorbed in fuel,

ϵ = fast fission factor,

p = resonance escape probability,

f = thermal utilization, the ratio of the number of thermal neutrons absorbed in fuel excluding those absorbed in U^{238} resonances, to the total number absorbed in the lattice, excluding those absorbed in the resonances of U^{238} and stainless steel.

The criticality constant is given by $k_{eff} = k \, e^{-B^2\tau} \, (1 + L^2B^2)^{-1}$.

The neutron leakage factors are discussed in detail in a later paragraph.

2.1.1. Neutron Yield: The yield of neutrons per neutron absorbed in fuel, has been obtained directly from the measured neutron cross sections. There has been a traditional discrepancy between values of η obtained from the cross sections and those inferred from exponential pile measurements, with values for natural uranium at room temperature ranging from 1.26 to 1.35. Figure 2.1 compares the calculated values of η as a function of enrichment, with values based on exponential experiments. The process of obtaining η from the measured buckling values in the exponential experiments usually involves calculated values of the resonance escape probability, p. Of the experimental values shown in the figure, only those reported by Kouts rest on measured values of p, and for these the disagreement with the calculated curve is comparatively small. In view of this fact, and also because there appeared to be no alternative for enriched fuel at elevated temperatures, the decision was made to employ calculated values of η throughout. The value used for each lattice can be found in Table 2.10.

2.1.2. Fast Effect: The fast fission factor expresses the increase in the net number of fission neutrons available to the chain reaction as a result of fissions produced in U^{238} and U^{235} by fast neutrons ($E_n \gtrsim 1$ Mev). It is given by the expression

$$\epsilon = 1 + \frac{(\nu - 1 - \sigma_c/\sigma_f)(\sigma_f/\sigma_t)\,P}{1 - \frac{\nu\sigma_f + \sigma_{el}}{\sigma_t}\,P'} \qquad (2.2)$$

where P, P' are the probabilities of collision within the fuel element of fission neutrons having a source distribution like the power distribution in the rod, and a uniform source distribution, respectively. (In the present calculation, P' was assumed to be equal to P). The quantities ν, σ_f, σ_c, σ_{el}, and σ_t are the fission neutron yield, the average cross sections for fission, capture, and elastic scattering, and the total cross section of the fuel, all averaged over the fission neutron spectrum. Values of the cross sections used in these calculations are somewhat different from those used in the past. For example, the values employed in early project days, and in the design of

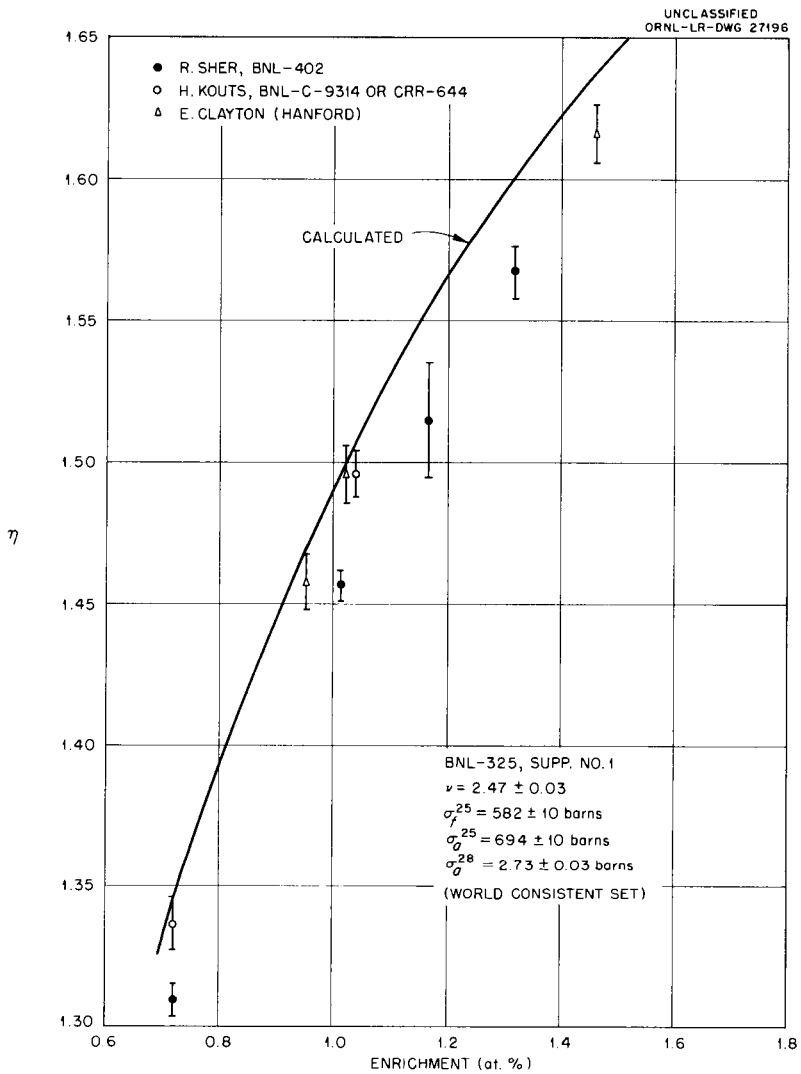

Fig. 2.1. Fission Neutrons Produced per Neutron Absorbed in Uranium.

the Brookhaven reactor, are typified by the numbers given in the Reactor Handbook.[1] Values used in the present calculations were computed from curves given in BNL-325 and its Supplement. All cross sections in the following table are in barns.

TABLE 2.1 CROSS SECTIONS USED IN CALCULATING FAST FISSION FACTOR

Quantity	R.H.	Present Calculation
σ_f	0.29	0.30
σ_a	0.06	0.07
σ_i	2.45	2.03
σ_{el}	1.5	4.9
σ_t	4.3	7.3
ν	2.55	2.50

The principal difference is seen to be in the elastic and total cross section. Since elastic scattering has comparatively little effect on ϵ, the results obtained with the two sets of cross sections are not expected to be very different. That this is the case can be seen from the following table of values of ϵ for various sizes of uranium metal rods.

Values of P as a function of σ_t and the rod radius are tabulated by Case, de Hoffman and Placzek.[2]

Values of the fast fission factor for uranium-metal rods and for UO_2 rods are given in Fig. 2.2. For a cluster of rods, the value of ϵ is expected to be between that for a single rod of the cluster and that for a single rod of

[1] Reactor Handbook, Vol. 1, Table 1.5.20, AECD-3645 (March 1955).

[2] K. M. Case, F. de Hoffman, and G. Placzek, Introduction to the Theory of Neutron Diffusion, Vol. 1, Los Alamos Scientific Laboratory (June 1953)

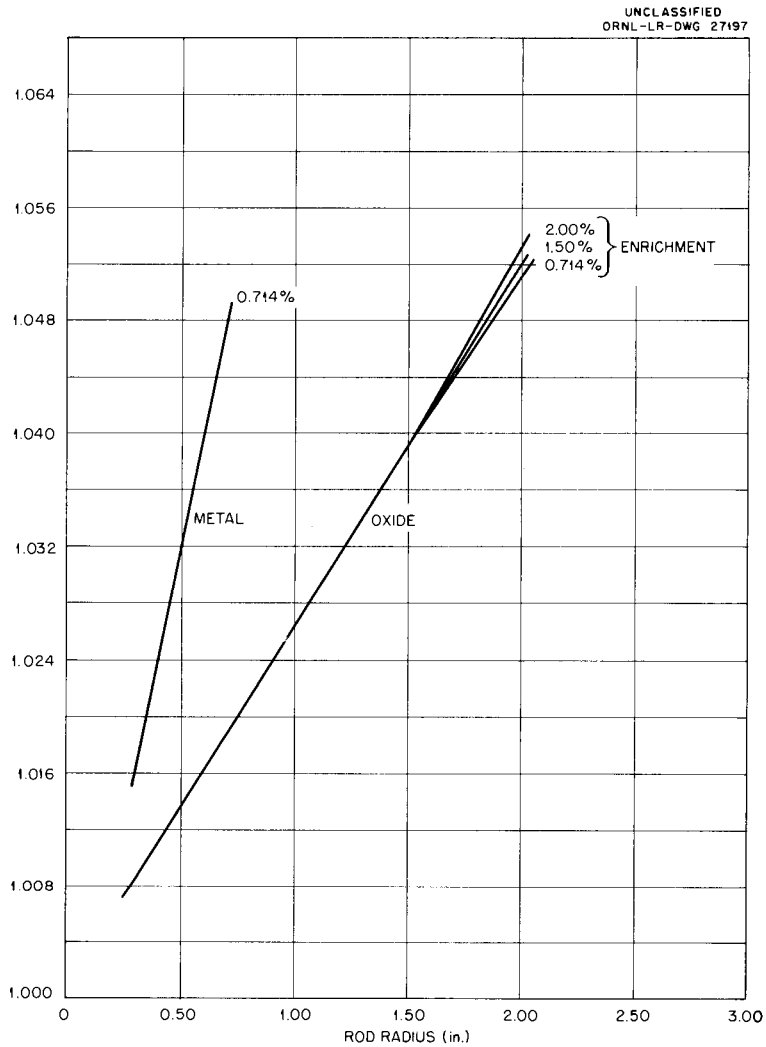

Fig. 2.2. Fast Fission Factor for UO_2 and U Metal Rods.

TABLE 2.2 EXPERIMENTAL AND THEORETICAL VALUES OF FAST FISSION FACTOR

Rod Diameter (in.)	Location of Rod in Pile	Experimental* Value of ϵ	Calculated Value of ϵ	
			P/606*	Present Calculation
0.750	Reflector	1.027	1.022	1.021
0.750	Fuel channel	1.022	1.022	1.021
1.10	Reflector	1.035	1.030	1.030
1.10	Fuel channel	1.034	1.030	1.030
1.345	Reflector	1.043	1.035	1.036
1.345	Fuel channel	1.046	1.035	1.036

*I. Kaplan and J. Chernick, Uranium Graphite Lattices, The Brookhaven Reactor, Geneva Conference P/606. (The cross section values used are approximately those quoted from the Reactor Handbook).

the same total cross sectional area as the cluster, and rather closer to the latter. An approximate calculation of the collision probability, P, for seven-rod clusters yields values slightly smaller than those for the equivalent single rod (of same total cross sectional area). Results for clusters of seven rods of various sizes are tabulated below.

TABLE 2.3 FAST FISSION FACTOR FOR CLUSTERS OF UO_2 RODS

Rod Diameter (in.)	ϵ	
	for Cluster	for Equivalent Single Rod
0.5	1.016	1.018
0.75	1.024	1.026
1.00	1.028	1.034

2.1.3 Resonance Escape Probability: The resonance escape probability for a lattice of infinite extent is here defined as the probability that a neutron produced in fission will slow down to an energy below the lowest resonance of U^{238}, that is, below about 6 ev, without capture in the resonances of U^{238} or of stainless steel. Epithermal captures in U^{235} or in any of the plutonium isotopes are disregarded in calculating the resonance absorption rate, because the effect of such captures on k is taken into account in calculating the thermal utilization (see Section 2.1.5 below). The same argument applies to captures in U^{238} and in stainless steel attributable to the 1/v portion of their epithermal capture cross sections. In keeping with these definitions, the resonance escape probability, p, is written

$$p = \exp - \left\{ \frac{\sigma_{r,u} + \frac{N_{c\ell}}{N_u} \sigma_{r,c\ell}}{\frac{N_m}{N_u} (\xi\sigma_s)_m + \frac{N_{c\ell}}{N_u} (\xi\sigma_s)_{c\ell} + \frac{N_o}{N_u} (\xi\sigma_s)_o + (\xi\sigma_s)_u} \right\}, \quad (2.3)$$

where

σ_r = effective resonance integral,

σ_s = elastic scattering cross section,

ξ = average logarithmic energy loss of a neutron in elastic collisions,

N = number of atoms in a cell divided by the volume of the cell.

The subscripts m, u, o, $c\ell$ refer to moderator, uranium, oxygen, and cladding, respectively.

The problem of computing p reduces essentially to that of determining σ_{ru}, the effective resonance integral of U^{238}. The theoretical treatment[3] of the subject is quite complex, and there are rather serious potential ambiguities associated both with the use of UO_2 instead of the metal, and with the cluster geometry. It is fortunate that the results of measurements made at Stockholm, by Hellstrand[4], on the resonance absorption of U^{238} in metallic and oxide rods, in various geometries including seven-rod clusters have recently become available.

---

[3] E. P. Wigner, E. Creutz, H. Jupnik, T. Snyder, "Resonance Absorption of Neutrons by Spheres," J. Appl. Phys., 26, 260 (1955).

[4] E. Hellstrand, "Measurements of the Effective Resonance Integral in Uranium Metal and Oxide in Different Geometries," AEF-84, AB Atomenergi, Stockholm, (June 1957)

The effective resonance integral has usually been expressed in the United States in the form

$$\sigma_r = A + B \cdot \frac{S}{M} , \tag{2.4}$$

where S/M is the surface-to-mass ratio of the fuel element, in cm^2/gram.

If depression of the resonance flux in the fuel is taken into account, the expression becomes

$$\sigma_r = \frac{A}{F} + B \cdot \frac{S}{M}, \tag{2.5}$$

where F is the ratio of the flux at the surface of the fuel lump to the average flux in the lump. For small lumps, a further correction has sometimes been applied to account for the possibility that resonance neutrons may pass through the lump without suffering a collision, and the expression takes the form

$$\sigma_r = \frac{A}{F} + C \cdot B \cdot \frac{S}{M} , \tag{2.6}$$

where C is the factor accounting for penetrability of the lump.

In the USSR,[5] the effective resonance integral has been written in the form

$$\sigma_r = A' + B' \, (S/M)^{1/2} . \tag{2.7}$$

It has been shown that the two forms do not differ much over a wide range of values of S/M. Hellstrand has found empirically that the experimental resonance integrals for both metal and oxide lumps correlate with Eq.(2.7) over a wider range of S/M. For this reason, Eq.(2.7)is the form that has been adopted. With a 1/v contribution of 1.2 barns deducted from the volume absorption term, the resonance integral for UO_2 lumps is found by Hellstrand to be

---

[5] I. I. Gurevich and I. Y. Pomeranchouk, "Resonance Absorption in Heterogeneous Systems," Proceedings of Geneva Conference, Vol. 5, P/649, p. 466.

$$\sigma_r = 4.05 + 26.6\ (S/M)^{1/2}\ ;\quad 0.08 \leq S/M \leq 0.7. \tag{2.8}$$

The experimental correlations of Hellstrand confirm a proposal by E. R. Cohen[6] that the surface to be used for a cluster of rods is the "rubber band" surface, that is, that of a membrane stretched tightly around the cluster.

It should be pointed out that Eq. (2.3) neglects the effect of non-uniform spatial distribution of the resonance flux in the moderator. This is customarily taken into account by writing $-\ln p = (T+X)^{-1}$, in analogy to the thermal utilization. Here T^{-1} is the exponential in Eq. (2.3) and X is given by

$$X = \frac{K_m r_2^2 - K_m^2 r_1^2}{2\,K_m r_1}\ \frac{I_1(K_m r_2)\ K_o(K_m r_1) + I_o(K_m r_1)\ K_1(K_m r_2)}{I_1(K_m r_2)\ K_1(K_m r_1) - I_1(K_m r_1)\ K_1(K_m r_2)}\ , \tag{2.9}$$

where r_1, r_2 are the inner and outer radii, respectively, of the moderator in the cell and K_m is an inverse diffusion length in the resonance region for the moderator,

$$K_m = \left[3\ N_m^2\ \sigma_{tr}\ \xi\ \sigma_s\ (\ln E_2/E_1)^{-1} \right]^{1/2}\ ; \tag{2.10}$$

E_1 and E_2 are the lower and upper limits of the resonance energy region; σ_{tr} is the transport cross section of the moderator. For UO_2 the quantity $\ln E_2/E_1$ is often taken to be about 7, although there is evidence[7] that a somewhat lower value is to be preferred. The point to be made here is that this part of the formalism probably fails to describe the physical situation in the moderator, with a combination of slowing down and diffusion occurring simultaneously which tends to smooth out the flux distribution. In the design of graphite reactors, such uncertainties have usually been absorbed in a consistent set of parameters, including η, ϵ, p, and f, which were based on measured values of the material buckling of the lattice. Including the term X of Eq. (2.9) would increase the

---

[6] E. Hellstrand, op. cit. p. 2.7.

[7] See F. L. Fillmore, Buckling of Graphite Moderated Lattices Containing Seven Fuel Rods, NAA-SR-1535.

value of p by 2 or 3% for the reference core design. However, this is believed to be an overestimate of the effect, and in the present calculations, employing calculated values of η, the depression of the resonance flux near the fuel was neglected.

It may be of interest to point out the relative importance of the terms in the exponent of Eq. (2.3). For the reference lattice (3/4-in.-dia rods, 8-in. lattice pitch, 2% enrichment), the UO_2 contributes about 2% of the denominator and the clad about 0.3%. In the numerator, the cladding contributes about 3%.

The temperature dependence of the resonance escape probability is quite important because it influences the change in reactivity of the reactor between room temperature and operating temperature, and because it contributes a significant negative component to the temperature coefficient of reactivity at operating temperature. The problem consists of two parts, that of determining the temperature dependence of the effective resonance integral, and that of determining the effective temperature of the fuel.

The temperature coefficient of the effective resonance integral has been reported for uranium metal by Davis and Rodeback,[8,9] and for UO_2 by Creutz, et al.[10] Between 40°C and 300°C, Davis finds

$$\frac{1}{\sigma_r} \frac{d\sigma_r}{dT} \sim (1.56 \pm 0.12) \times 10^{-4}/°C;$$

the coefficient is constant over this range. Between 20°C and 660°C, Rodeback reports

$$\frac{1}{\sigma_r} \frac{d\sigma_r}{dT} \sim 0.9 \times 10^{-4}/°C.$$

---

[8] M. V. Davis, "Resonance Absorption of Neutrons by Uranium Cylinders," J. Appl. Phys. 2, 250 (1957).

[9] G. W. Rodeback, Temperature Coefficients of Uranium and Thorium Resonance Integrals, NAA-SR-1641 (1956).

[10] E. Creutz, H. Jupnik, and E. P. Wigner, "Effect of Temperature on Total Resonance Absorption of Neutrons by Spheres of Uranium Oxide," J. Appl. Phys. 26, 276 (1955).

Between 20°C and 1000°C, Creutz et al., report

$$\frac{1}{\sigma_r} \frac{d\sigma_r}{dT} \sim 2 \times 10^{-4}/°C.$$

We have used Davis' result in the present calculations.

The mean temperature of the fuel has been determined rather approximately for an average heat flux. No attempt has been made to obtain a fuel temperature averaged over the reactor (as with perturbation theory, for example), but the distribution of resonance neutron absorptions within a single fuel element was taken into account. An average temperature was calculated for a single rod with a resonance absorption distribution, b(r), taken from Hellstrand's measurements.[11] The temperature distribution was considered to be parabolic, $T(r) = T_o - ar^2$, where T_o is the center temperature of the fuel rod, and the constant a contains information about the conductivity and the power density in the rod.

With

$$\bar{T} = \frac{\int_o^R T(r)\, b(r)\, r\, dr}{\int_o^R b(r)\, r\, dr} \tag{2.11}$$

(R ≡ rod radius) it can be shown that

$$\sigma_r(T) = \sigma_r(20°C) \exp\left\{Z(\bar{T} - 20°C)\right\}, \tag{2.12}$$

where $Z = +1.56 \times 10^{-4}/°C$ is the temperature coefficient of the resonance integral. For T_o = 1274°C (2325°F) and T(surface) = 620°C (1150°F), it is found that $\bar{T}_o$ = 760°C (1400°F). This lies closer to the surface temperature than to the central temperature for several reasons: the parabolic temperature distribution, the cylindrical geometry, and the concentration of resonance absorptions at the surface of the rod. There is some ambiguity

---

[11] E. Hellstrand, op. cit. p. 2.7.

in the choice of surface temperatures in the application of these calculations to the cluster geometry; thus, the precise value of the resonance integral to use at operating temperature is slightly uncertain. For 8-in. lattice pitch, 3/4-in.-dia rods in a seven-rod cluster, a change in the uranium temperature from 20°C to 760°C will decrease p, and hence k, by about 3%. The effect on the temperature coefficient of reactivity is discussed in more detail in Section 2.5

2.1.4. Thermal Utilization: The thermal utilization of a lattice cell is defined as the ratio of the number of thermal neutrons absorbed in the fuel of the cell, including those absorbed in the $\frac{1}{v}$ part of the U^{238} absorption to the total number of thermal neutrons absorbed in the cell, including those absorbed in the $\frac{1}{v}$ part of the U^{238} and cladding absorption. In terms of the appropriate cross sections it is therefore written as:

$$f = \frac{V_f \Sigma_a^f \bar{\phi}_f}{V_f \Sigma_a^f \bar{\phi}_f + V_m \Sigma_a^m \bar{\phi}_m + V_p \Sigma_a^p \bar{\phi}_p}, \qquad (2.13)$$

where Σ_a^f, Σ_a^m, and Σ_a^p are macroscopic effective absorption cross sections in the fuel, moderator, and poisons (cladding material, for example), respectively. The $\bar{\phi}_i$ are the average effective fluxes and the V_i are the volumes of the respective regions. The effective cross sections used in all room-temperature calculations were averaged over a Maxwellian flux spectrum with T_n = 20°C. High-temperature calculations were done with the cross sections developed in Section 2.1.5. For the reasons set forth in the section on check calculations, it was decided to use the P_3 spherical harmonics approximation in computing the fluxes required to determine the thermal utilization of the lattices for the ORNL-GCR-2 design study. These calculations were done on the IBM 650 computer, using a program prepared at KAPL by Weil. The loss of numerical significance which sometimes results with high-order spherical harmonics approximations, due to the propagation of small errors from one region to the next, is substantially eliminated in this formulation of the problem through the use of a set of reduced Bessel functions whose magnitudes remain of order unity despite large changes in the parameters in going from one region to the next. The program places no restriction on the number of regions in the

cell, and anisotropic scattering up to the P_2 term of the spherical harmonics expansion of the scattering cross section is allowed. The input data required for a calculation consists of one card for each region containing the values of the source constant, absorption cross section, total cross section, two coefficients of the harmonic expansion of the scattering cross section, and the inner and outer radii of the region. The machine time required for one of the six region calculations commonly used in the current study was about 25 min.

The only complication which arose with the use of the program came from the restriction that zero absorption was not allowed. In problems involving a single fuel rod in the cooling channel, the program was therefore made to compute the fluxes under the assumption that each component is continuous across the gap between the fuel and moderator regions. The procedure developed by Newmarch[12] was then used to take into account the depression of the flux across the cooling channel due to the probability that some neutrons will enter the cooling channel from the moderator and fail to strike the fuel rod. Newmarch has shown that within the diffusion theory approximation the flux shapes in the fuel and moderator are not affected by the presence of the channel, the only effect being that the flux at the inner surface of the moderator is greater than the flux at the outer surface of the fuel rod by a factor R which is given by

$$R = 1 + \frac{a}{\lambda_a^f} \frac{1}{G(K_f a)} \left\{ 1 - \frac{2}{\pi} \left(\arcsin \frac{a}{c} + \frac{a}{c} \sqrt{1 - \frac{a^2}{c^2}} \right) \right\} , \qquad (2.14)$$

where $\lambda_a^f = \frac{1}{\Sigma_a^f}$ is the absorption mean free path of the fuel rod and

$$G(K_f a) = \frac{K_f a}{2} \frac{I_o(K_f a)}{I_1(K_f a)} , \quad K_f^2 = 3 \Sigma_t^f \Sigma_a^f . \qquad (2.15)$$

---

[12] D. A. Newmarch, "A Modification to the Diffusion Theory of the Thermal Fine Structure in a Reactor to Account for the Effect of Air Channels," J. Nuc. Energy, 2, 52 (1955).

a is the radius of the fuel rod, c is the radius of the cooling channel, and the function $G(K_f a)$ is the diffusion theory expression for the ratio of the flux at the surface of the rod to the average flux in the rod.

In the calculations of the thermal utilization for the fuel element cluster no attempt was made to take into account the variation of the flux in the void regions between the rods. This was due in part to the difficulty in computing the R factors for the complicated cluster geometry. It was felt, however, that the spread of the cluster over most of the cooling channel would make the effect smaller in this geometry than with a single rod, where the decrease in thermal utilization was of the order of 0.5%.

Due to the extremely good interpolation properties of the thermal utilization over the region covered by the present calculations, it was unnecessary to do a flux calculation for each lattice pitch at which the value of k_∞ was required. For example, with the clusters of 0.75-in.-dia oxide rods it was found that a linear interpolation of f from the 6-in. to the 11-in. lattice pitch falls about 0.5% below the computed values at the 8-in. and 9-in. pitches. The slightly non-linear interpolation which was actually used throughout the study to give the value of f at any missing intermediate lattice pitches gave values with an accuracy better than 0.2%.

As dis sed in Section 2.1.6 on check calculations the results of the extensive room temperature flux calculations were cast in a quite general form which eliminated the necessity of doing machine calculations of the fluxes for all of the high-temperature lattices studied. This method, referred to as the extrapolated method, was used for most of the high temperature calculations.

2.1.5. Cross Sections: Cross sections at operating temperature were needed for the calculations of initial reactivity (Sections 2.1 – 2.3) and also for the study of reactivity vs exposure (Section 2.4). For most purposes, it was convenient to use effective one-group cross sections. Thus the resonance absorption effects of all materials other than U^{238} and stainless steel were included in effective cross sections $\hat{\sigma}$ as defined, for example, by Westcott:[13]

---

[13] C. H. Westcott, The Specification of Neutron Flux and Effective Cross Sections in Reactor Calculations, CRRP-662 (August 15, 1956).

$$\hat{\sigma} = (\text{reaction rate per target nucleus})/Nv_{2200},$$
$$\hat{\sigma} = (g + rs)\ \sigma_{2200}. \tag{2.16}$$

Here N is the total neutron density, v_{2200} is the velocity 2200 m/s, and σ_{2200} is the cross section for neutrons at 2200 m/s. The flux spectrum is assumed to consist of a Maxwellian component at temperature T_n, plus a dE/E tail cut off at a lower limit of 5 kT_n. The factor g takes into account the averaging of the cross section over the Maxwellian part of the neutron distribution; r is $\frac{\sqrt{5\pi}}{4}$ times that fraction of neutrons which lies in the dE/E tail; and s depends on the resonance integral $\int_{5kT_n}^{\infty} \sigma\, dE/E$. For a 1/v absorber, g = 1 and s = o. (The factor is always positive; but s is negative when $\int_{5kT_n}^{\infty} \sigma\, dE/E$ is less than the corresponding integral with σ set equal to $g\ \sigma_{2200}\ v_{2200}/\ v$.)

The assumption of this simplified form for the spectrum by-passes such questions as how the resonance absorptions distort the dE/E tail, how this tail fits on to the Maxwell component, and how the Maxwell component is distorted inside the fuel element both by preferential absorption of lower energy neutrons and by scattering of neutrons with energetic atoms in the high-temperature fuel rods. However, even the determination of the parameters T_n and r for the simplified spectrum poses non-trivial problems.

The temperature T_n which best describes the thermal neutron distribution may be significantly different from the temperature T_m of the moderator atoms. For an infinite homogeneous medium with 1/v capture cross section, Coveyou et al. find[14]

$$T_n \sim T_m\ (1 + 1.11\ AK).$$

Here A is the mass number of the scatterer and

$$K = (2/3)^{1/2}\ (293/T_m)^{1/2}\ \frac{\Sigma_a(2200\ \text{m/s})}{\Sigma_s}\ ;$$

Σ_a and Σ_s are the macroscopic cross sections of the absorbing and scattering species. The reliability of this recipe for computing T_n has

---

[14] R. R. Coveyou, R. R. Bate, and R. K. Osborn, J. Nuc. Eng., 2, 153 (1956).

been confirmed experimentally for homogeneous mixtures.[15] Though its usefulness for heterogeneous reactors is uncertain,[16] it was considered the best guide available for the present study. The formula was applied to the heterogeneous reactor under consideration by replacing its lattice cell with one in which all materials are uniformly distributed over the cell. K is then computed with flux-weighted cross sections as suggested by disadvantage factors from the P_3 calculation (see Sections 2.1.4 and 2.1.6). The results are given in Table 2.4.

TABLE 2.4

NEUTRON TEMPERATURE

(8-in. lattice pitch, seven 3/4-in. dia UO_2 rods, 3 1/4-in. cooling channel, T_m - 750°F)

(atom % U^{235})	T_n/T_m	T_n(°K)
1.2	1.164	782
1.5	1.179	792
2.0	1.204	809
2.5	1.221	821

The neutron temperature chosen for calculations at the operating temperature was 814°K. In Table 2.5 are listed g factors for this temperature. The values in column 3 were derived by numerical integration of the cross sections in BNL-325[17] over a Maxwell spectrum at 814°K. The g values

---

[15] M. J. Poole, A Measurement of the Neutron Spectra in Aqueous Moderators and Reactor Lattices by Time-of-Flight Methods Using a Pulsed Linear Accelerator, NRDC 95, (1956).

[16] Very recent information received from Harwell, by private communication, suggests a slightly better fit is obtained experimentally for heterogeneous graphite lattices via $T_n \sim T_m (1 + 1.08\ AK)$.

[17] Neutron Cross Sections, BNL-325 and Supplement No. 1 to BNL-325.

TABLE 2.5

EFFECTIVE CROSS SECTIONS AT T_n = 814°K

(See text for details)

1	2	3	4	5	6	7	8
Material	Reaction	g_1	g_2	s_1	s_2	σ_{2200} (barns)	$\hat{\sigma}$ (barns)
U^{235}	absorption	0.905	0.923	0.132	0.129	694	642
U^{235}	fission	0.913	0.911	0.007	0.008	582	525
Pu^{239}	absorption	2.200	2.345	-1.39	-1.30	1025	2128
Pu^{239}	fission	1.875	2.030	-1.39	-1.17	738	1290
Pu^{240}	absorption	1.188	1.205	59.3	62.2	250	1792
Pu^{241}	absorption					1326*	2085*
Pu^{241}	fission	1.660	1.663	-0.96	-0.82	971	1527
Graphite	absorption	1		0		.004	.004
Stainless Steel 430	absorption	1		0		2.59	2.59

*The ratio $\sigma_a^{41}/\sigma_f^{41}$ = 1.365 was assumed for all neutron energies.

(Note regarding stainless steel clad thickness: Throughout the tables and the figures of this section, the thicknesses listed are those for 430 stainless steel, whose thermal neutron absorption cross section is 0.2166 cm^{-1} (at 2200 m/sec). Corresponding cross section for 304 stainless steel is 0.2465 cm^{-1}. Thus, for equal absorption, the thickness of 304 stainless steel is 0.88 that of 430 stainless steel, for example, 0.020-in. 430 stainless steel is equivalent to 0.0176-in. 304 stainless steel. Although 430 stainless steel was initially considered, the design is now predicated on the use of 304 stainless steel.)

in column 4 were derived by extrapolating values given by Westcott[18] for the region 20°C to 400°C.

The s factors listed in column 5 of Table 2.5 were derived by numerical integration over the BNL-325 cross sections for U^{235} and Pu^{239}, and for the other isotopes by comparison with other experimental data in the resonance region. The s values in column 6 were derived by extrapolating Westcott's values to 814°K.

An estimate of the factor r may be made by relating the fission-neutron production rate with the slowing-down density. The latter is in turn related to the magnitude of the dE/E tail in the neutron spectrum. When U^{235} and U^{238} are the only fissionable materials in the reactor,

q_o = number of neutrons produced in fission per unit time per unit volume of reactor,

$$q_o = \epsilon N_{25}\, \nu_{25} \left[g\, N_f^{\text{Maxwell}}\, v_{2200} \sigma_{f,\,2200}^{25} + \int_{5k\,T_n}^{\infty} \sigma_f^{25} \frac{q_o}{(\xi\Sigma_t)_{sd}} \frac{p\ (E)}{1+B^2\tau_E} \frac{dE}{E} \right]. \tag{2.17}$$

Here q_o is the slowing-down density at the top of the slowing-down region; N_{25} is the number of U^{235} atoms per unit volume in the homogenized cell; N_f^{Maxwell} is the neutron density in the fuel, counting only those neutrons in the Maxwellian component; σ_f^{25} is the U^{235} fission cross section; $(\xi\Sigma_t)_{sd}$ is the effective slowing-down power in the homogenized cell; and $q_o\, p(E)/(\xi\Sigma_t)_{sd}\ (1+B^2\tau_E)E$ is the non-Maxwellian part of the flux, where the effects of resonance absorption and leakage have been taken into account. The equation can be solved for q_o, to give

$$q_o = \frac{N_{25}\ \nu_{25}\ g\ N_f^{\text{Maxwell}}\ v_{2200}\ \sigma_{f,2200}^{25}}{\dfrac{1}{\epsilon} - \dfrac{\nu_{25}\ N_{25}}{(\xi\ \Sigma_t)_{sd}}\ \dfrac{p'}{1 + B^2\tau'} \displaystyle\int_{5kT_n}^{\infty} \sigma_f^{25}\ dE/E} \tag{2.18}$$

Here $p'\ /(1+B^2\tau')$ is a mean value of this energy-dependent quantity.

---

[18] C. H. Westcott, Effective Cross Section Values for Well-Moderated Thermal Reactor Spectra, CRRP-680 (January 25, 1957).

Then r for neutrons in the fuel can be calculated in terms of q_o from the relation

$$r = \frac{\sqrt{5\pi}}{4} \int_{5kT_n}^{\infty} \frac{1}{v} \phi_{1/E}(E)\, dE/N_f$$

$$= \frac{\sqrt{5\pi}}{4} \frac{q_o}{(\xi\Sigma_t)_{sd}} \left(\frac{p'}{1 + B^2\tau'}\right) \int_{5kT_n}^{\infty} \frac{dE}{Ev} \Big/ N_f. \qquad (2.19)$$

A calculation following the procedure just outlined was made for the seven-rod cluster of 0.75-in.-dia UO_2 rods of 2% enrichment, for 8.0-in. lattice pitch. The result was r = 0.22. With 1% enrichment the same lattice has r = 0.11. However, for the lifetime calculations of this project, a value r = 0.1 was assumed for all cell configurations and all enrichments. This choice was made early in the project when it was expected that the optimum enrichment would be much lower than the 2% which emerged as the work progressed. In column 8 of Table 2.5 are listed the values of σ (r = 0.1) used in the lifetime calculations. These are based in the main on the g and s factors in columns 3 and 5 of the table. Graphs of $\hat{\sigma}$ vs neutron temperature and r for U^{235}, Pu^{239}, Pu^{240}, and Pu^{241} are given in Figs. 2.3a –2.3d. These are based on Westcott's results, with the cross sections from 400°C to 600°C calculated from extrapolations of Westcott's g and s factors. In the case of Pu^{239}, where the extrapolations seem questionable, the point at 600°C was independently calculated by numerical integration of the cross section from BNL-325 over the Maxwell spectrum.

2.1.6. Check Calculations: In order to choose accurate methods of analysis and to estimate the final over-all accuracy of the physics calculations, a series of check calculations was performed as described below.

We discuss first the calculation of the flux distributions required to obtain the thermal utilization of the lattice. The two methods which were immediately available were one-group approximations to the transport equation by the P_3 spherical harmonics approximation and by the diffusion approximation.

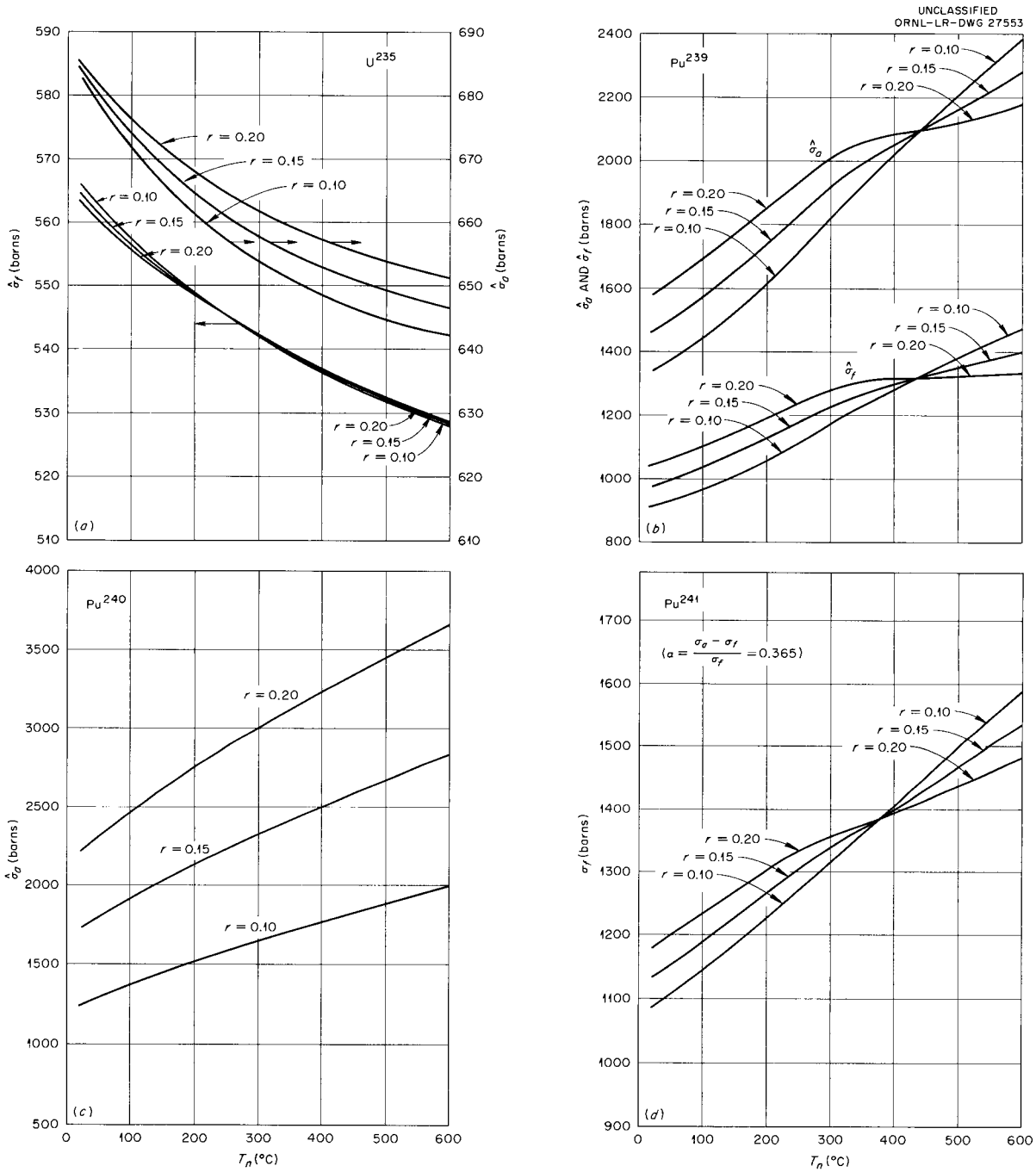

Fig. 2.3. Effective Cross Sections of Uranium and Plutonium vs Neutron Temperature. (*a*) U^{235}. (*b*) Pu^{239}. (*c*) Pu^{240}. (*d*) Pu^{241}.

For the P_3 method a program was available for use on the IBM 650 electronic computer (see Section 2.1.4) and for the diffusion method the calculations would be done by hand.

Figures 2.4a and 2.4b show flux plots for both of these methods for two cases of interest. The cell which the curves in Fig. 2.4a represent is a heavy-water-moderated system for which experimental measurements have been made by Cohen.[19] It can be seen, as expected, that the diffusion approximation fails to give the large flux depression near the fuel rod which is characteristic of higher spherical harmonics approximations. Figure 2.4b shows the degree of agreement between the experimental results and the P_3 calculations over a wide range of lattice pitches. The experimental thermal utilizations tabulated in the figure are based directly on measured flux distributions within the cells.

The diffusion theory calculations described above were done with all constants computed from measured cross sections. It is known that diffusion theory can be made to give more accurate results if the characteristic constants appearing in the equations are modified, which is equivalent to saying that a set of experimentally determined fictitious cross sections is used. This approach has been used with success for uranium-metal-fueled reactors, but the absence of extensive experimental measurements with UO_2 cluster fuel elements seemed to rule the method out for the reactors under consideration here.

On the basis of the above comparisons it appeared that the use of the diffusion approximation would give values of the thermal utilization which would be roughly 1% too high, and it was decided to do all of the flux calculations with the P_3 computer program.

A check on the over-all accuracy of the methods used in the physics calculations was then made by doing calculations for several lattices for which accurate data exist from exponential experiments. The results of the exponential experiments have been compared with the calculations by comparing the value of the thermal utilization implied by the experiment with that computed by the P_3 program. In the exponential experiment, B^2 is

---

[19] E. R. Cohen "Exponential Experiments on D_2O-Uranium Lattices," Proceedings of the Geneva Conference, Vol. 5, P/603, p. 268 (1955).

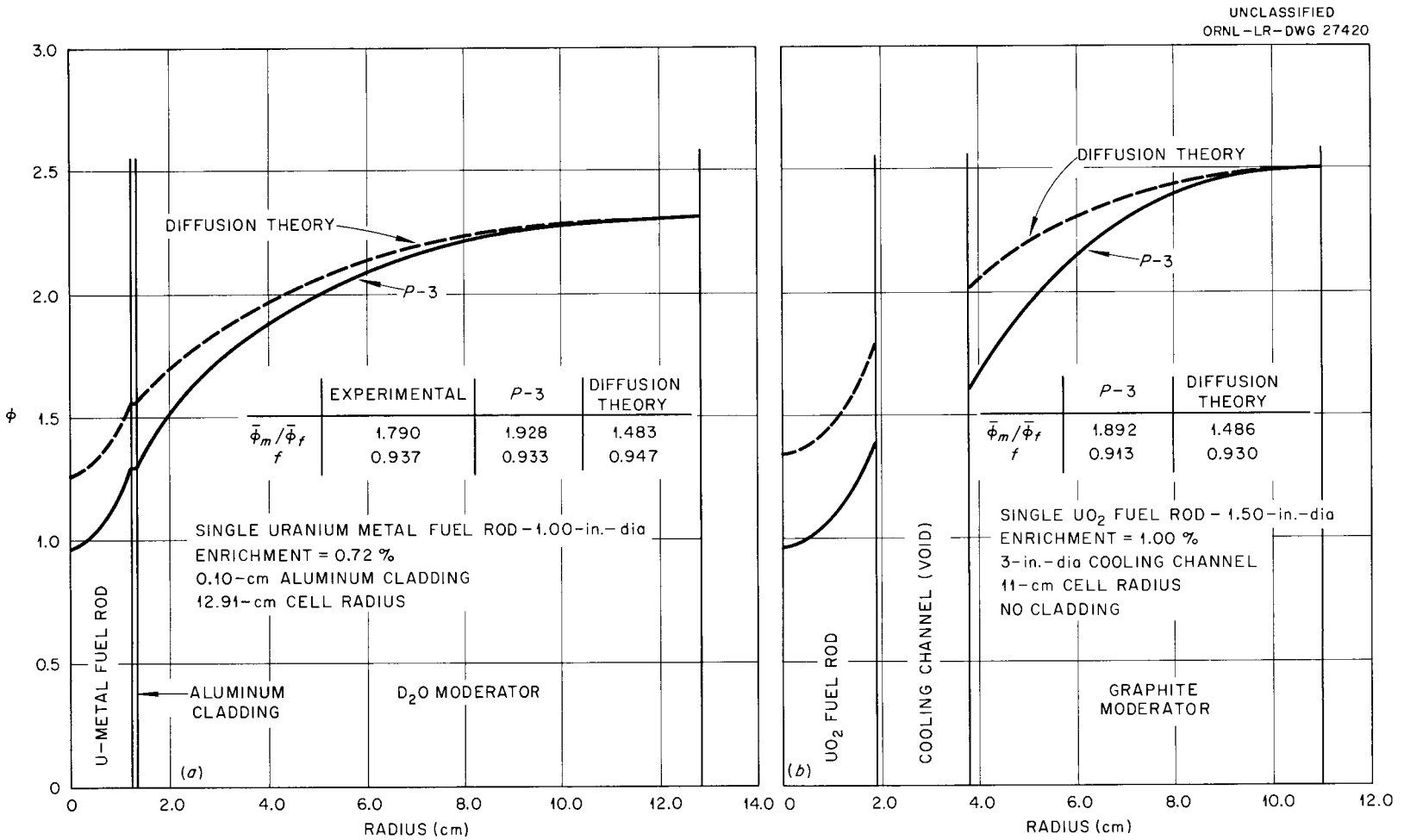

Fig. 2.4. Comparison of Flux Distributions given by Diffusion Theory and by P_3 Approximation.
(*a*) Uranium metal rod – D_2O moderator. (*b*) UO_2 rod – graphite moderator.

determined from the slope of the flux so that we may write

$$1 = \frac{\eta \, \epsilon \, p \, f \, e^{-B^2 \tau}}{1 + L^2 B^2} \tag{2.20}$$

where $B^2 = B_\perp^2 + B_{\parallel}^2$, $L^2 = L_m^2(1 - f)T$, and T is the correction factor which takes into account the voids of the cooling channels and the absorption in the clad. If the above equation is solved for the thermal utilization the result is:

$$f_{exp} = \frac{1 + L_m^2 \, T \, B^2}{\eta \, \epsilon \, p \, e^{-B^2 \tau} + L_m^2 \, T \, B^2} \, . \tag{2.21}$$

Computed values for η, ϵ, p, τ, T, and L_m^2 are combined with the experimental value of B^2 to give f_{exp}. This is a rather stringent over-all check on the methods of calculation since the term $L_m^2 \, T \, B^2$ is of order unity for most exponential experiments, thus the computed values of L^2, η, ϵ, and p all enter strongly in determining f_{exp}.

Comparisons of the above type were made for five exponential experiments. Four of these were taken from the extensive measurements of E. D. Clayton at Hanford[20] and the fifth is a measurement by Booker et al.,[21] at Harwell. It was of interest to consider experiments with large cooling channel voids and the Harwell measurements, with a 3-in.-square cooling channel, were the best data found of this nature. The Hanford exponential experiments which were used contained highly enriched uranium-aluminum alloy fuel rods in both a "wet lattice" and a "dry lattice", that is, with and without water in the cooling channel (see Figs. 2.5a, 2.5b). The absorption cross section in the alloy fuel element was about the same as that in a UO_2 element with 2%

---

[20] We wish to express our thanks to the General Electric Company, Hanford, for communicating these results to us in advance of publication.

[21] D. V. Booker et al., The Measurements of the Laplacian in a Lattice of Uranium Metal Rods and Graphite, AERE N/R 134 (1956).

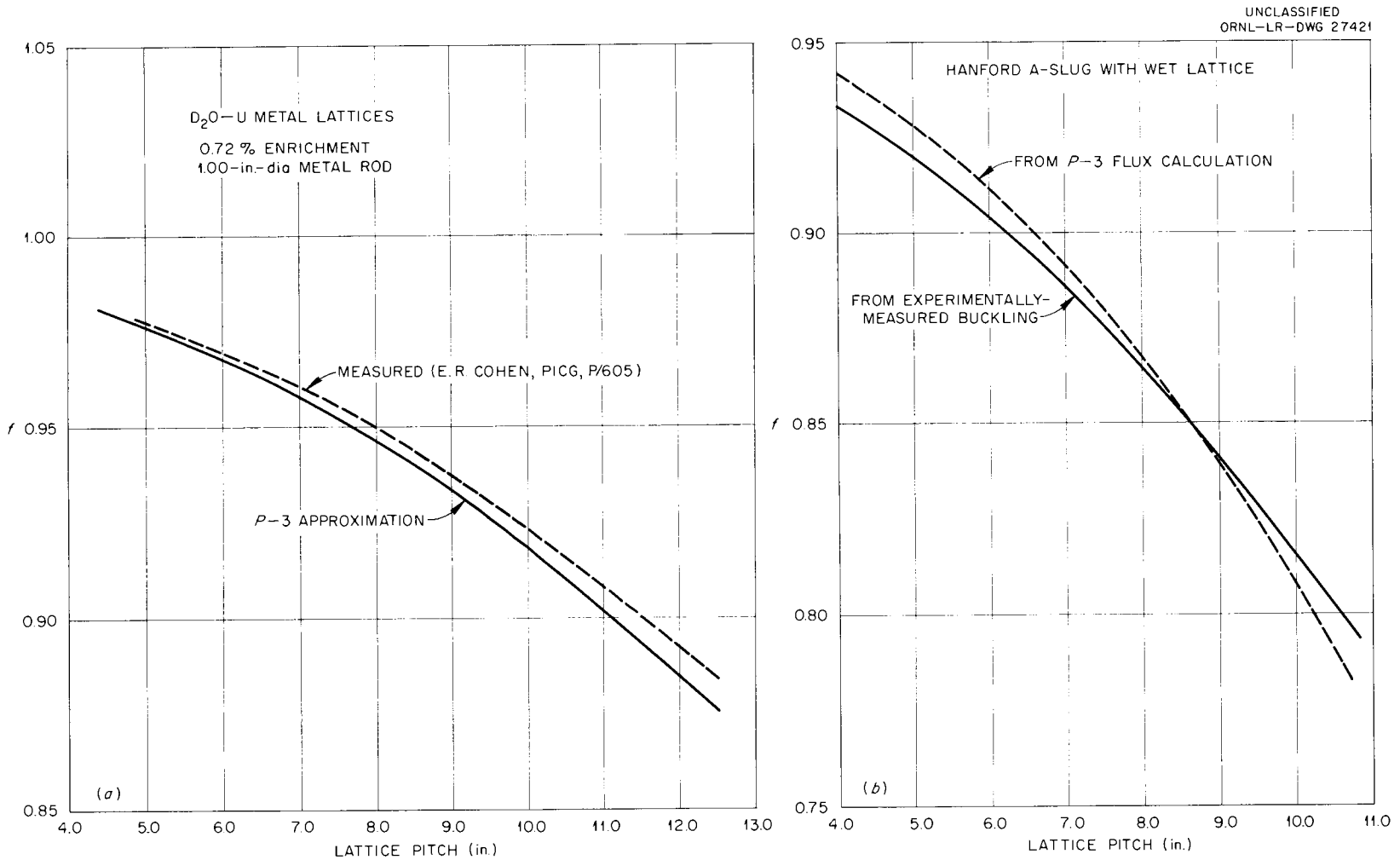

Fig. 2.5. Comparison of Measured and Calculated Thermal Utilization. (*a*) Uranium metal – D_2O lattice. (*b*) Hanford "A" slug wet lattice.

enrichment. A summary of these calculations is given in Table 2.6. The first three lines are the "wet lattice" calculations. These are compared with the P_3 calculations in Fig. 2.5b. Line four is the "dry lattice" calculation and line five is the Harwell measurement with the 3-in.-square cooling channel.

TABLE 2.6

SUMMARY OF CALCULATIONS ON EXPONENTIAL EXPERIMENTS

Rod Diameter (cm)	Void Volume (cc/cm)	Pitch (in.)	B^2 (μb)	L^2 (cm^2)	τ (cm^2)	η	ϵ	p	f_{exp}	f_{P_3}
3.41	0.00	4.19	1855	56.0	384	2.07	1.000	1.000	0.939	0.931
3.41	0.00	7.19	1163	194.7	348	2.07	1.000	1.000	0.888	0.882
3.41	0.00	10.38	678	451.3	340	2.07	1.000	1.000	0.794	0.806
3.41	2.57	7.19	1114	228.4	356	2.07	1.000	1.000	0.901	0.906
3.45	48.7	8.91	91.31	196.0	491	1.34	1.037	0.868	0.882	0.875

In addition to these exponential experiments, a check calculation on the over-all accuracy of the methods was provided by the Calder Hall reactor, which was computed as part of a study of the effect of enrichment on uranium metal-magnesium-clad reactors. The calculation was done with a 4-in.-dia cooling channel and thus represents a reactor whose geometry is intermediate between those of the two innermost regions of the Calder Hall core.[22] The results of this calculation are given in Table 2.7. The values quoted for Calder Hall are for a 4-in.-dia cooling channel as interpolated between the two innermost regions of the Calder Hall core.

The agreement between the values of k_∞ might appear to be fortuitous since there is poor agreement between the values of η, ϵ, p, and f. It must be remembered, however, that the values of the constants used by the British

[22] G. Packman and B. Cutts, J. Brit. Nucl. Energy Conf. 2, 105 (1957).

in the Calder Hall calculations were derived from the exponential experiments of Mummery,[23] whereas, the calculations at the Oak Ridge National Laboratory were done with the world consistent set of cross sections.[24] These two sets of cross sections and the values of η for U^{235} and for natural uranium are given in Table 2.8.

TABLE 2.7

COMPARISON OF COMPUTED AND PUBLISHED CONSTANTS FOR THE CALDER HALL REACTORS

	Computed	Calder Hall
η	1.342	1.266
ϵ	1.032	1.030
p	0.8570	0.8778
f	0.8971	0.9305
k_{∞}	1.065	1.065
R_c	0.825	0.85

TABLE 2.8

COMPARISON OF CROSS SECTIONS AND η

	World Consistent Set	Mummery P/429
σ_a^{235}	694	721
σ_f^{235}	582	638
σ_a^{238}	2.73	2.77
η^{235}	2.071	1.937
η^{u}	1.342	1.266

[23] P. W. Mummery, "The Experimental Basis of Lattice Calculations," Proceedings of the Geneva Conference, Vol. 5, P/429, p 282 (1955).

[24] D. J. Hughes and R. B. Schwartz, Neutron Cross Sections, BNL-325, Supplement No. 1 (January 1, 1957).

The value $\eta = 1.266$ for the Calder Hall reactor is thus the value which is consistent with the exponential experiments of Mummery, and the ϵ, p, and f which are quoted for this reactor can be considered to form a set which is internally consistent with the experimentally determined multiplication factor. The good agreement between the computed value of k_∞ and that listed for the Calder Hall reactor is therefore felt to be more significant than the disagreement in detail between the factors η, ϵ, p, and f.

The above check calculations seemed to indicate an over-all accuracy of about 1% or better for the proposed methods of calculating k_∞ and k_{eff} for room-temperature systems of rather conventional cell geometry.

In calculating flux patterns for more complicated cell geometries, like the seven-rod-cluster fuel elements proposed for the ORNL-GCR-2, the problem was encountered of finding a one-dimensional model with which to approximate the fuel system for purposes of flux calculations. Two approximations were studied. In the first approximation, all of the fuel was lumped into a single rod with all of the cladding material placed around the single rod. In the second approximation, the outer six rods of the cluster were replaced by an annulus of the same volume as the rods themselves. Half of the cladding of these six rods was placed on the inner surface of the annulus and half was placed on the outer surface. The annulus was located in the cooling channel in such a way that it was divided into two equal volumes by the circle which forms the locus of the centers of the original six rods. The seventh rod of the cluster, the central rod, was represented by its actual radius and clad thickness. Curves of f, p, and k_∞ for these fuel systems are shown in Figs. 2.6a and 2.6b. Data for the annulus method are included for two locations of the ring of outer rods. In the ORNL-GCR-2 cluster the outer rods are placed rather close to the inner surface of the graphite, and the other case, which is included for comparison, has the outer rods placed midway between the central rod and the inner graphite surface.

It can be seen that there is little difference between the values of k_∞ computed with the two models, the most important difference being a slightly higher k_∞ at the optimum lattice with the annulus model due to

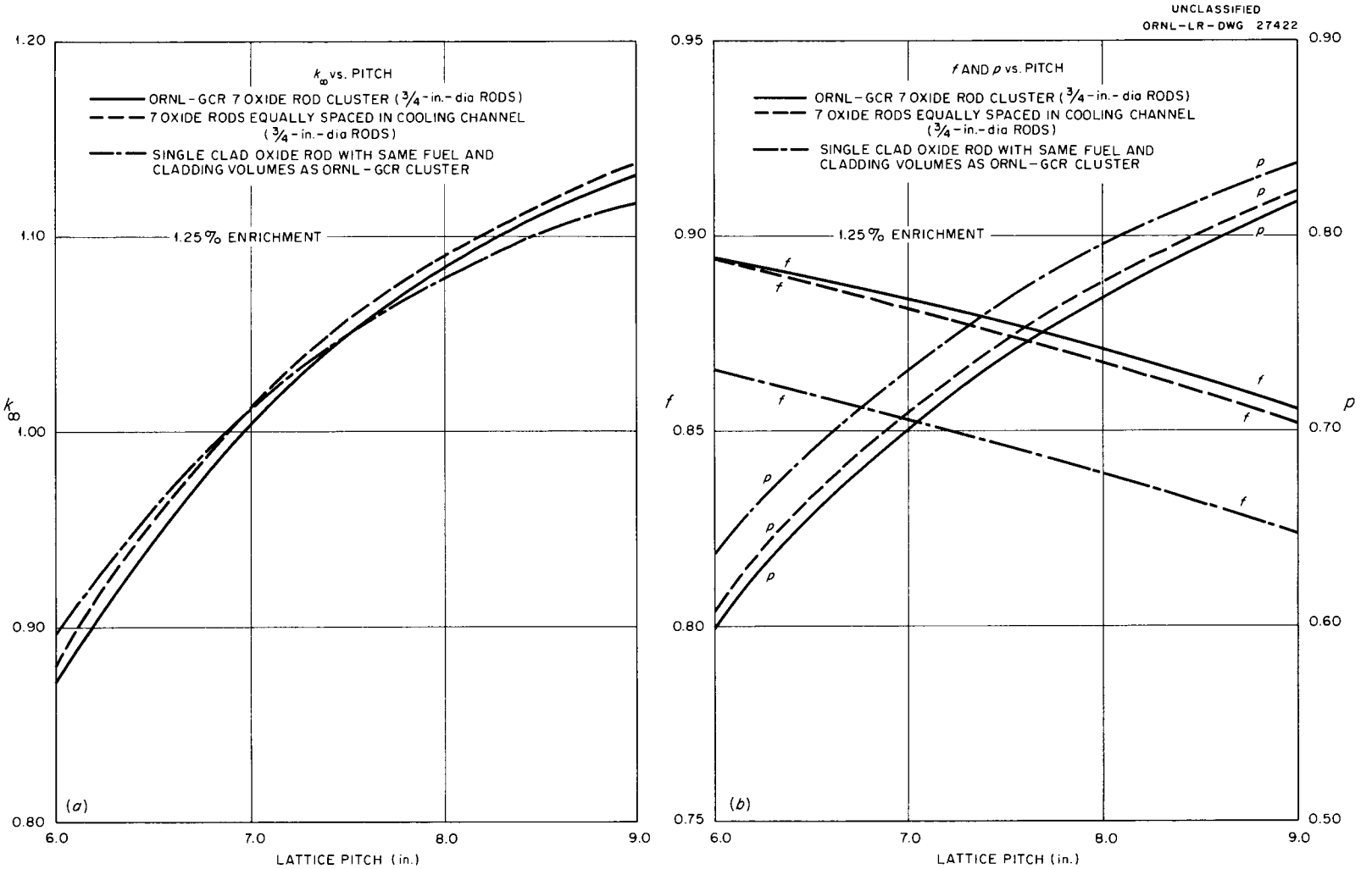

Fig. 2.6. Effect of Approximations in Calculations for Seven-Rod Clusters. (*a*) Multiplication factor. (*b*) Thermal utilization and resonance escape probability.

the greater homogenization of the highly absorbing clad. The balance between p and f is seen to be different, however, and because of this the calculations presented here were all done with the annulus model. It can also be seen from Figs. 2.6a and b that the exact radius at which the outer rods are located has little effect on the calculations.

At the time when the methods of calculation were sufficiently advanced to provide acceptable data at the reactor operating temperature, a large number of cells had been studied at room temperature, and it was felt desirable to cast these calculations into a general form which would make them useful for further studies at room temperature or at operating temperature. This was found to be possible due to the strong dependence of the cell disadvantage factors on the absorption in the fuel and clad, and the weak dependence on the absorption in the moderator. The moderator disadvantage factors were found to be linear functions of the homogenized rod absorption cross section,

$$\Sigma^a_{rod} = \Sigma^a_f + \frac{V_{c\ell}}{V_f} \Sigma^a_{c\ell} , \tag{2.22}$$

where Σ^a_f and $\Sigma^a_{c\ell}$ are the macroscopic absorption cross sections for the fuel and clad, respectively. The clad disadvantage factor was found to depend linearly on the fuel absorption cross section alone. The usefulness of such a treatment is shown in Figs. 2.7a and 2.7b. The curves on these figures were drawn from room-temperature calculations alone, whereas, the indicated points are the result of P_3 flux calculations with the actual cross sections at the operating temperature. Sample thermal utilizations for the clusters of 0.75-in.-dia rods computed by the exact method and by the use of these extrapolated disadvantage factors are given in Table 2.9. It can be seen from these calculations that the extrapolated method is an entirely acceptable means of computing the high-temperature thermal utilizations for the reactors under consideration here.

2.2 Results of Lattice Calculations

As mentioned before, the objective of these calculations was to determine the multiplication factor, k, of lattices having fuel of various degrees of enrichment, various fuel element geometries, and a wide range of lattice spacings. It should be kept in mind in examining the results of these

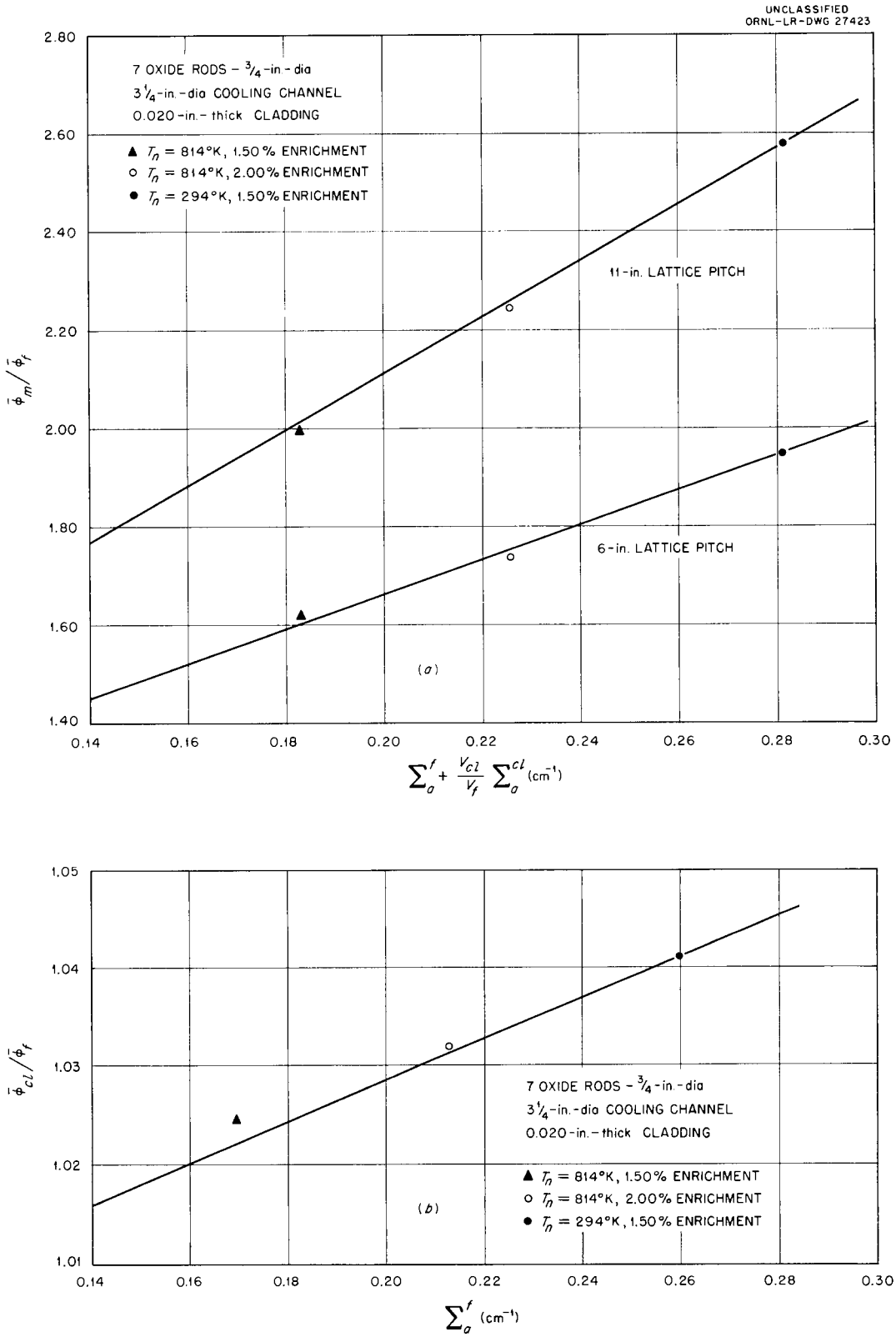

Fig. 2.7. Flux Disadvantage Factors vs Fuel Absorption Cross Section. (*a*) Moderator disadvantage factor. (*b*) Cladding disadvantage factor.

TABLE 2.9

COMPARISON OF EXACT P_3 AND EXTRAPOLATED METHODS FOR COMPUTING f AT OPERATING TEMPERATURE (T_n = 814°K)

Enrichment (Atomic %)	Pitch (in.)	Thermal Utilization	
		Exact Method	Extrapolated Method
1.50	6.0	0.9157	0.9160
1.50	7.0	0.9062	0.9067
1.50	8.0	0.8970	0.8972
1.50	9.0	0.8865	0.8866
1.50	10.0	0.8746	0.8744
1.50	11.0	0.8610	0.8595
2.00	6.0	0.9293	0.9290
2.00	7.0	0.9258	0.9250
2.00	8.0	0.9137	0.9115
2.00	9.0	0.9025	0.9015
2.00	10.0	0.8913	0.8900
2.00	11.0	0.8793	0.8771

calculations, that one of the major benefits expected to follow from the use of enriched fuel is a more compact lattice and consequently a higher power for a given core size. Another major benefit is the increase in average fuel exposure (and consequent reduction in power cost chargeable to fuel fabrication and reprocessing) that results from more reactive fuel.

Over 400 lattices have been studied, of which 337 are reported here. They fall into two main groups, lattices at room temperature, including uranium metal rods, UO_2 rods, and clusters of UO_2 rods, and lattices with a neutron temperature of 814°K (clusters only).

A description of the lattice and the values of η, ϵ, p, f, k, and the conversion ratio, R_c, are given for all cases in Table 2.10.

Results are also plotted in several figures, and are grouped as indicated below.

2.2.1. Uranium Metal Lattices - Fig. 2.8: The fuel element for these lattices is that of the Calder Hall reactor. The calculations were undertaken to relate our method and cross sections to a familiar case, and also to investigate the effect of enrichment on the Calder Hall reactor with no other changes in the fuel element or operating conditions (same temperatures and heat flux). It can be seen that enrichment to 1.00% U^{235} would permit reducing the lattice pitch from 8 in. to about 6 in., a 75% increase in the number of fuel elements, and hence in the power of the core. The effect of this increase in power density on the power cost is discussed in Section 11. It is interesting to note that the value of k obtained for natural uranium at 8-in. lattice pitch, k = 1.065, is precisely that quoted for the Calder Hall reactor. The significance of this agreement is discussed in Section 2.1.6.

2.2.2. Lattices with Single UO_2 Rods - Figs. 2.9 – 2.16: These calculations, done before the high-temperature cross sections had been established, helped to reveal many of the significant aspects of the system, including the effect of the stainless steel cladding. Clad thicknesses used in these calculations were chosen either to simulate the total amount of clad that would be present in a seven-rod cluster with the same UO_2 volume and 0.020-in. clad thickness on each rod, or to represent the volume of metal in fins for single rod fuel elements. It can be seen from Fig. 2.14 that fuel with 1.0 to 1.25% U^{235} content would be required to give the same multiplication factor

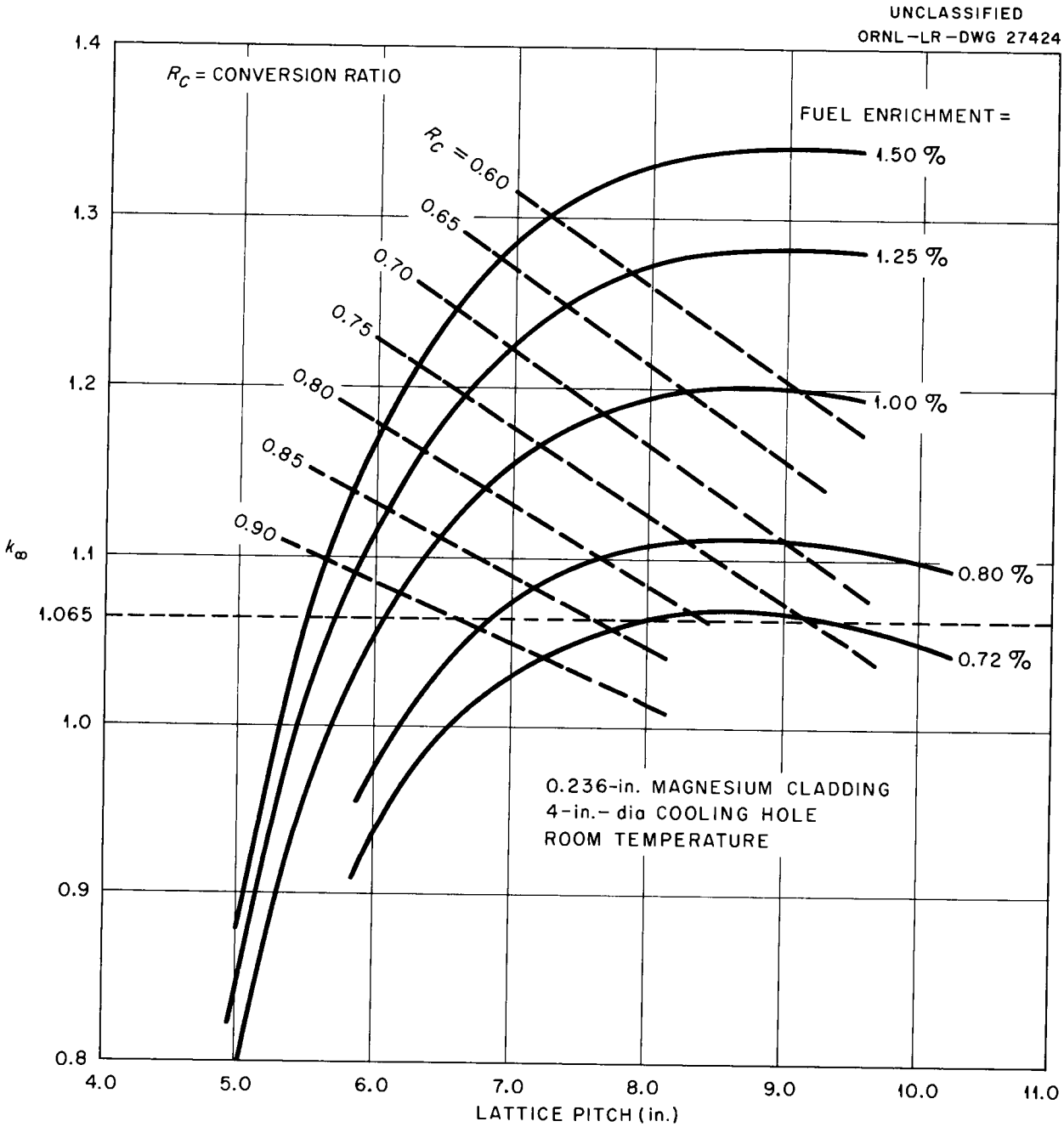
UNCLASSIFIED
ORNL-LR-DWG 27424
R_C = CONVERSION RATIO
FUEL ENRICHMENT =
1.50 %
1.25 %
1.00 %
0.80 %
0.72 %
R_C = 0.60
0.65
0.70
0.75
0.80
0.85
0.90
k_∞
1.4
1.3
1.2
1.1
1.065
1.0
0.9
0.8
4.0
5.0
6.0
7.0
8.0
9.0
10.0
11.0
LATTICE PITCH (in.)
0.236-in. MAGNESIUM CLADDING
4-in.- dia COOLING HOLE
ROOM TEMPERATURE

with stainless steel cladding (0.040 to 0.060 in.) that natural uranium would give without cladding. It is also apparent that the process of using enrichment to reduce the lattice pitch (hence increase power density) is subject to the law of diminishing returns. For example, in Figs. 2.9 – 2.11, as well as in Fig. 2.8, it can be seen that curves of k vs pitch for different enrichments come quite close together when the lattice spacing is much smaller than the optimum (that is, the pitch at which a given fuel rod has maximum k). It can be surmised from this evidence, and is borne out by the economic analysis (Section 11) that about a factor of 2 increase in power density is feasible by using enrichment to allow a more compact lattice, but that a greater increase in power density than this begins to require excessive enrichment. This does not, of course, preclude further increases in power density by other means, such as higher surface temperature, or fuel elements with greater surface area but possibly less reactivity.

Figures 2.12 through 2.14 show the effect of cooling-channel diameter, fuel-rod diameter, and cladding thickness. The diameter of the cooling channel has little effect on k near the maximum-k lattice pitch, but for smaller lattices the decrease in resonance escape probability associated with an increase in hole size more than balances the increase in thermal utilization, and a loss of reactivity results. Depending upon the core dimensions, there would also be an increase in the neutron leakage as the diameter of the cooling channel is increased. The net effect is not large enough, however, to have a major influence on selection of lattice parameters. Figure 2.16 shows the initial conversion ratio as a function of lattice pitch. Two interesting effects are exhibited, both of them fairly well known: (1) increasing the enrichment produces a drastic reduction in conversion ratio for a given lattice pitch, and (2) a small amount of enrichment can produce a significant increase in conversion ratio for a given multiplication factor. These facts must both be borne in mind in considering the effect of different lattice parameters on core life.

A point of major interest is the difference in multiplication factor between reactors having uranium-metal fuel rods and otherwise similar reactors having UO_2 rods. At issue is the question of whether a natural uranium reactor (graphite moderated) can operate with UO_2 fuel elements. A comparison of two

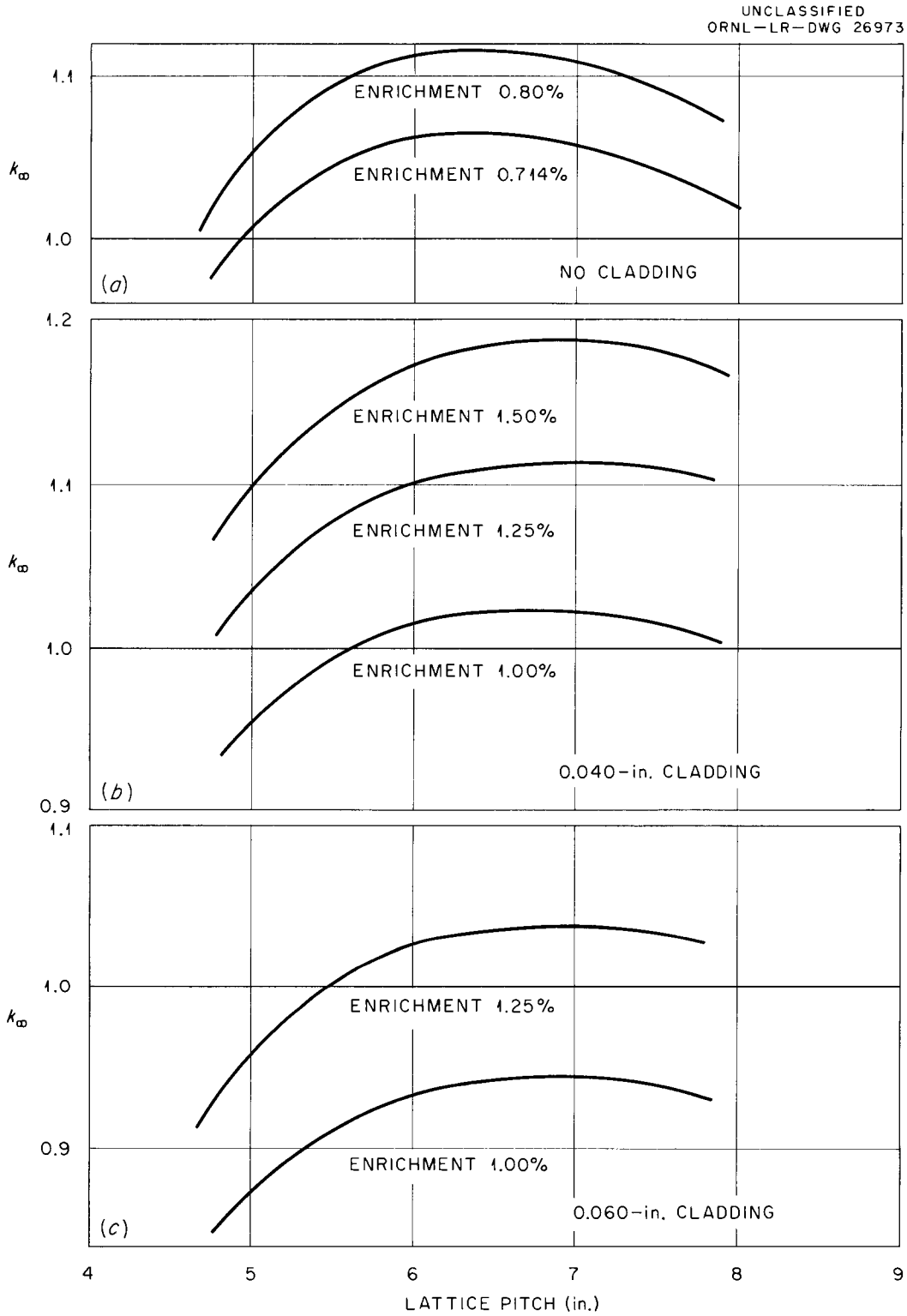

Fig. 2.9. Multiplication Factor vs Lattice Pitch and Enrichment – 1.0-in.-dia UO_2 Rods, 3.0-in.-dia Cooling Channel, T_n = 20°C. (*a*) No clad. (*b*) 0.040 in. clad. (*c*) 0.060 in. clad.

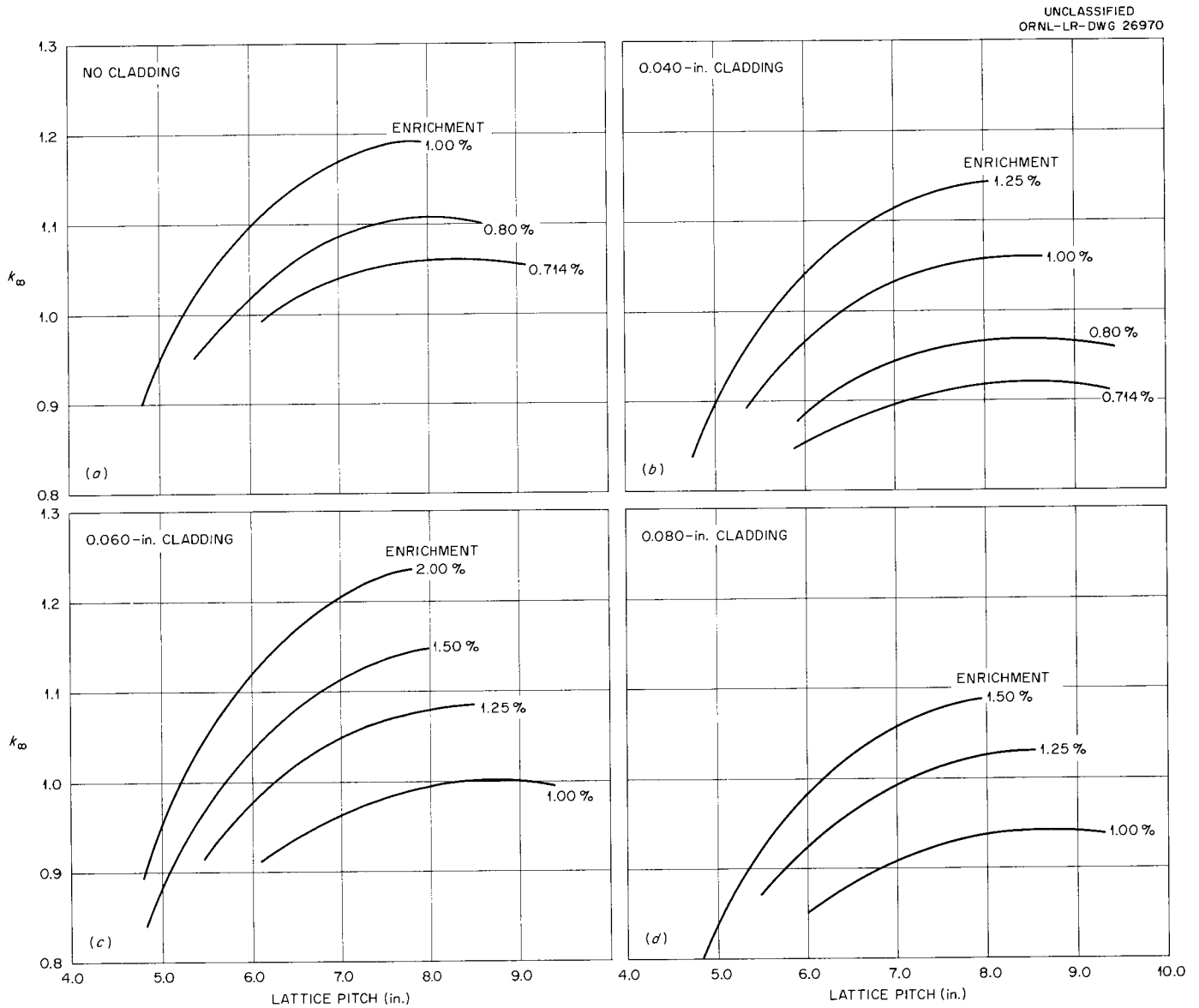

Fig. 2.10. Multiplication Factor vs Lattice Pitch and Enrichment – 1.5-in.-dia UO_2 Rods, 3.0-in. Cooling Channel, T_n = 20°C. (*a*) No clad. (*b*) 0.040 in. clad. (*c*) 0.060 in. clad. (*d*) 0.080 in. clad.

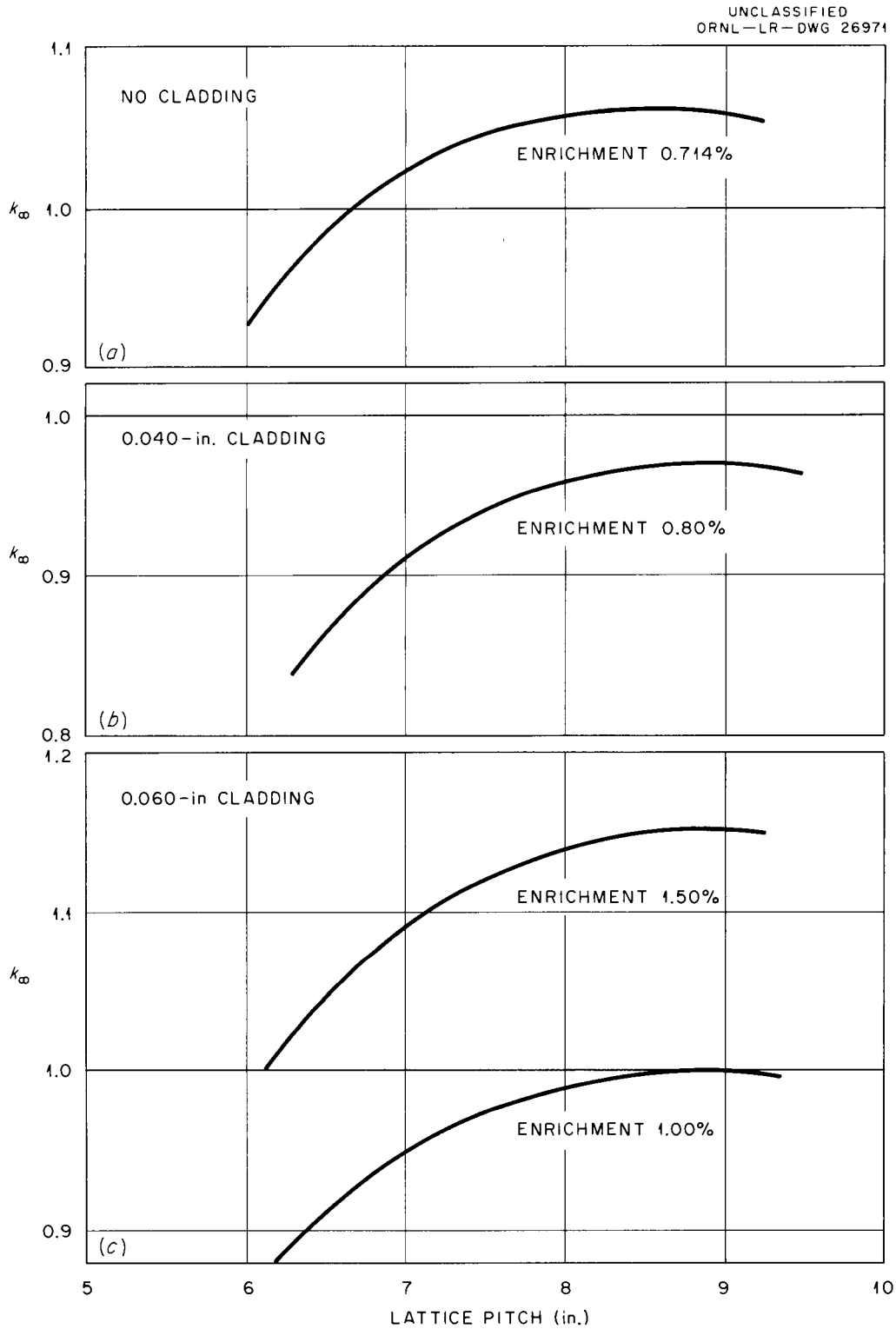

Fig. 2.11. Multiplication Factor vs Lattice Pitch and Enrichment – 1.5-in.-dia UO_2 Rods, 4.0-in. Cooling Channel, T_n = 20°C. (*a*) No clad. (*b*) 0.040 in. clad. (*c*) 0.060 in. clad.

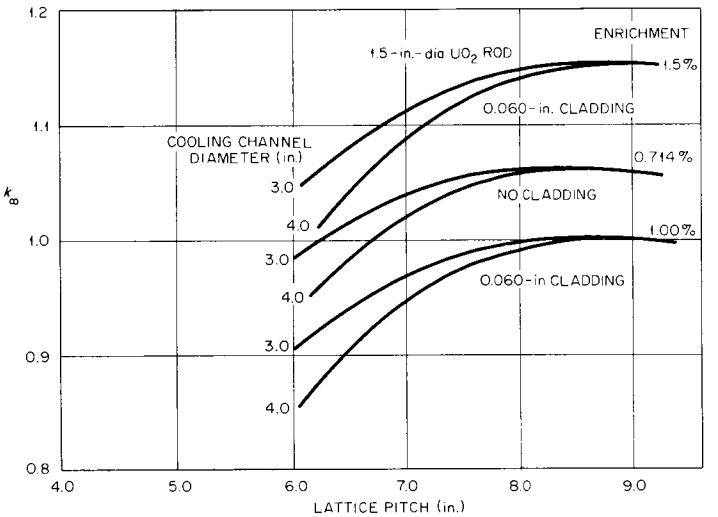

Fig. 2.12. Effect of Cooling Channel Diameter on Multiplication Factor.

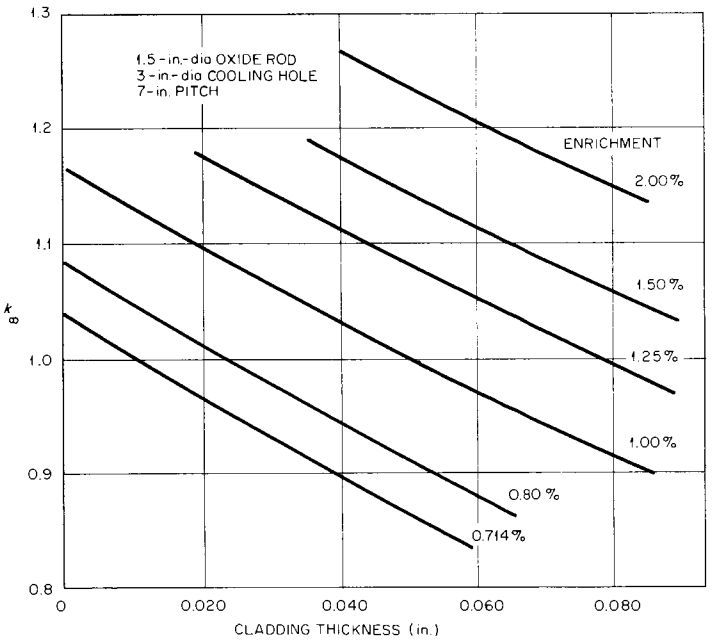

Fig. 2.14. Effect of Clad Thickness on Multiplication Factor.

UNCLASSIFIED
DRNL-LR-DWG 26967

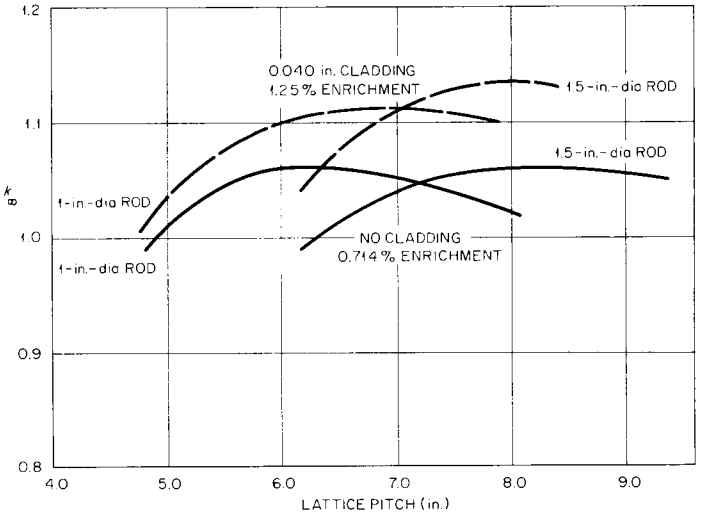

Fig. 2.13. Effect of Fuel Rod Diameter on Multiplication Factor.

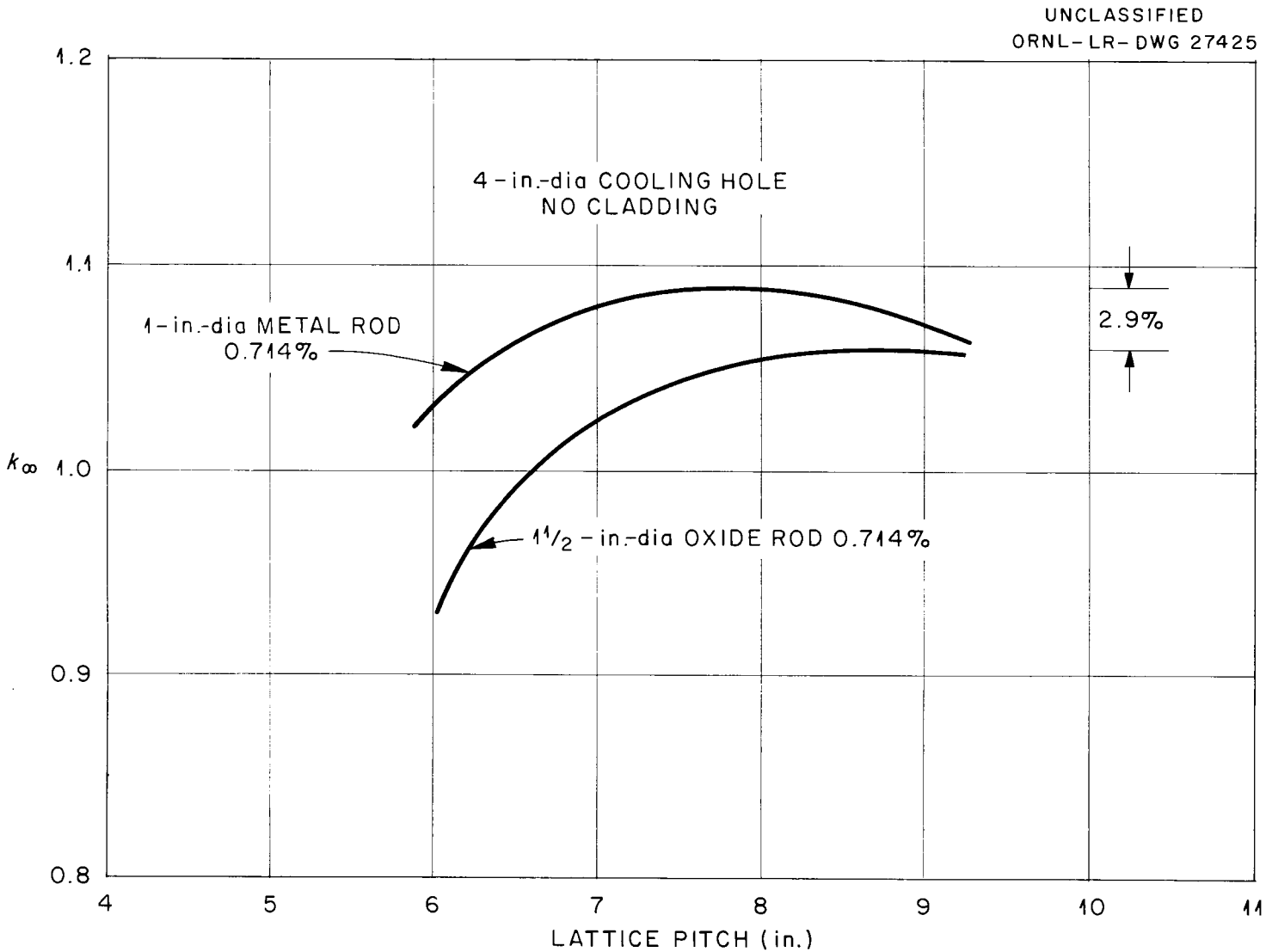

Fig. 2.15. U Metal – UO_2 Reactivity Difference.

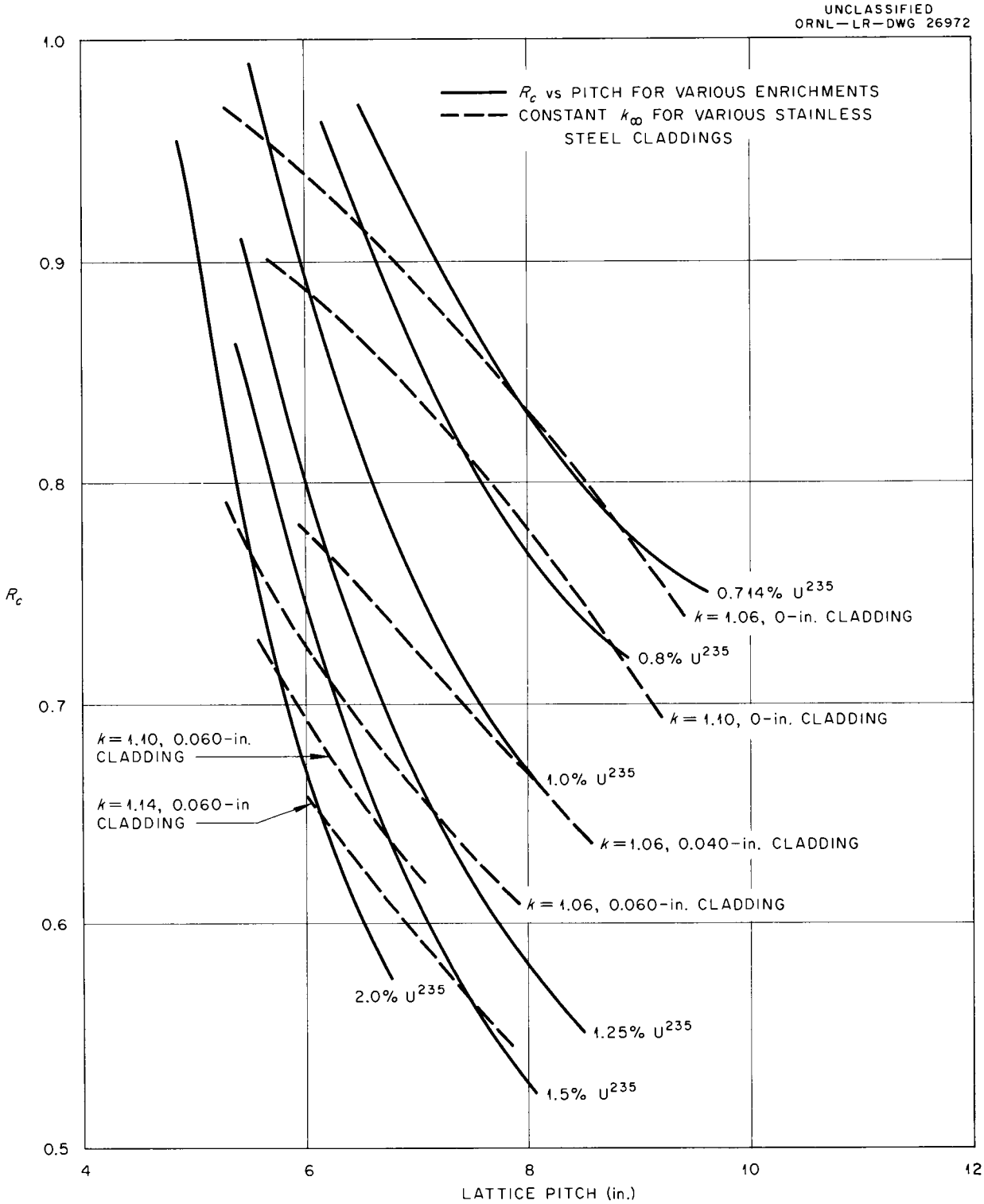

Fig. 2.16. Conversion Ratio vs Lattice Pitch and Enrichment.

such reactors is shown in Fig. 2.15. The 1.5-in. UO_2 rod gives roughly the same optimum lattice pitch as the 1.0-in. metal rod. The exact equivalence is unimportant, however, since in either case (metal or oxide) rather large changes in fuel-rod diameter produce small changes in the maximum attainable k (though major changes in the lattice spacing at which this maximum value of k occurs). It is seen that the difference in the maximum values of k is 2.9%.

2.2.3. Lattices with Clusters of UO_2 Rods - Figs. 2.17 – 2.27: These lattices exhibit the same general characteristics as those with single-rod fuel elements, although certain interesting differences do appear. In particular, the balance between thermal utilization and resonance escape probability is different. On the one hand, f is greater for clusters than for single rods having the same volumes of fuel and cladding material, (Fig. 2.6b) because for clusters the clad is in effect more or less uniformly mixed with the fuel, while for single rods it lies entirely on the outer surface. On the other hand, p is smaller for clusters because the surface-to-mass ratio is greater (at least for the rod spacings of interest in the gas-cooled reactor). Consequently, for large lattice spacings clusters have a higher k than equivalent single rods, while for small lattice spacings, single rods have the higher k. A comparison of k for rods and clusters is given in Fig. 2.21. Figure 2.22 shows that for equal k the cluster has the higher conversion ratio.

Figure 2.25 illustrates the point, made earlier, that enrichment of the fuel to about 1.0% of U^{235} is required to accommodate 0.020-in. stainless steel clad (relative to natural uranium, unclad). Enrichment above 1.0% is therefore chargeable to the production of a higher power density and to increasing fuel lifetime.

Figure 2.26 contains the results having the most direct bearing on the final core configuration. These curves are for seven-rod clusters with 0.018-in. clad thickness (430 stainless steel equivalent), and the average operating neutron temperature of 540°C. The figures show the conversion ratio as well as the multiplication factor as functions of lattice pitch and enrichment.

The need for a volume in which fission product gases could accumulate became apparent when the economic analysis indicated a preference for the very

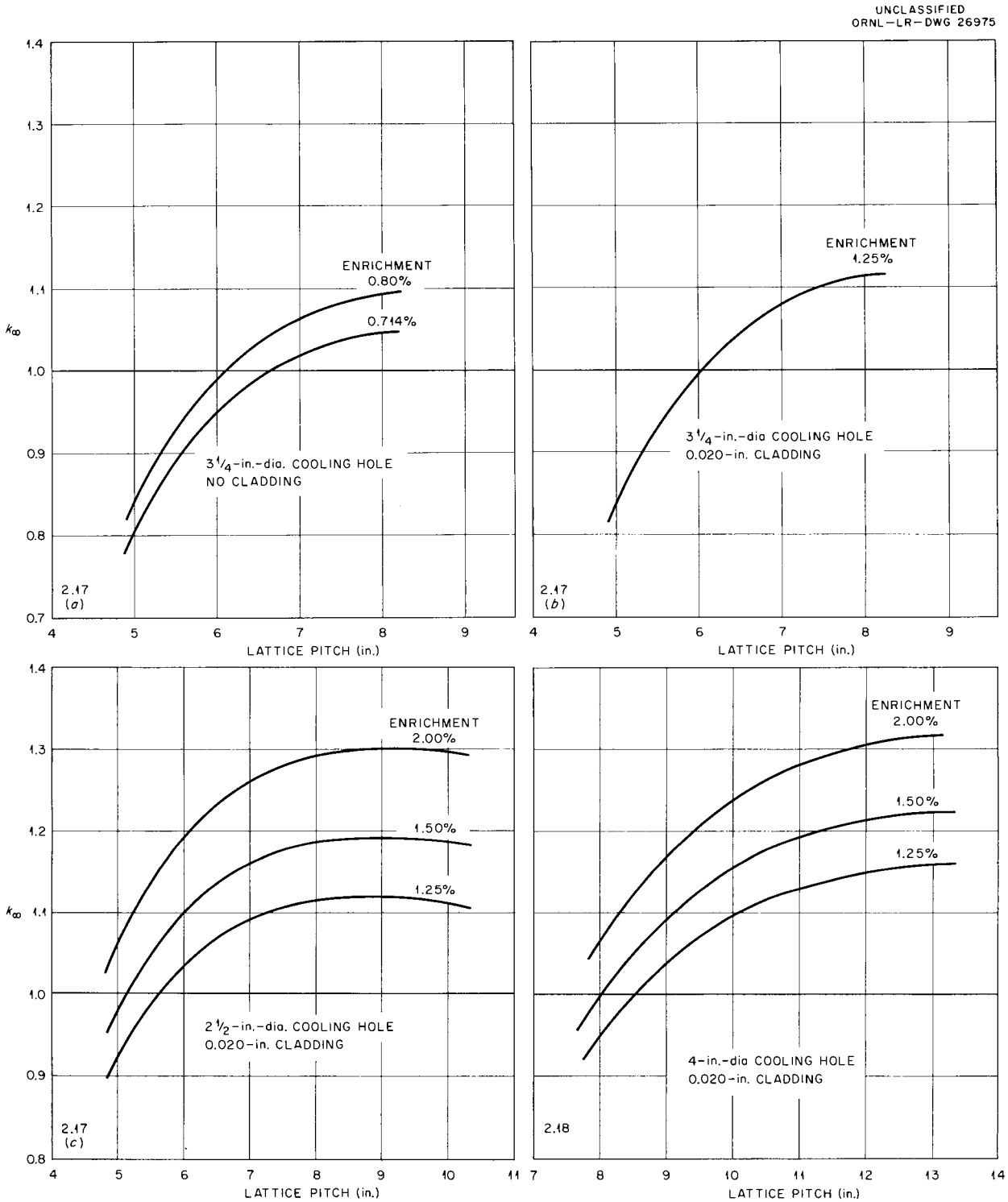

Fig. 2.17. Multiplication Factor vs Lattice Pitch and Enrichment – Seven UO_2 Rods, 0.5-in.-dia T_n = 20°C. (*a*) 3.25-in. cooling channel, no clad. (*b*) 3.25-in. cooling channel, 0.20 in. clad. (*c*) 2.50-in. cooling channel, 0.20 in. clad.

Fig. 2.18. Multiplication Factor vs Lattice Pitch and Enrichment – Seven UO_2 Rods, 1.0-in.-dia. 4.0 in. Cooling Channel, T_n = 20°C.

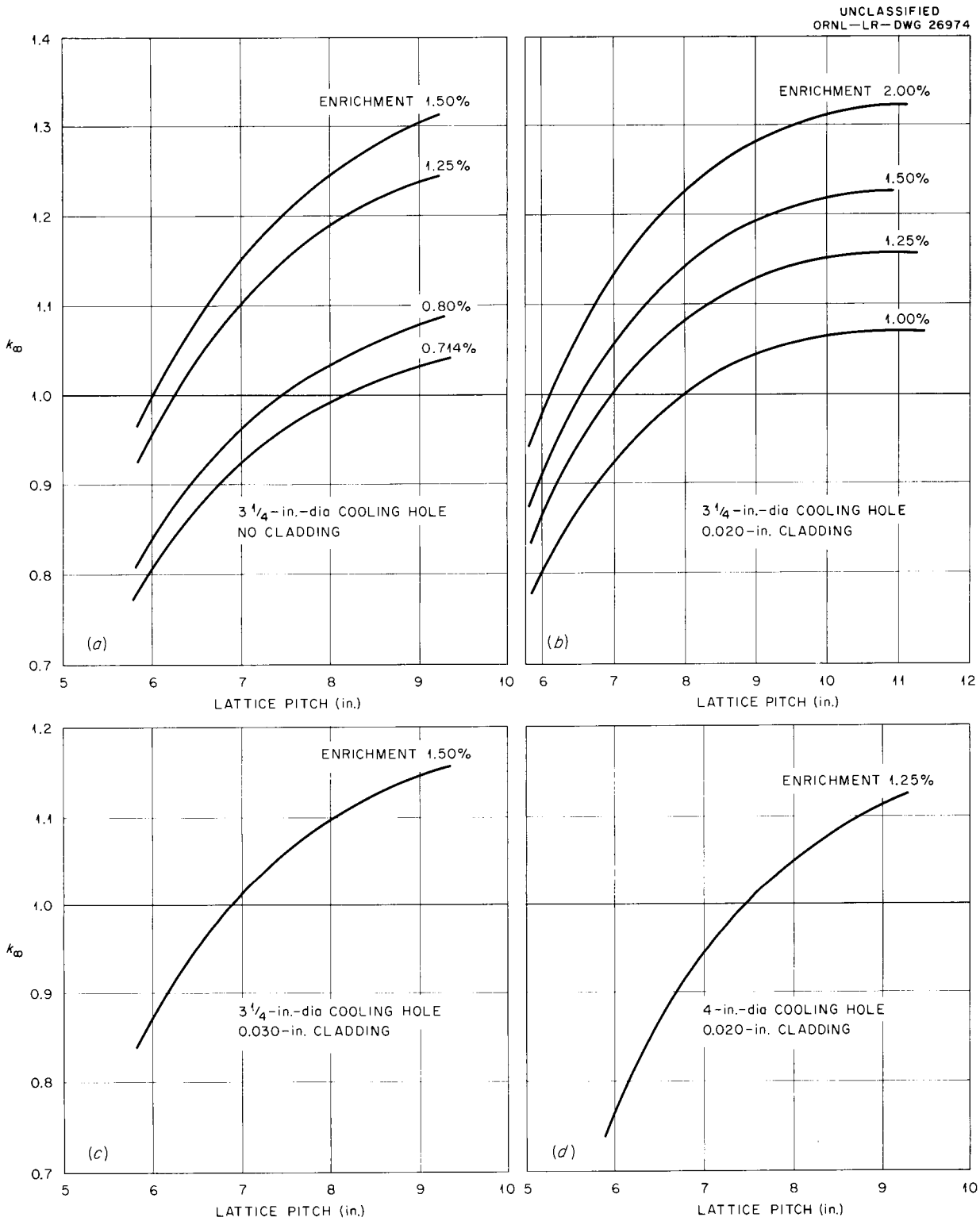

Fig. 2.19. Multiplication Factor vs Lattice Pitch and Enrichment – 7 UO_2 Rods, 0.75-in.-dia, T_n = 20°C. (*a*) 3.25-in. cooling channel, no clad. (*b*) 3.25-in. cooling channel, 0.020 in. clad. (*c*) 3.25-in. cooling channel, 0.030 in. clad. (*d*) 4.00-in. cooling channel, 0.020 in. clad.

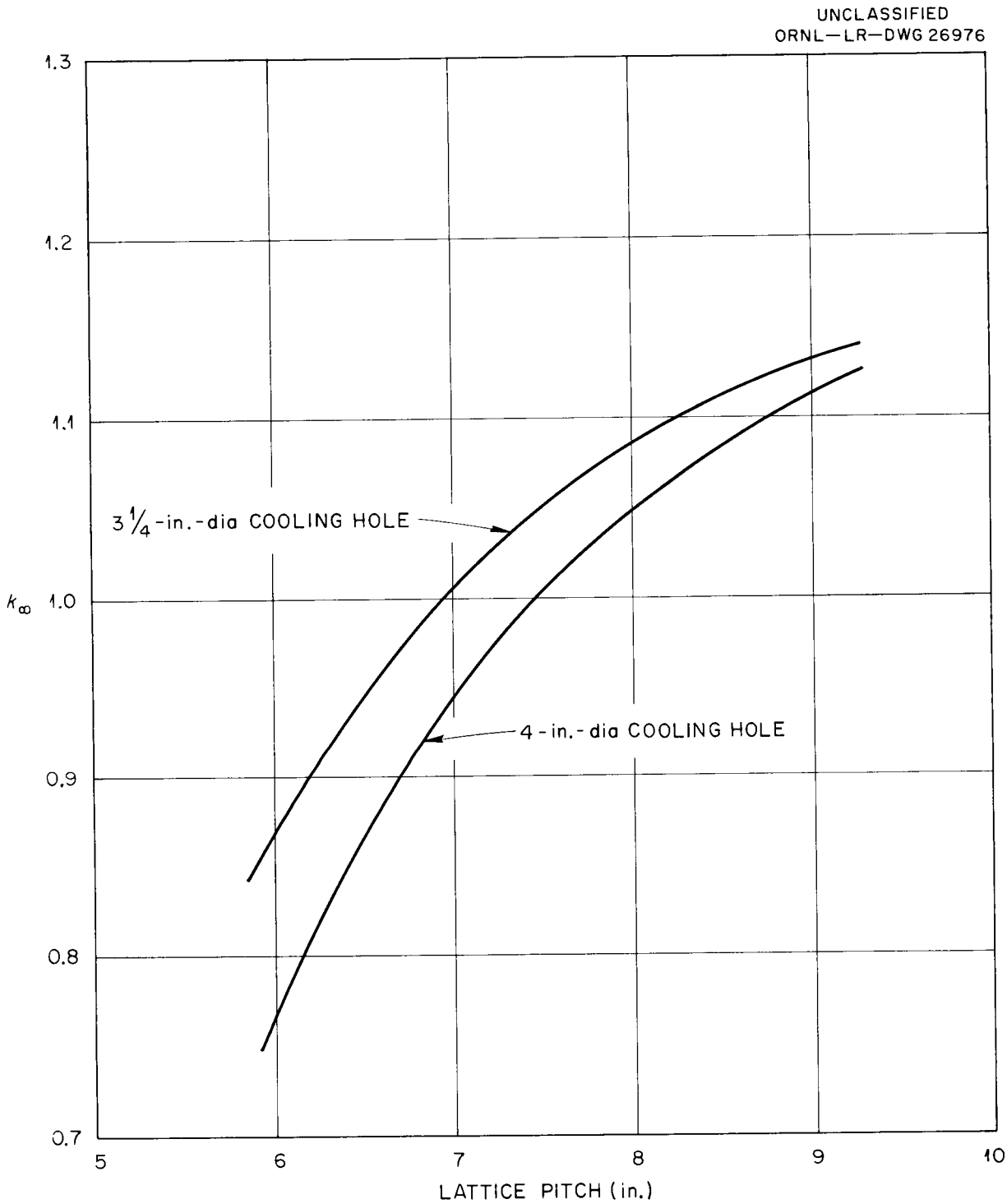

Fig. 2.20. Effect of Cooling-Channel Diameter on Multiplication Factor – $7UO_2$ Rods, 0.75-in.-dia, Enrichment 1.25%, T_n = 20°C.

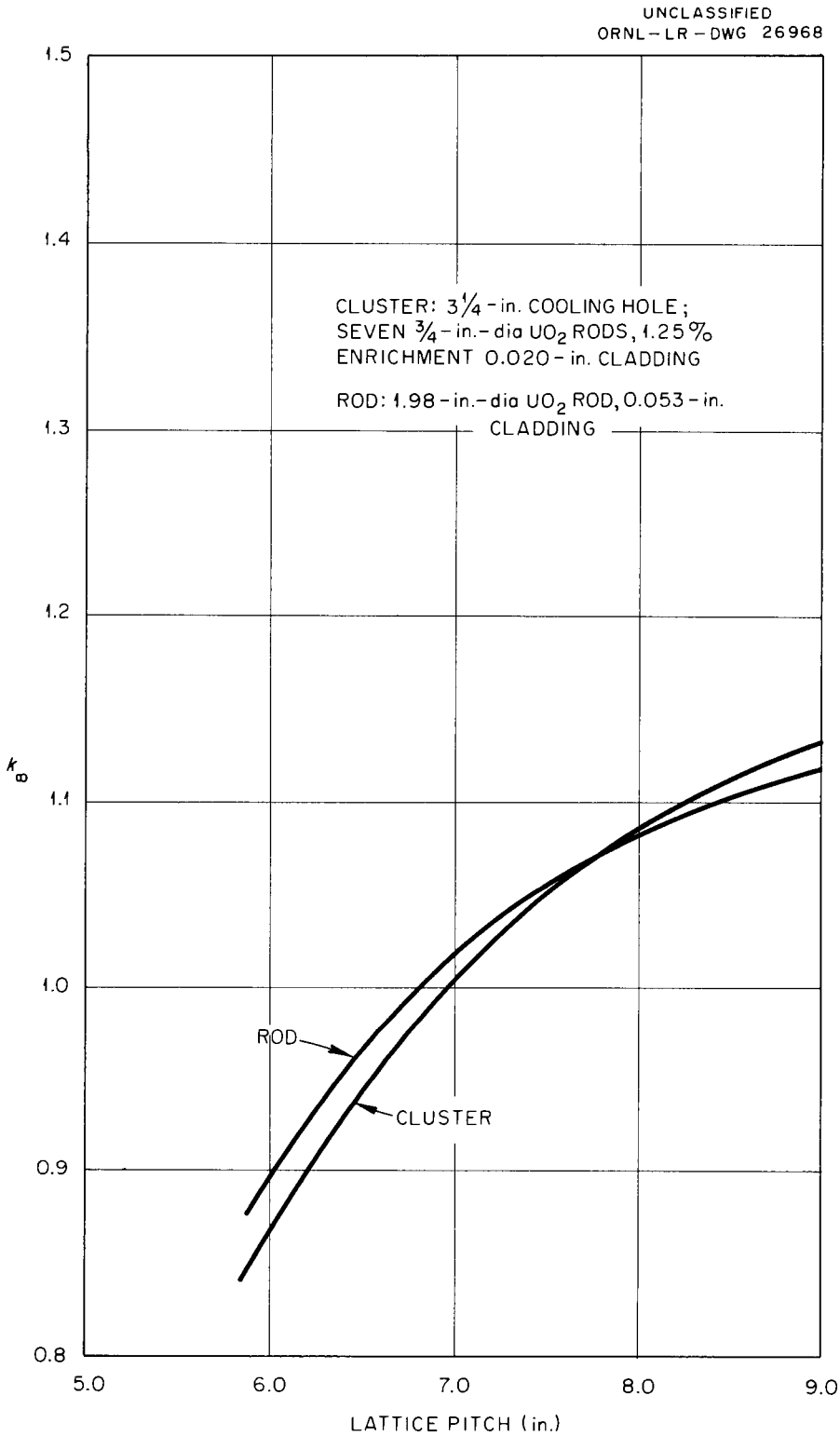

Fig. 2.21. Comparison of Cluster and Single Rod of Equal Volume.

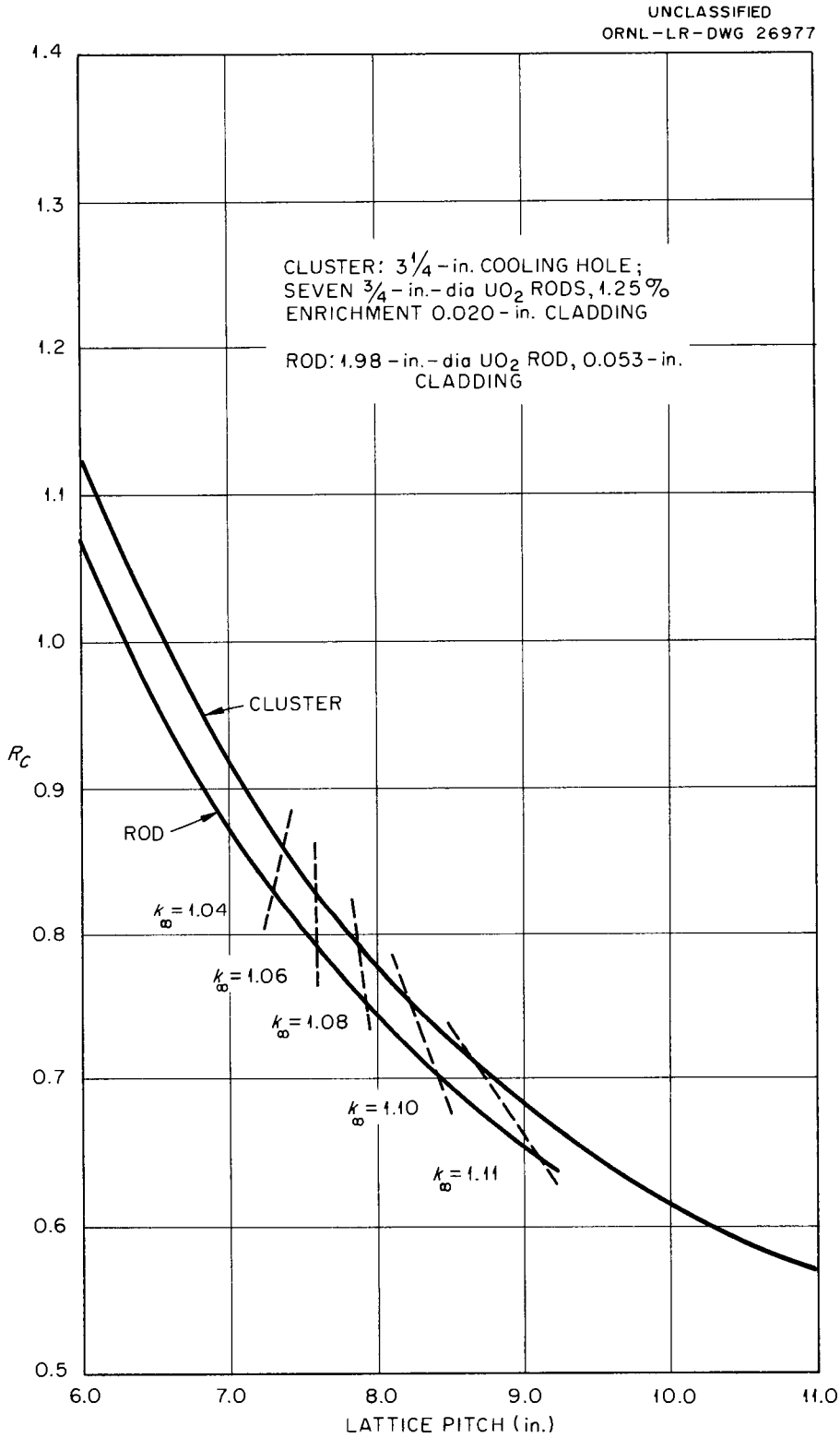

Fig. 2.22. Comparison of Conversion Ratio for Single Rod and Cluster.

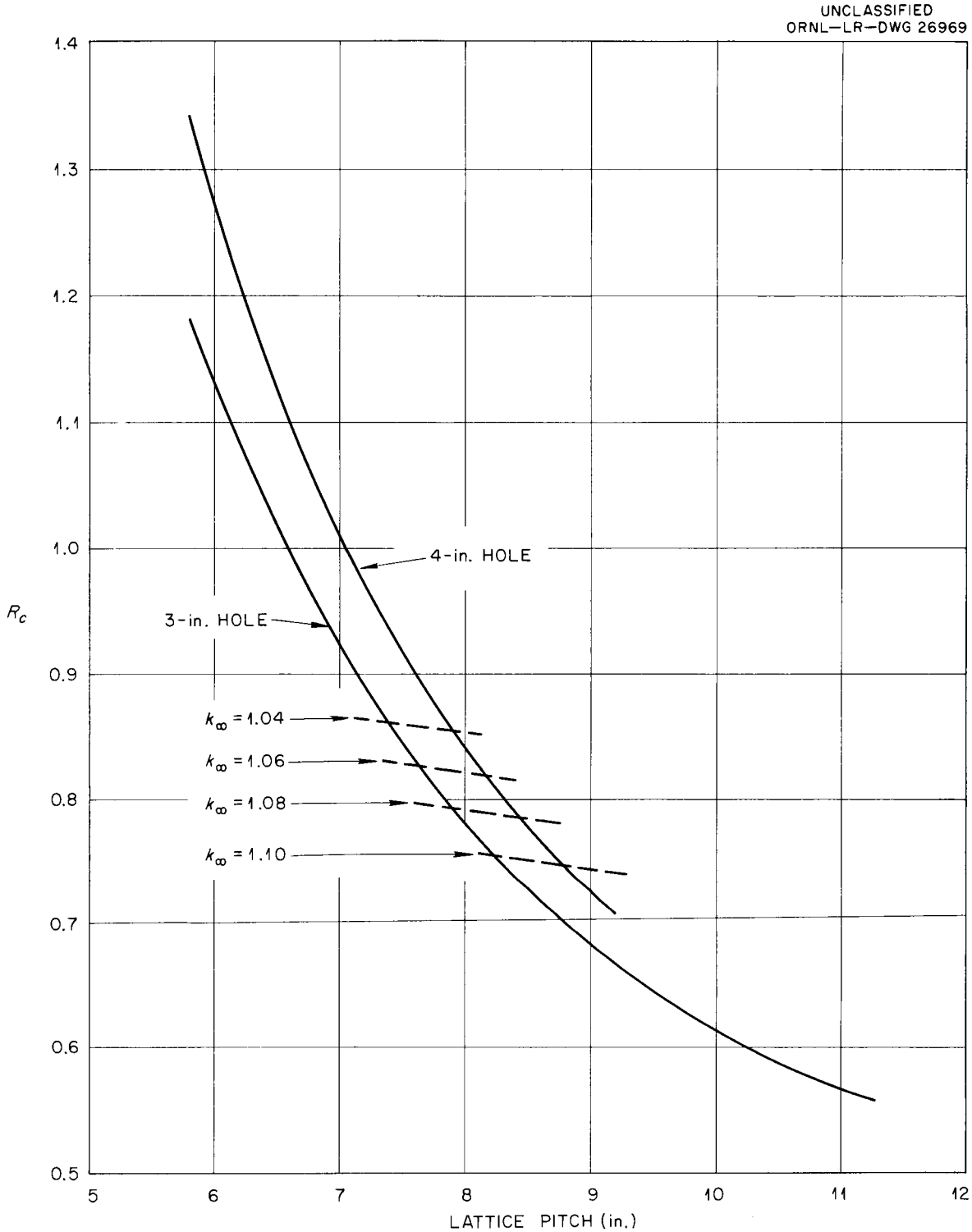

Fig. 2.23. Effect of Cooling-Channel Diameter on Conversion Ratio.

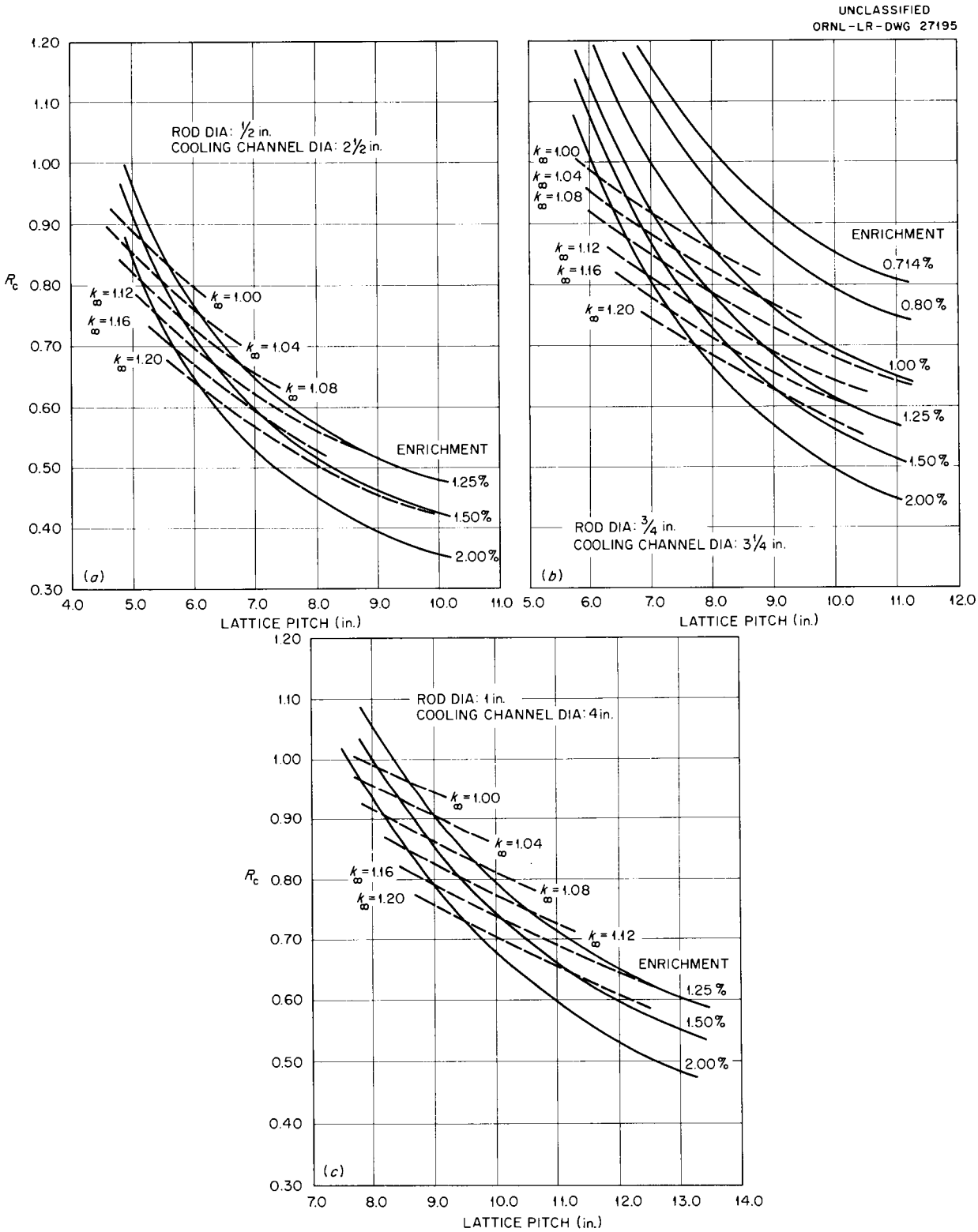

Fig. 2.24. Conversion Ratio vs Lattice Pitch and Enrichment. (*a*) Seven 0.5-in.-dia rods. (*b*) Seven 0.75-in.-dia rods. (*c*) Seven 1.0-in.-dia rods.

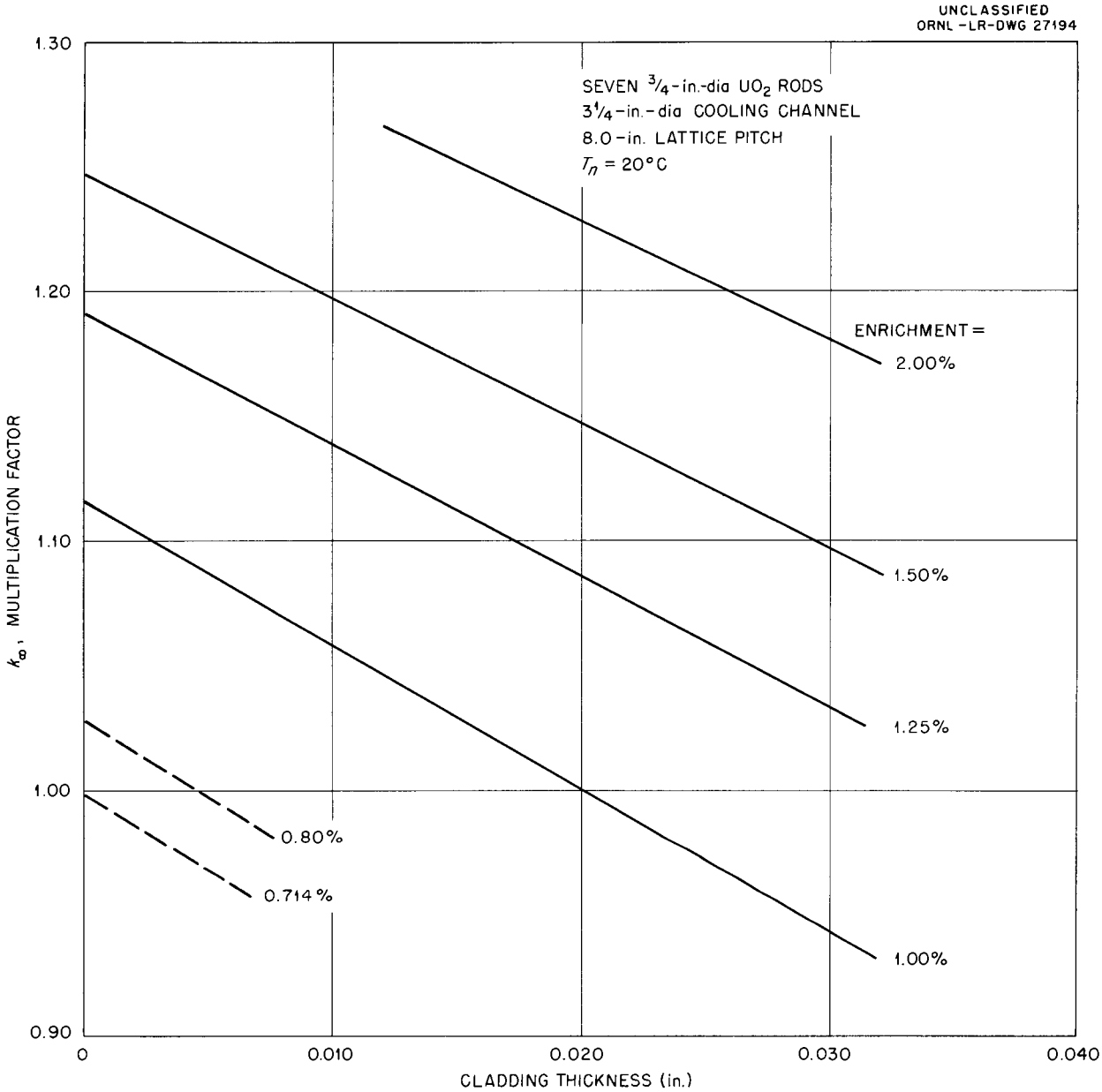

Fig. 2.25. Effect of Clad Thickness on Multiplication Factor.

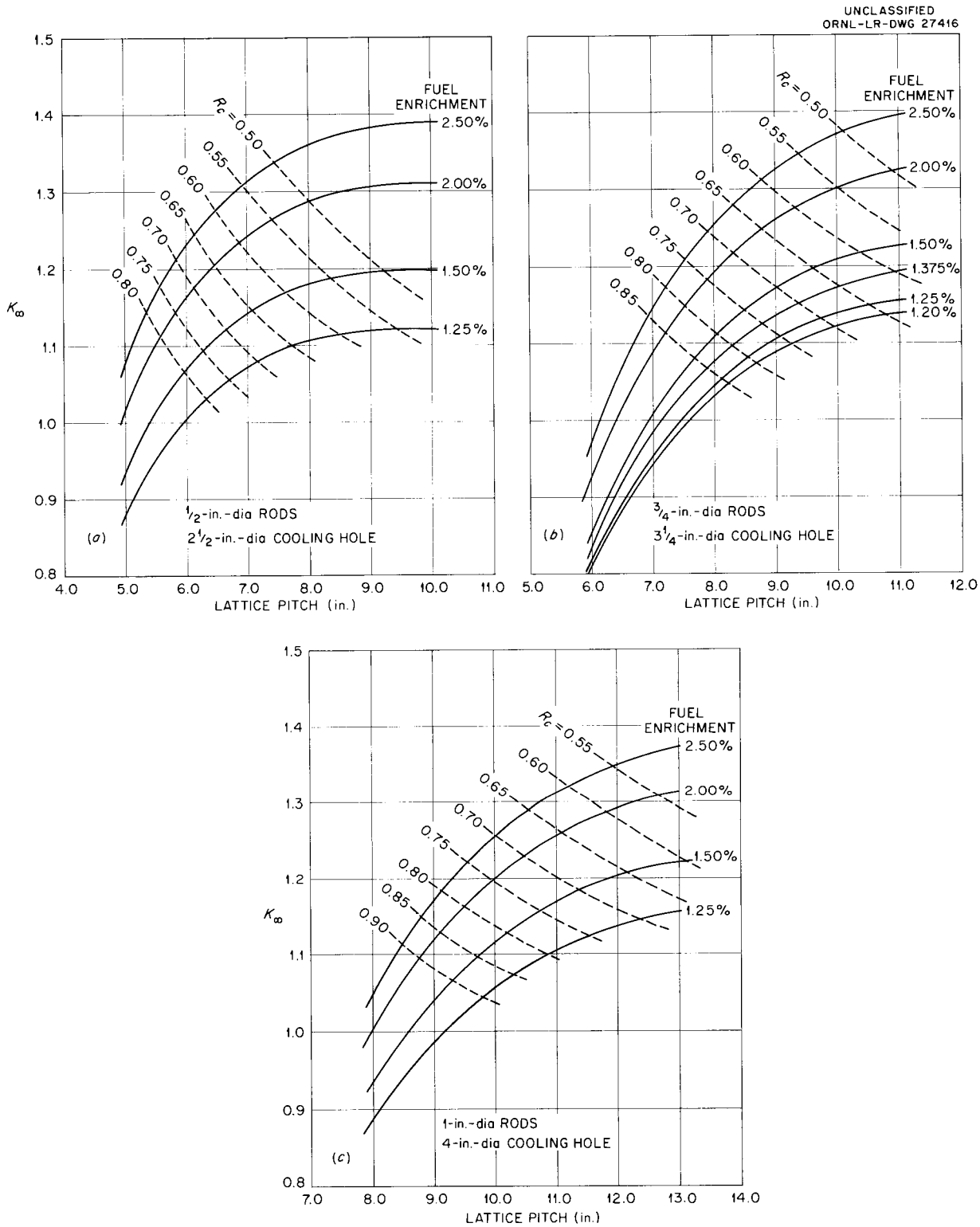

Fig. 2.26. Multiplication Factor vs Lattice Pitch Enrichment, T_n = 814°K. (*a*) Seven UO_2 rods – 0.5-in.-dia. (*b*) Seven UO_2 rods – 0.75-in.-dia. (*c*) Seven UO_2 rods – 1.0-in.-dia.

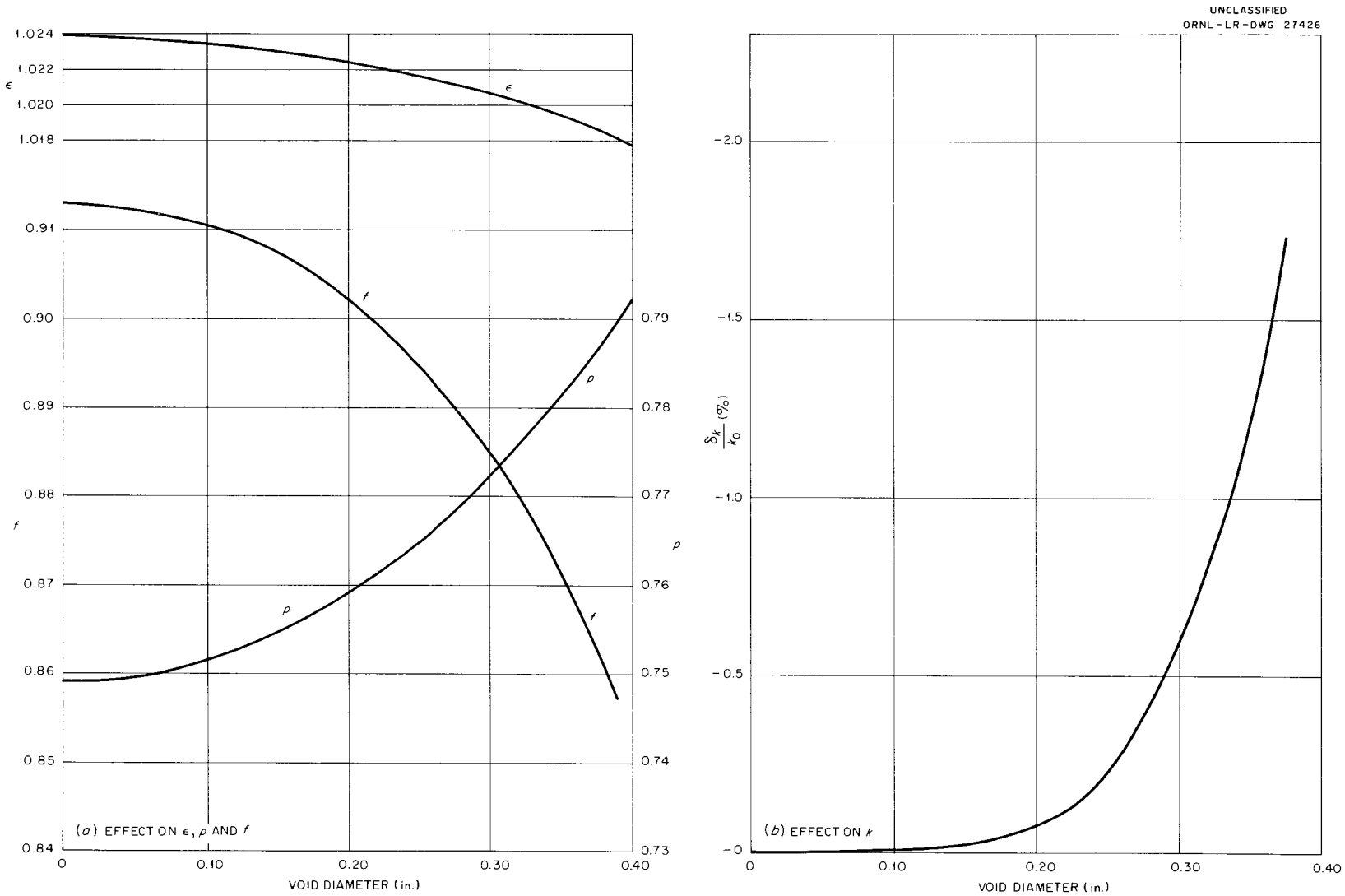

Fig. 2.27. Effect of Central Hole in Fuel Rods. (*a*) Effect on f, p, and ϵ. (*b*) Effect on multiplication factor – 7 UO_2 rods, 0.75-in.-dia, 3.25-in. cooling-channel dia.

long-lived fuel configurations. The effect on pile reactivity of providing a central hole in each of the fuel rods was therefore studied, and the results for 0.75-in.-dia rods are shown in Fig. 2.27. It is apparent that small holes make practically no difference in multiplication factor, but that a significant reduction in k sets in for holes with diameters between 0.3 and 0.4 in. It was decided that a 5/16-in.-dia hole in each rod was a reasonable compromise between the requirements for gas accumulation volume and the need to maintain reactivity. The loss in k is 0.9%.

2.2.4. General Conclusions: The significance of the above results can be made apparent only when they are integrated with the heat-transfer calculations and other design considerations, since the final choice of a lattice configuration reduces to a question of minimum power cost. This matter is discussed in Section 11. Certain preliminary conclusions can be drawn, however, without considering the economics of the over-all plant.

One important decision to be made in selecting core parameters is the choice of the diameter of the individual fuel rods in the cluster. It can be rather confidently predicted that the best rod size to use is the one that permits extracting the greatest amount of heat per unit volume of core. It is intuitively obvious that the smaller diameter fuel rods will permit the greater heat extraction per unit volume of fuel. The lattice reactivity calculations, however, show that larger rods permit a greater volume of fuel per unit volume of core. Figure 2.28 shows the multiplication factor vs volume fraction of UO_2 (fuel volume/core volume) for 0.5, 0.75, and 1.0-in.-dia rods in seven-rod clusters. The ratios of UO_2 volume fractions at constant k for the different rod diameters are nearly the same over quite a wide range of k, $1.05 \leq k \leq 1.2$. This range of k is emphasized because the lattice pitch chosen will certainly be less than that for maximum k since high power density is desired. For k = 1.2, the average fuel densities in the core stand in the ratios 1.0/1.39/1.62 in order of increasing rod diameter. On the other hand, the specific power densities (power/unit volume of fuel) under conditions of optimum heat transfer stand approximately in the ratios 1.0/0.77/0.59. The products are 1.0/1.07/0.96. It would therefore appear that from the point of view of power generation per unit volume of core, there exists a broad

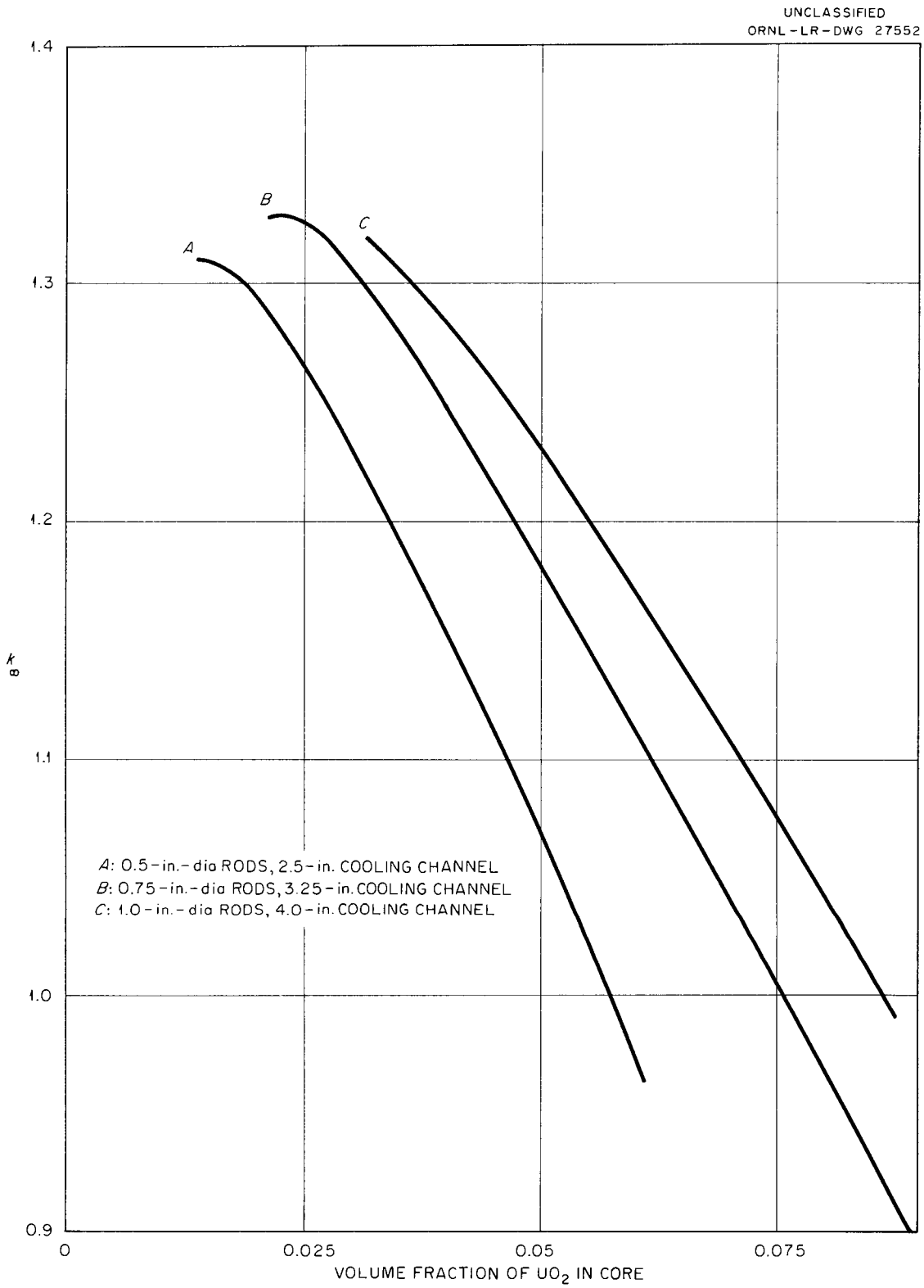

Fig. 2.28. Multiplication Factor vs UO_2 Volume Fraction – Fuel Enrichment 2.00%.

TABLE 2.10

RESULTS OF CALCULATIONS OF k_∞ AND CONVERSION RATIO

The following pages list in detail the values of η, ϵ, p, f, k_∞, and R_c for the lattices analyzed in the ORNL-GCR-2 design study. The methods which were used in computing each of these factors are described elsewhere in this report. This table is divided into sections as outlined below:

I. Moderator at Room Temperature (Neutron Temperature = 294°K)
   - A. Single UO_2 Rod Fuel Element, Stainless Steel 430 Clad
   - B. Single Uranium Metal Fuel Rod, Magnesium Clad
   - C. Seven-Rod Clusters of UO_2 Fuel Rods, Stainless Steel 430 Clad

II. Moderator Temperature = 750°F (Neutron Temperature = 814°K)
   - A. Seven-Rod Clusters of UO_2 Fuel Rods, Stainless Steel 430 Clad

I. MODERATOR AT ROOM TEMPERATURE (NEUTRON TEMPERATURE = 294°K)

A. SINGLE UO_2 ROD FUEL ELEMENT, STAINLESS STEEL 430 CLAD

Case Number	Rod Diameter (in.)	Clad Thickness (in.)	Enrichment (Atomic %)	Cooling Hole Diameter (in.)	Lattice Pitch (in.)	η	ϵ	p	f	k_∞	R_c
1	1.50	0.040	0.714	3.00	6.27	1.339	1.020	0.7761	0.8149	0.864	1.009
2	"	"	"	"	6.97	"	"	0.8209	0.8009	0.898	0.918
3	"	"	"	"	7.67	"	"	0.8534	0.7854	0.915	0.852
4	"	"	"	"	8.36	"	"	0.8777	0.7685	0.921	0.803
5	"	"	"	"	9.06	"	"	0.8965	0.7505	0.919	0.765
6	1.50	0.040	0.80	3.00	6.27	1.392	1.020	0.7761	0.8231	0.907	0.949
7	"	"	"	"	6.97	"	"	0.8209	0.8093	0.943	0.858
8	"	"	"	"	7.67	"	"	0.8534	0.7941	0.962	0.792
9	"	"	"	"	8.36	"	"	0.8777	0.7773	0.969	0.743
10	"	"	"	"	9.06	"	"	0.8965	0.7597	0.967	0.705
11	1.50	0.040	1.00	3.00	5.58	1.491	1.020	0.7117	0.8502	0.920	0.981
12	"	"	"	"	6.27	"	"	0.7761	0.8382	0.989	0.849
13	"	"	"	"	6.97	"	"	0.8209	0.8255	1.031	0.758
14	"	"	"	"	7.67	"	"	0.8534	0.8107	1.052	0.692
15	"	"	"	"	8.36	"	"	0.8777	0.7946	1.061	0.643
16	1.50	0.040	1.25	3.00	4.88	1.580	1.020	0.6142	0.8733	0.864	1.101
17	"	"	"	"	5.58	"	"	0.7117	0.8643	0.991	0.901
18	"	"	"	"	6.27	"	"	0.7761	0.8533	1.067	0.769
19	"	"	"	"	6.97	"	"	0.8209	0.8406	1.112	0.678
20	"	"	"	"	7.67	"	"	0.8534	0.8263	1.136	0.612
21	1.50	0.000	0.714	3.00	6.27	1.339	1.020	0.7822	0.9396	1.004	1.009
22	"	"	"	"	6.97	"	"	0.8261	0.9217	1.040	0.918
23	"	"	"	"	7.67	"	"	0.8578	0.9023	1.057	0.852
24	"	"	"	"	8.36	"	"	0.8815	0.8812	1.061	0.803
25	"	"	"	"	9.06	"	"	0.8997	0.8592	1.056	0.765
26	1.50	0.000	0.80	3.00	5.58	1.392	1.020	0.7190	0.9574	0.977	1.081
27	"	"	"	"	6.27	"	"	0.7822	0.9415	1.046	0.949
28	"	"	"	"	6.97	"	"	0.8261	0.9242	1.084	0.858
29	"	"	"	"	7.67	"	"	0.8578	0.9055	1.103	0.792
30	"	"	"	"	8.36	"	"	0.8815	0.8857	1.108	0.743

Case Number	Rod Diameter (in.)	Clad Thickness (in.)	Enrichment (Atomic %)	Cooling Hole Diameter (in.)	Lattice Pitch (in.)	η	ϵ	p	f	k_∞	R_c
31	1.50	0.000	1.00	3.00	4.88	1.491	1.020	0.6228	0.9731	0.922	1.181
32	"	"	"	"	5.58	"	"	0.7190	0.9585	1.048	0.981
33	"	"	"	"	6.27	"	"	0.7822	0.9440	1.123	0.849
34	"	"	"	"	6.97	"	"	0.8261	0.9285	1.167	0.758
35	"	"	"	"	7.67	"	"	0.8578	0.9128	1.191	0.692
36	1.50	0.060	1.00	3.00	6.27	1.491	1.020	0.7728	0.7903	0.929	0.849
37	"	"	"	"	6.97	"	"	0.8182	0.7780	0.968	0.758
38	"	"	"	"	7.67	"	"	0.8512	0.7648	0.990	0.692
39	"	"	"	"	8.36	"	"	0.8758	0.7500	0.999	0.643
40	"	"	"	"	9.06	"	"	0.8948	0.7342	0.999	0.605
41	1.50	0.060	1.25	3.00	5.58	1.580	1.020	0.7079	0.8185	0.934	0.901
42	"	"	"	"	6.27	"	"	0.7728	0.8085	1.007	0.769
43	"	"	"	"	6.97	"	"	0.8182	0.7968	1.051	0.678
44	"	"	"	"	7.67	"	"	0.8512	0.7837	1.075	0.612
45	"	"	"	"	8.36	"	"	0.8758	0.7692	1.086	0.563
46	1.50	0.060	1.50	3.00	4.88	1.646	1.020	0.6099	0.8399	0.860	1.047
47	"	"	"	"	5.58	"	"	0.7079	0.8317	0.988	0.847
48	"	"	"	"	6.27	"	"	0.7728	0.8223	1.067	0.715
49	"	"	"	"	6.97	"	"	0.8182	0.8107	1.114	0.624
50	"	"	"	"	7.67	"	"	0.8512	0.7981	1.141	0.558
51	1.50	0.060	2.00	3.00	4.88	1.737	1.020	0.6099	0.8586	0.928	0.981
52	"	"	"	"	5.58	"	"	0.7079	0.8510	1.067	0.781
53	"	"	"	"	6.27	"	"	0.7728	0.8419	1.153	0.649
54	"	"	"	"	6.97	"	"	0.8182	0.8309	1.204	0.558
55	"	"	"	"	7.67	"	"	0.8512	0.8185	1.234	0.492
56	1.50	0.080	1.00	3.00	6.27	1.491	1.020	0.7697	0.7451	0.872	0.849
57	"	"	"	"	6.97	"	"	0.8155	0.7342	0.911	0.758
58	"	"	"	"	7.67	"	"	0.8488	0.7219	0.932	0.692
59	"	"	"	"	8.36	"	"	0.8738	0.7084	0.941	0.643
60	"	"	"	"	9.06	"	"	0.8931	0.6938	0.942	0.605
61	1.50	0.080	1.25	3.00	5.58	1.580	1.020	0.7041	0.7753	0.880	0.901
62	"	"	"	"	6.27	"	"	0.7697	0.7657	0.950	0.769
63	"	"	"	"	6.97	"	"	0.8155	0.7555	0.993	0.678
64	"	"	"	"	7.67	"	"	0.8488	0.7433	1.017	0.612
65	"	"	"	"	8.36	"	"	0.8738	0.7299	1.028	0.563

Case Number	Rod Diameter (in.)	Clad Thickness (in.)	Enrichment (Atomic %)	Cooling Hole Diameter (in.)	Lattice Pitch (in.)	η	ϵ	p	f	k_∞	R_c
66	1.50	0.080	1.50	3.00	4.88	1.646	1.020	0.6056	0.7983	0.812	1.047
67	"	"	"	"	5.58	"	"	0.7041	0.7913	0.935	0.847
68	"	"	"	"	6.27	"	"	0.7697	0.7823	1.011	0.715
69	"	"	"	"	6.97	"	"	0.8155	0.7718	1.057	0.624
70	"	"	"	"	7.67	"	"	0.8488	0.7599	1.083	0.558
71	1.00	0.000	0.714	3.00	4.88	1.339	1.014	0.7843	0.9401	1.001	1.003
72	"	"	"	"	5.58	"	"	0.8442	0.9150	1.049	0.879
73	"	"	"	"	6.27	"	"	0.8815	0.8887	1.064	0.801
74	"	"	"	"	6.97	"	"	0.9066	0.8583	1.056	0.749
75	"	"	"	"	7.67	"	"	0.9243	0.8249	1.035	0.713
76	1.00	0.000	0.80	3.00	4.88	1.392	1.014	0.7843	0.9430	1.044	0.943
77	"	"	"	"	5.58	"	"	0.8442	0.9220	1.099	0.819
78	"	"	"	"	6.27	"	"	0.8815	0.8955	1.114	0.741
79	"	"	"	"	6.97	"	"	0.9066	0.8655	1.108	0.689
80	"	"	"	"	7.67	"	"	0.9243	0.8317	1.085	0.653
81	1.00	0.040	1.00	3.00	4.88	1.491	1.014	0.7843	0.8044	0.944	0.843
82	"	"	"	"	5.58	"	"	0.8442	0.7878	0.998	0.719
83	"	"	"	"	6.27	"	"	0.8815	0.7691	1.019	0.641
84	"	"	"	"	6.97	"	"	0.9066	0.7484	1.021	0.589
85	"	"	"	"	7.67	"	"	0.9243	0.7257	1.010	0.553
86	1.00	0.040	1.25	3.00	4.88	1.580	1.014	0.7843	0.8241	1.025	0.763
87	"	"	"	"	5.58	"	"	0.8442	0.8070	1.083	0.639
88	"	"	"	"	6.27	"	"	0.8515	0.7887	1.108	0.561
89	"	"	"	"	6.97	"	"	0.9066	0.7692	1.112	0.509
90	"	"	"	"	7.67	"	"	0.9243	0.7484	1.104	0.473
91	1.00	0.040	1.50	3.00	4.88	1.646	1.014	0.7762	0.8391	1.087	0.709
92	"	"	"	"	5.58	"	"	0.8379	0.8237	1.152	0.585
93	"	"	"	"	6.27	"	"	0.8766	0.8067	1.180	0.507
94	"	"	"	"	6.97	"	"	0.9026	0.7873	1.186	0.455
95	"	"	"	"	7.67	"	"	0.9210	0.7659	1.177	0.419
96	1.00	0.060	1.00	3.00	4.88	1.491	1.014	0.7721	0.7431	0.867	0.843
97	"	"	"	"	5.58	"	"	0.8347	0.7277	0.918	0.719
98	"	"	"	"	6.27	"	"	0.8741	0.7112	0.940	0.641
99	"	"	"	"	6.97	"	"	0.9005	0.6933	0.944	0.589
100	"	"	"	"	7.67	"	"	0.9192	0.6742	0.937	0.553

Case Number	Rod Diameter (in.)	Clad Thickness (in.)	Enrichment (Atomic %)	Cooling Hole Diameter (in.)	Lattice Pitch (in.)	η	ϵ	p	f	k_∞	R_c
101	1.00	0.060	1.25	3.00	4.88	1.580	1.014	0.7721	0.7673	0.949	0.763
102	"	"	"	"	5.58	"	"	0.8347	0.7530	1.007	0.639
103	"	"	"	"	6.27	"	"	0.8741	0.7376	1.033	0.561
104	"	"	"	"	6.97	"	"	0.9005	0.7193	1.038	0.509
105	"	"	"	"	7.67	"	"	0.9192	0.7000	1.031	0.473
106	1.50	0.000	0.714	4.00	6.27	1.339	1.020	0.7439	0.9498	0.965	1.086
107	"	"	"	"	6.97	"	"	0.8024	0.9320	1.021	0.965
108	"	"	"	"	7.67	"	"	0.8423	0.9123	1.049	0.882
109	"	"	"	"	8.36	"	"	0.8709	0.8911	1.060	0.823
110	"	"	"	"	9.06	"	"	0.8923	0.8679	1.058	0.779
111	1.50	0.040	0.80	4.00	6.27	1.392	1.020	0.7370	0.8306	0.869	1.026
112	"	"	"	"	6.97	"	"	0.7967	0.8177	0.925	0.905
113	"	"	"	"	7.67	"	"	0.8375	0.8030	0.956	0.822
114	"	"	"	"	8.36	"	"	0.8669	0.7865	0.968	0.763
115	"	"	"	"	9.06	"	"	0.8888	0.7667	0.967	0.719
116	1.50	0.060	1.00	4.00	6.27	1.491	1.020	0.7334	0.7965	0.888	0.926
117	"	"	"	"	6.97	"	"	0.7937	0.7846	0.947	0.805
118	"	"	"	"	7.67	"	"	0.8351	0.7715	0.980	0.722
119	"	"	"	"	8.36	"	"	0.8648	0.7570	0.996	0.663
120	"	"	"	"	9.06	"	"	0.8870	0.7404	0.999	0.619
121	1.50	0.060	1.50	4.00	6.27	1.646	1.020	0.7334	0.8281	1.020	0.792
122	"	"	"	"	6.97	"	"	0.7937	0.8167	1.088	0.671
123	"	"	"	"	7.67	"	"	0.8351	0.8044	1.128	0.588
124	"	"	"	"	8.36	"	"	0.8648	0.7902	1.147	0.529
125	"	"	"	"	9.06	"	"	0.8870	0.7744	1.153	0.485

B. SINGLE URANIUM METAL FUEL ROD, MAGNESIUM CLAD

Case Number	Rod Diameter (in.)	Clad Thickness (cm)	Enrichment (Atomic %)	Cooling Hole Diameter (in.)	Lattice Pitch (in.)	η	ϵ	p	f	k_∞	R_c
136	1.00	0.00	0.714	4.00	6.27	1.339	1.030	0.8103	0.9382	1.048	0.951
137	"	"	"	"	6.97	"	"	0.8552	0.9160	1.080	0.857
138	"	"	"	"	7.67	"	"	0.8851	0.8926	1.089	0.795
139	"	"	"	"	8.36	"	"	0.9065	0.8679	1.085	0.750
140	"	"	"	"	9.06	"	"	0.9221	0.8406	1.069	0.718
141	1.00	0.32	0.714	4.00	6.27	1.339	1.030	0.8021	0.9336	1.033	0.951
142	"	"	"	"	6.97	"	"	0.8487	0.9128	1.068	0.857
143	"	"	"	"	7.67	"	"	0.8799	0.8900	1.080	0.795
144	"	"	"	"	8.36	"	"	0.9021	0.8646	1.076	0.750
145	"	"	"	"	9.06	"	"	0.9185	0.8370	1.060	0.718
146	1.00	0.32	0.80	4.00	5.58	1.392	1.030	0.7272	0.9547	0.996	0.891
147	"	"	"	"	6.27	"	"	0.8021	0.9365	1.077	0.797
148	"	"	"	"	6.97	"	"	0.8487	0.9165	1.115	0.735
149	"	"	"	"	7.67	"	"	0.8799	0.8945	1.129	0.690
150	"	"	"	"	8.36	"	"	0.9021	0.8702	1.126	0.658
1001	1.15	0.60	0.72	4.00	6.0	1.342	1.032	0.7141	0.9482	0.937	1.103
1002	"	"	"	"	7.0	"	"	0.8046	0.9245	1.030	0.927
1003	"	"	"	"	8.0	"	"	0.8570	0.8971	1.065	0.825
1004	"	"	"	"	9.0	"	"	0.8904	0.8666	1.068	0.761
1005	"	"	"	"	10.0	"	"	0.9130	0.8329	1.053	0.717
1006	1.15	0.60	0.80	4.00	6.0	1.392	1.032	0.7141	0.9499	0.975	1.048
1007	"	"	"	"	7.0	"	"	0.8046	0.9262	1.071	0.872
1008	"	"	"	"	8.0	"	"	0.8570	0.8990	1.107	0.770
1009	"	"	"	"	9.0	"	"	0.8904	0.8690	1.112	0.706
1010	"	"	"	"	10.0	"	"	0.9130	0.8369	1.098	0.662
1011	1.15	0.60	1.00	4.00	5.0	1.491	1.032	0.5334	0.9710	0.797	1.305
1012	"	"	"	"	6.0	"	"	0.7141	0.9535	1.048	0.948
1013	"	"	"	"	7.0	"	"	0.8046	0.9313	1.153	0.772
1014	"	"	"	"	8.0	"	"	0.8570	0.9065	1.195	0.670
1015	"	"	"	"	9.0	"	"	0.8904	0.8766	1.201	0.606
1016	1.15	0.60	1.25	4.00	5.0	1.580	1.032	0.5334	0.9730	0.846	1.225
1017	"	"	"	"	6.0	"	"	0.7141	0.9530	1.110	0.868
1018	"	"	"	"	7.0	"	"	0.8046	0.9310	1.222	0.692
1019	"	"	"	"	8.0	"	"	0.8570	0.9078	1.269	0.590
1020	"	"	"	"	9.0	"	"	0.8904	0.8828	1.282	0.526

Case Number	Rod Diameter (in.)	Clad Thickness (cm)	Enrichment (Atomic %)	Cooling Hole Diameter (in.)	Lattice Pitch (in.)	η	ϵ	p	f	k_∞	R_c
1021	1.15	0.60	1.50	4.00	5.0	1.646	1.032	0.5334	0.9744	0.883	1.171
1022	"	"	"	"	6.0	"	"	0.7141	0.9571	1.162	0.814
1023	"	"	"	"	7.0	"	"	0.8046	0.9372	1.281	0.638
1024	"	"	"	"	8.0	"	"	0.8578	0.9135	1.330	0.536
1025	"	"	"	"	9.0	"	"	0.8904	0.8872	1.342	0.472

C. SEVEN ROD CLUSTERS OF UO_2 FUEL RODS, STAINLESS STEEL 430 CLAD

Case Number	Rod Diameter (in.)	Clad Thickness (in.)	Enrichment (Atomic %)	Cooling Hole Diameter (in.)	Lattice Pitch (in.)	η	ϵ	p	f	k_∞	R_c
181	0.50	0.000	0.714	3.25	5.0	1.339	1.016	0.6126	0.9692	0.808	1.358
182	"	"	"	"	6.0	"	"	0.7413	0.9442	0.952	1.092
183	"	"	"	"	7.0	"	"	0.8147	0.9195	1.019	0.940
184	"	"	"	"	8.0	"	"	0.8605	0.8945	1.047	0.845
185	0.50	0.000	0.80	3.25	5.0	1.392	1.016	0.6126	0.9709	0.841	1.298
186	"	"	"	"	6.0	"	"	0.7413	0.9470	0.993	1.032
187	"	"	"	"	7.0	"	"	0.8147	0.9232	1.064	0.880
188	"	"	"	"	8.0	"	"	0.8605	0.8994	1.095	0.785
189	0.50	0.020	1.25	3.25	5.0	1.580	1.016	0.6046	0.8603	0.835	1.118
190	"	"	"	"	6.0	"	"	0.7349	0.8453	0.997	0.852
191	"	"	"	"	7.0	"	"	0.8096	0.8294	1.078	0.700
192	"	"	"	"	8.0	"	"	0.8565	0.8120	1.116	0.605
276	0.50	0.020	1.25	2.50	5.0	1.580	1.016	0.6749	0.8509	0.922	0.970
277	"	"	"	"	6.0	"	"	0.7734	0.8342	1.035	0.771
278	"	"	"	"	7.0	"	"	0.8334	0.8160	1.091	0.650
279	"	"	"	"	8.0	"	"	0.8724	0.7960	1.114	0.572
280	"	"	"	"	9.0	"	"	0.8992	0.7754	1.119	0.518
281	"	"	"	"	10.0	"	"	0.9183	0.7532	1.110	0.480

Case Number	Rod Diameter (in.)	Clad Thickness (in.)	Enrichment (Atomic %)	Cooling Hole Diameter (in.)	Lattice Pitch (in.)	η	ϵ	p	f	k_∞	R_c
282	0.50	0.020	1.50	2.50	5.0	1.646	1.016	0.6749	0.8665	0.978	0.916
283	"	"	"	"	6.0	"	"	0.7734	0.8500	1.099	0.717
284	"	"	"	"	7.0	"	"	0.8334	0.8323	1.160	0.596
285	"	"	"	"	8.0	"	"	0.8724	0.8135	1.187	0.518
286	"	"	"	"	9.0	"	"	0.8992	0.7932	1.192	0.464
287	"	"	"	"	10.0	"	"	0.9183	0.7723	1.186	0.426
288	0.50	0.020	2.00	2.50	5.0	1.737	1.016	0.6749	0.8891	1.059	0.850
289	"	"	"	"	6.0	"	"	0.7734	0.8740	1.193	0.651
290	"	"	"	"	7.0	"	"	0.8334	0.8573	1.261	0.530
291	"	"	"	"	8.0	"	"	0.8724	0.8395	1.293	0.452
292	"	"	"	"	9.0	"	"	0.8992	0.8202	1.302	0.398
293	"	"	"	"	10.0	"	"	0.9183	0.8003	1.297	0.360
153	0.75	0.000	0.714	3.25	6.0	1.339	1.024	0.6064	0.9716	0.808	1.371
154	"	"	"	"	7.0	"	"	0.7077	0.9540	0.926	1.161
155	"	"	"	"	8.0	"	"	0.7755	0.9360	0.995	1.021
156	"	"	"	"	9.0	"	"	0.8222	0.9186	1.036	0.924
157	0.75	0.000	0.80	3.25	6.0	1.392	1.024	0.6064	0.9728	0.841	1.311
158	"	"	"	"	7.0	"	"	0.7077	0.9556	0.964	1.101
159	"	"	"	"	8.0	"	"	0.7755	0.9386	1.038	0.961
160	"	"	"	"	9.0	"	"	0.8222	0.9216	1.080	0.864
161	0.75	0.000	1.25	3.25	6.0	1.580	1.024	0.6064	0.9774	0.959	1.131
162	"	"	"	"	7.0	"	"	0.7077	0.9642	1.104	0.921
163	"	"	"	"	8.0	"	"	0.7755	0.9500	1.192	0.781
164	"	"	"	"	9.0	"	"	0.8222	0.9325	1.241	0.684
165	0.75	0.000	1.50	3.25	6.0	1.646	1.024	0.6064	0.9790	1.001	1.077
166	"	"	"	"	7.0	"	"	0.7077	0.9675	1.154	0.867
167	"	"	"	"	8.0	"	"	0.7755	0.9550	1.248	0.727
168	"	"	"	"	9.0	"	"	0.8222	0.9385	1.301	0.630
211	0.75	0.020	1.00	3.25	6.0	1.491	1.024	0.5995	0.8780	0.804	1.211
212	"	"	"	"	7.0	"	"	0.7021	0.8650	0.927	1.001
213	"	"	"	"	8.0	"	"	0.7704	0.8517	1.002	0.861
214	"	"	"	"	9.0	"	"	0.8179	0.8372	1.046	0.764
215	"	"	"	"	10.0	"	"	0.8522	0.8206	1.068	0.693
216	"	"	"	"	11.0	"	"	0.8777	0.8000	1.072	0.648

Case Number	Rod Diameter (in.)	Clad Thickness (in.)	Enrichment (Atomic %)	Cooling Hole Diameter (in.)	Lattice Pitch (in.)	η	ϵ	p	f	k_∞	R_c
169	0.75	0.020	1.25	3.25	6.0	1.580	1.024	0.5995	0.8947	0.868	1.131
170	"	"	"	"	7.0	"	"	0.7021	0.8836	1.004	0.921
171	"	"	"	"	8.0	"	"	0.7704	0.8705	1.085	0.781
172	"	"	"	"	9.0	"	"	0.8179	0.8551	1.132	0.684
209(a)	"	"	"	"	10.0	"	"	0.8522	0.8370	1.154	0.613
209	"	"	"	"	11.0	"	"	0.8777	0.8175	1.161	0.568
173	0.75	0.020	1.50	3.25	6.0	1.646	1.024	0.5995	0.9053	0.915	1.077
174	"	"	"	"	7.0	"	"	0.7021	0.8942	1.058	0.867
175	"	"	"	"	8.0	"	"	0.7704	0.8820	1.145	0.727
176	"	"	"	"	9.0	"	"	0.8179	0.8675	1.196	0.630
210(a)	"	"	"	"	10.0	"	"	0.8522	0.8500	1.221	0.559
210	"	"	"	"	11.0	"	"	0.8777	0.8308	1.229	0.514
270	0.75	0.020	2.00	3.25	6.0	1.737	1.024	0.5995	0.9203	0.981	1.011
271	"	"	"	"	7.0	"	"	0.7021	0.9091	1.135	0.801
272	"	"	"	"	8.0	"	"	0.7704	0.8960	1.228	0.661
273	"	"	"	"	9.0	"	"	0.8179	0.8817	1.283	0.564
274	"	"	"	"	10.0	"	"	0.8522	0.8662	1.313	0.493
275	"	"	"	"	11.0	"	"	0.8777	0.8497	1.326	0.448
294	1.00	0.020	1.25	4.00	8.0	1.580	1.028	0.6428	0.9039	0.944	1.055
295	"	"	"	"	9.0	"	"	0.7147	0.8915	1.035	0.907
296	"	"	"	"	10.0	"	"	0.7674	0.8776	1.094	0.797
297	"	"	"	"	11.0	"	"	0.8068	0.8625	1.130	0.716
298	"	"	"	"	12.0	"	"	0.8371	0.8465	1.151	0.653
299	"	"	"	"	13.0	"	"	0.8609	0.8300	1.160	0.604
300	1.00	0.020	1.50	4.00	8.0	1.646	1.028	0.6428	0.9125	0.992	1.001
301	"	"	"	"	9.0	"	"	0.7147	0.9012	1.090	0.853
302	"	"	"	"	10.0	"	"	0.7674	0.8882	1.153	0.743
303	"	"	"	"	11.0	"	"	0.8068	0.8737	1.192	0.662
304	"	"	"	"	12.0	"	"	0.8371	0.8577	1.215	0.599
305	"	"	"	"	13.0	"	"	0.8609	0.8404	1.224	0.550
306	1.00	0.020	2.00	4.00	8.0	1.737	1.028	0.6428	0.9252	1.062	0.935
307	"	"	"	"	9.0	"	"	0.7147	0.9142	1.167	0.787
308	"	"	"	"	10.0	"	"	0.7674	0.9020	1.236	0.677
309	"	"	"	"	11.0	"	"	0.8068	0.8885	1.280	0.596
310	"	"	"	"	12.0	"	"	0.8371	0.8732	1.306	0.533
311	"	"	"	"	13.0	"	"	0.8609	0.8570	1.318	0.484

II. MODERATOR TEMPERATURE = 750°F (NEUTRON TEMPERATURE = 814°K)

A. SEVEN ROD CLUSTERS OF UO_2 FUEL RODS, STAINLESS STEEL 430 CLAD

Case Number	Rod Diameter (in.)	Clad Thickness (in.)	Enrichment (Atomic %)	Cooling Hole Diameter (in.)	Lattice Pitch (in.)	η	ϵ	p	f	k_{∞}	R_c
342	0.50	0.018	1.25	2.50	5.0	1.539	1.016	0.6531	0.8639	0.882	1.064
343	"	"	"	"	6.0	"	"	0.7570	0.8502	1.006	0.849
344	"	"	"	"	7.0	"	"	0.8208	0.8356	1.072	0.717
345	"	"	"	"	8.0	"	"	0.8625	0.8200	1.106	0.630
346	"	"	"	"	9.0	"	"	0.8912	0.8028	1.119	0.571
347	"	"	"	"	10.0	"	"	0.9118	0.7847	1.119	0.529
348	0.50	0.018	1.50	2.50	5.0	1.609	1.016	0.6531	0.8783	0.938	1.006
349	"	"	"	"	6.0	"	"	0.7570	0.8655	1.071	0.791
350	"	"	"	"	7.0	"	"	0.8208	0.8518	1.143	0.659
351	"	"	"	"	8.0	"	"	0.8625	0.8370	1.180	0.572
352	"	"	"	"	9.0	"	"	0.8912	0.8204	1.195	0.513
353	"	"	"	"	10.0	"	"	0.9118	0.8025	1.196	0.471
354	0.50	0.018	2.00	2.50	5.0	1.706	1.016	0.6531	0.8994	1.018	0.933
355	"	"	"	"	6.0	"	"	0.7570	0.8875	1.165	0.718
356	"	"	"	"	7.0	"	"	0.8208	0.8746	1.244	0.586
357	"	"	"	"	8.0	"	"	0.8625	0.8610	1.287	0.499
358	"	"	"	"	9.0	"	"	0.8912	0.8456	1.306	0.440
359	"	"	"	"	10.0	"	"	0.9118	0.8289	1.310	0.398
384	0.50	0.018	2.50	2.50	5.0	1.770	1.016	0.6531	0.9140	1.074	0.889
385	"	"	"	"	6.0	"	"	0.7570	0.9033	1.230	0.674
386	"	"	"	"	7.0	"	"	0.8208	0.8914	1.316	0.542
387	"	"	"	"	8.0	"	"	0.8625	0.8780	1.362	0.455
388	"	"	"	"	9.0	"	"	0.8912	0.8635	1.384	0.396
389	"	"	"	"	10.0	"	"	0.9118	0.8478	1.390	0.354
248	0.75	0.018	1.20	3.25	6.0	1.522	1.024	0.5657	0.9037	0.797	1.260
249	"	"	"	"	7.0	"	"	0.6744	0.8936	0.940	1.035
250	"	"	"	"	8.0	"	"	0.7486	0.8837	1.031	0.881
251	"	"	"	"	9.0	"	"	0.8001	0.8723	1.088	0.775
252	"	"	"	"	10.0	"	"	0.8377	0.8591	1.122	0.697
253	"	"	"	"	11.0	"	"	0.8655	0.8438	1.138	0.639

Case Number	Rod Diameter (in.)	Clad Thickness (in.)	Enrichment (Atomic %)	Cooling Hole Diameter (in.)	Lattice Pitch (in.)	η	ϵ	p	f	k_∞	R_c
230	0.75	0.018	1.25	3.25	6.0	1.539	1.024	0.5657	0.9059	0.808	1.245
231	"	"	"	"	7.0	"	"	0.6744	0.8961	0.953	1.020
232	"	"	"	"	8.0	"	"	0.7486	0.8858	1.045	0.866
233	"	"	"	"	9.0	"	"	0.8001	0.8748	1.103	0.760
234	"	"	"	"	10.0	"	"	0.8377	0.8622	1.138	0.682
235	"	"	"	"	11.0	"	"	0.8655	0.8466	1.155	0.624
236	0.75	0.018	1.375	3.25	6.0	1.576	1.024	0.5657	0.9109	0.832	1.214
237	"	"	"	"	7.0	"	"	0.6744	0.9016	0.982	0.989
238	"	"	"	"	8.0	"	"	0.7486	0.8913	1.077	0.835
239	"	"	"	"	9.0	"	"	0.8001	0.8797	1.135	0.729
240	"	"	"	"	10.0	"	"	0.8377	0.8667	1.172	0.651
241	"	"	"	"	11.0	"	"	0.8655	0.8530	1.192	0.593
242	0.75	0.018	1.50	3.25	6.0	1.609	1.024	0.5657	0.9160	0.854	1.187
243	"	"	"	"	7.0	"	"	0.6744	0.9067	1.008	0.962
244	"	"	"	"	8.0	"	"	0.7486	0.8972	1.107	0.808
245	"	"	"	"	9.0	"	"	0.8001	0.8866	1.169	0.702
246	"	"	"	"	10.0	"	"	0.8377	0.8744	1.207	0.624
247	"	"	"	"	11.0	"	"	0.8655	0.8595	1.226	0.566
336	0.75	0.018	2.00	3.25	6.0	1.706	1.024	0.5657	0.9290	0.918	1.114
337	"	"	"	"	7.0	"	"	0.6744	0.9205	1.084	0.889
338	"	"	"	"	8.0	"	"	0.7486	0.9115	1.192	0.735
339	"	"	"	"	9.0	"	"	0.8001	0.9015	1.261	0.629
340	"	"	"	"	10.0	"	"	0.8377	0.8900	1.302	0.551
341	"	"	"	"	11.0	"	"	0.8655	0.8771	1.326	0.493
378	0.75	0.018	2.50	3.25	6.0	1.770	1.024	0.5657	0.9391	0.963	1.070
379	"	"	"	"	7.0	"	"	0.6744	0.9312	1.138	0.845
380	"	"	"	"	8.0	"	"	0.7486	0.9226	1.251	0.691
381	"	"	"	"	9.0	"	"	0.8001	0.9133	1.325	0.585
382	"	"	"	"	10.0	"	"	0.8377	0.9025	1.370	0.507
383	"	"	"	"	11.0	"	"	0.8655	0.8901	1.396	0.449

Case Number	Rod Diameter (in.)	Clad Thickness (in.)	Enrichment (Atomic %)	Cooling Hole Diameter (in.)	Lattice Pitch (in.)	η	ϵ	p	f	k_∞	R_c
360	1.00	0.018	1.25	4.00	8.0	1.539	1.028	0.6091	0.9174	0.884	1.155
361	"	"	"	"	9.0	"	"	0.6861	0.9087	0.986	0.996
362	"	"	"	"	10.0	"	"	0.7430	0.8993	1.057	0.878
363	"	"	"	"	11.0	"	"	0.7860	0.8890	1.106	0.789
364	"	"	"	"	12.0	"	"	0.8192	0.8770	1.137	0.720
365	"	"	"	"	13.0	"	"	0.8454	0.8634	1.155	0.666
366	1.00	0.018	1.50	4.00	8.0	1.609	1.028	0.6091	0.9255	0.932	1.097
367	"	"	"	"	9.0	"	"	0.6861	0.9170	1.041	0.938
368	"	"	"	"	10.0	"	"	0.7430	0.9082	1.116	0.820
369	"	"	"	"	11.0	"	"	0.7860	0.8980	1.168	0.731
370	"	"	"	"	12.0	"	"	0.8192	0.8866	1.201	0.662
371	"	"	"	"	13.0	"	"	0.8454	0.8731	1.221	0.608
372	1.00	0.018	2.00	4.00	8.0	1.706	1.028	0.6091	0.9369	1.001	1.024
373	"	"	"	"	9.0	"	"	0.6861	0.9288	1.118	0.865
374	"	"	"	"	10.0	"	"	0.7430	0.9200	1.199	0.747
375	"	"	"	"	11.0	"	"	0.7860	0.9100	1.254	0.658
376	"	"	"	"	12.0	"	"	0.8192	0.8991	1.292	0.589
377	"	"	"	"	13.0	"	"	0.8454	0.8867	1.315	0.535
390	1.00	0.018	2.50	4.00	8.0	1.770	1.028	0.6091	0.9439	1.046	0.980
391	"	"	"	"	9.0	"	"	0.6861	0.9361	1.169	0.821
392	"	"	"	"	10.0	"	"	0.7430	0.9275	1.254	0.703
393	"	"	"	"	11.0	"	"	0.7860	0.9178	1.313	0.614
394	"	"	"	"	12.0	"	"	0.8192	0.9066	1.351	0.545
395	"	"	"	"	13.0	"	"	0.8454	0.8930	1.374	0.491

optimum with respect to fuel rod diameter, having a maximum in the neighborhood of 0.75 in. There are other considerations, of course, that may influence the choice of fuel rod diameter, some of which are discussed in Section 3. These also indicate that 0.75 in. is a favorable diameter.

2.3 Loss of Neutrons by Leakage

In calculating the effect of neutron leakage on the multiplication factor the standard relation has been used:

$$k_{eff} = \frac{k_\infty \, e^{-B^2\tau}}{1 + L^2B^2} \, . \tag{2.23}$$

The small size of the factors $B^2\tau$ and L^2B^2 for reactors of the ORNL-GCR-2 type allows this to be simplified into the form

$$k_{eff} \approx \frac{k_\infty}{1 + M^2B^2} = \frac{k_\infty}{1 + M_{11}^2 \, B_{11}^2 + M_\perp^2 \, B_\perp^2}, \tag{2.24}$$

where

$M_{11}^2 = L_{11}^2 + \tau_{11}$ = axial migration area,

$M_\perp^2 = L_\perp^2 + \tau_\perp$ = radial migration area,

$B_{11}^2 = (\frac{\pi}{H+2\delta})^2$ = axial buckling,

$B_\perp^2 = (\frac{2.405}{R+\delta})^2$ = radial buckling,

H and R are the core height and radius and δ is the reflector savings.

The evaluation of the above expressions in the absence of large voids in the reactor lattice is rather straightforward. For the heterogeneous lattice the diffusion length is written as:

$$L^2 = \sum_i f_i L_i^2 \, ,$$

where L_i^2 is the diffusion length in the ith region of the cell (fuel, clad, or moderator), and f_i is the thermal utilization of the ith region. That is, if f is the ordinary thermal utilization (the thermal utilization of the fuel) then

$$f_i = f \frac{V_i}{V_f} \frac{\Sigma_a^i}{\Sigma_a^f} \frac{\bar{\phi}_i}{\bar{\phi}_f} . \tag{2.26}$$

Note that $\sum_i f_i = 1$.

If we let $F_i = \bar{\phi}_i/\bar{\phi}_f$ and write L_i^2 as

$$L_i^2 = \frac{D_i}{\Sigma_a^i} , \tag{2.27}$$

then the diffusion length in a three-region cell can be written as

$$L^2 = f_m L_m^2 \left(1 + \frac{V_f}{V_m} \frac{1}{F_m} \frac{D_f}{D_m} + \frac{V_c}{V_m} \frac{F_c}{F_m} \frac{D_c}{D_m}\right) = f_m L_m^2 (1 + S). \tag{2.28}$$

The subscripts f, m, and c refer to fuel, moderator and clad, respectively. For the lattices under consideration in the ORNL-GCR-2 design study, the correction term, S, is less than 5% so that $L^2 = f_m L_m^2$ is a good approximation in the absence of voids.

In the absence of voids in the reactor lattice the age can be written as:

$$\tau_o = \left[\tau_{th}(1 - P) + \tau_1 P\right] \left[\bar{X}\right] \left[\frac{1.65}{\rho_m}\right]^2 , \tag{2.29}$$

where

$$\tau_{th} = 311 \text{ cm}^2 + \frac{\bar{D}}{\xi \Sigma_t} \ln \frac{1.44 \text{ ev}}{E_{th}},$$

$$\tau_1 = 178 \text{ cm}^2 + \frac{\bar{D}}{\xi \Sigma_t} \ln \frac{1.44 \text{ ev}}{E_{th}},$$

P = probability that a fission neutron will suffer an inelastic collision before escaping from the fuel ($P = P_1 \frac{\sigma_{in}}{\sigma_t}$ where P_1 is the first flight collision probability),

$\underline{\overline{X}}$ = weighted age correction discussed below,

ρ_m = density of moderator

The ages τ_{th} and τ_1 are respectively the ages to thermal energies of fission neutrons and fission neutrons which have been degraded in energy by one inelastic collision in uranium. For graphite of density 1.65 g/cc and a thermal neutron distribution with $T_n = 814°K$, these ages are:

$$\tau_{th} = 324 \text{ cm}^2,$$
$$\tau_1 = 208 \text{ cm}^2.$$

For the seven-rod cluster of 3/4-in. UO_2 fuel rods the value $P = 0.084$ has been computed. For a single rod of equal total area the result would be $P = 0.093$. The correction $\underline{\overline{X}}$ is the ratio of the age in the lattice to the age in the moderator. If we write

$$\tau_o = \frac{\overline{D}}{\overline{\xi \Sigma_t}} \int_o^{u^{th}} du', \tag{2.30}$$

then

$$\tau_o = \tau_m \frac{\left(\frac{V_m + V_f + V_c}{V_m}\right)^2}{\left(1 + \frac{\overline{\Sigma^f_{tr}}\, V_f}{\overline{\Sigma^m_{tr}}\, V_m} + \frac{\overline{\Sigma^c_{tr}}\, V_c}{\overline{\Sigma^m_{tr}}\, V_m}\right)\left(1 + \frac{(\overline{\xi \Sigma_t})_f\, V_f}{(\overline{\xi \Sigma_t})_m\, V_m} + \frac{(\overline{\xi \Sigma_t})_c\, V_c}{(\overline{\xi \Sigma_t})_m\, V_m}\right)}. \tag{2.31}$$

The average cross sections are flux-weighted averages over the following spectrum

$$\phi(u) = \frac{1}{\xi(u)\, \Sigma_t(u)} \left\{ \int_o^u f(u') \exp\left[- \int_{u'}^{u''} \frac{D(u'')\, B^2 + \Sigma_a(u'')}{\xi(u'')\, \Sigma_t(u'')} du'' \right] du' \right\}, \tag{2.32}$$

where the weighting function f (u') is the lethargy distribution of fission neutrons. The above expression for τ_o has been evaluated for the reference lattice of the ORNL-GCR-2 design study. In this case the result is:

$$\tau_o \approx \tau_m \left(\frac{V_m + V_f + V_c}{V_m}\right) = \tau_m(1+R), \tag{2.33}$$

where

$$R = \frac{V_f + V_c}{V_m}$$

so that $\underline{\bar{X}} \approx (1+R)$. For a graphite-moderated reactor with uranium metal fuel the denominator of Eq. (2.31) for τ_o is essentially equal to unity and the result in that case is:

$$\tau_o = \tau_m(1+R)^2. \tag{2.34}$$

The presence of the voids in the cooling channels increases both the age and the diffusion length for the lattice. The calculations of Behrens[25] have been used to determine this correction factor. If L_o and τ_o are the diffusion length and age in the lattice without voids then

$$L_{11}^2 = L_o^2 T_{11} \qquad \tau_{11} = \tau_o F_{11}$$

$$L_\perp^2 = L_o^2 T_\perp \qquad \tau_\perp = \tau_o F_\perp$$

where

$$T_{11} = 1 + 2\phi + \frac{\phi^2 \left(\frac{2r}{\phi \lambda_t}\right)}{\exp\left[\frac{2r}{\phi \lambda_t}\right] - 1} + \frac{3}{2}\,\frac{Q\,r\,\phi}{\lambda_t},$$

---

[25] D. J. Behrens, "The Effect of Holes in a Reacting Material on the Passage of Neutrons," Proc. Phys. Soc., (London) 62A, 607 (1949).

and

$$T_{\perp} = 1 + 2\phi + \frac{\phi^2 \left(\frac{2r}{\phi \lambda_t}\right)}{\exp\left[\frac{2r}{\phi \lambda_t}\right] - 1} + \frac{3}{4} \frac{Q\, r\, \phi}{\lambda_t} .$$

The F correction factors are the same as the T factors except that λ_t, the mean free path for thermal neutrons, is replaced by λ_f, the mean free path for fast neutrons. The other quantities in these factors are defined as follows:

ϕ = ratio of void volume-to-volume of solid material,

r = hydraulic radius of the voids, $r = 2V/S$,

λ = mean free path = $1/\Sigma_{tr}$, (λ_t = 2.5 cm, λ_f = 3.1 cm)

Q = ratio of the mean square passage length through the holes to the square of the mean free path.

The quantity Q has been evaluated for several geometries by Behrens and by Case et al.,[26] but has not previously been evaluated for cluster fuel elements. For the seven-rod cluster of the ORNL-GCR-2 lattice, the value Q = 1.7 has been estimated and is believed to be accurate within about 15%. This was found to be sufficient accuracy since a 20% error in Q causes only a 2% error in the migration area.

The reflector savings were computed using the approximate expression given by J. Chernick.[27] This is written as:

$$\delta = 1.2\, L_m \tanh\left(\frac{T}{L_m}\right), \qquad (2.35)$$

where T is the reflector thickness and L_m is the diffusion length in the moderator. For L_m = 74 cm (T_n = 814°K) and T = 2.5 ft, the reflector savings is found to be δ = 67 cm. A value of 65 cm was used in all of the leakage calculations.

---

[26] K. M. Case, F. de Hoffman and G. Placzek, Introduction to the Theory of Neutron Diffusion, Vol. 1, Los Alamos Scientific Laboratory (June 1953).

[27] J. Chernick and I. Kaplan, Proceedings of the Geneva Conference, Vol. 5, P/606, p. 295.

For the reference reactor core design of the ORNL-GCR-2 study (seven 3/4-in. UO_2 fuel rods in a 3 1/4-in.-dia cooling channel, 2% enrichment, 8-in. lattice pitch, 20-ft height, 30-ft core diameter, 2.5-ft reflector on all sides) the following quantities have been computed.

$$\tau_{\perp} = 409 \text{ cm}^2 \qquad \tau_{11} = 419 \text{ cm}^2$$

$$L_{\perp}^2 = 187 \text{ cm}^2 \qquad L_{11}^2 = 194 \text{ cm}^2$$

$$M_{\perp}^2 = 596 \text{ cm}^2 \qquad M_{11}^2 = 613 \text{ cm}^2$$

$$B_{\perp}^2 = 21.22 \ \mu b \qquad B_{11}^2 = 18.05 \ \mu b$$

$$M^2B^2 = 0.0237$$

These may be compared with corresponding values for British Calder Hall reactor (Zone B) which are:

$$\tau_{\perp} = 589 \text{ cm}^2 \qquad \tau_{11} = 653 \text{ cm}^2$$

$$L_{\perp}^2 = 392 \text{ cm}^2 \qquad L_{11} = 439 \text{ cm}^2$$

$$M_{\perp}^2 = 981 \text{ cm}^2 \qquad M_{11}^2 = 1092 \text{ cm}^2$$

$$B_{\perp}^2 = 20.3 \ \mu b \qquad B_{11}^2 = 17.0 \ \mu b$$

$$M^2B^2 = 0.0385$$

The somewhat greater leakage of the Calder Hall reactor, despite the similarity in core dimensions, is due in part to the difference in fuel enrichment and in part to the greater volume fraction of the voids in the Calder Hall core.

The sensitivity of the leakage in the ORNL-GCR-2 core to such factors as lattice pitch, fuel enrichment, cooling-channel diameter, and core size is shown in Figs. 2.29, 2.30, and 2.31. Figure 2.29 shows the leakage for the design lattice as a function of core dimensions. The leakage of the ORNL-GCR-2 core is indicated by the cross. The effects of fuel enrichment and lattice pitch, for the reference fuel element, are shown in Fig. 2.30. The leakage increases for large lattice spacings because of the increase in diffusion length associated with the lower concentration of fuel and clad. Leakage increases for small lattice spacings because of the marked increase in fast leakage that results from crowding the cooling channels together. This last effect is exhibited more clearly in Fig. 2.31, which shows the void correction factors for fast and slow neutrons.

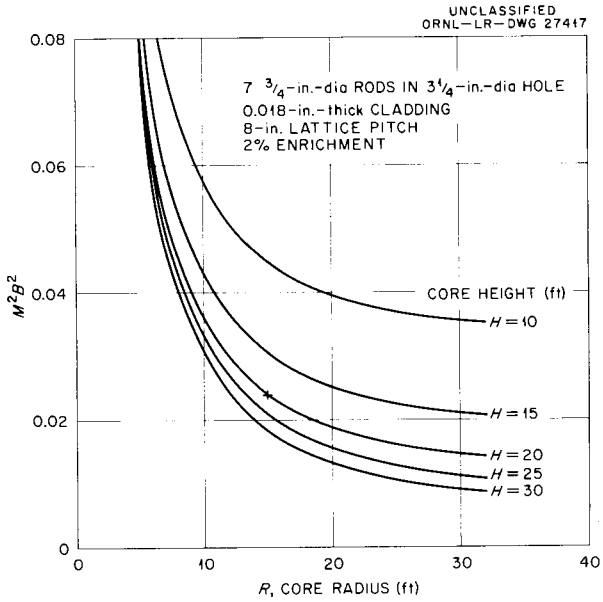

Fig. 2.29. Neutron Leakage vs Core Height and Diameter.

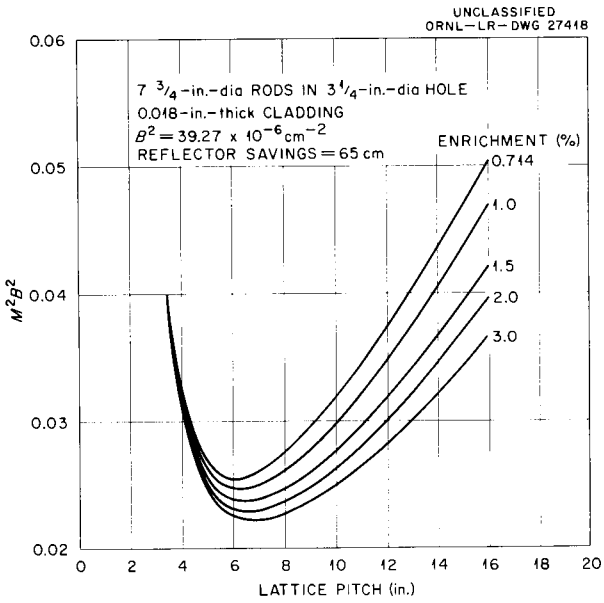

Fig. 2.30. Neutron Leakage vs Lattice Pitch and Enrichment.

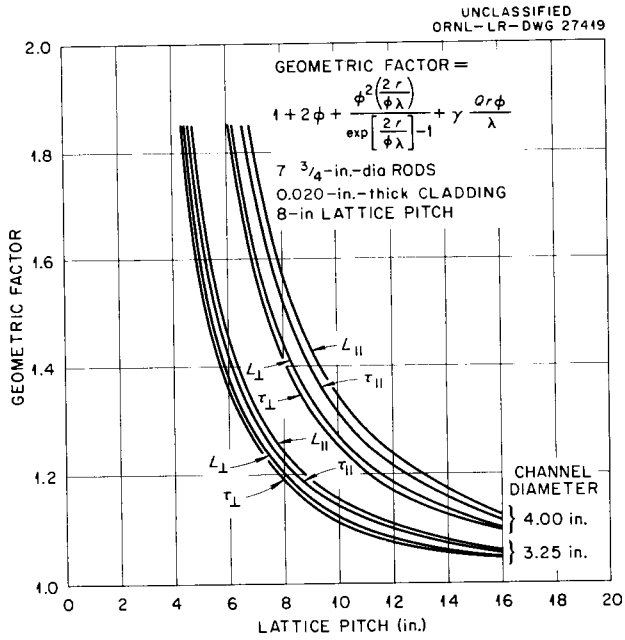

Fig. 2.31. Effect of Cooling Channel Size on Fermi Age and Diffusion Length.

2.4 Reactivity Limitations on Fuel Exposure

While the values of the multiplication factor discussed in Section 2.2 are of interest in themselves, to the extent that they help to determine, for example, the amount of reactivity that the control rods must override, the reactivity is significant chiefly through its effect on the attainable fuel exposure. As discussed in Section 3, the resistance of UO_2 fuel elements to unfavorable changes under irradiation makes possible very much longer fuel exposures than could be achieved with uranium metal fuel. Indeed, the relatively high fabrication cost expected for UO_2 fuel, as compared,for example, to the Magnox-clad uranium metal elements, makes long fuel irradiation a very urgent objective. One of the major problems in the nuclear analysis, therefore, is to obtain reasonably reliable estimates of the reactivity lifetime of the various possible fuel configurations and to determine the isotopic composition of the fuel as a function exposure. The fuel exposure is expressed as the total thermal energy, in megawatt days, extracted from a tonne of uranium fuel(Mwd/T)before that fuel is finally discharged from the pile. It is sometimes expressed as the energy obtained from the fuel per gram of U^{235} in fresh fuel,Mwd/g U^{235}. This may exceed the amount of energy released by the fissioning of all the U^{235} in the fuel, since U^{238}, via plutonium, is also being consumed.

It will be helpful in discussing the problem of reactivity lifetime to recognize three distinct modes of fuel irradiation, which will yield different average fuel lifetimes. Case No. 1 is the "batch loading" case, in which all of the fuel is charged to the reactor at the same time and all discharged at the same time, when the reactivity of the fuel has fallen to the point where the chain reaction can no longer be maintained under the desired operating conditions. For this case the power density is assumed to be uniform throughout the pile. Case No. 2 is the same as Case No. 1, except that the power distribution is not assumed to be uniform. In Case No. 3, the excess neutrons available with fresh fuel are used to extend the irradiation of old fuel that has a reactivity too low to sustain the pile by itself. Fresh fuel is added to the core and the most highly irradiated fuel removed, more or less continuously, in such a way that a constant equilibrium composition of fuel is maintained at all times at all parts of the reactor. This is the case

referred to by Spinrad[28] as the case of uniformly graded fuel irradiation.

Many calculations have been made of the reactivity lifetime for various core configurations, and many workers have attempted to express these results in terms of sufficiently general parameters to permit application of the results to a variety of reactors. There is enough difference, however, in our operating temperature, in the relative importance of epithermal absorptions, and in other aspects of the neutron balance to establish the need for independent calculations for this study.

The method used for these calculations is similar to that used by Triplett,[29] except that the resonance integrals have been absorbed in the effective thermal cross sections for all isotopes other than U^{238}. The problem has been programmed for the ORACLE digital computer,[30] and, as we have used it, involves the solution of the differential equations:

$$\frac{dN_5}{dt} = -N_5 \hat{\sigma}_5 \phi$$

$$\frac{dN_8}{dt} = -N_8 \hat{\sigma}_8 \phi - N_8 \int \sigma_8 \phi_{\frac{1}{E}} dE$$

$$\frac{dN_9}{dt} = -N_9 \hat{\sigma}_9 \phi + \frac{dN_8}{dt}$$

$$\frac{dN_0}{dt} = -N_0 \hat{\sigma}_0 \phi + \beta_9 \frac{dN_9}{dt}$$

$$\frac{dN_1}{dt} = -N_1 \hat{\sigma}_1 \phi + \frac{dN_0}{dt}$$

$$\frac{dN_p}{dt} = -N_p \hat{\sigma}_p \phi + \Sigma_f \phi$$

---

[28] B. I. Spinrad et al., "Reactivity Changes and Reactivity Lifetimes of Fixed-Fuel Elements in Thermal Reactors," Proc. of Geneva Conference, P/835.

[29] J. R. Triplett, Reactivity Changes and Isotope Yields at High Exposures, HW-33912 (January 1955).

[30] S. Jaye, P. R. Kasten, and M. P. Lietzke, Lifetimes of Slightly Enriched Heterogeneous Reactors, ORNL-2479 (1958).

In these equations, the subscripts 5, 8, 9, 0, 1, and p refer respectively to U^{235}, U^{238}, Pu^{239}, Pu^{240}, Pu^{241}, and stable fission products except Sm^{149}; $\beta_9 \equiv \sigma_{9\ capture}/\sigma_{9\ absorption}$; Σ_f is the combined macroscopic fission cross section of U^{235}, Pu^{239}, and Pu^{241}. The cross sections σ are effective absorption cross sections and $\phi \equiv Nv_{2200}$ (see Section 2.1.5). The effective multiplication factor of the reactor is defined as the ratio of the number of fission neutrons produced per second to the number of neutrons removed from the pile per second by leakage and absorption (exclusive of control rods). It is computed at intervals (for example, 160 Mwd/T) with the isotopic concentrations given by integrating the above differential equations, and the lifetime of the core is that fuel exposure for which k_{eff} has decreased to unity.

The results of the lifetime calculations are shown in Figs. 2.32 – 2.39. A number of approximations were made in these calculations, of which the following are the most important.

1. The slow neutron flux distribution within a cell was assumed to be unchanged during the irradiation; that is, the clad and moderator disadvantage factors were assumed to be constant. This assumption produces very little error, since only about 4% of the neutrons are absorbed in graphite, the moderator disadvantage factor varies slowly with fuel cross section (Fig. 2.7) and the fuel cross section varies slowly with exposure (Fig. 2.36). The clad disadvantage factor is always very close to unity.
2. The self-shielding of the 1 ev resonance of Pu^{240} was neglected. For the long exposures reached for some of the lattices studied, the effective cross section of Pu^{240} could drop by a factor of two or more. While the effect of such a reduction in cross section could in principle be quite important, it is believed that the resulting errors in the present lifetime estimates are not great. The direction of this error is to cause an underestimate of the lifetime.
3. The effective cross sections were not changed from one lattice to another. The lattices that proved to be of the greatest interest have a larger average absorption cross section, and therefore, have relatively more epithermal neutron absorptions than the case for which the effective cross sections were calculated (see Section 2.1.5).

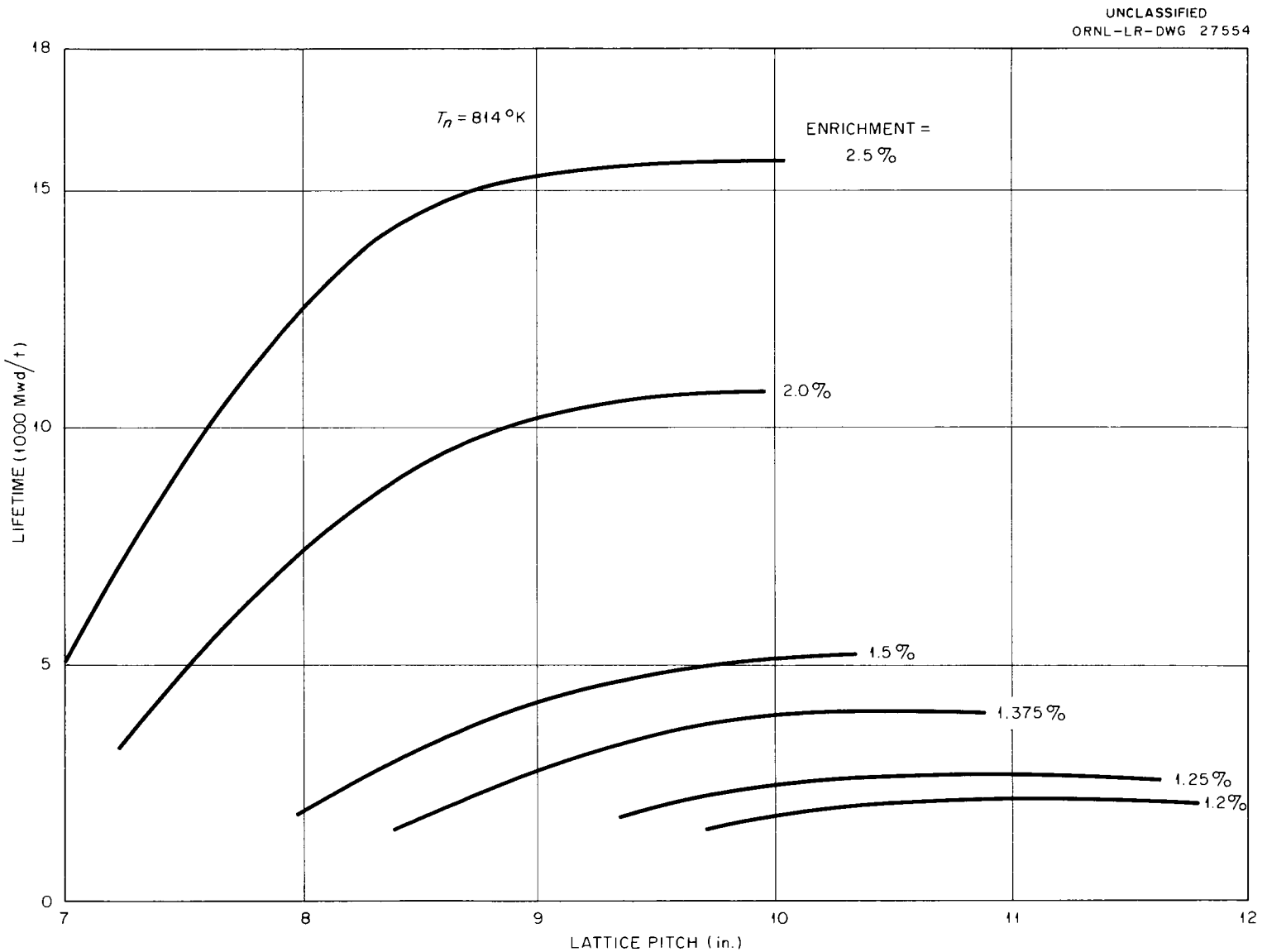

Fig. 2.32. Fuel Lifetime vs Lattice Pitch and Enrichment.

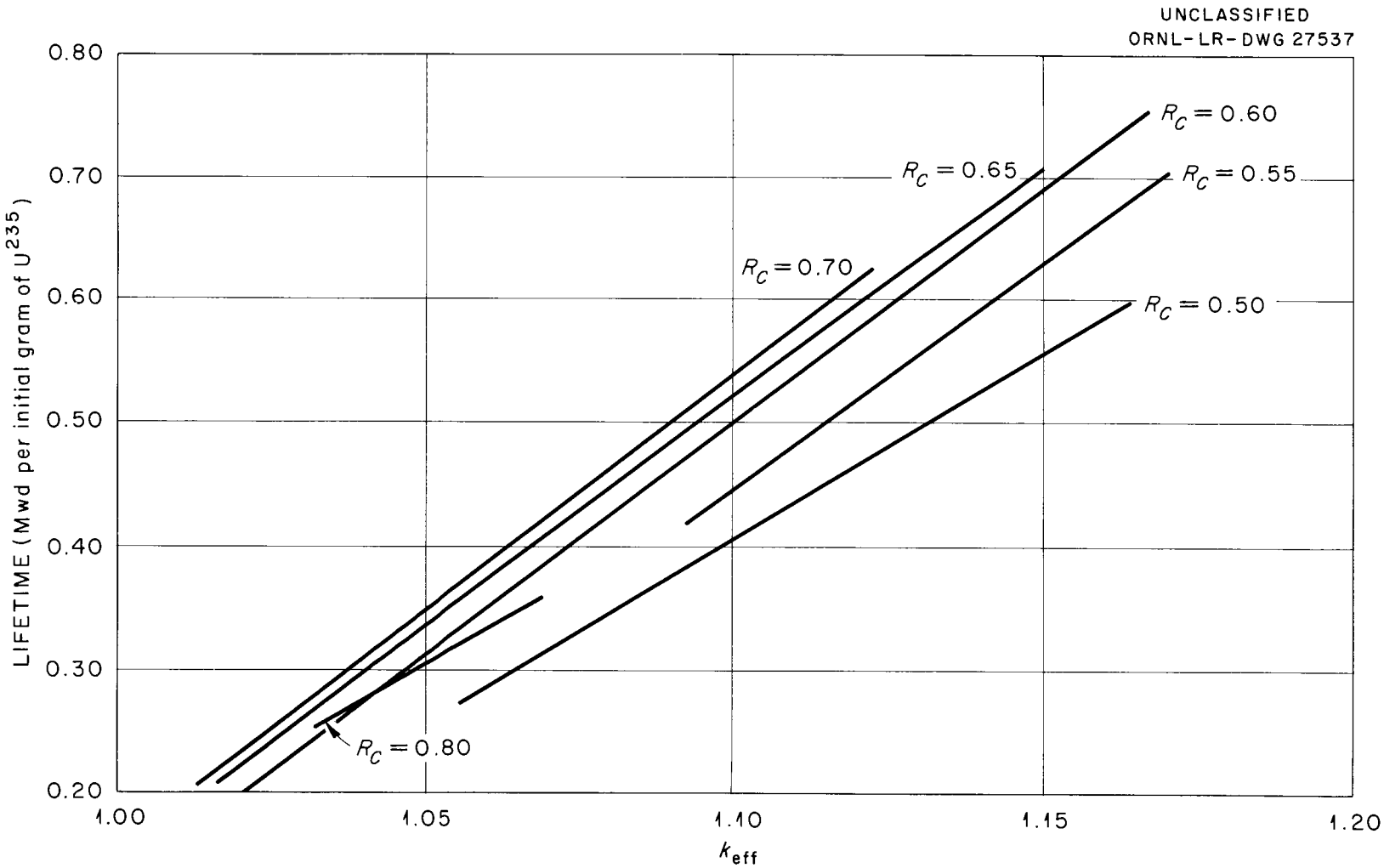

Fig. 2.33. Fuel Lifetime vs Multiplication Factor and Conversion Ratio.

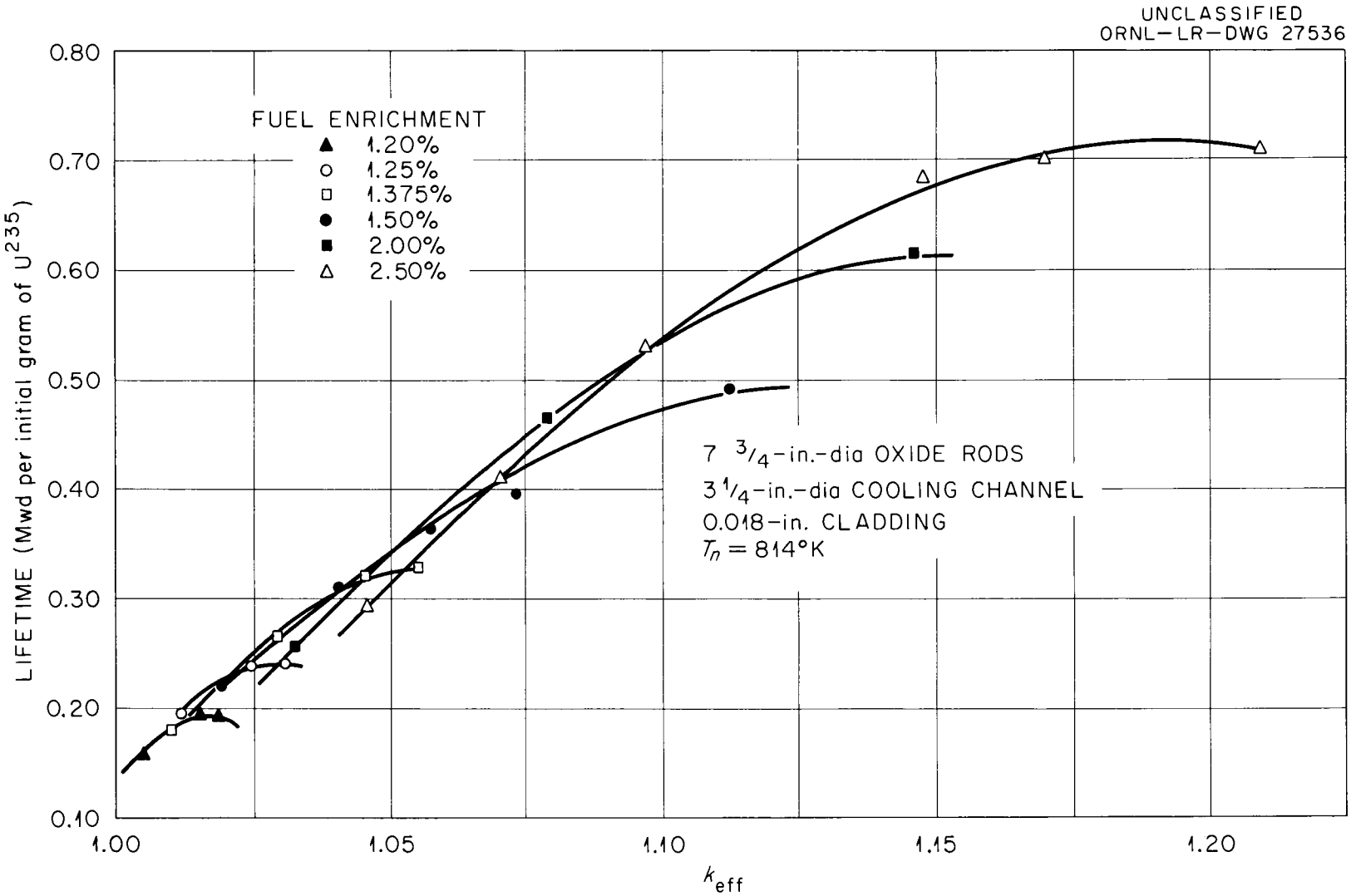

Fig. 2.34. Fuel Lifetime vs Multiplication Factor and Enrichment.

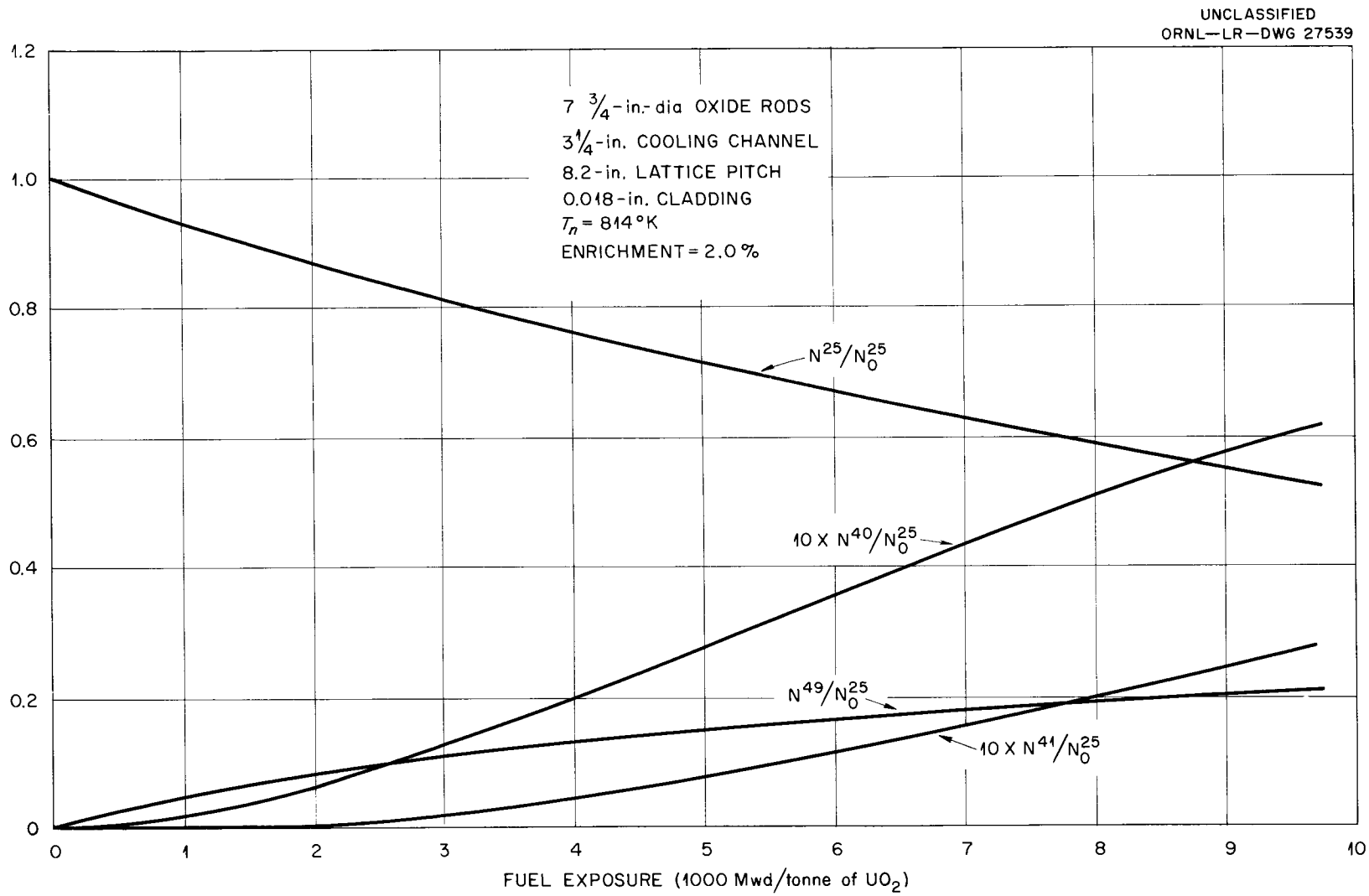

Fig. 2.35. Isotopic Composition of Fuel vs Exposure.

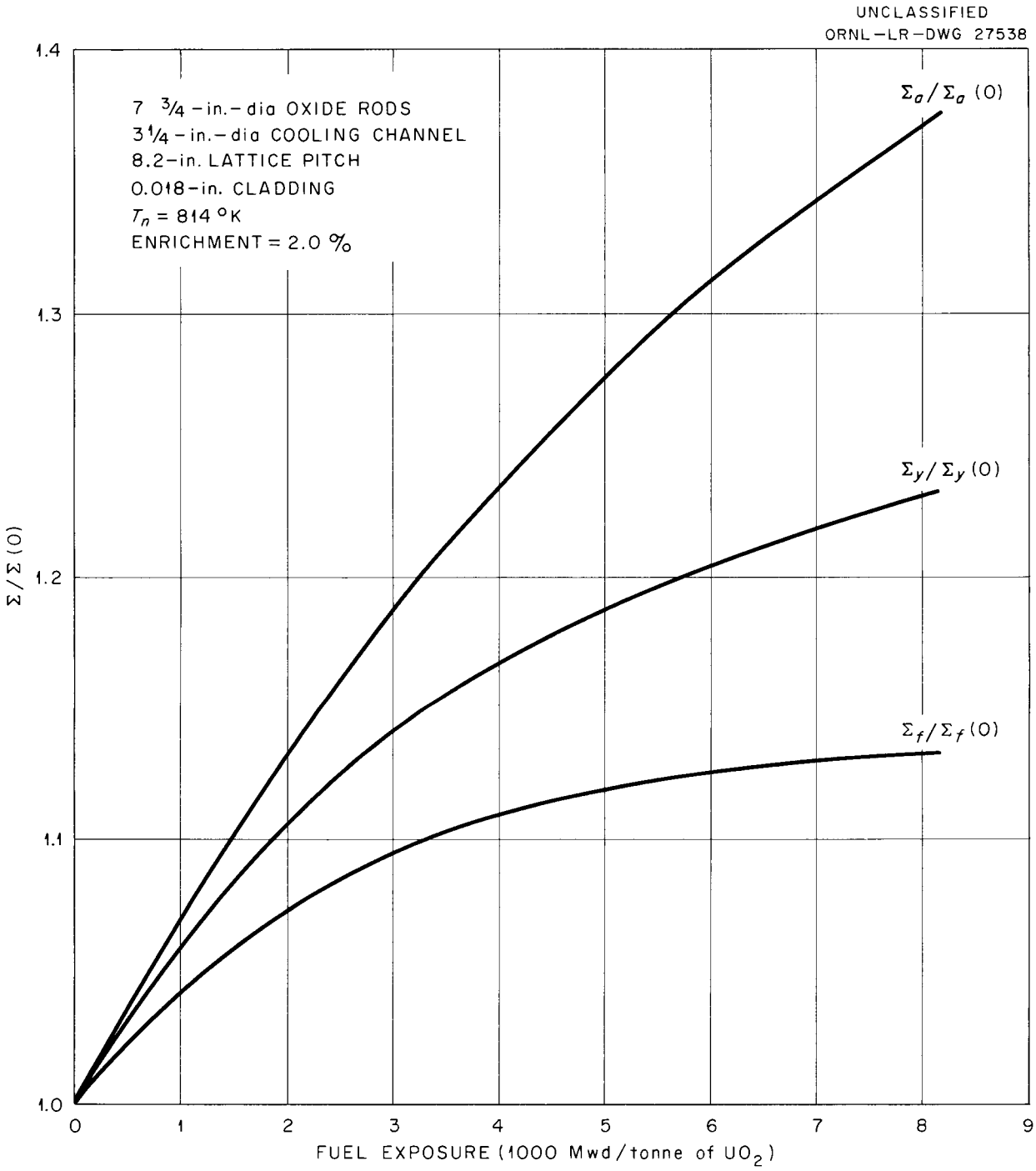

Fig. 2.36. Neutron Yield, Fuel Absorption, and Fission Cross Section vs Exposure.

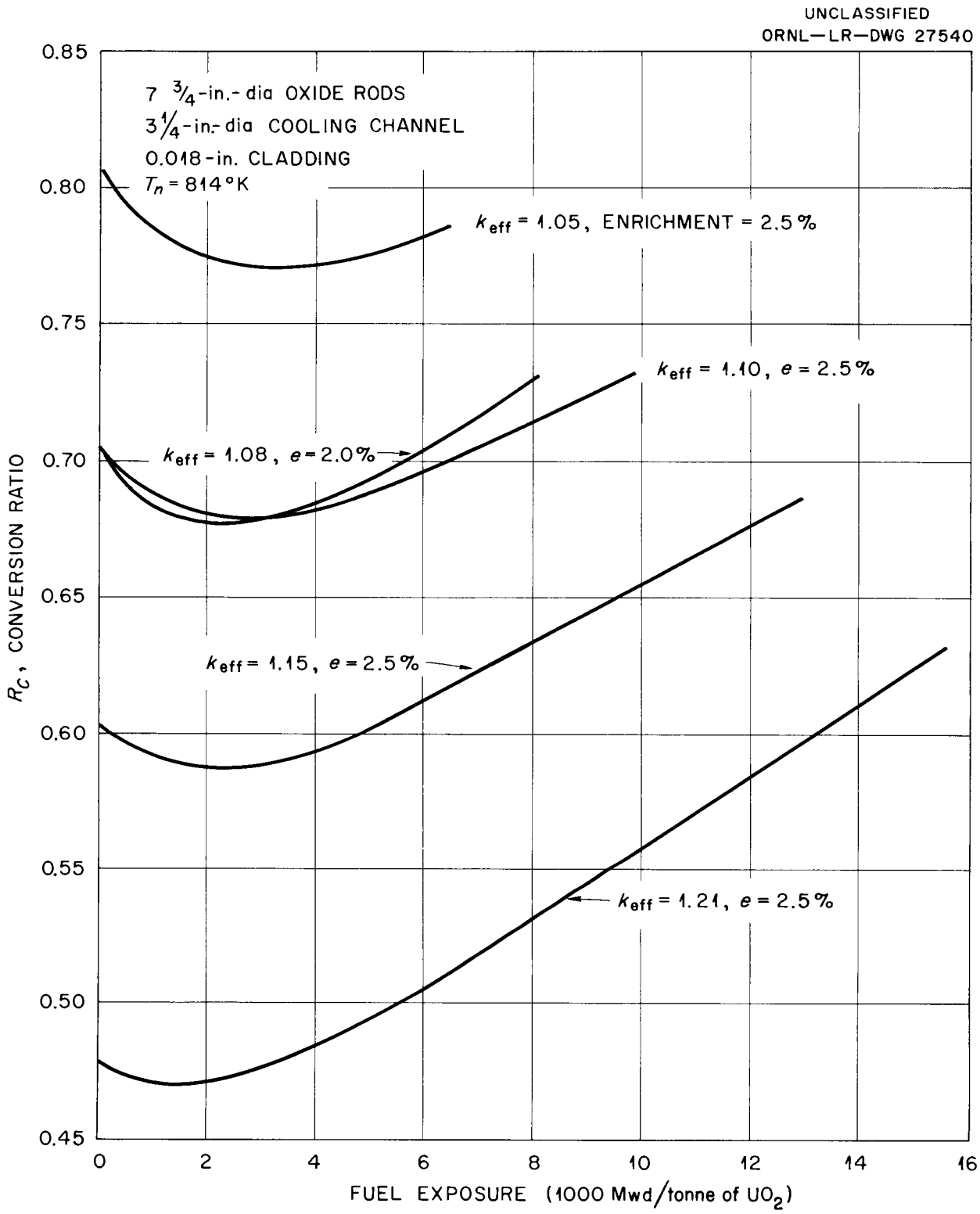

Fig. 2.37. Conversion Ratio vs Exposure.

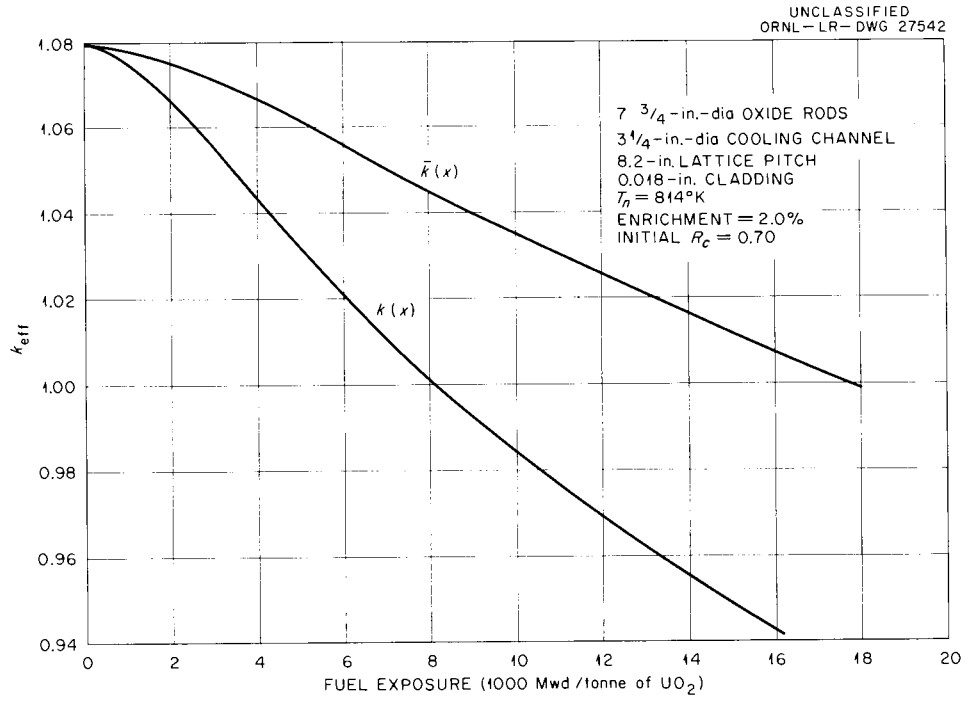

Fig. 2.38. Multiplication Factor vs Exposure.

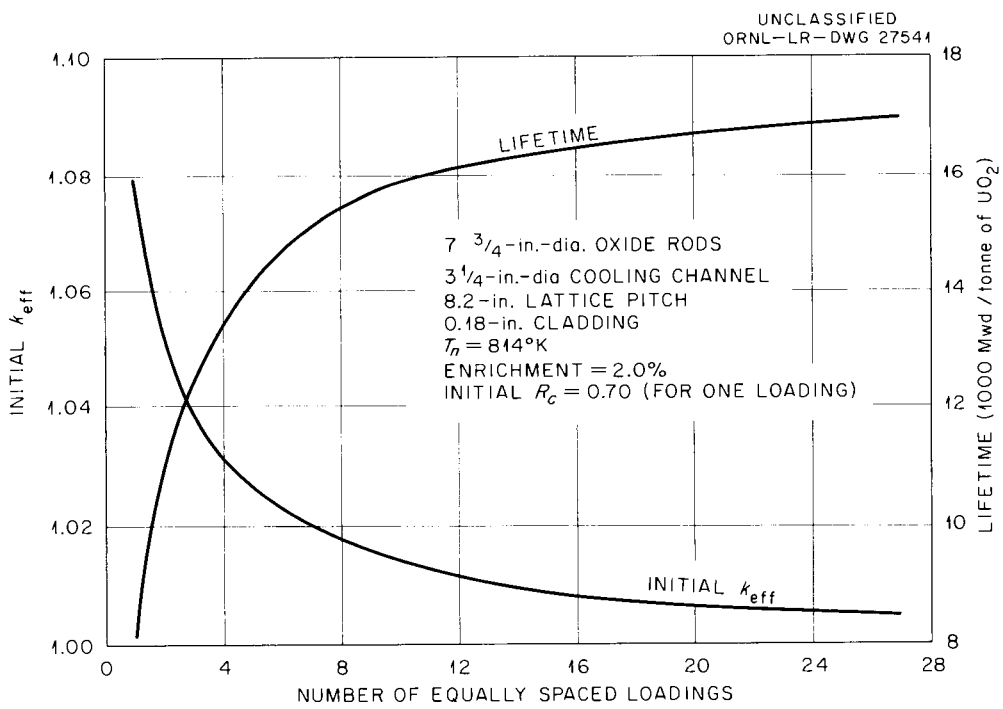

Fig. 2.39. Effect of Staggered Loading on Fuel Lifetime.

The cross section most strongly affected is that of Pu^{240}, which has a greater relative importance for the more intermediate (epithermal) spectra. Thus, this effect tends to compensate the neglect of self-shielding.

4. In addition to these approximations, it has been found that the allowance for neutron leakage in these burn-up calculations, was too high by an amount corresponding approximately to 1% in k. (The effect on lifetime of 1% in k can be seen in Fig. 2.34).
5. It is suspected that too great an allowance was made for fission product poisoning, although this point cannot be established with certainty.[31] The cross section used for the stable poisons, not including Sm^{149}, was 80 barns/fission at 2200 m/sec which is certainly on the conservative side.

The effective cross sections and values of ν used for the uranium and plutonium isotopes, reduced to 2200 m/sec values, were σ_{a5} = 642b, σ_{f5} = 525b, σ_{a8} = 2.73b, σ_{a9} = 2128b, σ_{f9} = 1290b, σ_{a0} = 1792b, σ_{a1} = 2088b, σ_{f1} = 1527b, ν_5 = 2.48, ν_9 = 2.88, ν_1 = 3.30.

The immediate result of these calculations is the fuel lifetime corresponding to Case No. 1 (batch loading, uniform exposure). Values of the lifetime in Mwd/T are given in Fig. 2.32 as functions of lattice pitch and fuel enrichment for clusters of seven 0.75-in.-dia UO_2 rods, with 0.018-in. 430 stainless steel (equivalent) clad, and at an average neutron temperature of 814°K (~541°C). For this fuel element, lifetimes of several thousand megawatt days per tonne will certainly require enrichment to 2 or 3 times the U^{235} concentration of natural uranium. (The fuel cycle costs that follow from the exposure levels and fuel compositions given by these calculations are discussed in Section 11.)

It is rather interesting to present the same results in other ways. Figure 2.33 shows the burn-up, in megawatt days per gram of U^{235} contained in fresh fuel, as a function of the initial value of k_{eff} and the initial conversion ratio. Figure 2.34 shows the same function for various enrichments of the fresh fuel.

---

[31] See J. B. Sampson et al., Poisoning in Thermal Reactors Due to Stable Fission Products, KAPL-1226 (October 1954).

For a lattice very close to the reference design (8.2-in. pitch instead of the reference pitch of 8 in.), the isotopic composition of the fuel as a function of exposure level is shown in Fig. 2.35. It can be seen that the Pu^{239} almost reaches an equilibrium concentration, while the Pu^{240} and Pu^{241} continue to build up throughout the irradiation. Figure 2.36 shows the variation of the neutron yield cross section, $\sum_i \nu_i N_i \sigma_{fi}$, and of the fuel absorption cross section. Figure 2.37 shows the variation of the conversion ratio (rate of production of Pu^{239} and Pu^{241} divided by rate of consumption of U^{235}, Pu^{239}, and Pu^{241}). The rise in R_c reveals the importance of Pu^{240} as a fertile material for long irradiations.

The variation of k_{eff} with exposure level depends upon the initial conversion ratio and on the fuel enrichment. Whereas, for natural uranium feed the reactivity at first increases (following Sm^{149} saturation), the tendency with 2% enriched fuel is monotonically downward. Figure 2.38 shows the dependence of k_{eff} on exposure for the same case as the previous figures (essentially the reference reactor). Also shown is the function

$$\bar{k}(X) = \frac{1}{X}\int_0^X k(X')\,dX', \tag{2.36}$$

where X is the exposure in Mwd/T. The exposure for which $\bar{k}(X) = 1$ is rather close to the lifetime which can be achieved by continuous fuel loading (Case No. 3), and illustrates the benefits to be gained by absorbing the excess neutrons from fresh fuel in highly irradiated fuel rather than in control rods. (Actually, the lifetime attainable by continuous loading is a few per cent less than $\bar{k}$ as defined above.) It is seen that continuous loading can extend the lifetime of the fuel by roughly a factor of 2, relative to Case No. 1. For an actual batch-loaded exposure (Case No. 2), Spinrad has estimated[32] that the lifetime would be less than that of Case No. 1 by a factor roughly equal to the average-to-maximum power density ratio, for example, 0.5 to 0.7. Thus, the benefits of continuous loading are very substantial indeed.[33,34]

---

[32] Spinrad et al., op cit. p. 2.74.

[33] Spinrad et al., op cit. p. 2.74.

[34] W. B. Lewis, Low Cost Fueling Without Recycle, DR-39 (December, 1956).

In fact, the lifetime indicated for the reference design (8-in. pitch, 2% enrichment) corresponds to a residence time of fuel in the reactor that is a large fraction of the design life of the reactor, which is about 20 yr. The Case No. 1 lifetime (Fig. 2.32 is about 7350 Mwd/T. For continuous fueling, this should be increased to 14,000 to 15,000 Mwd/T. Since the specific power level of the reference design is about 5 Mw/T, this would yield an average residence time of about 10-1/2 yr (load factor of 0.80). Since the devices that would permit continuous onstream loading of the reactor pose quite serious engineering problems, it is desirable to investigate the possibility of approximating the continuous loading cycle by reloading a rather substantial fraction of the total number of fuel channels at a time, at appropriate intervals. Figure 2.39 shows fuel lifetime (in Mwd/T) as a function of the number of intervals into which the loading cycle might be divided. For example, for N = 10, one would remove from the core, at one time, the 10% of the fuel elements that had received the greatest exposure, and replace them with fresh fuel. Thus, for an average residence time of 10 yr, it would be necessary to replace 10% of the core at roughly 1 yr intervals. After each refueling operation, the core would contain equal numbers of fuel elements that had been in the core for 9, 8, 7, 2, 1, 0 yr, each age group being uniformly distributed through the core. (A deviation from this uniform distribution, for purposes of flattening the power distribution, is discussed in Section 2.7.) It is seen from Fig. 2.39 that 10 steps will give nearly as long a fuel exposure as continuous loading. Also shown is the effective multiplication factor of the core after each refueling operation, which indicates the amount of reactivity the control rods must take care of with each fresh fuel charge.

It is recognized that with such long residence times as those mentioned above, an equilibrium fueling cycle might never be established in the lifetime of the reactor. The question of the best way to approach an equilibrium fueling cycle has not been resolved, though it is certain that there will be some sacrifice in average fuel exposure, averaged over all the fuel charged to the reactor throughout its life. As a result of the uncertainty surrounding this question, it was decided to carry out the economic analysis of the system on the basis of the Case No. 1 lifetimes, although fission gas release from the UO_2 and deformation of the stainless steel capsule have been studied in terms of the Case No. 3 lifetime.

2.5 Temperature Coefficient of Reactivity:

If the effect of the temperature dependent reactor poisons, that is xenon and samarium, is included in the thermal utilization, then the thermal utilization is written as:

$$f' = \frac{1}{1 + C + M + P} . \tag{2.37}$$

The quantities C, M, and P are ratios of the neutron absorption rates in the clad, moderator, and xenon and samarium poisons to the absorption rate in the fuel. Since P is generally small, f' can be written as:

$$f' \cong \frac{1}{(1 + C + M)(1 + P)} = \frac{f}{1 + P} ,$$

where f is the ordinary thermal utilization without poisons. The effective multiplication constant can therefore be written as:

$$k_{eff} = \frac{\eta \, \epsilon \, p \, f \, e^{-B^2\tau}}{(1 + L^2B^2)(1 + P)} . \tag{2.38}$$

If this is differentiated with respect to temperature, the temperature coefficient of reactivity becomes

$$\frac{1}{k_{eff}} \frac{d\,k_{eff}}{dT} = \frac{1}{\epsilon} \frac{d\epsilon}{dT} + \frac{1}{p} \frac{dp}{dT} + \frac{1}{f} \frac{df}{dT} + \frac{1}{\eta} \frac{d\eta}{dT} - \tau B^2 \frac{1}{\tau} \frac{d\tau}{dT} \tag{2.39}$$

$$- \frac{L^2B^2}{1 + L^2B^2} \frac{1}{L^2} \frac{dL^2}{dT} - M^2B^2 \frac{1}{B^2} \frac{dB^2}{dT} - \frac{P}{1 + P} \frac{dP}{dT} .$$

If this form it is convenient to calculate each part of the temperature coefficient separately and add them to obtain the over-all coefficient.

It was desired to compute this temperature coefficient as a function of both temperature and fuel exposure. This was done by using the temperature dependent cross sections developed in Section 2.1.5, together with the isotopic concentrations as a function of fuel exposure that were given by the burn-up calculations described in Section 2.4.

The temperature coefficient of the resonance escape probability, $\frac{1}{p}\, dp/dT$, arises from the Doppler broadening of the U^{238} absorption resonance and therefore depends on the fuel temperature. If p is expressed as

$$p(T_f) = \exp\left\{ - \frac{\sigma_r\,(T_f)}{\frac{N_m}{N_u}\,\xi\,\Sigma_s^m} \right\} \tag{2.40}$$

then

$$\frac{1}{p}\,\frac{dp(T_f)}{dT_f} = \frac{\ln p(T_f)}{\sigma_r(T_f)}\,\frac{d\,\sigma_r(T_f)}{dT_f}\,.$$

Since it is shown in Section 2.1.3 that

$$\frac{1}{\sigma_r(T_f)}\,\frac{d\,\sigma_r(T_f)}{dT_f} \cong 1.56 \times 10^{-4}/°C,$$

and that this quantity is independent of fuel temperature, the temperature coefficient of the resonance escape probability can be written as

$$\frac{1}{p(T_f)}\,\frac{dp(T_f)}{dT_f} = (1.56 \times 10^{-4})\,\ln p(T_f)/°C. \tag{2.41}$$

If $p(T_f)$ is known at some reference temperature, say T_f^o, then it may be computed at any other temperature by integrating Eq. (2.41). The result is

$$\ln \ln p(T_f) = \ln \ln p(T_f^o) - (1.56 \times 10^{-4}/°C)\,(T_f^o - T_f). \tag{2.42}$$

For the ORNL-GCR-2 lattice cell with seven 3/4-in. UO_2 fuel rods in a 3 1/4-in.-dia cooling channel and 8-in. lattice pitch, the effective fuel temperature has been computed to be 760°C when the moderator temperature is 400°C and the effective neutron temperature is 541°C (see Section 2.1.3). Under these conditions p = 0.74 and the temperature coefficient of the resonance escape

probability is therefore

$$\frac{1}{p}\ \frac{dp}{dT} = -4.69 \times 10^{-5}/°C.$$

Application of Eq. (2.41) to the Brookhaven reactor yields a calculated temperature coefficient of $-1.92 \times 10^{-5}/°C$, which is to be compared with a measured value[35] of $-1.95 \times 10^{-5}/°C$.

In order to relate the Doppler coefficient to the neutron temperature, the effective fuel temperature was assumed to vary linearly with the neutron temperature from $T_f = 760°C$ when $T_n = 541°C$ (814°K) to $T_f = 20°C$ when $T_n = 20°C$. This

$$T_f = 20°C + 1.421\ (T_n - 20°C). \tag{2.43}$$

This is one of several possible assumptions concerning the dependence of T_f on T_n and neglects the dependence of T_f on specific power in the fuel, for example.

The temperature coefficient of the fast fission effect, $\frac{1}{\epsilon}\ d\epsilon/dT$, arises chiefly from the expansion of the fuel elements accompanying a change in fuel temperature. Carlvik and Pershagen[36] have computed ϵ as a function of the density radius (ρr) of UO_2 fuel rods and find very nearly a linear dependence of ϵ on the density radius. That is,

$$\epsilon - 1 = C\ \rho\ r, \tag{2.44}$$

where ρ is the density of the rod, r is its radius, and C is a constant. With this functional form it can be shown that

$$\frac{1}{\epsilon}\ \frac{d\epsilon}{dT_f} = -\frac{\epsilon - 1}{\epsilon}\ \alpha,$$

---

[35] J. Chernick and I. Kaplan, "Uranium-Graphite Lattices--The Brookhaven Reactor," Proceedings of the Geneva Conference, Vol. 5, P/606 (1955).

[36] I. Carlvik and B. Pershagan, The Fast Effect in a Cylindrical Fuel Element, AEF-70 (1956).

where α is the coefficient of linear expansion for the fuel material. For the reference lattice of the gas-cooled reactor $\epsilon = 1.024$ and $\alpha = 9 \times 10^{-6}/°C$. The temperature coefficient of the fast effect is therefore

$$\frac{1}{\epsilon} \frac{d\epsilon}{dT} = -2.11 \times 10^{-7}.$$

In computing the temperature coefficient of reactivity due to the xenon and samarium fission products, the concentrations of these elements were computed from the usual relationships,[37]

$$N_{Xe} = \frac{(\gamma_I + \gamma_{Xe})\, \Sigma_{fiss}\, \phi}{\lambda_{Xe} + \sigma_{Xe}\, \phi} \tag{2.45}$$

and

$$N_{Sm} = \frac{\gamma_{Sm}\, \Sigma_{fiss}}{\sigma_{Sm}} .$$

For the isotopes indicated by the respective subscripts, the γ's are the fission yields, the σ's are the absorption cross sections, and the λ's are the decay constants. ϕ is the thermal neutron flux and Σ_{fiss} is the fission cross section of the fuel. The values used in these calculations are as follows:

$$\gamma_I + \gamma_{Xe} \doteq 0.059,$$

$$\gamma_{Sm} = 0.014,$$

$$\lambda_{Xe} = 2.1 \times 10^{-5}\ sec^{-1},$$

$$\sigma_{Xe}\ (814°K) = 1.62 \times 10^{-18}\ cm^2,$$

$$\sigma_{Sm}\ (814°K) = 5.08 \times 10^{-20}\ cm^2,$$

$$\phi = 0.8 \times 10^{-13}\ n/cm^2\text{-sec}.$$

---

[37] S. Glasstone and M. C. Edlund, The Elements of Nuclear Reactor Theory, (D. Van Nostrand Co., Inc., New York) (1952).

The quantities P_{Xe} and P_{Sm} required for the temperature coefficient can be written as

$$P_{Xe}(X,T_n) = N_{Xe}(X)\,\frac{\sigma_{Xe}(T_n)}{\Sigma_a^f(X,T_n)}\ ,$$

and

$$P_{Sm}(X,T_n) = N_{Sm}(X)\,\frac{\sigma_{Sm}(T_n)}{\Sigma_a^f(X,T_n)}\ ,$$

where X = fuel exposure, and Σ_a^f = fuel absorption cross section.

It has been found that P_{Xe} reaches its peak value after about one day of operation and then decreases with further fuel exposure due to the decrease of σ_{Xe}/Σ_a^f. The peak value of P_{Sm} is reached after about 20 days of operation and likewise decreases with further fuel exposure due to the decrease of σ_{Sm}/Σ_a^f. The temperature coefficient of reactivity due to these two poisons changes appreciably between room temperature and the reactor operating temperature, as is shown by the following typical results:

$$\frac{P_{Xe}}{1 + P_{Xe}}\ \frac{dP_{Xe}}{dT_n} = \begin{cases} +\ 0.8 \times 10^{-5}/°C \text{ at } T_n = 814°K \\ -\ 0.7 \times 10^{-5}/°C \text{ at } T_n = 293°K \end{cases}$$

$$\frac{P_{Sm}}{1 + P_{Sm}}\ \frac{dP_{Sm}}{dT_n} = \begin{cases} +\ 0.1 \times 10^{-5}/°C \text{ at } T_n = 814°K \\ -\ 1.1 \times 10^{-5}/°C \text{ at } T_n = 293°K \end{cases}$$

The dependence of the combined xenon and samarium temperature coefficient on fuel exposure is shown in Fig. 2.41.

The general conclusions reached for each of the components of the over-all temperature coefficient are as follows:

$\frac{1}{\epsilon}\frac{d\epsilon}{dT}$ -- always negative; represents a small contribution,

$\frac{1}{p}\frac{dp}{dT}$ -- always negative; independent of fuel exposure, becomes more negative as the temperature is increased at all temperatures,

$\frac{1}{f}\frac{df}{dT}$ -- always positive; increases as fuel exposure is increased,

$\frac{1}{\eta}\frac{d\eta}{dT}$ -- always negative; becomes more negative at all temperatures as fuel exposure is increased,

$\tau B^2 \frac{1}{\tau}\frac{d\tau}{dT}$ -- always negative; represents a small contribution,

$\frac{L^2B^2}{1 + L^2B^2}\ \frac{1}{L^2}\ \frac{dL^2}{dT}$ -- always negative; represents a small contribution,

$M^2B^2\ \frac{1}{B^2}\ \frac{dB^2}{dT}$ -- always negative; represents a small contribution,

$\frac{P}{1 + P}\ \frac{dP}{dT}$ -- changes from negative to positive as the temperature is increased.

Values of the moderator temperature coefficient (not including contributions of xenon and samarium or the Doppler coefficient) are shown in Fig. 2.40. The coefficient is negative at all temperatures and fuel exposures. As Pu^{239} builds up in the fuel, the coefficient becomes less negative for temperatures below 600°K. A calculation for a natural uranium lattice, similar to that of the Calder Hall reactors, showed the moderator coefficient to go strongly positive, as expected, at exposures above about 1000 Mwd/T. In the present case, however, the coefficient levels out with increasing exposure and then goes more negative again. At a neutron temperature of 814°K, the trend of the temperature coefficient with increasing exposure is increasingly negative over the whole exposure range. The qualitative difference in behavior between the present case and the natural uranium-graphite reactors is probably due to several circumstances, such as the enrichment of the fuel and the much larger epithermal component of the neutron energy spectrum. The latter factor emphasizes the relative importance of Pu^{240}, and may be responsible for the downward turn of the curves in

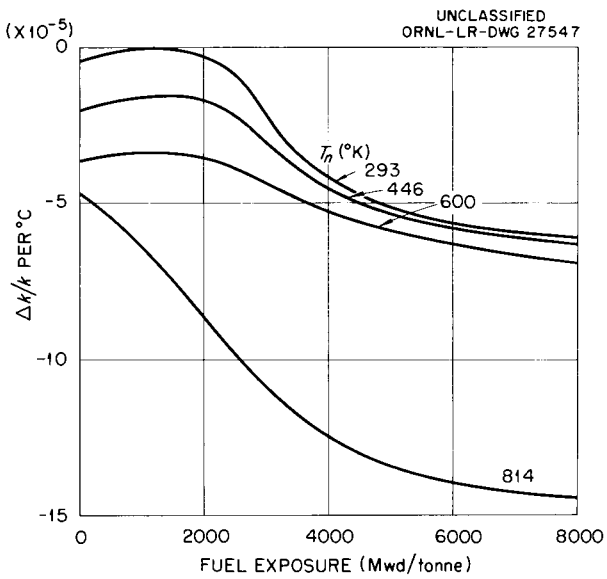

Fig. 2.40. Moderator Temperature Coefficient of Reactivity vs Neutron Temperature and Fuel Exposure – Excluding Xe^{135} and Sm^{149}.

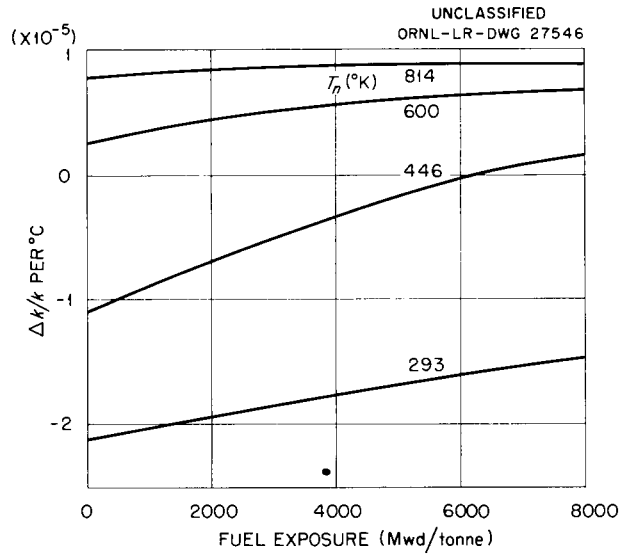

Fig. 2.41. Contribution of Xe^{135} and Sm^{149} to Moderator Temperature Coefficient of Reactivity.

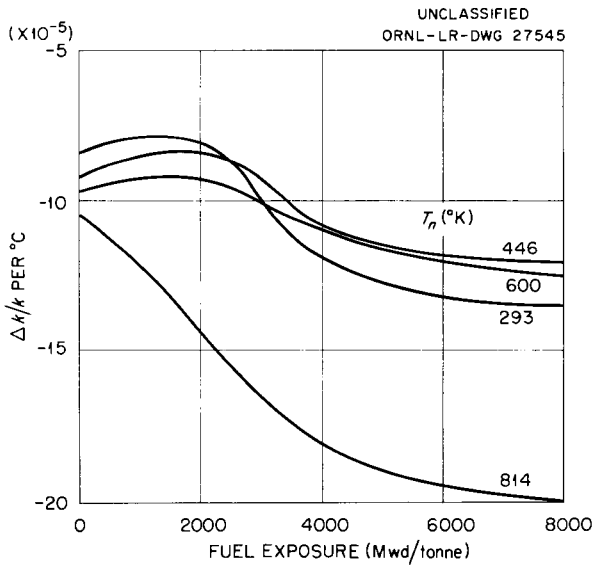

Fig. 2.42. Total Moderator Temperature Coefficient of Reactivity vs Fuel Exposure.

Fig. 2.40 between 2000 and 4000 Mwd/T. The nature of the competition for neutrons as a function of temperature and exposure is revealed in part by the relative derivatives σ_f^{49} and σ_f^{25} with respect to temperature. Table 2.11 gives ratios of these derivatives for r = 0.1 and r = 0.2 (see Section 2.1.5), as well as some other important temperature-dependent parameters.

It should be pointed out that the effective cross sections used in the burn-up calculations were computed for r = 0.10, whereas, those employed in computing the temperature coefficient used r = 0.20, which is believed to be closer to the correct value for the 2% enriched fuel and 8-in. lattice pitch that proved to be of interest. Uncertainties in the cross sections, which result to a considerable degree from uncertainty about the neutron energy spectrum in the fuel, have been discussed in Section 2.1.5, and the effect of these uncertainties on the neutron lifetime calculations has been discussed in Section 2.4. There is a corresponding ambiguity in the results for the temperature coefficient given above, for essentially the same reasons as given in Section 2.4. The temperature coefficient was also calculated, at temperatures between 300°C and 600°C and exposures up to several thousand megawatt days per tonne, using cross sections computed with r = 0.1. Though somewhat smaller in magnitude than the corresponding values illustrated in Fig. 2.40, these results exhibited the same tendency to become less negative for short exposures, and the same tendency to turn over and remain negative for all exposures.

The curves of Fig. 2.41 show the contribution of the fission poisons Xe^{135} and Sm^{149} to the moderator temperature coefficient. Figure 2.42 gives an over-all moderator temperature coefficient including a contribution from the Doppler effect computed under the assumptions discussed earlier.

Calculation of the moderator temperature coefficient is a rather delicate matter, and further work on the cross sections will be required before these results can be established with certainty.

2.6 Control Rods

The maximum reactivity to be controlled occurs in the start-up condition. The approximate control reactivity ($\Delta k/k$) requirements for this condition can be listed as follows:

TABLE 2.11

PERTINENT NUCLEAR PARAMETERS AFFECTING TEMPERATURE COEFFICIENTS

Parameters	r	T_n (-°K) 293	446	600	814
$\frac{1}{\hat{\sigma}_f^{49}} \frac{d\hat{\sigma}_f^{49}}{dT_n} / \frac{1}{\hat{\sigma}_f^{25}} \frac{d\hat{\sigma}_f^{25}}{dT_n}$	0.2	-4.0	-8.0	-5.0	-1.0
$\frac{1}{\hat{\sigma}_f^{49}} \frac{d\hat{\sigma}_f^{49}}{dT_n} / \frac{1}{\hat{\sigma}_f^{25}} \frac{d\hat{\sigma}_f^{25}}{dT_n}$	0.1	-4.1	-9.5	-10.7	-9.5
$1 + \alpha_{49}$	0.2	1.517	1.548	1.575	1.618
$1 + \alpha_{25}$	0.2	1.216	1.217	1.221	1.230
$\hat{\sigma}_a^{40}$ - barns	0.2	2210	2670	3060	3540
$\hat{\sigma}_a^{40}$ - barns	0.1	1235	1477	1678	1925
$\frac{\hat{\sigma}_a^{40}}{\hat{\sigma}_a^{49}}$	0.2	1.397	1.478	1.502	1.651

Cold clean critical to hot clean critical, %	3.9	
Equilibrium poisons (Xe and Sm), %	2.1	
Excess required to achieve desired fuel lifetime, %	4.0	10.0
	10.0	16.0
Shutdown margin, %	4.0	4.0
	14.0%	20.0%

The larger value of the initial excess reactivity, given in the last column of the table above, is for a full core loading of fresh fuel elements at 2% enrichment. Since the reactivity excursions for a staggered fueling cycle would be much less than this value (see Fig. 2.39) the discrepancy between reactivity required and the control rod capacity, would occur only for the initial core loading. This apparent difficulty would be circumvented either by prepoisoning the core with a burnable poison, by using lower enrichment for the first core loading, or by other means consistent with the most favorable approach to an equilibrium fueling cycle.

The control requirements will be met by 61 cylindrical silver rods, worth in the aggregate 0.17 in δk or 14.5% in reactivity.

Although cylindrical control rods are not the most effective way of utilizing a given volume of absorber, they were selected because of their convenience and ease of handling.

There are two general approaches for determining multiple control rod worths:

1. The first approach is to consider that the sole action of the control rods is to increase the buckling of the neutron density, producing both an extra leakage to the outside and a migration of neutrons to the rods, themselves.
2. The second approach, and the one used here, is to consider that the ganged control rods introduce an effective homogeneous poison whose cross section is represented by

$$\Sigma_a^p = \frac{N\ S\ E}{4A}, \tag{2.46}$$

where

S = outer perimeter of each rod, in the plane normal to the rod axis,

N = total number of rods, assumed to be uniformly spaced over the core cross section,

A = core cross sectional area normal to control rod axis,

E = volume effectiveness of control materials relative to hafnium. Values of E larger than one indicate appreciable resonance absorption. The volume effectiveness of control materials is dependent to some extent on the particular reactor and associated neutron spectrum, however, the values used are reasonably representative.

Thus,the control region is represented by a local multiplication factor and a local migration area. Weighting the control and active core regions appropriately the over-all k for the reactor can be readily obtained.

An analysis of various control material was made in an effort to select, on the basis of over-all considerations, the best material for the gas-cooled reactor. The three principal considerations were:

1. The required configuration for 10% reactivity. The configuration will, of course, depend on the particular reactor's nuclear parameters, that is, Σ_a^p/Σ_a^F, L^2B^2, etc.; however, since the control rods are evaluated on an equivalent basis, the relative comparisons will apply to any reactor.
2. The lifetime of the control material, based on an allowable 10% burn-up of control material in 20 yr. Depletion of the control material was calculated on the assumption that the reactor would always run with the control rods inserted to absorb 1% reactivity. Many of the control materials have several isotopes with large absorption cross sections, thus increasing the lifetime. A notable example is europium, where the average atom can undergo capture four times before it is finally depleted.
3. The costs of the control rods, based on the latest material costs wherever possible.

The other considerations which are important for control materials are melting temperature, strength and level of induced radioactivity. All the

control materials would require several inches of lead shielding to bring the dose level from induced activity within tolerance limits for direct handling.

Silver was selected as the control material, however its low melting point and low creep strength require a stainless steel can for support.[38] The disposition of the control rods was based on the locations of the 69 charge holes. The weight factor associated with the region accessible through the eight peripheral charge holes is 0.02, representing a reactivity of ~ 0.35%. These channels were therefore not used, leaving a total of 61 rods. The 18-ft active length of the rods results in a loss of reactivity worth of ~ 0.7% as compared to rods equal in length to the height of the active core. The annular cylinder of silver used in the control rod has a 2 in. OD and 1.25 in. ID.

The heat generation per rod is 10 kw with 65% of the heat generation due to external sources, that is, fission product gamma rays, capture gamma rays in the clad, etc., and the remainder due to gamma and beta sources in the silver. The control-rod flow channels are orificed at the bottom of the reactor to maintain the exit-gas temperature.

2.7 Power Flattening

One of the possible uses of fuel enrichment is to permit such distributions of fissionable material in the reactor as will tend to produce a uniform power density in all fuel elements. The potential advantages of such an arrangement are great since all heat-transfer surfaces operate at the maximum allowable heat flux and all fuel elements operate at the maximum allowable power density. Unfortunately, as implied by the need for fuel enrichment, such uniform-power arrangements are always less reactive than configurations having uniform fuel distribution, and it becomes necessary to find an economical compromise between requirements for maximum power density and the need to maintain reactivity. Some of the benefits that accrue from power flattening can be realized, at least in part, by properly matching the flow of coolant in each channel to the power produced in that channel. The degree to which this procedure can approximate the benefits of power flattening depends very much on what the limitations on heat transfer are, in the particular system under study, and on the relative magnitudes of certain characteristic temperature differences

---

[38] For more details on this selection of silver as the control material, see Section 3 of this report.

in the core, for example, the coolant temperature rise through the core, the film drop between fuel surface and mean coolant temperature, and the internal temperature rise within the fuel element. Broad generalities about the effectiveness of orificing the flow should be interpreted with caution; each system must be studied independently. In the case of the GCR-2 core, the fuel element surface temperature is the principal limitation on heat transfer; internal temperature rise appears to be less crucial (especially if the gap between clad and UO_2 is very small) since the central oxide temperature is in any case well below melting. (Larger fuel-rod diameter, or higher surface-film drop, could change this situation.) Under these conditions, it has been found that the core can be made to produce nearly as much power with a radial peak-to-average power ratio of 1.3 to 1.5, as with a uniform radial power distribution, provided the coolant flow is properly matched to the power distribution. This matching is best achieved by varying the cooling-channel diameters, but can be accomplished almost as well by orifices. It appears, therefore, that the incentive for power flattening is not great, and the criterion has been adopted that as much power flattening will be provided as can be accomplished without sacrificing significantly in the effective use of fissionable material in other ways. It will be shown in the following paragraphs that the radial peak-to-average power density ratio (hereafter designated (P_m/P_{av})) can easily be reduced to 1.25 to 1.3.

The general method for flattening the power distribution is to reduce the infinite multiplication factor at the center of the reactor core and increase it near the boundaries of the core. This may be done in several ways. For a homogeneous system, it may be accomplished by increasing the concentration of the fissionable material towards the outer regions of the core by poisoning the central region of the core, as with control rods, In a heterogeneous system, it may also be accomplished by varying the lattice pitch, so as to modify the balance between thermal utilization and resonance escape probability. A fourth approach, for constant lattice pitch and constant fuel enrichment, is simply to allow the fuel near the center to reach a higher exposure level, and hence lower reactivity, than the fuel near the core boundaries.

An approximate discussion of the power-flattening problem can conveniently be carried out in terms of a three-region, one-neutron group

diffusion model. The core is divided into a central, low k region, surrounded by an annular high k region, which is in turn surrounded by the reflector. The problem is simplified in the present case by the fact that a flat power distribution implies approximately a flat flux distribution, for cases of variable lattice pitch and variable fuel exposure level (since the fission cross section changes slowly with exposure level, see Fig. 2.36). The variable enrichment case is a little more complex (see integral method, following pages).

The diffusion equation for the three regions is:

$$\nabla^2 \phi + \frac{(k - 1)}{M^2} \phi = 0, \qquad (2.47)$$

or $\nabla^2 \phi + B^2 \phi = 0 \qquad B^2 = (k - 1)/M^2.$

Separating the radial and axial components of the flux, we write $\phi = \phi(r) \cos \beta Z$

$$\nabla_r^2 \phi + b^2 \phi = 0 \qquad b^2 = B^2 - \beta^2 \qquad \beta^2 = \left(\frac{\pi}{H}\right)^2$$

In region 1: $\nabla_r^2 = 0$; and $k = 1 + M^2\beta^2$

region 2: $\phi = C_1 J_o(br) + C_2 Y_o(br)$

region 3: $\phi = E_1 I_o(Kr) + E_2 K_o(Kr)$

where C_1, C_2, E_1, E_2 are integration constants, J_o, Y_o, I_o, K_o are the Bessel functions, and K is the reciprocal diffusion length in the reflector. Application of the usual boundary conditions on fluxes and currents establishes a relationship between the radius, a, of region 1, and the radial buckling, b, of region 2. The ratio P_m/P_{av} can of course be determined from the resulting flux distribution. Figure 2.43 shows the radius of region 1 and P_m/P_{av} as a function of the radial buckling of region 2. Figure 2.44 shows the power distributions for several values of a and b. Figure 2.45 shows the values of the lattice pitch that would produce the power distributions shown in Fig. 2.44. These are for just-critical reactors, and neglect the extra reactivity required to prolong fuel life. It can be seen that the average lattice pitch does not increase very rapidly for dimensions of the central region that will produce

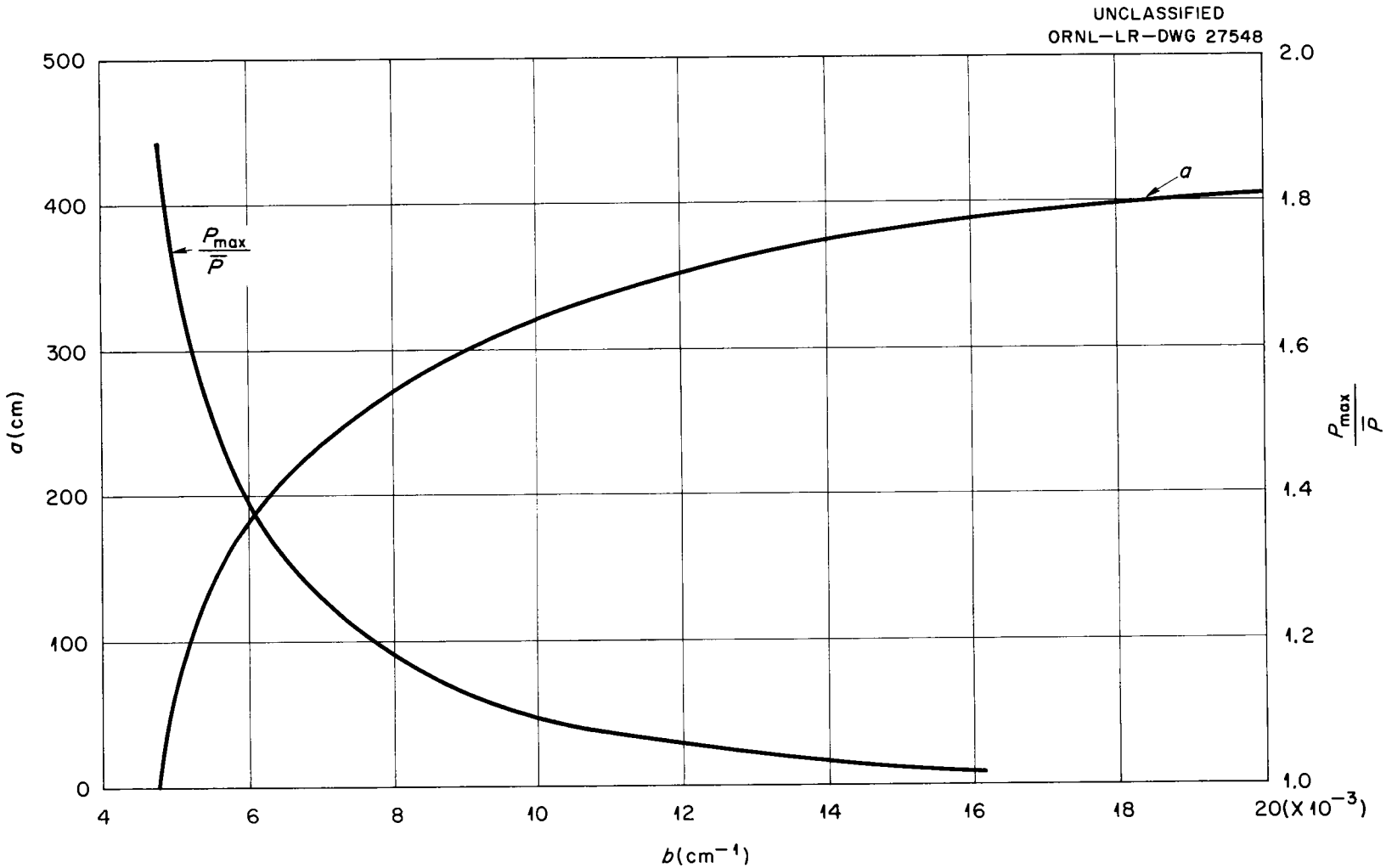

Fig. 2.43. Radius of Flat Flux Region and Power Density Ratio vs Buckling of Annulus.

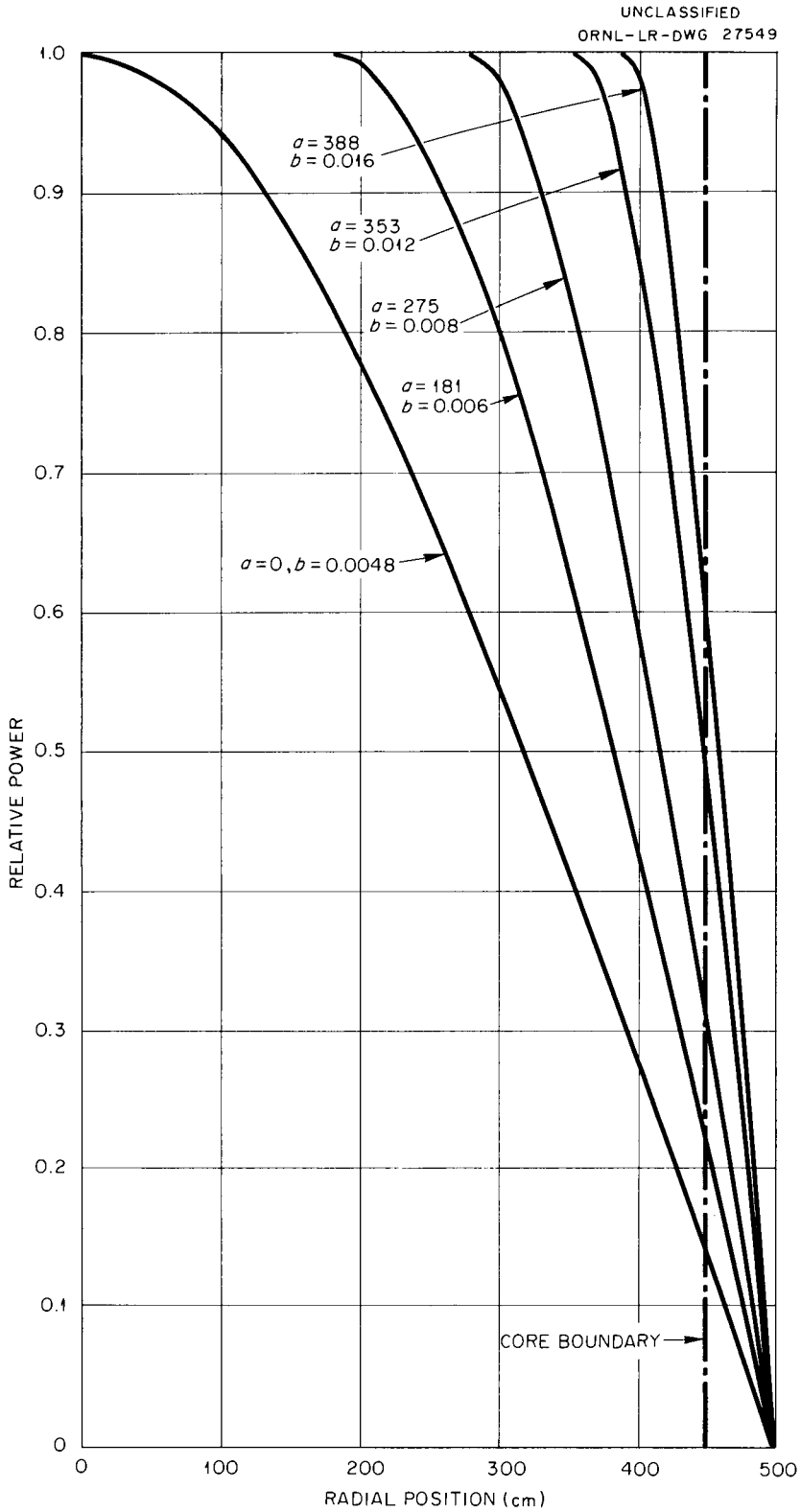

Fig. 2.44. Power Density Distributions.

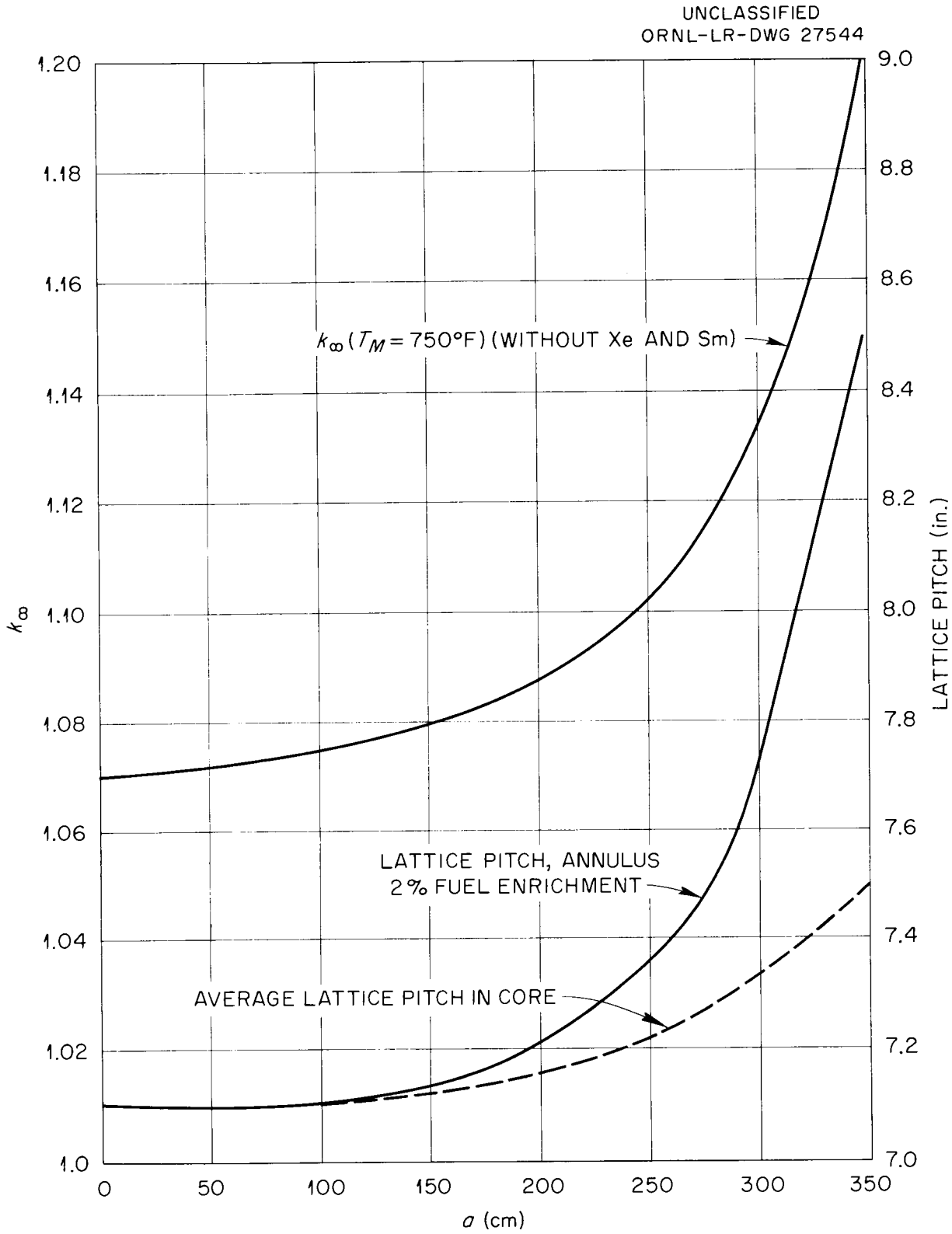

Fig. 2.45. Average Lattice Pitch vs Radius of Flat Flux Region.

quite favorable P_m/P_{av} (for example, $P_m/P_{av} = 1.2$, a = 2.65 cm, increase in lattice pitch = 2.1%, decrease in average power density 4.1%). While this is not the design case (having no excess reactivity) it would appear that a modest decrease in power density could pay for a significant reduction in P_m/P_{av}.

As mentioned above, some flattening of the power could also be achieved by maintaining the fuel in the central region at an average exposure level, and hence reactivity, that will just provide for the axial neutron leakage; the average exposure level in the annular region then depends upon the radius, a, of the central region. Figure 2-46 shows how the over-all average exposure is affected, relative to a uniform core, if a is chosen to produce various values of P_m/P_{av}. It appears that a power ratio of 1.25 to 1.3 can be achieved with a very nominal sacrifice in fuel life, but that a further reduction in P_m/P_{av} would be quite costly.

The problem of flux flattening by variable fuel enrichment has been examined by an integral method,[39] in which the critical equation is written

$$\phi(r) = \int_0^R \phi(r')\, \Sigma_f(r')\, \nu\epsilon \left[G_{ft}(r',r) - G_{ftRp}(r',r) \right] dr' - \int_0^R \phi(r') \left[\Sigma_a(r') - \Sigma_{mod} \right] G_t(r',r)\, dr', \tag{2.48}$$

where G_{ft} is the composite slowing down and diffusion kernel for an infinite block of moderator; G_{ftRp} is the composite slowing down and diffusion kernel, for the finite core (radius R) taking into account the possibility of variable resonance escape probability p, and G_t is simply the thermal diffusion kernel. Other quantities have the same meanings as elsewhere in this chapter. (Cross sections are averaged over the lattice cell.) A solution of the integral equation must be found subject to the constraint $\phi\Sigma_f V_c$ = constant, (V_c = cell volume). Results have been obtained for a core that is critical with a uniform fuel enrichment of 1.25% U^{235}; Fig. 2.47 shows the average fission cross section and the fuel enrichment as a function of radial position in the

---

[39] R. L. Murray, Uniform Power in Heterogeneous Reactors by Variable Enrichment and Lattice Spacing, Memorandum to A. M. Perry (January 1958).

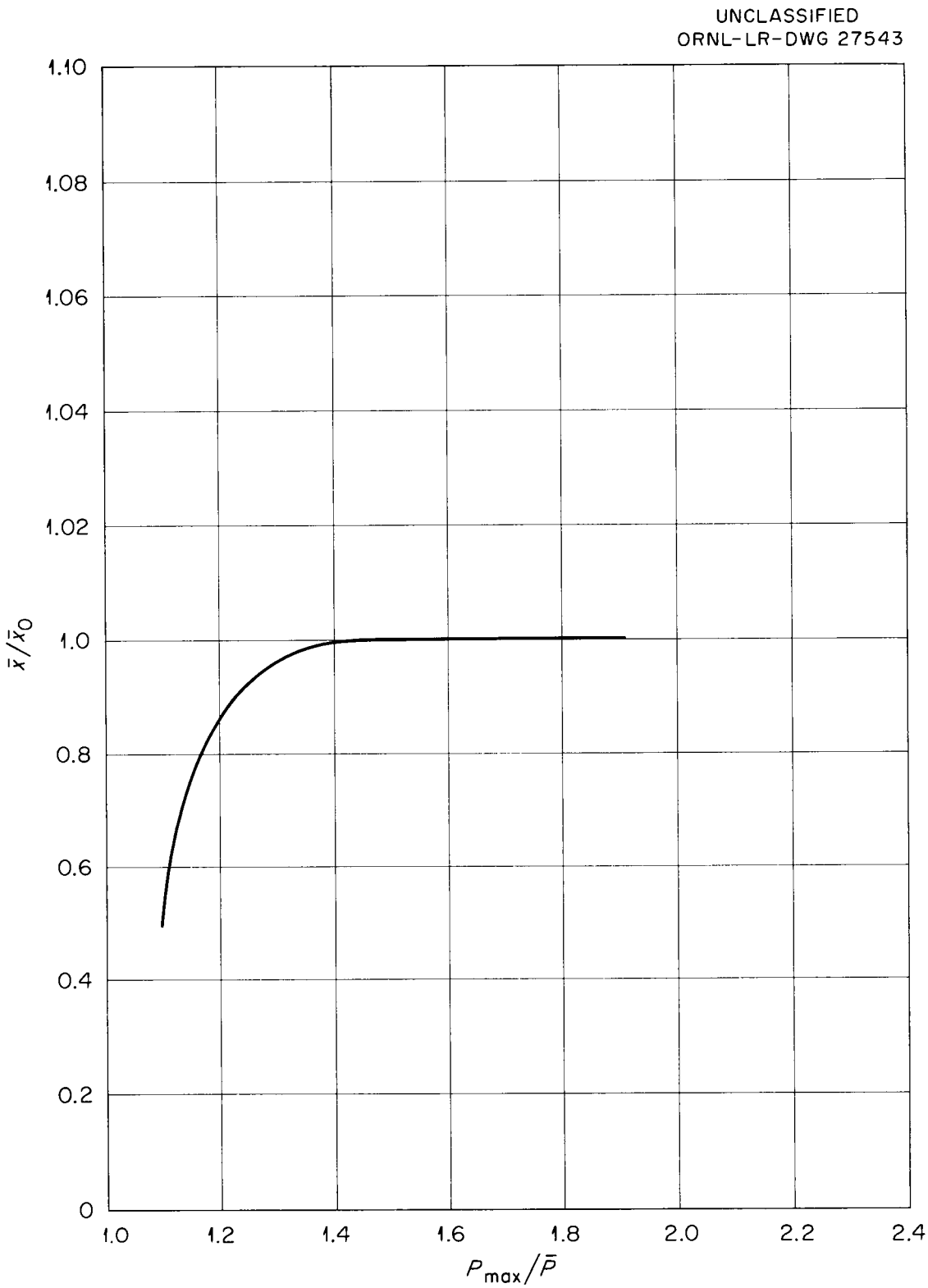

Fig. 2.46. Effect on Core Life of Reducing Power Density.

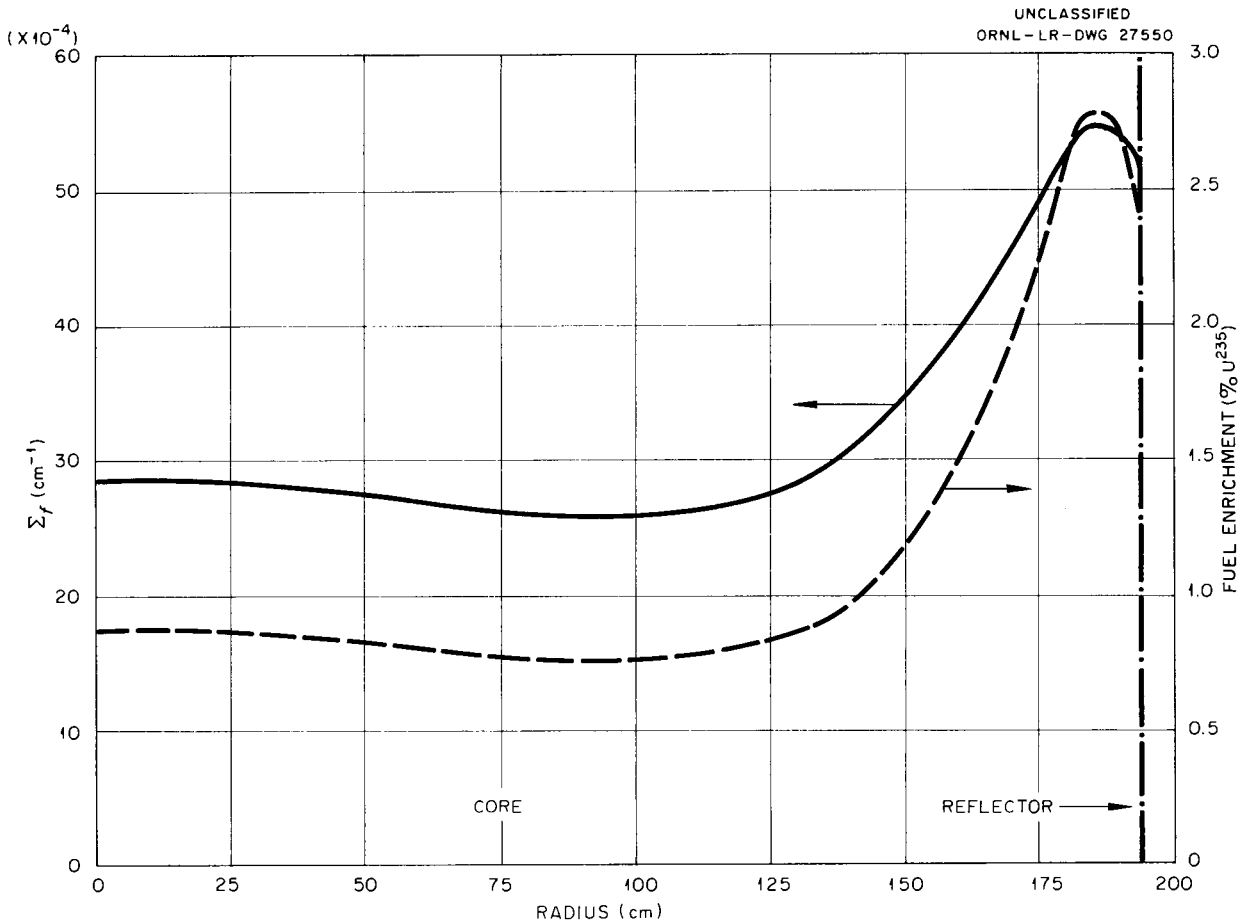

Fig. 2.47. Fuel Enrichment vs Position for Flat Power Distribution.

core. It is found that the total amount of U^{235} required for criticality is about 17 % greater with the flat power distribution than for a uniform core loading. The shape of the flux distribution which is inversely proportional to Σ_f in this variable enrichment case is qualitatively similar to that found by the diffusion theory approach (see preceding pages). The integral method, of course, describes the fast and thermal neutron behavior in the reflector better than the one-group diffusion approach.

The treatment of flux flattening in the gas-cooled reactor, described above, has been rather approximate to date; a more careful study is now underway. Nontheless, two key features have emerged; the power ratio P_m/P_{av} can be reduced to 1.2 to 1.3 with only slight sacrifice in other core performance criteria; the power distribution is established well enough to permit a clear definition of the steps required to match the coolant flow. It is probable that power flattening would be undertaken by the method of variable fuel exposure level. Here, as in the case of fuel lifetime, the difficulties associated with reaching an equilibrium fueling cycle require further study.

2.8 Shielding

The primary purpose of the shielding calculations performed to date has been to establish the integrity of the 9-ft biological shield when this reactor operates at a power of 700 Mw.

2.8.1. Gamma-Ray Dose Rate: The results of calculations on the gamma-ray dose rate are given in Table 2.12 in the form of dose rate, in r/hr, for various shield thicknesses. Comparison of the total with the last line indicates the effectiveness of the boron-containing pyrex neutron shield around the reflector. It saves about 2 ft or more of concrete.

The core gamma-ray sources include the following:

1. Prompt gamma rays in the fuel.
2. Decay gamma rays in the fuel.
3. Capture gamma rays in the clad.
4. Gamma rays due to inelastic neutron scattering in the clad.
5. Capture gamma rays in the moderator.

TABLE 2.12

DOSE RATE (r/hr) FROM GAMMA RAYS FOR SEVERAL SHIELD THICKNESSES

Sources	Distance from the Inside Surface of the Concrete Shield, in ft			
	0	3	6	9
Core gamma rays	6.4×10^{3}	14.7	4.8×10^{-2}	0.24×10^{-3}
Capture gamma rays in reflector	4.9×10^{3}	7.8	1.0×10^{-2}	0.03×10^{-3}
Capture gamma rays in pressure vessel (with pyrex)	0.4×10^{3}	0.7	0.3×10^{-2}	0.01×10^{-3}
Total	1.2×10^{4}	23	6.1×10^{-2}	0.3×10^{-3}
Capture gamma rays in pressure vessel (without pyrex)	4×10^{5}	700	3	13×10^{-3}

The capture gamma rays from graphite were assumed to be given off at 5 Mev.[40] The spectra of all of the other sources were divided up into six energy groups with average energies of 0.5, 1.0, 2.0, 4.0, 6.0, and 8.0 Mev. The contributions to the total dose from each energy group were calculated separately for each field point.

The source strengths of the gamma rays in the fuel were calculated from the average power per unit volume of fuel rod. The capture gamma-ray source strength in the clad was calculated using an average thermal neutron flux of 0.8×10^{13} n/cm^2 sec. The source strength of the capture gamma-ray source in the moderator was calculated using a neutron flux of twice this value, since the moderator disadvantage factor in this reactor is about 2.

---

[40] P. A. Mittelman and R. A. Liedtke, "Gamma Rays from Thermal Neutron Capture," Nucleonics, 13, 5, 50 (1955).

The source strength of the gamma rays from inelastic neutron scattering was calculated from an estimated fast flux of 5×10^{12} n/cm^2 sec unit lethargy. The gamma rays emitted by this process were assumed to be given off at 1 Mev.

All source strengths thus calculated were then averaged over a typical lattice cell to give an average source strength in the cell at the average reactor power.

The dose-rate calculations were made for the shield at the side of the reactor. In calculating the dose from the core gamma rays, the geometry was idealized to infinite slab geometry where each succeeding cylindrical shell of the core, 1 ft thick, was treated as an infinite slab source. The source strengths in each shell were modified to account for the variation of the average power density in each shell from the average power density in the reactor. The sources in the reflector were treated in the same way.

Calculation of the thermal neutron flux in the pressure vessel leaves much to be desired. A rather hasty comparison of the calculated fluxes in the pressure vessel and concrete of this reactor with measured thermal neutron fluxes in the concrete of the X-10 reactor[41] indicate that the calculated fluxes may be low by as much as a factor of 10.

However, if the calculated dose rates, in Table 2.12, due to capture gamma rays in the pressure vessel are multiplied by a factor of 10, one can see that the total dose rate for 9 ft of concrete is still well below tolerance, if pyrex is used. Without pyrex, the total dose rate is already above tolerance but this is not the design case.

The dose rate at the surface of the shield from capture gamma rays in the concrete was found to be negligible. In the first place, an approximate calculation indicates that the thermal neutron flux in the concrete from fast neutrons slowing down in the concrete should not exceed 10^9 n/cm^{2}sec near the inside surface of the concrete. Capture gamma rays, from this flux, would give a negligible dose rate at the outside surface of the shield. In the second place, the measured thermal neutron flux in the concrete of the X-10 reactor[42] was scaled up by the ratio of the power levels. It was scaled down

---

[41] T. V. Blosser, Oak Ridge National Laboratory, private communication.
[42] Ibid.

by the amount the pressure vessel alone is expected to depress the thermal neutron flux. The capture gamma-ray source strength arising from this adjusted flux gave a dose rate of about 0.1 of tolerance at the outside surface of the shield. The presence of the pyrex will reduce the flux in the concrete, and thus the dose rate at the surface of the shield, to negligible values.

The scaling up of the data from the X-10 pile by the ratio of the power levels is probably pessimistic since the X-10 reactor is smaller; it has a reflector which is 6 in. smaller, and the reflector is perforated with 1 3/4-in.-square holes on an 8-in. pitch.

2.8.2 Fast and Thermal Neutron Dose Rate: The experimentally measured fast neutron dose rate in the X-10 reactor[43] was scaled up by the ratio of the power levels. Measurements were available with concrete thicknesses up to 5 ft and the results extrapolated to a concrete thickness of 9 ft.

The tolerance dose rate of fast neutrons is achieved with about 6.2 ft of concrete.

The X-10 shield is made such that the inner and outer 1-ft sections of the shield were of regular Portland concrete, while the inner 5-ft-thick section was composed of Barytes-Haydite concrete. Blosser states that the central 5 ft can no longer be considered to be Barytes-Haydite since chemical analysis of the material indicates it has lost its water content.

Thus it can be concluded, with reasonable safety, that 9 ft of concrete is quite adequate for our purposes since the fast neutron dose rate is reduced well below tolerance.

Blosser's data indicate that the thermal neutron flux at the surface of the shield would also be well below tolerance.

The 9-ft thickness of concrete appears to be adequate for this reactor and can be used as the basic shield thickness.

Further study is required in the regions where the shield is penetrated; in particular, the areas above the reactor where the shield is penetrated by the control rods and fuel-loading holes, and all areas of instrumentation penetrations.

---

[43] Ibid.

One further note of interest is the fact that of the various contributions to the dose rate from gamma rays originating in the core, the predominant contributors are the capture gamma rays in the stainless steel clad.

2.8.3. Heating in the Concrete: The gamma-ray energy flux, calculated for shielding purposes, was used in calculating the heat deposition rate in the concrete.

The above gamma-ray flux was multiplied by the ratio of the buildup factor for energy absorption to the dose buildup factor, and then multiplied by the gamma-energy-absorption coefficient of concrete for each energy group.

The results for gamma rays and neutrons are given in Table 2.13 in watts/cc.

TABLE 2.13

HEATING FROM GAMMA RAYS AND NEUTRONS FOR SEVERAL SHIELD THICKNESSES (w/cc)

Sources	Distance from the Inside Surface of the Concrete, in ft	
	0	3
Core gamma rays	4.3×10^{-5}	1×10^{-7}
Capture gamma rays in reflector	2.9×10^{-5}	0.5×10^{-7}
Capture gamma rays in pressure vessel (with pyrex)	0.2×10^{-5}	0.05×10^{-7}
Heating due to fast neutrons	4.0×10^{-5}	---
Total	11.4×10^{-5}	1.6×10^{-7}
Capture gamma rays in pressure vessel (without pyrex)	2×10^{-3}	5×10^{-6}

It should be noted that the presence of the pyrex reduces the heating in the concrete to levels such that no thermal shield is required for the concrete.

The neutron heating at the surface of the concrete was estimated to be about 4×10^{-5} w/cc. This estimate was made by multiplying the fast neutron dose rate at the surface of the shield, given in Fig. 2.48 in ergs/gm of tissue/hr, by the equivalent water content of concrete (taken to be 0.3 gm/cc) and converting to watts per cc.

The heating in the concrete due to capture gamma rays in the concrete was estimated and found to be negligible.

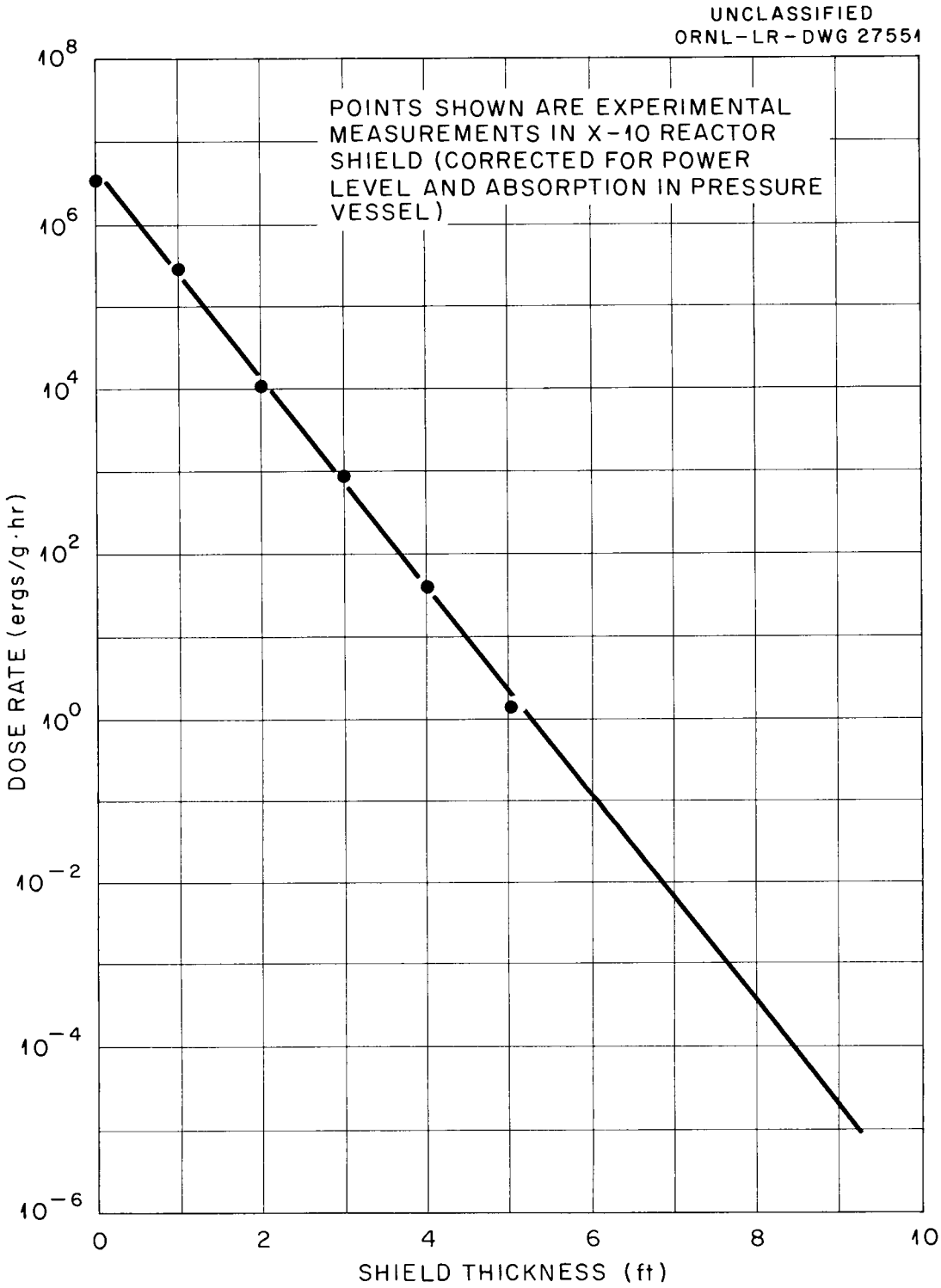

Fig. 2.48. Fast Neutron Dose Rate in Concrete Shield.

SECTION 3

MATERIALS

3. MATERIALS

CONTENTS

3.1 Selection of the Fuel 3.1

3.1.1 UO_2 Fabrication Studies 3.8

3.2 Selection of the Capsule Material 3.13

3.3 Selection of Gas Coolant 3.17

3.3.1 Contamination Problems 3.19

3.3.2 Degassing of Graphite 3.20

3.3.3 Carbon Mass Transfer 3.22

3.4 Selection of Materials for Pressure Vessel 3.23

3.5 Ductwork, Bellows, Valves and Pumps 3.35

3.6 Control Rod Materials 3.37

3.7 The Selection of Shield Materials for the Boron Curtain 3.40

3. MATERIALS

Materials that are to be used as principal components of the proposed reactor are indicated in Table 3.1 together with the major developmental problems posed by each material. It should be noted that no exotic or uncommon materials are included although there is very little relevant operating experience available on the environments in which the materials are to be exposed. There is, therefore, some uncertainty regarding the long time serviceability of certain of the materials in the reactor. These uncertainties can be resolved only by experimentation.

The detailed reasons for the choice of materials and the problems posed in preparing and using the materials are given below.

3.1 Selection of the Fuel

The basic criteria on which a selection of the fuel was made for GCR-2 were: (1) that it be inexpensive, (2) that it operate at relatively high temperatures, and (3) that it withstand high burn-ups. The cost of power depends directly on how well these criteria are satisfied. The choice of fuel for the GCR-2 is uranium dioxide (UO_2) with a density of 95% of the theoretical value.

At first glance, natural uranium metal would appear to be the logical fuel choice since its density is high enough (19.05 g/cm^3) so that its use avoids the expense of an isotope separation. In practice, however, severe penalties in performance are incurred in attempting to use natural uranium metal. First of all, uranium is attacked by air at temperatures below the boiling point of water while above 349°C the rate is such that the reaction is self-sustaining.[1] Thus, a cladding material is required to prevent any reaction between uranium and contaminants in the gas stream.

---

[1] Tom Bishop, "Metallurgical Aspects of Calder Hall," Metal Progress, 71, No. 6, 65, (June, 1957).

TABLE 3.1

SUMMARY OF PRINCIPAL COMPONENTS OF GCR-2

Component	Material Selected	Status of Technology	Major Materials Developmental Problems
Fuel	UO_2, 95% Theoretical density	Good	Reducing cost of conversion to UO_2 and production of pellets
Capsule	Type 304 Stainless steel	Advanced	Possible oxidation and/or carburization
Coolant	Helium	High-purity gas available	Supply is limited
Moderator	Graphite	Advanced	Outgassing and possibly stored energy
Pressure Vessel	SA-212B Steel	Advanced	Details of field erection Possibility of brittle fracture at low temperatures under irradiation
Ductwork	5% Chromium-1/2% Molybdenum steel	Advanced	Joining to other steels
Expansion Bellows	Type 347 Stainless steel	Advanced	Joining to 5% chromium-1/2% molybdenum steel
Heat Exchangers	5% Chromium-1/2% Molybdenum steel	Advanced	Leak tightness requirement
Neutron Curtain	Pyrex	Good	Verification of reported resistance to radiation damage
Control Rods	Silver clad with stainless steel	Advanced	None

If a reactor is to operate using natural uranium fuel, the cladding material must be one of the low cross section elements: aluminum, magnesium, beryllium, silicon, or zirconium. Uranium reacts with aluminum above ~ 350°C to form brittle intermetallic compounds.[2] Aluminum and magnesium have relatively low melting points, 660 and 650°C respectively, and low strengths above ~ 450°C. Beryllium is highly toxic, is difficult to fabricate and join, and has low high-temperature strength. Zirconium is expensive, has low high-temperature strength, and is embrittled by the contaminants in the coolant stream. Silicon and high-silicon alloys are so brittle that they cannot be fabricated. After considering the relative merits of these low cross section materials as a cladding for uranium metal, the British selected a magnesium-base alloy containing 1% aluminum and 0.05% beryllium for use at Calder Hall;[3] whereas, the French selected magnesium containing 0.75% zirconium for use at Marcoule.

When metallic uranium is used as the fuel, the principal operating limitation placed on the reactor is the severe radiation damage suffered by the fuel. This damage manifests itself in three ways: loss in ductility, growth, and swelling. Irradiated uranium metal exhibits extremely low ductility even at very low exposures, corresponding to less than 0.035 at. % burn-up.[4] Post-irradiation annealing at temperatures up to 700°C does not restore the pre-irradiation properties of the metal. Since fuel materials are seldom used as structural members, this effect is primarily of academic interest.

Growth is a type of radiation damage that is particularly troublesome at low temperatures, becoming less severe as the temperature of irradiation is increased. Growth also occurs if a polycrystalline sample of uranium is subjected to thermal cycling. It has been shown that the amount of growth

---

[2] R. Keissling, "The Solid State Reaction Between Uranium and Aluminum," Proceedings of the International Conference on the Peaceful Uses of Atomic Energy, 9, 69 (1956).

[3] Tom Bishop, Op. cit. p. 3.1

[4] R. E. Hueschen, R. S. Kemper, and W. S. Kelly, The Effects of Irradiation on the Tensile Properties of Uranium, HW-41690 (February 9, 1955).

observed at low temperatures may be directly correlated with the degree of preferred orientation in the uranium.[5] The experimentally observed values of the density decrease of 3–4% per 1 at. % burn-up agree closely with the theoretically computed value of 2.54% given by Howe and Weber[6], which is based on the assumption that the volume increase is directly proportional to the difference in volume between uranium consumed and the fission products formed (assuming that all atoms including xenon and krypton are in the condensed state). This density decrease would produce less than a one per cent change in any linear dimension with one per cent burn-up. With uranium which has a high degree of preferred orientation, the observed changes in certain linear dimensions may be several hundred per cent. Fortunately, growth may be eliminated by giving the uranium a proper heat treatment to produce a randomly oriented grain structure.

Swelling, the third type of radiation damage, is the most serious problem. It occurs at temperatures above ~ 400°C, where the strength of uranium is quite low. Swelling is accompanied by decreases in density which far exceed the theoretical vlaue of 2.54% for 1 at. % burn-up. The per cent density change is closely related to the temperature, increasing rapidly with increasing temperatures, as illustrated in Fig. 3.1,[7] for irradiated powder compacts of unalloyed uranium. (Compacting and sintering powders is an alternate way of producing a material with a randomly oriented grain structure). Kittel and Paine obtained similar results with the following uranium alloys: uranium-1.0, 1.4, 2.0, 2.5, and 3.5 wt % molybdenum and uranium-1.6 and 0.42 wt % silicon. Although this work may be criticized because the sample temperatures were computed rather than measured and because no attempt was made to control the specimen temperatures, swelling is clearly a real and reproducible effect. Swelling has been observed by the British[8], who have shown that small alloy additions were

---

[5] Frank G. Foote, "Physical Metallurgy of Uranium," Nuclear Metallurgy 1, AIME, 65 (October 17, 1955).

[6] C. E. Weber to W. D. Manly, Private Communications, (February 14, 1958).

[7] J. H. Kittel and S. H. Paine, Effects of Irradiation on Powder Compacts of Uranium and Some Uranium-Base Alloys, ANL-5664 (June, 1957).

[8] I. F. Barwood, AERE-M/R-2004, (August 28, 1956)

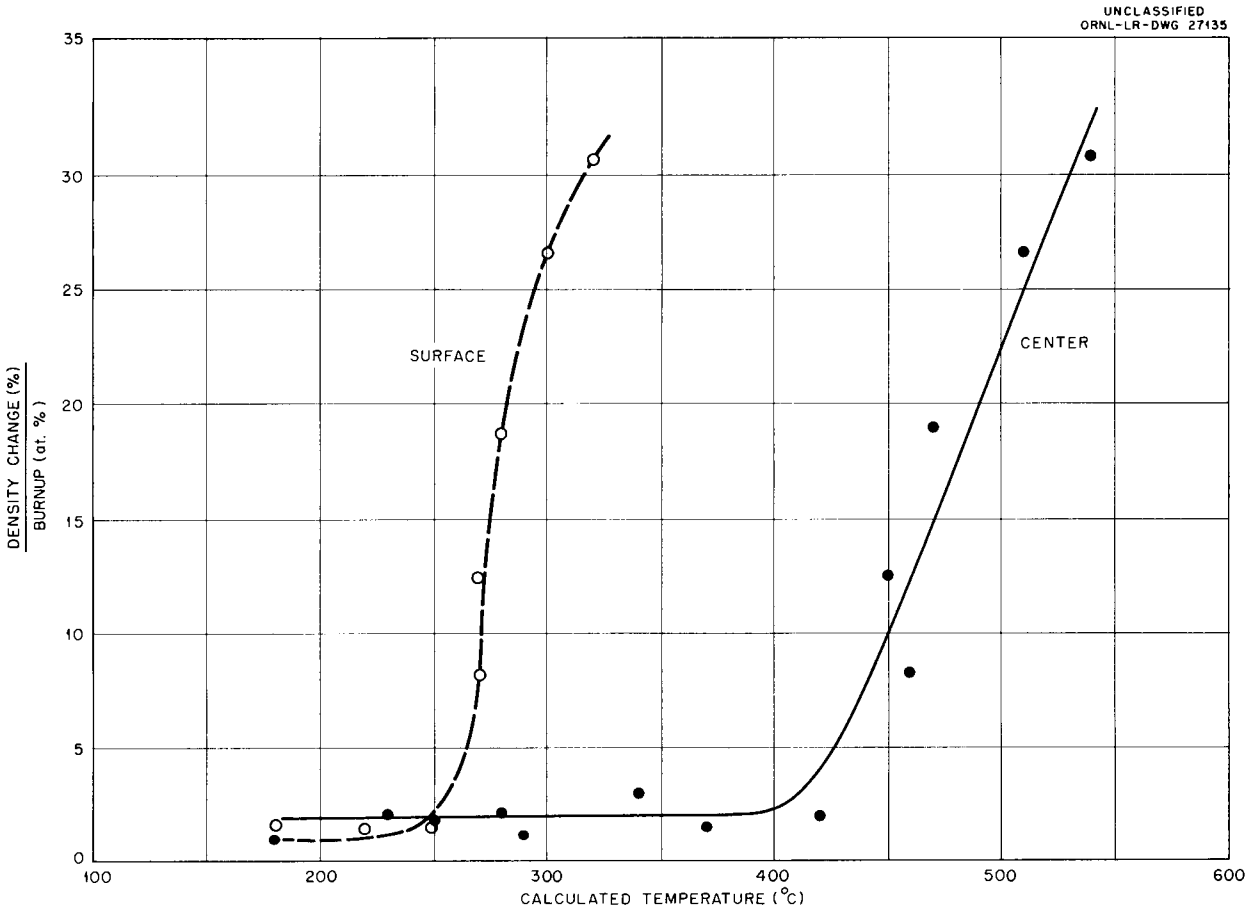

Fig. 3.1. Swelling of Powder Compacts of Unalloyed Uranium.

not effective in reducing the amount of swelling. Alloys containing 10–20 wt % of either molybdenum[9,10] or niobium[11] have been reported to be resistant to swelling at temperatures in excess of 400°C. Unfortunately, these additives have such high neutron absorption cross sections that they cannot be considered for use in a natural uranium system. Although the cause of swelling is not positively known, it is generally believed that swelling is produced by expansion of the fission product gases, xenon and krypton, at imperfection sites in the uranium lattice. Swelling is not observed at lower temperatures where uranium has sufficient strength to withstand the high pressures developed by the fission product gases. The beneficial effects of molybdenum and niobium are consistent with this theory, since these elements are effective in increasing the high-temperature strength of uranium. It has also been suggested that these alloy additions decrease the rate of swelling by changing the rates of nucleation and growth of voids.[12] Fillnow[13] has postulated that below 600°C the swelling in uranium alloys is accelerated by the short-circuit diffusion of the gaseous fission products at the interface between the radiation-stabilized gamma phase and the thermodynamically stable alpha plus gamma prime. Due to the cycling of a reactor during normal operation, the fuel temperature fluctuates widely so that the uranium alloy may transform many times. The gamma-alpha interface sweeps back and forth and permits the short-circuit diffusion to occur. Alloys such as molybdenum and columbium which retard the gamma decomposition reduce the number of transformation cycles and thus reduce the swelling.

From the amount of information presently available on the effects of irradiation on uranium metal with or without small alloy additions, it appears that the maximum surface temperature of this type of fuel element is limited to ~ 400°C and the burn-up is limited to ~ 6000 Mwd/T even if a 10–15% expansion of the fuel element is allowed for in the design.

---

[9] I. F. Barwood, Op. cit. p 3.4.

[10] L. C. Cook, AEC Memo 7219-1-1-2-1.

[11] P. C. Daly, B. P. -AT 88.

[12] I. F. Barwood, Op. cit. p 3.4.

[13] R. N. Fillnow, WAPD, Private Communication (November, 1957).

(It should be noted that the reactivity lifetime of a natural uranium-graphite reactor is ~ 5500 Mwd/T.) Thus, if the reactor is to be operated at high temperatures and the fuel is to be subjected to higher burn-ups a better fuel is needed.

With present technology, the fuel which best meets these needs is UO_2. Uranium dioxide has many advantages, the most important of which is that it has a defect lattice which permits a considerable retention of fission products with no lattice distortion. Under some conditions no growth or swelling has been observed in UO_2 at burn-ups of 25,000 Mwd/T.[14] In addition, UO_2 is a stable material which is chemically compatible with most container materials and coolants. This is important because there is no danger of a catastrophic fire even if a fuel element failure occurs. Finally, there exists a well-developed technology on UO_2.[15,16]

There are, of course, disadvantages associated with the use of UO_2. Since it is a ceramic material, its thermal conductivity is low so that at high power levels the heat cannot be dissipated by thick sections and coring occurs in the center of the elements. This coring, which is the result of sublimation or melting of the center of the element, is accompanied by complete release of the gaseous fission products, xenon and krypton, from the over-heated material. Coring is eliminated by proper design of the system and should not be considered a serious problem.

Another characteristic of UO_2 is that it has low resistance to thermal shock so that samples placed in a radiation field invariably fracture. For this reason, UO_2 cannot be used as a structural member and a cladding material must be used to contain it.

Another problem associated with the use of UO_2 is the partial release of the gaseous fission products, xenon and krypton. Lustman[17] has shown that the kinetics of the fission-gas release can be explained quantitatively

---

[14] J. D. Eichenberg, P. W. Frank, T. J. Kisiel, B. Lustman, and K. H. Vogel, Effects of Irradiation on Bulk UO_2, WAPD-183 (October, 1957).

[15] Ibid

[16] J. Belle and B. Lustman, Properties of UO_2, WAPD-184 (September, 1954).

[17] B. Lustman, Release of Fission Gases From UO_2, WAPD-173, (March, 1957).

on the basis of a diffusion mechanism. On this basis, the amount of fission-gas release is a function of the density of the UO_2 compacts and the operating temperature. Lustman's theory agrees with the experimental evidence that if the density of UO_2 is above 94% of the theoretical density, less than one per cent of the fission gases will be released at the maximum temperature expected for the reference design fuel element. The precise knowledge of the amount of fission gas released is important, because an excessive release of xenon and krypton can result in high pressures within the fuel cladding which could rupture the fuel capsule. Calculations have shown that for the fuel element being considered for the GCR-2 the pressure inside the fuel capsule will always be below the external pressure of 300 psi even if the burn-ups exceed the design limit of 10,000 Mwd/T.

3.1.1 UO_2 Fabrication Studies: Uranium dioxide can be made by many methods, each of which produces an oxide with individual characteristics which make the material more or less suited for the fabrication of high density fuel slugs. Fluffy, fine-grained oxides which are made from uranium compounds precipitated from a uranyl salt solution followed by reduction to UO_2 at low temperatures are characterized by small imperfectly formed crystallites, a large surface-to-volume ratio, low bulk and packing density, a moderate-to-high oxygen-to-uranium ratio for UO_2, and a color which ranges from very light brown to olive drab. Oxides of this type are well suited to the usual ceramic fabrication processes for forming and sintering bulk UO_2 shapes such as slugs, plates, rods, and tubes.

The dense, coarse-grained oxides are made by heating either UO_2 or a uranium compound at very high temperatures in a protective atmosphere. Oxides of this type are characterized by very dense, well-agglomerated particles which can range in size from several microns to large massive chunks; surface-to-volume ratio is low, bulk and packing density are high, oxygen-to-uranium ratio is generally close to stoichiometric, the color ranges from dark brown to black, and the grains are very free-flowing, dense, hard, and unreactive. Oxides of this type are well suited for use in matrix-type fuel elements, but are poorly suited to fabricating bulk UO_2 shapes.

Many types of UO_2 exist between the two described, but in general, none of them are well suited for use in matrix-type fuel elements or for fabrication by the usual ceramic techniques. Densities of the order of 95% of theoretical can be achieved with almost any type of UO_2 if the as-received material is suitably prepared and fabricated; however, the preparation and fabrication processes become complicated, time-consuming, and costly, when one is trying to achieve high densities from a type of UO_2 which is entirely unsuited to fabricating bulk shapes. Fused UO_2, as dense and inert a type of the oxide as can be obtained, has been fabricated into rods of 94% of theoretical density, but this density was difficult to achieve. The material had to be reduced by milling to an extremely fine particle size and compacted by isostatic pressing to achieve a sufficiently high green density to produce the required sintered density. Such processes are inherently too expensive.

The vast differences in fabricability of different oxides is illustrated in Fig. 3.2, showing two types of oxide, both derived from ammonium diuranate, as the granulated powder, the green compact and the sintered piece. The oxide at the top is fluffy and fine-grained, and is well suited to the usual fabrication processes. It was cold pressed at 10 tsi in a steel die to a density of 40% and sintered to 93% of theoretical density. Shrinkage was very large (58%) but uniform, so that the piece retained its shape; the hour-glass effect resulted in a diametral difference of about one mil.

The oxide at the bottom of Fig. 3.2 was fabricated by the same procedure, but is completely unsuited to this process. Its green density is 58%, but the final sintered density is only 67%. Fabrication of suitable pieces from this oxide would require reduction of particle size by milling and use of high-compacting pressures.

In general, the dense coarse-grained oxides can be produced more economically than the fluffy fine-grained oxides so that if one desires a high density slug, he is faced with the choice of using an expensive oxide which may be fabricated cheaply or a low-cost oxide which entails expensive fabrication costs. With the present technology the latter approach is

UNCLASSIFIED
PHOTO 30287

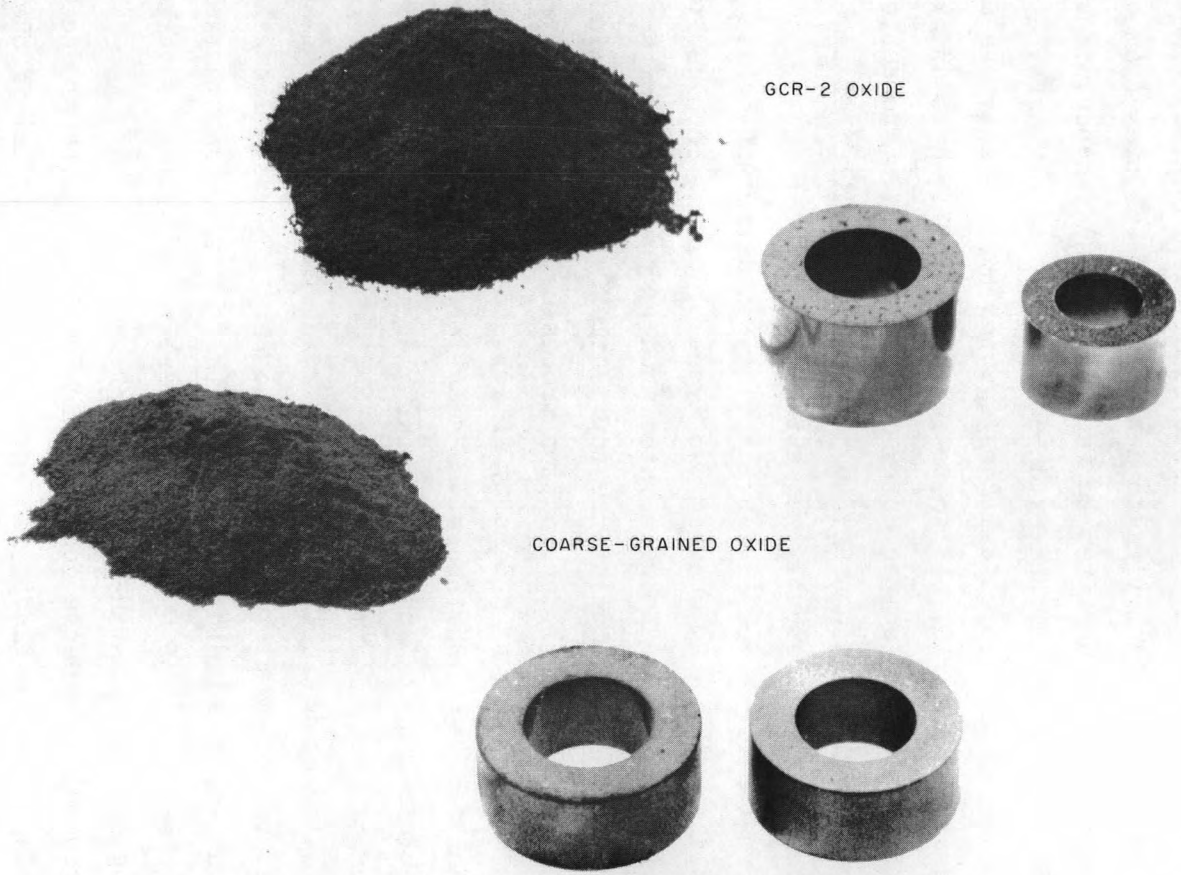

Fig. 3.2. Two Types of UO_2 Derived from Ammonium Diuranate and Fabricated by the Same Process. Each unit shown weighs 25 g.

slightly more economical. However, since it is felt that the maximum reduction of fabrication costs for the dense grades of UO_2 has already been achieved, whereas a significant reduction in the production costs of the fluffy, fine-grained oxides should be attainable, the UO_2 selected for the GCR-2 was the fluffy, fine-grained type, shown at the top of Fig. 3.2.

The present method for producing the fluffy, fine-grained UO_2 has been discussed in detail by Curtis and Johnson.[18] Uranium hexafluoride is reduced to uranium metal with calcium. The metal is dissolved in nitric acid to form uranyl nitrate, and then precipitated as ammonium diuranate by the addition of ammonium hydroxide. This diuranate cake is dried and converted to UO_2 by reduction in hydrogen at 800°C. The excellent properties arise from the extremely fine particle size of the rapidly precipitated ammonium diuranate.

A sizeable reduction in the cost of fine-grained UO_2 would result from the elimination of the step wherein UF_4 is reduced to uranium metal. A process which has been proposed for doing this is shown in Fig. 3.3. In this process the UF_6 is dissolved in water to form UO_2F_2. Upon the addition of ammonium hydroxide insoluble ammonium diuranate forms. Unfortunately, the presence of the fluoride ion affects the nature of the precipitate particle size so that further development work on this process will be required before the desired material will be obtained. The development work being planned is described elsewhere in this report.

The fabrication method for UO_2 slugs from fluffy, fine-grained oxide is also illustrated in Fig. 3.3. The as-received UO_2 is compacted at low pressures in a steel die, and the briquet is broken through a screen to produce granulated powder. The granulated powder is cold-pressed dry with a pressure of 11 tsi and sintered in hydrogen for one hour at 1750°C. This process will produce a slug with a density in excess of 94% of theoretical. For comparison, Fig. 3.4 shows the steps required to fabricate slugs for the PWR from dense, coarse-grained UO_2.[19]

---

[18] J. R. Johnson and C. E. Curtis, "The Technology of UO_2 and ThO_2," Proceedings of the International Conference on the Peaceful Uses of Atomic Energy, 9, 169 (1956).

[19] T. J. Burke, J. Glatter, H. R. Hoge, and B. E. Schaner, "Fabrication of High-Density Uranium Dioxide Fuel Elements for the First Pressurized Water Reactor Core," Nuclear Metallurgy, 4, AIME, 135 (1957).

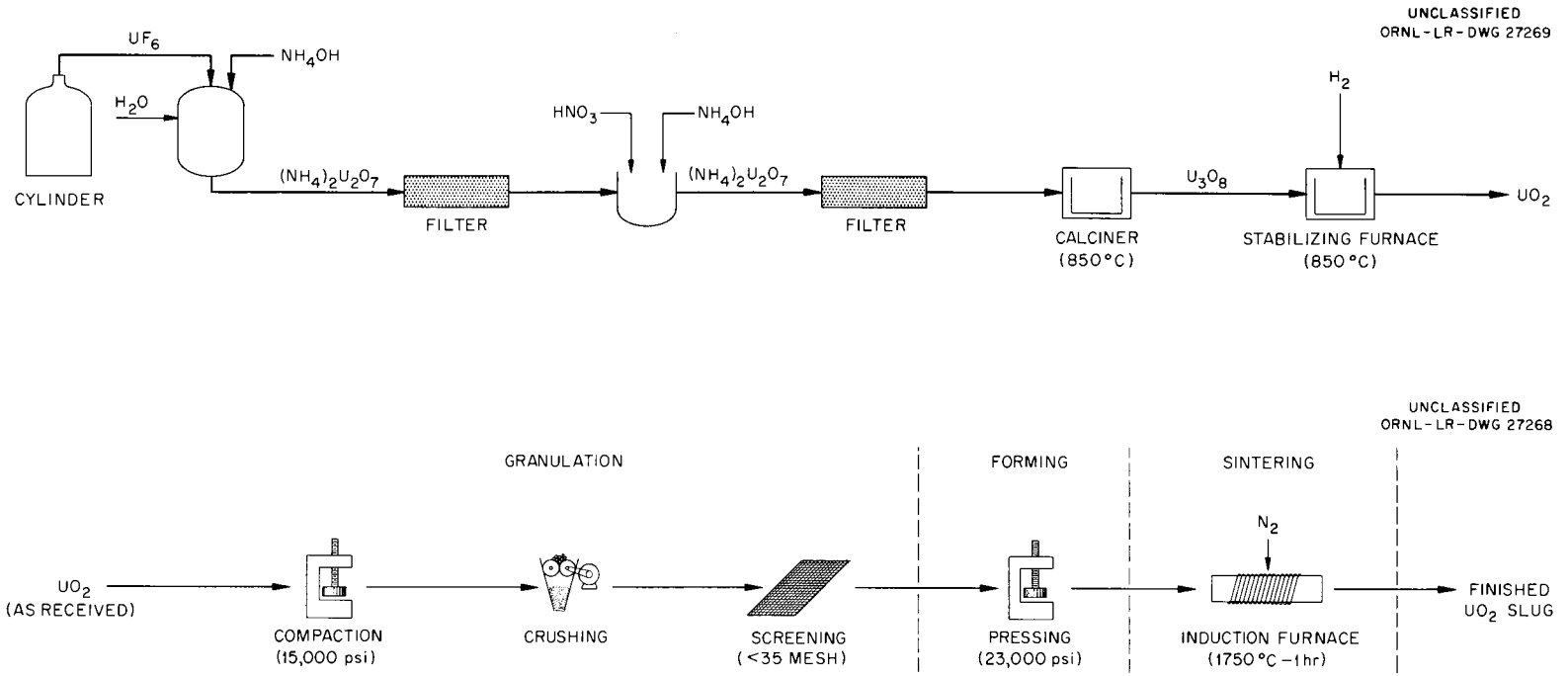

Fig. 3.3. Proposed Flow Sheet for Producing UO_2 from UF_6 for GCR-2 and Fabrication Process Proposed for GCR-2 Fuel.

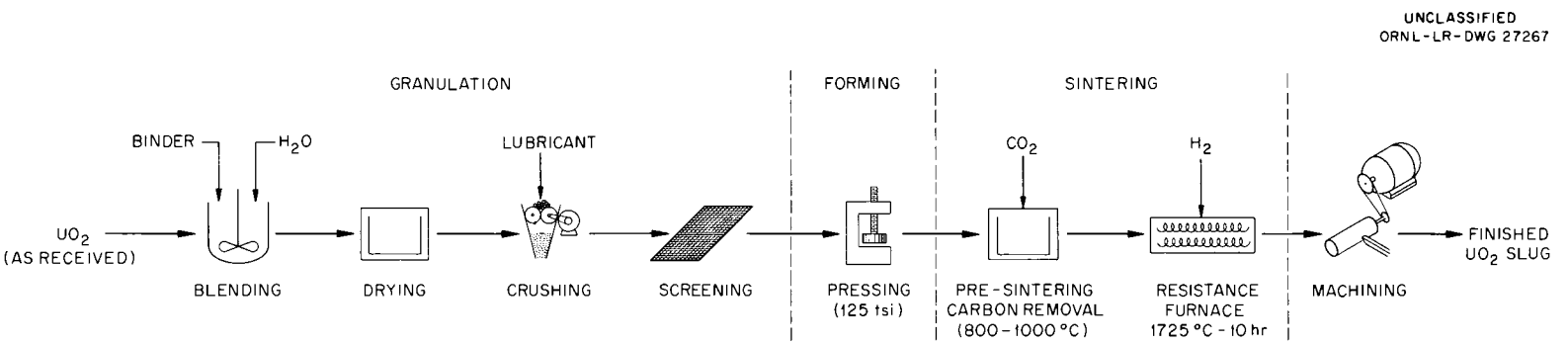

Fig. 3.4. Fabrication Process for UO_2 of a Different Type Than That Selected for GCR-2.

To reduce costs further an attempt is being made to eliminate the grinding operation usually given sintered slugs to attain the necessary dimensional tolerances. This goal can be achieved by a combination of three techniques; (1) relax tolerances, (2) maintain the length/diameter ratio < 1 so that a minimum of hour-glassing will occur, and (3) control process variables so that a highly reproducible product can be attained. Further development work will be required before this objective can be met. The fabrication study to date indicates quite positively that on a limited scale the UO_2 selected for the GCR-2 can be fabricated to the specified density and tolerances with a minimum of operations and with simplified equipment. This should definitely tend to hold the fuel fabrication costs to a reasonable value.

3.2 Selection of the Capsule Material

The material to be used for the capsule material has to fulfill the following criteria:

1. Compatibility with UO_2
2. Compatibility with contaminated helium (non-radioactive gaseous contaminants)
3. Adequate strength at the operating temperatures
4. Ability to retain fission products
5. Lowest possible cross section
6. Good fabricability
7. Low cost

A study of the materials which might meet these criteria quickly showed that two alternatives were possible. The first would be to use one of the low-cross section materials: aluminum, magnesium, beryllium, or zirconium, and adjust the maximum temperature so that the other criteria would be met. Zirconium had to be discarded from consideration because it would be rapidly embrittled by the contaminants in the helium. Beryllium was eliminated from consideration for a first reactor because the present fabrication technology is inadequate as a basis for a reactor design. Thus, the maximum temperature which could be sustained by the possible capsule materials is no higher than $\sim 900°F$, because aluminum and magnesium have very low strengths above this temperature.

The second approach considered was to select a material which could be used at much higher temperatures and accept the unfavorable absorption cross section which this choice entailed. On this basis the austenitic stainless steels appeared to be the most suitable materials because of their low cost, good high-temperature strength, good fabricability, excellent compatibility with UO_2, and generally excellent corrosion resistance. Of the austenitic stainless steels, type 304 (18 wt % Cr, 8 wt % Ni, 2 wt % Mn max, 0.08 wt % C max) appeared to be superior for the following reasons:

1. It contains the lowest amount of nickel; this is important from the standpoints of cost and neutron absorption cross section.
2. It does not exhibit the instability, i.e., sigma phase formation, typical of types 310 and 316 steels after prolonged heating.
3. It does not exhibit catastrophic oxidation as does type 316.
4. It is cheaper than other candidates.
5. It is easy to weld and fabricate.

Calculations based on the creep strength of type 304 stainless steel show that, for the reference design fuel element, a 0.020-in. cladding can sustain the load imposed by the fuel for times in excess of the expected life of the fuel (7 yr) at 1250°F, even if transient temperatures up to 1500°F were experienced. The creep-strength values on which these calculations were based are shown in Fig. 3.5.[20,21]

The analysis shows that the advantages of high-temperature operation more than offset the economic penalties imposed by the required additional enrichment. Thus, type 304 stainless steel was selected as the capsule material. In the above comparison, only commercially available materials were considered because of the early date proposed for the completion of

---

[20] "Armco 304 and 304L, Filing Code: SS-55 Stainless Steel," Alloy Digest, (May, 1957).

[21] Steel for Elevated Temperature Service, United States Steel Company, USS Pub. No. ADV-18566, 60 (1952).

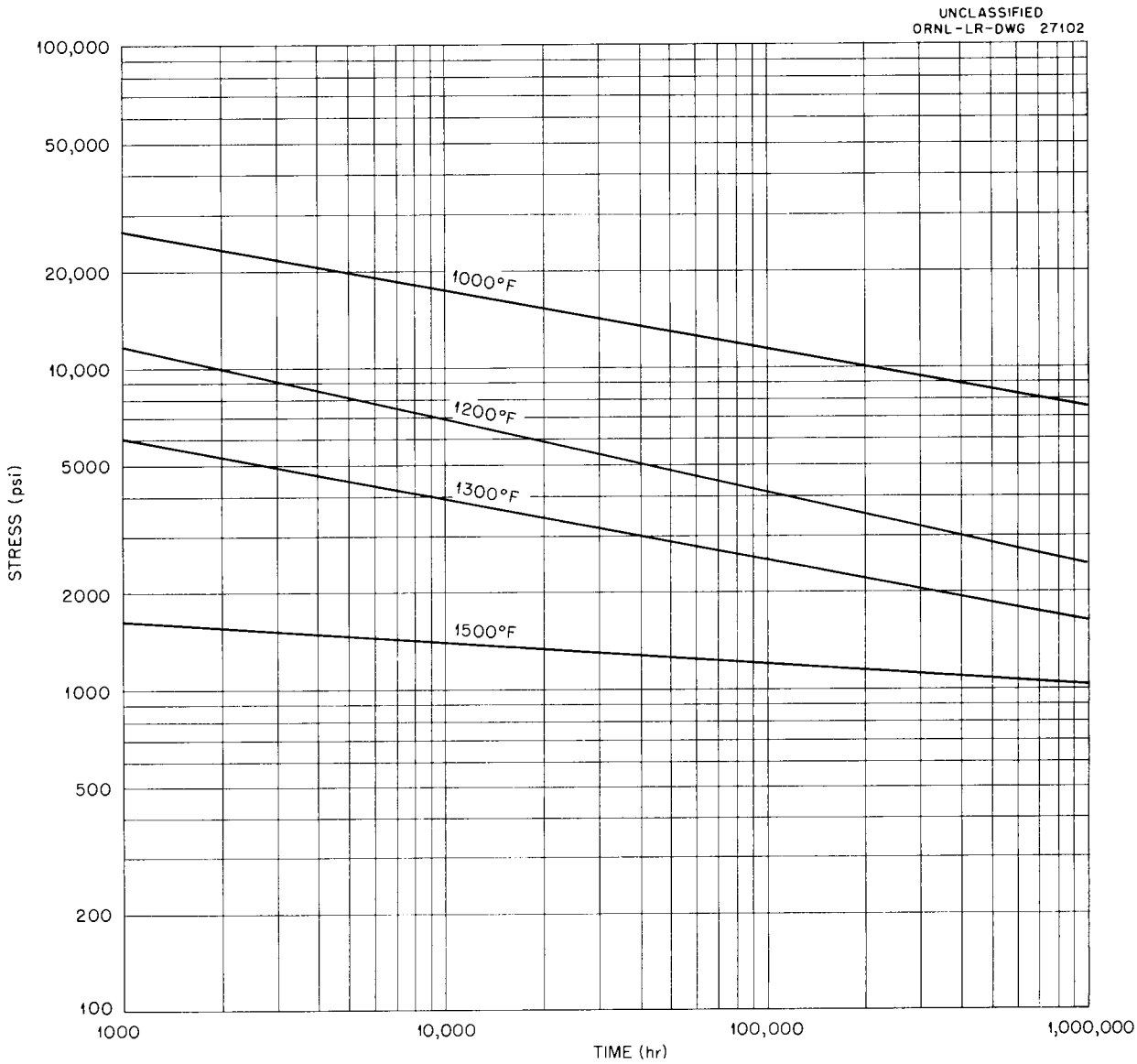

Fig. 3.5. Time for 1% Strain of Type 304 Stainless Steel.

a gas-cooled prototype reactor. The research and development program required to develop potentially superior materials such as beryllium, impervious graphite, ceramic claddings, or iron-aluminum alloys is described later in this report.

Certain questions remain unanswered about the applicability of type 304 stainless steel for the capsule material. The most important of these is whether or not carburization or preferential chromium oxidation will occur in the stainless steel through an interaction with the contaminants in the helium coolant. Contaminants such as O_2 and H_2O, which arise from outgassing of the graphite and possibly insufficient purging, will react with graphite to form CO, CO_2, H_2, and hydrocarbons. The capsule material may be selectively oxidized, carburized, or decarburized by such gases. Nickel-base alloys containing chromium are subject to a poorly understood form of internal oxidation termed "green rot" so-called because the Cr_2O_3 which forms below the surface of the metal has a characteristic green color. Copson and Lang[22] have shown that one type of green rot can be caused by exposure to CO. If carburization occurs, it may affect the mechanical properties of type 304 stainless steel by reacting with the chromium in the alloy to form chromium carbides. These carbides would be expected to increase the creep strength of the material and lower the ductility. The loss in ductility could presumably result in brittle fatigue-type failures. The precipitation of equilibrium phases, ferrite and possibly sigma, following prolonged aging at the temperatures of the reactor core may also result in a low ductility. It would be of great advantage to establish the limiting conditions for this type of behavior in the stainless steels. The necessary experimental work to establish the limiting conditions for the internal oxidation of stainless steels will be described later.

---

[22] H. R. Copson and F. S. Lang, Some Experiments on Internal "Green-Rot" Oxidation of Nickel-Chromium Alloys, The International Nickel Company, Inc., Research Laboratory, TP: No. 277, Submitted for publication in Corrosion, (January, 1958).

3.3 Selection of Gas Coolant

In evaluating the various gases for possible use as the coolant in GCR-2, it was assumed that graphite would be the moderator, and further, that the coolant gas would be in direct contact with a very extensive surface of the graphite at temperatures as high as 565°C so that compatibility of the gas with graphite is one of the prime requisites of the coolant. From the engineering standpoint, the characteristics of principal importance in a reactor of this type appear to be the heat transfer coefficient and the pumping horsepower of the various gases. Hydrogen is by far the best coolant based on these criteria while carbon dioxide and helium, being inferior to hydrogen in these properties are nevertheless to be given serious consideration. Other gases, such as argon, nitrogen, and carbon monoxide having heat transfer properties inferior to those of carbon dioxide and helium, will not be given further consideration. Factors other than the heat-transfer properties of the three gases, hydrogen, helium, and carbon dioxide, which must be considered in evaluating the potentials of these gases as the coolant include safety, cost, availability, purity, thermal and irradiation stability. A comparison of these factors is given in Table 3.2.

Hydrogen possesses superior heat transfer properties and favorable nuclear properties. It is cheap and readily available at high purity. Some disadvantages of its use include inflammability, diffusion through metals, metal embrittlement, and chemical reactivity at elevated temperatures.

Operation of the CO_2-cooled Calder Hall reactors indicate that CO_2 is a suitable coolant at temperatures up to 400°C. The projected temperatures for the GCR-2 (600–700°C or higher) would probably result in serious interaction of carbon dioxide at 300 psi with reactor components. The reaction $C + CO_2 \rightleftarrows 2CO$ would occur at these temperatures resulting in a burnout of graphite in the hot region and a deposition of soot on the cold heat exchanger surfaces which would cause a decrease in the heat-transfer rate. Carbon dioxide attack on the pressure vessel is another

TABLE 3.2. SOME CHARACTERISTICS OF SELECTED POTENTIAL GASEOUS COOLANTS

	ρ, Density (g/cm^3)	C_p, Specific Heat (cal/g·°C)	μ, Viscosity (g/cm·sec)	k, Thermal Conductivity (cal/sec·cm·°C)	ρC_p, Volumetric Specific Heat ($cal/cm^3 \cdot °C$)	Pumping Power Index*	Cooling Efficiency Index**	σ_T, Thermal Neutron Absorption Cross Section (barns/nucleus)	Induced Activity	Approximate Loss in Reactivity	Chemical Activity (Corrosion)	Radiation Stability
Hydrogen (1 atm)	6.6×10^{-5}	3.43	10^{-4}	5.33×10^{-4}	2.26×10^{-4}	4.4×10^{6}	17.5×10^{-8}	0.33	None	0.0007	?	
Helium (1 atm)	1.4×10^{-4}	1.25	2.2×10^{-4}	4.0×10^{-4}	1.75×10^{-4}	2.09×10^{7}	3.83×10^{-8}	~ 0	H^3; 0.018-Mev β	0	Inert	
Air (1 atm)	9.5×10^{-4}	0.240	2.1×10^{-4}	7.57×10^{-5}	2.28×10^{-4}	6.28×10^{7}	1.25×10^{-8}	1.5	N^{16}; 7.3 s, 6-Mev γ A^{41}; 1.8 h, 1.4-Mev γ	0.003	Oxidizing	
Carbon Dioxide (1 atm)	1.5×10^{-3}	0.218	1.8×10^{-4}	5.0×10^{-5}	3.27×10^{-4}	3.7×10^{7}	2.34×10^{-8}	0.003	N^{16}; 7.3 s, 6-Mev γ	0	Oxidizing	Some dissociation

* $\dfrac{\mu}{p^2 C_p^2 k\ (C_p \mu / k)\ 0.4}$ (lowest is best).

** $\rho^2 C_p^3$ (highest is best).

possible source of trouble as is corrosion of the fuel element capsule.

The outstanding advantage of helium is its chemical inertness. Pure helium would produce no corrosion problems even at elevated temperatures. In practice, the contamination of the helium by small quantities of water vapor, carbon dioxide, carbon monoxide, and hydrogen would lead to some attack on the reactor components which would not be serious unless the concentrations of the contaminants build up significantly. This could be controlled by a suitable gas-purification system. The principal disadvantage of using helium arises from its high cost. Whether or not this is an important factor in the over-all cost of the power produced will depend primarily on the leak rate of the system.

Helium appears to be the most suitable gas coolant available for the GCR-2 from the materials point of view. Future work may show that hydrogen is suitable. It seems unlikely that carbon dioxide is suitable at these temperatures if graphite is to be used as the moderator.

3.3.1 Contamination Problems: The components of a helium-cooled reactor should, in principle, show no deterioration in any property through coolant-induced chemical reactions during operation. This ideal situation will not be obtained in practice since the coolant helium will, at best, bear traces of gaseous as well as particulate impurities. The gaseous impurities arise from the following sources:

1. Impurities introduced with the He.
2. Air leakage into the system (a) during operation and (b) during shutdown for reloading or moving fuel.
3. Leakage of water (steam) into system as consequence of minor defects in heat exchanger (boiler), cooling system for canned motors and/or possible cooling system for side-stream purification of gas.
4. Leakage of oil and oil vapors into the system from motor and shaft lubrication systems, possible valve packings, etc.
5. Transmutation reactions.
6. Introduction into coolant gas of metal from fuel element cladding as consequence of bombardment with fast neutrons.

7. Evolution of fission products from fissionable material as tramp impurities in outer surface of fuel element cladding.
8. Leakage of fission products from minor defects in the fuel element cladding.
9. Evolution of absorbed gases from valve packings, electrical insulation, and numerous similar small sources as well as evolution of adsorbed gases from metal surfaces of system.
10. Evolution of absorbed gases from the graphite moderator matrix.

If no deliberate attempt is made to remove these contaminants, the mechanisms for their elimination from the system are few in number. They include:

1. Leakage from the system at a slow rate along with the He.
2. Transmutation and/or radioactive decay.
3. Reaction with reactor components.

It is reasonable to expect that fuel elements clad with 20 mils of 304 stainless steel will survive in this atmosphere at surface temperatures of 1250°F (with hot spot maxima at 1500°F) for five to seven years. Further, it is expected that the graphite matrix and other components of the assembly will have a lifetime of about twenty years. It is, accordingly, necessary to assess carefully the degree of contamination expected in order to guarantee these component lifetimes.

3.3.2 Degassing of Graphite: The principle source of gaseous impurities is the graphite matrix. Contamination from this source overshadows all other likely sources with the possible exception of in-leakage steam through heat exchanger defects. The quantity of sorbed gases in graphite depends upon the conditions of graphitization, purification, gases present during cooling, and probably most important of all, the handling and storage conditions to which the graphite is subjected between manufacture and the completion of stacking in the reactor. The rate of evolution of the sorbed gases is determined by the temperature and the partial pressures of the evolved gases over the graphite. The temperature also controls the composition of the gas mixture evolved.

The volume of gases evolved upon heating at 1800°C may be as low as 0.02 cc/g if adequate precautions, such as wrapping in aluminum foil, are taken. It is assumed, however, that the graphite in this reactor will have been exposed to ambient atmosphere for six months or longer and therefore, will evolve many times this volume of gases upon being heated to operating temperature. British[23] experience suggests that the water content may be as high as 0.4 lb/t. The equilibrium water content, estimated at 0.8 lb/t, probably will not be attained despite the long storage period. Thus, it is estimated that the graphite stack will contain 400–800 lb of water. If provision is made for heating the graphite stack prior to start-up, part of the water can be removed by a combination of heat and a flow of dry gas or reduction of pressure. Alternatively, a very slow increase in power at start-up can be utilized. Such treatment might reduce the water content to 100–200 lb. The remaining water would react with the graphite to form CO and CO_2 at a fairly rapid rate after start-up. In addition to the water and nitrogen which are evolved readily below 500°C, sorbed gases amounting to 0.05–0.15 cc/g are retained more tenaciously by the graphite and slowly evolved at 500–600°C. The gas mixture evolved contains principally CO_2 and small quantities of CO, N_2, and H_2O. The CO_2 probably arises from chemisorbed oxygen and water reacting with the graphite. The rate at which these sorbed gases are evolved is strongly temperature dependent, being rapid at 1800°C, and is probably mainly determined by the diffusion rates of the gases through the graphite. The evolution of CO_2 at 500°C might be balanced by the pure helium added to compensate for leakage out of the system. The projected leak rate of 0.1 to 1% per day, however, does not appear adequate from this point of view and a build-up of CO_2 is likely in the early stages of operation at power. It is estimated that as much as 200 lb of CO_2 could be added to the coolant in this manner.

---

[23] R. V. Moore, "The Design of Construction of the Plant," J. British Nuclear Energy Conference, 2, No. 2, 64 (April, 1957).

This quantity, plus that arising from the reaction of the water present in the helium with the graphite might lead to as much as 0.5 vol % of CO_2 in the helium. This corresponds to a burn-up of approximately 70 kg of graphite which is less than 0.01%.

3.3.3 Carbon Mass Transfer: The presence of the contaminants in the helium gas presents two major problems. The first is the possible interactions between the contaminants and the fuel capsule material. This has already been discussed. The second problem which must be considered is the mass transfer of carbon by the following reactions:

$$C + CO_2 \rightleftarrows 2CO \tag{3.1}$$

$$C + O_2 \rightleftarrows CO_2 \tag{3.2}$$

$$C + H_2O \rightleftarrows CO + H_2 \tag{3.3}$$

$$C + 2H_2O \rightleftarrows CO_2 + 2H_2 \tag{3.4}$$

In addition to these graphite-gas reactions, the following reaction will occur in the gas phase:

$$CO_2 + H_2 \rightleftarrows CO + H_2O \tag{3.5}$$

It is not possible to make accurate predictions of concentrations of the various gases at the steady-state condition since chemical equilibrium is not expected to prevail in such a complex system under irradiation. The hydrogen concentration is expected to be very low. It is anticipated that the concentration of carbon dioxide will be considerably higher than that of the other contaminants and that the carbon monoxide concentration will be equal to, or probably greater than, the equilibrium concentration corresponding to reaction.

Although the amount of graphite burnout due to the reaction $C + CO_2 \rightleftarrows 2CO$ is not expected to have any important effect on the mechanical properties of the graphite, the temperature gradients present in the reactor will produce some movement of carbon by a shift in the chemical equilibrium.

Some removal of carbon from the area of the higher graphite temperatures and a deposition of soot on the cooler graphite surfaces will very likely occur. In addition, deposition of soot on the cooler heat exchanger surfaces is expected. Deposition in this region could have an adverse effect on the heat transfer and flow properties of the system. No significant deposition of soot on the metal canning material is anticipated since these metal surfaces will be at the maximum temperature prevailing in the reactor. An experimental program will be required to determine what impurity levels will be found in the GCR-2 and the effects of these contaminants on their environment.

A gas-purification system will very likely be required to remove the substantial quantities of contaminants that will be introduced into the helium during the start-up and early stages of operation. After the concentration of the contaminants is reduced to the desired level, operation of the purification system may be put on an intermittent basis or eliminated entirely, depending on the rate of evolution of gases from the graphite, the leak rate of the reactor, and the steam pickup from the heat exchangers. This can be determined from periodic measurements of the CO_2 and water content. The desirability of tritium removal may dictate continuous operation of the purification system.

The proposed purification system will be able to maintain the concentration of H_2O, CO_2, CO and H_2 at or less than 0.01 vol % after the large quantities released in the early stages of operation have been removed from the coolant. This concentration is equivalent to the following quantities present in the helium: H_2O-5 lb, CO_2-12 lb, CO-8 lb, and H_2-0.5 lb. The dew point of the coolant is -21°C at pressure with 0.01 vol % of water present.

3.4 Selection of Materials for Pressure Vessel

Design and construction of the GCR-2 pressure vessel should proceed according to the ASME Boiler Code. Section VIII of the ASME Boiler Code covers the construction of unfired pressure vessels. In order to calculate the required thickness of a spherical shell under internal pressure, Par. UG-27 (d) specifies the formula:

$$t = \frac{PR}{2SE - 0.2P}$$

where

t = minimum required thickness of shell plates, exclusive of corrosion allowance, in inches.

P = design pressure, in pounds per square inch.

R = inside radius of the core shell under consideration, before corrosion allowance is added, in inches.

S = maximum allowable stress value, in pounds per square inch.

E = joint efficiency.

For double-welded butt joints, which will be used in the construction of the GCR vessel, joint efficiencies ranging from 80 to 95% are specified. Neither radiography nor stress relief are required, with a joint efficiency of 80%, while an efficiency of 95% requires both.

The selection of applicable steels was based on the material presented in Table UCS-23, which is shown herein in abridged form as Table 3.3. Note that t_{max} gives the maximum thickness in inches that the Code will allow for a given material to be used in pressure vessel construction. Since preliminary indications were that the shell thickness would probably be somewhat greater than two inches, only those steels whose t_{max} was greater than two inches were selected. For any steel, a maximum thickness of three inches was arbitrarily set as a field-erection limit. The experience of heavy construction firms shows this to be a reasonable figure, and it is generally felt that great difficulties would be encountered in field erection of vessels more than 3-1/2-in. thick.

Using the shell thickness formula given above, and the stress values from Table 3.3, curves of t vs PR were plotted for the various steels which give various compatible combinations of design pressure and vessel size. Figure 3.6 shows such curves for a maximum metal temperature of 650°F and a joint efficiency of 95%. The design point for a 50-ft-dia sphere with a 300 psi internal pressure is at a PR value of 90,000.

Figure 3.6 shows that for PR of 90,000, the usable materials are: T-1, SA302B, SA203C, SA204C, SA225B, SA302A, SA225A, SA212B, SA203B, SA203E, SA204B, SA301A, SA212A, SA203A, SA203D, SA204A, and by going to a thickness slightly greater than 3 in., SA201B and SA301E.

TABLE 3.3

MAXIMUM ALLOWABLE STRESS VALUES IN TENSION FOR CARBON AND LOW-ALLOY STEEL, IN POUNDS PER SQUARE INCH*

Material and Spec. No.	Grade	Nominal Composition	t_{max}	Spec. Min. Tensile	For Metal Temperatures Not Exceeding °F -20 to 650	800	950
PLATE STEELS							
Carbon Steels							
SA-201	A	C-Si	12	55000	13750	10200	4500
SA-201	B	C-Si	8	60000	15000	10800	4500
SA-212	A	C-Si	6	65000	16250	11400	4500
SA-212	B	C-Si	6	70000	17500	12000	4500
Low-Alloy Steels							
SA-203	A,D	2-1/2 and 3-1/2 Ni	4	65000	16250	11400	4500
SA-203	B,E	2-1/2 and 3-1/2 Ni	4	70000	17500	12000	4500
SA-203	C	2-1/2 Ni	4	75000	18750	12600	4500
SA-204	A	C-1/2 Mo	6	65000	16250	15650	10000
SA-204	B	C-1/2 Mo	6	70000	17500	16900	10000
SA-204	C	C-1/2 Mo	4	75000	18750	18000	10000
SA-225	A	Mn-V	4	70000	17500	--	--
SA-225	B	Mn-V	4	75000	18750	--	--
SA-301	A	1/2 Cr - 1/2 Mo	6	65000	16250	15650	10000
SA-301	B	1 Cr - 1/2 Mo	6	60000	15000	14750	11000
SA-302	A	Mn - 1/2 Mo	4	75000	18750	18000	10000
SA-302	B	Mn - 1/2 Mo	4	80000	20000	19100	10000
Quenched and Tempered Steel							
T-1		Mn-Ni-Cr-Mo-V	2	105000	26250	--	--

*ASME Code Section VIII, 1956.

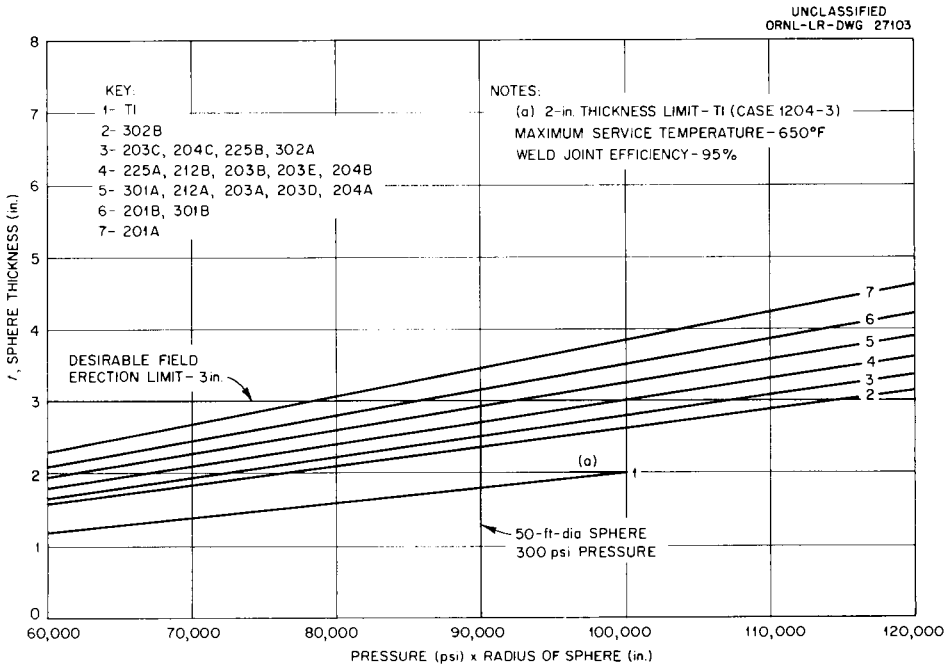

Fig. 3.6. ASTM Pressure Vessel Steels.

In order to illustrate the change in thickness requirements with temperature, curves of t vs T were plotted for the steels under consideration (Fig. 3.7). The thickness values at 650°F hold without change to -20°F. The limiting conditions for Fig. 3.7 were taken to be: PR = 90,000; joint efficiency = 80%. Whereas, the carbon and lower alloy grade steels lose their strength very rapidly as the temperature increases, the low-alloy steels represented by curves 6 through 10 retain their strengths to a higher temperature, but beyond 775°F they too begin to weaken. Thus, the advantages to be gained by keeping the pressure vessel at a temperature less than or equal to 650°F are evident. The same conclusions are valid for vessels having 95% weld-joint efficiency.

The use of high-strength steels for pressure vessel construction has been under study by the Pressure Vessel Research Committee of the Welding Research Council, and the results of these studies have been reported in the Welding Journal of the American Welding Society.[24] The data in Table 3.3 and Fig. 3.6 show several steels with tensile strengths in excess of that typical of the carbon steels, SA201 and SA212. These stronger materials are approved for pressure vessel fabrication, but unfortunately, relatively little service information for them is presently available.

Since the GCR-2 pressure vessel will be wholly of welded construction, a factor of prime importance in the selection of a pressure vessel material is weldability. In their comparison[25] of six high-strength steels with SA201, Stout and Gross investigated the welding characteristics of the materials. The findings of the study indicated that the cracking tendency of the high-strength steels was somewhat greater than that of SA201, and that a more careful control of welding variables is necessary for the high-strength steels. A. P. Bunk[26,27] has reported similar results on the weldability of the high-strength steels. His observations showed that

---

[24] R. D. Stout and J. H. Gross, "The Performance of High-Strength Pressure Vessel Steels," The Welding Journal, 35, No. 3, 115-s (March, 1956).

[25] Ibid

[26] A. P. Bunk, "Welding Procedure Qualification Tests for Six High-Yield Strength Steels," The Welding Journal, 34, No. 4, 197s (April, 1955).

[27] A. P. Bunk, "Welding of High-Strength Pressure Vessel Steels in Heavy Sections," The Welding Journal, 36, No. 2, 62s (February, 1957).

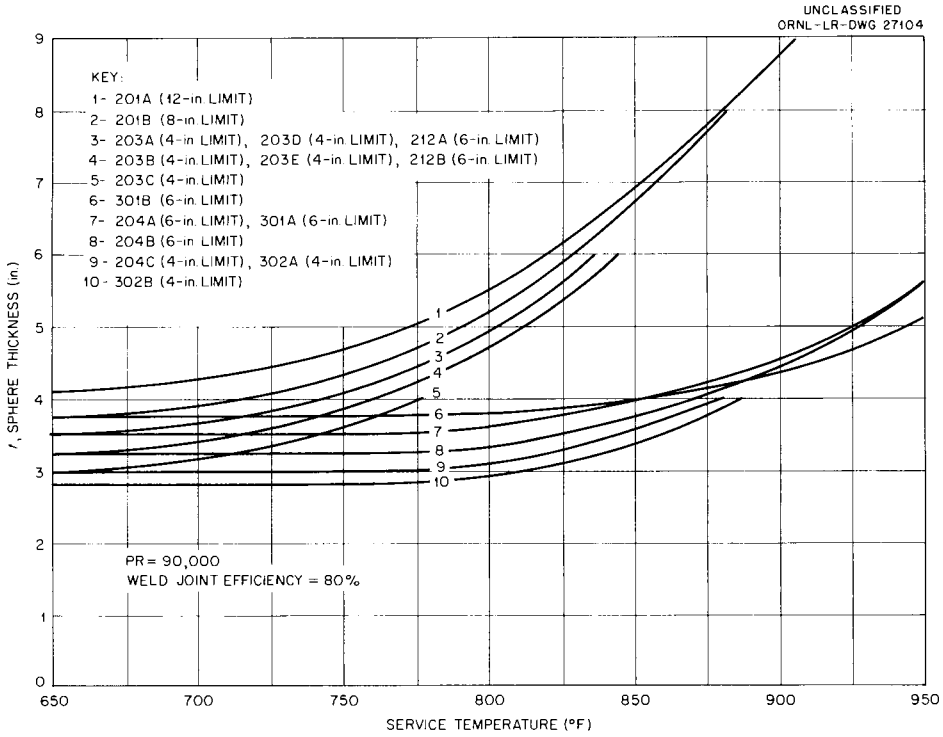

Fig. 3.7. Effect of Service Temperature on Thickness Requirements of ASTM Pressure Vessel Steels.

SA201, Grade A, steel in a 4-in. thickness met all the requirements of the ASME code when welded with E7016 electrodes, and subsequently stress relieved. On the other hand, tests on 4-in.-thick SA302, Grade B, indicated that a 300°F preheat was necessary to avoid cracking.

Bunk's work included a study of the behavior of a quenched and tempered steel corresponding to the T-1 designation. This material was satisfactorily welded in 4-in. thicknesses with E12016 (Ni-Mo-V) electrodes, with or without the use of preheat. Unfortunately, in order to realize 95% joint efficiency the Code requires stress relieving which causes the weld deposit from an E12016 electrode to embrittle as a result of its vanadium content. Consequently, E9015 electrodes were used in studies of stress-relieved welds. When these welds were made without preheat, some slight tendency toward cracking was noticed, but the use of preheat insured crack-free welds. In an account[28] of the construction of two Hortonspheres in Tokyo, in which the T-1 alloy was used, P. C. Arnold pointed out that in order to produce consistently sound welds in T-1 with E11016 (vanadium-free) electrodes, a preheat was definitely necessary. The minimum preheat temperature was found to be 150°F, with an increase to 250°F for thicknesses of one inch or greater.

R. D. Stout[29] has recently investigated the properties of the high-strength steels in heavy sections. Some of his results which are applicable to this discussion are summarized in Table 3.4. It is evident that the tendency toward underbead cracking, and hence the requirement for precautionary measures and rigid control of welding procedures is substantially greater for the alloy steels.

It is now possible to make some generalizations regarding weldability, and the selection of a pressure vessel material on this basis. It has been found through experience[30] that in thicknesses greater than 1-1/2 in. all

---

[28] P. C. Arnold, "Problems Associated with the Welding of T-1 Material," The Welding Journal, 36, No. 8, 373s (August, 1957)

[29] R. D. Stout and J. H. Gross, "Properties and Weldability of High-Strength Pressure Vessel Steels in Heavy Sections," The Welding Journal, 36, No. 3, 157s (March, 1957).

[30] Chicago Bridge and Iron Company to E. A. Franco-Ferreira, Private Communication (January, 1958).

TABLE 3.4

METALLURGICAL PROPERTIES OF PRESSURE VESSEL STEELS

IN 4 INCH THICKNESSES*

Material	Yield Strength	Tensile Strength	Elongation	Underbead Cracking	Charpy V-Notch Impact	
					15 ft-lb As Rec'd	Transition Strain Aged
SA-201A	28,500 psi	55,000 psi	35%	0%	35°F	110°F
SA-302B	66,500 psi	88,000 psi	21%	30%	-70°F	-15°F
T-1	91,700 psi	105,000 psi	23%	15%	-80°F	-10°F

*R. D. Stout and J. H. Gross, "Properties and Weldability of High-Strength Pressure Vessel Steels in Heavy Sections," The Welding Journal, 36, No. 3, 157s (March, 1957).

steels must be welded with care. In addition, however, there is evidence that weldability decreases with increasing alloy content and, thus greater care would be required in the welding of the high-strength steels. The problems associated with heavier sections (plain-carbon steels) will almost certainly be overriden by the avoidance of the problems associated with decreased weldability (high-strength steels). Application of the criterion of weldability to the problem of material selection, thus argues for the choice of a plain-carbon steel, SA201 or SA212.

The extensive investigations of brittle fracture which have been carried out at the Naval Research Laboratory show that the notch toughness of a pressure vessel material is an important property. Table 3.4 indicates that the ductile-to-brittle transition temperature of a material usually decreases as its alloy content increases. In order to avoid brittle failure, it is of prime importance to operate the vessel at a temperature above its nil ductility temperature, since with the existence of a small "crack starter" brittle failure will be initiated by engineering loads at temperatures below the NDT. The plain-carbon steels, SA201 and SA212, may have their impact properties improved by being made to ASME specification SA300, "Steel Plates for Pressure Vessels for Service at Low Temperatures," a fine-grained practice. This specification requires a minimum Charpy keyhole energy of 15 ft-lb at -50°F. W. S. Pellini[31] and co-workers, however, argue that the Charpy V-notch is a more reliable test than the Charpy keyhole. P. P. Puzak[32] of NRL has pointed out that some alloy steels, including T-1, exhibit a so-called "low-energy ductile fracture." In these materials, even though the transition temperature is low, the ductile portion of the impact curve reaches a rather low value of maximum impact energy. According to Puzak, a low-energy ductile failure can be as disastrous and as easy to initiate as a brittle failure. Thus, for materials which behave this way there may be no protection in operating above the NDT.

---

[31] P. P. Puzak, M. E. Schuster, and W. S. Pellini, "Applicability of Charpy Test Data," The Welding Journal, 33, 433s (September, 1954).

[32] Naval Research Laboratory to E. A. Franco-Ferreira, Private Communication, (January, 1958).

The notch toughness of pressure vessel steels is adversely affected by neutron irradiation, as shown by Berggren and Wilson.[33] In radiation-damage tests on various steels including SA212, SA301, and T-1, the higher alloy grades showed no intrinsic advantages over the plain-carbon type. Most radiation damage data to date have been obtained on medium-carbon steels in the normalized condition (SA212, SA106, etc.) and the materials are somewhat less sensitive to adverse effects of irradiation than steels of lower carbon content, including low-carbon alloy steels. It has been shown that the deleterious effects of irradiation are minimized as the temperature of irradiation is raised. It is obvious that more data are needed regarding radiation effects on pressure vessel materials, especially weld metal.

The last column in Table 3.4 indicates the effects of strain aging on the materials. Alloy content does not appear to affect appreciably the susceptibility to strain aging. However, it is known that a fine-grained material is less sensitive to strain aging, and on this basis the relatively poor performance of the SA201 is explained by the coarse grains of that particular specimen. Thus, for the plain-carbon steels further support is given to the advisability of ordering to SA300.

Since the reactor vessel will be operated at 460°F or slightly higher, the expectation is that brittle fracture will not be a problem during operation. However, during cold start-ups after charging, and during the hydrostatic proof test required by the Code, measures must be taken to insure that engineering loads are not applied at a temperature below that which is deemed to be safe. Such a temperature will result from an accurate survey of the Charpy V-notch transition temperature of all the material in the vessel.

After consideration of the notch toughness of the available materials, it is still evident that the plain-carbon steels are a practical choice. The relative advantage of lower transition temperature possessed by the alloy steels is effectively minimized by ordering the carbon steels to

---

[33] R. G. Berggren and J. C. Wilson, Recent Data on the Effects of Neutron Irradiation on Structural Metals and Alloys, ORNL CF 56-11-1 (January 30, 1957).

SA300, and by exercising suitable precautions with regard to the operating temperature of the vessel.

An additional factor which has not yet been discussed is vendor preference as based on their experience in field pressure vessel fabrication. Personnel of a major erector have indicated[34] a preference for SA201 or SA212. They report that fabrication difficulties are significantly greater with the higher strength steels, thus minimizing the cost advantages resulting from a reduction in thickness.

It has been emphasized that the question of fittings becomes increasingly troublesome as tensile strength improves. The multiplicity of penetrations through the GCR vessel should be noted. All these penetrations must be reinforced. Such reinforcement will necessitate heavier sections for the smaller penetrations, and large forgings for the coolant inlets and outlets. The use of easily fabricated steel such as SA201 or SA212, substantially reduces the difficulties imposed by these necessary design features. Such preferences are further justified by the recent observation[35] that good design and excellent workmanship are equally as important in the life of a pressure vessel as high-notch toughness in plate materials and weld metal.

Finally, costs are an important item in optimizing the over-all economic performance of the reactor system. The basic materials costs, i.e., for unformed plate, may be shown to increase linearly with PR, as illustrated in Fig. 3.8. These costs are presented in terms of dollars per square foot of pressure vessel surface. The figures result from calculations of the weight of material required, and the valuation comes from per pound mill prices as reported in the December 5, 1957, issue of The Iron Age. As can be seen, the most suitable steel, in terms of lowest initial material cost is SA212, Grade B. It is also evident that, except for T-1, the plain-carbon grades are all consistently cheaper than the alloy steels, even though they must be used in slightly greater thickness.

---

[34] Chicago Bridge and Iron Company, Op. cit. p. 3.29.

[35] O. R. Carpenter and C. Floyd, "Heat Treatment of Carbon and Low-Alloy Pressure Vessel Steels," The Welding Journal, 36, No. 2, 67s (February, 1957).

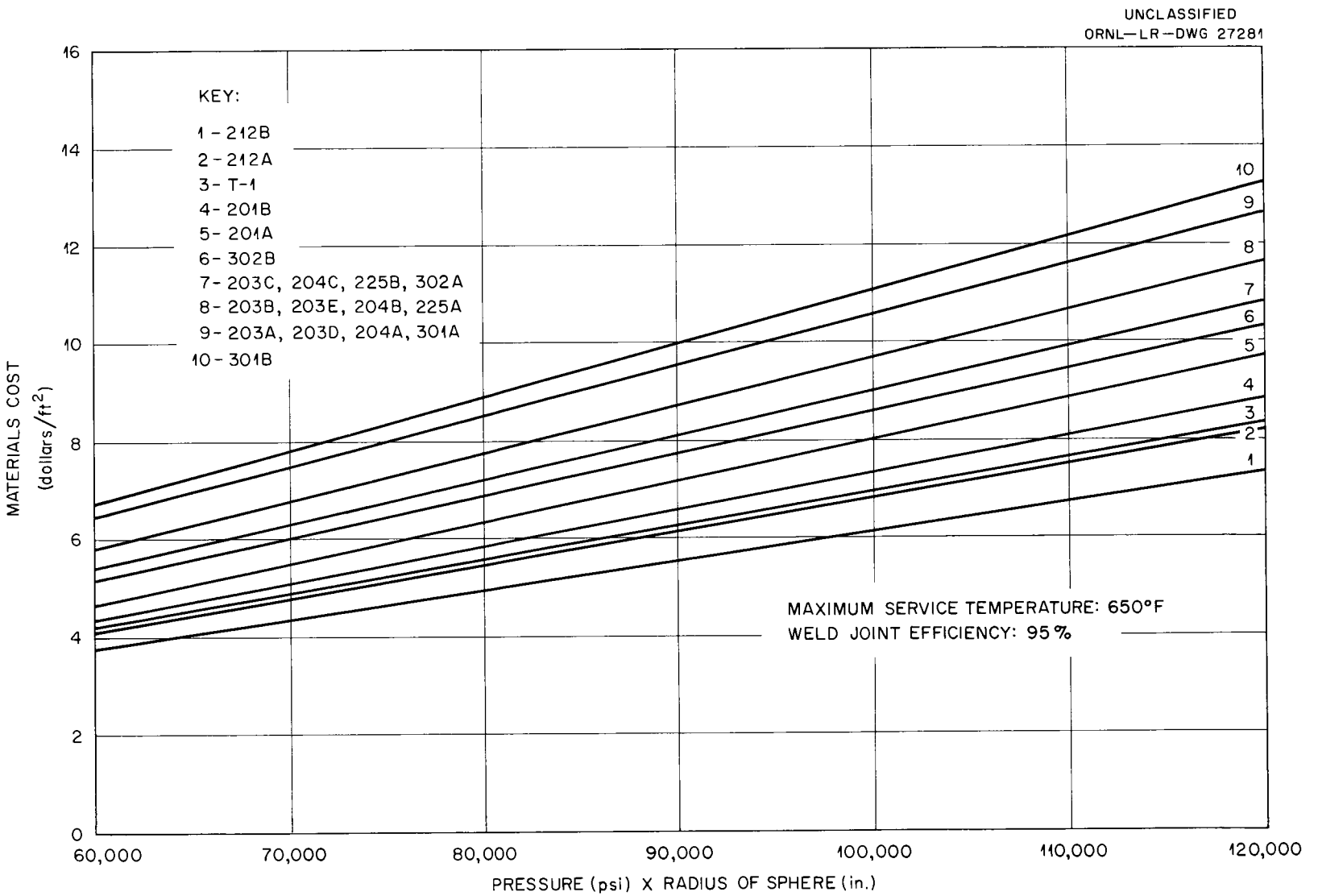

Fig. 3.8. Pressure Vessel Material Costs as a Function of Operating Conditions.

In general, welding costs increase approximately with the square of the metal thickness for thicknesses greater than 1-1/4 in. Thus, one might argue for the advantages to be gained by use of a lighter section of alloy steel. However, an inspection of Fig. 3.8 will show that the required thickness of SA212B is not substantially greater than that of some of the alloy steels, and is actually less than that required of others. It is anticipated that the over-all welding costs for the alloy steels will not benefit fully from the reduction in thickness due to the additional costs imposed by the special procedures which must be followed when welding such material.

On the strength of the foregoing analysis, SA212, Grade B, has been chosen as the material for the fabrication of the GCR-2 pressure vessel. It is felt that this choice represents the best possible compromise between the various advantages and disadvantages inherent in the array of pressure vessel materials which were considered. The cost of the pressure vessel as a function of core size and pressure level, both for spherical and cylindrical configurations, can be seen in Fig. 3.9.

3.5 Ductwork, Bellows, Valves and Pumps

Fabrication of the components (i.e., ductwork, bellows, valves and pumps) between the pressure vessel and the heat exchanger presents no unusual problems. The 60-in. dia ductwork will be fabricated from 7/8-in.-thick SA212B steel on the cold-gas side and 1-3/8-in.-thick SA387B low-alloy steel on the hot-gas side. Both the hot-gas and cold-gas legs will be suitably reinforced with stiffening ribs. Welding techniques for these thicknesses and types of steel have been developed in industry and proven satisfactory.

The bellows will be of the constant flexure-reinforced type and will be fabricated from type 347 stainless steel 0.065 in. thick. Many bellows of this type have been found reliable over long periods of service under similar operating conditions.

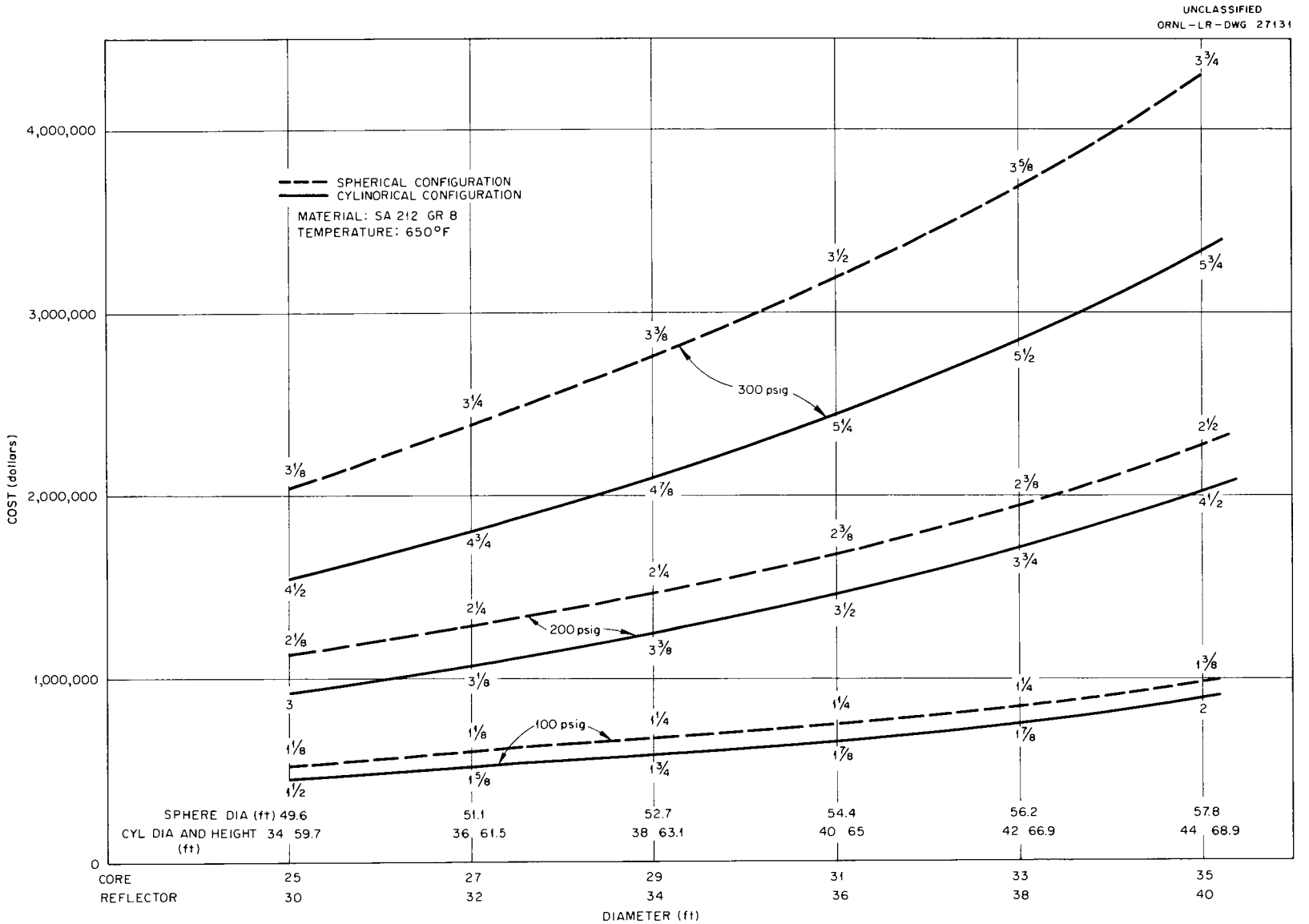

Fig. 3.9. Pressure Vessel Costs vs Core Size for Various Pressures in Spherical and Cylindrical Configurations.

Valves and pumps of this size are presently being built to withstand temperatures up to 460°F.

A problem in joining the pressure vessel to the heat exchangers will be in developing welding techniques for the dissimilar metal joints between the pressure vessel and the low-alloy hot pipes, the low-alloy hot pipes and the bellows, and the cold-steel pipes and the bellows. Investigations on weldments of this type are presently being carried out on smaller diameter thin-wall materials but no techniques on joining large-diameter heavy-wall material are presently available. To obtain reliable joints of this nature, welding techniques must be developed and proved reliable. It also would be necessary to run tests imposing the stresses, temperatures, and environments which will be encountered in service on the weld joints fabricated by the selected procedure.

3.6 Control Rod Materials

The nuclear requirements for the control rods in the GCR-2 are easily fulfilled by several materials. The only restrictions which must be considered here are those of low cost and operation at 1100°F. The rods must have sufficient effectiveness so that approximately 60 rods (one per fuel loading hole) will provide adequate control. They should also have a low-residual activity so that shielding of rods during fuel charging will not be a serious problem.

The relevant properties of a number of control materials which have been considered are summarized in Table 3.5. The important disadvantages of each which are included in Table 3.5 will be discussed more fully.

Boron dispersions or boron steels cannot be seriously considered for use because of the dimensional changes expected from high burn-up of boron and operation at the relatively high temperature.

Clad Eu_2O_3 dispersions in stainless steel and crystal-bar hafnium are too expensive to consider, though either would be a very effective control material. Hafnium sponge which is cheaper and more plentiful may warrant further consideration. Such low-purity hafnium would present fabrication problems and would require cladding.

TABLE 3.5. PROPERTIES OF POSSIBLE CONTROL MATERIALS

(Configuration Chosen to Provide 10% Δk)

Material	Configuration for 10% Δk	$\Sigma_{a_{eff}}$, cm^{-1} (0.07 ev)	Effectiveness Relative to Hafnium (volume)	Years Lifetime for 1% Continuous Δk Allowing 10% Absorption (~ effective atoms per original atoms)	Total Material Required	Fabrication Cost ($)	Material Cost ($)	Total Cost ($)	Melting Point (°F)	Radioactivity: 2 ft Active Rod – 6 ft from Source; 30 Days Decay, Lead Shields to 30 mr/hr	Comments
Hafnium	65 – 1-in. rods (solid)	2.1	1.00	75 (2.4)	5,000	65,000 (1000/rod)	624,000 (125/lb)	690,000	4000	Hf^{181} (46 d) ~1–0.48 Mev γ, 83 r/hr – 2 in. Pb	Cost given for crystal-bar hafnium; protective cladding would be required
Silver Alloy 80% Ag, 15% In, 5% Cd	65 – 1-in. rods (solid)	5.4	1.00	55 (1.4)	3,800	98,000 (1500/rod)	65,000 (17/lb)	163,000	~1650 Cd (610)	Cd^{115} (43 d) 0.02–0.96 Mev, 0.01–1.3 Mev Ag^{110} (270 d) ~3–0.8 Mev γ, 113 r/hr – 5 in. Pb	Melting point low Very poor creep strength
Silver	74 – 1-in. rods (solid)	1.9	0.88	80 (1.5)	5,300	110,000 (1500/rod)	64,000 (12/lb)	174,000	1760	Ag^{110} (270 d) ~3–0.8 Mev γ, 237 r/hr – 4 in. Pb	Melting point low; poor creep strength
15% Eu_2O_3 Steel (304 stainless steel)	69 – 1-in. rods	7.6	0.94	10						Eu^{154} (16 y) 0.5–1.12 Mev, 0.4–0.78 Mev, 7 r/hr – 4 in. Pb; Co in steel not considered	Cost prohibitive
20% Eu_2O_3 Steel (304 stainless steel)	45 – 1.5-in. rods	11.4		20 (4.0)	830 (Eu_2O_3)	45,000 (1000/rod)	1,130,000 (3/gram)	1,175,000	~3000		
100% Lindsay Code 920 Mixture 63.8% Sm_2O_3 26.3% Gd_2O_3 4.8% Dy_2O_3 0.9% Nd_2O_3 4.2% Yb_2O_3	45 –1.5-in. rods	110	1.00	7 (0.4)	2,800	45,000 (1000/rod)	140,000 (50/lb)	185,000	3000	Numerous radioactive atoms; 3 r/hr – 4 in. Pb	Poor lifetime; assuming solid slug, effective cooling would be difficult
Cobalt	93 – 1-in. rods	1.7	~0.70	67 (1.0)	5,600	140,000 (1500/rod)	15,000 (2.6/lb)	155,000	2720	Co^{60} (5.28 y) 1–1.17 Mev, 1–1.33 Mev, 12,700 r/hr – 9 in. Pb; Co^{58} also important	Difficult to fabricate
Nickel	350 – 1-in. rods (solid)	0.22	~0.20	800 (1.0)	22,000	175,000 (500/rod)	15,000 (0.70/lb)	190,000	2650	0.05% Co, Co^{60} (5.28 y) 1–1.17 Mev, 1–1.33 Mev, 27 r/hr – 5 in. Pb; Co^{58} also important	Number of rods prohibitive
5% Boron Steel	~40 – 1.5-in. rods, 90% B^{10} bottom to natural at top	~21	1.10	20	B^{10}, 100 B steel, 4800 B^{11}, 140	80,000 (2000/rod)	454,000 16,000 470,000 (B^{10}, 10/g)	550,000	2140	Assumes 10% Ni ⟶ 0.005% Co Co^{60} (5.28 y) 1–1.17 Mev, 1–1.33 Mev, 3 r/hr – 3.5 in. Pb; Co^{58} also important	Poor radiation stability
British Calder Hall ¼-in.-thick inserts 4% steel at bottom ⅛-in.-thick inserts 3% boron steel at top	8% Δk 60 – 1.5-in. rods Inserts	6.0	1.10	20	3,200						

British Calder Hall

$\phi^{th} = 0.8 \times 10^{12}$ neutrons·cm^{-2}·sec^{-1}

Rod active length used = 21 ft

182 Mw

ORNL – GCR

$\phi^{th} = 1 \times 10^{13}$ neutrons·cm^{-2}·sec^{-1}

Rod active length used = 20 ft

700 Mw

The Ag-In-Cd alloy and pure silver are both relatively low in cost and would easily provide sufficient control. However, the low creep strength of both choices presents support problems. The stress to produce one per cent strain in 10,000 hr at 600°F is only 135 psi for the alloy, while for pure silver the respective stress at 1100°F is estimated to be 250 psi. Rods of either of these materials could easily be fabricated and canned in stainless steel for effective support. At the design temperature no compatibility problems would exist between a steel capsule and the pure silver rod.

Cobalt is of little interest because of the very high-residual activity and because of the fabrication problems inherent in the brittle nature of cobalt and high-cobalt alloys. Nickel, on the other hand, would be easily fabricated but effective control could only be obtained with a prohibitive number of rods.

Lindsay Code 920, largely a mixture of Gd_2O_3 and Sm_2O_3, is of interest. It is not highly expensive and can readily be fabricated into solid refractory slugs which could be canned in stainless steel capsules. Cooling of rods made up from such slugs would not be efficient, however, and warping under service would be a definite possibility.

After considering the various materials, the use of a canned silver rod was recommended for the following reasons:

1. No compatibility problem is expected.
2. It is relatively easy to fabricate.
3. High conductivity should make for effective cooling and good thermal stability.
4. Sufficient control can be achieved with about 61 rods of 2 in. diameter.

The design of these control rods is tentatively as follows: length - 18 ft; stainless steel capsule - 2 in. OD x 0.065 in. wall; and silver insert - 1-7/8 in. OD x 1-1/4 in. ID. Such a rod could be fabricated by drawing (sinking) the stainless steel tube over the extruded silver rod, followed by suitable end closures. The stress in the capsule walls would not be greater than ~ 300 psi. An inner tube of stainless steel 1-1/4 in. OD x 0.035 in. wall should add considerably to the thermal stability and strength of the rod without detracting from its effectiveness.

3.7 The Selection of Shield Materials for the Boron Curtain

The boron shield to be placed next to the reflector is justified on the basis of simplifying the shielding of access holes, reducing the heating and thermal stresses in the pressure vessel, and reducing the thickness and cost of the concrete biological shield. In order to perform satisfactorily, the shield should contain about 60 mg of boron per sq cm of surface, should be stable at ~ 500°F, and resistant to an integrated neutron flux of about 10^{19} nvt (thermal) over the life of the reactor. Several materials were considered, including boron steel, Boral, Pyrex glass and canned B_4C powders.

Wrought boron-steel sheet approximately 3/8 in. thick would contain sufficient boron; however, these steels are not dimensionally stable under irradiation and become very brittle.[36] Reliable joining methods for such sheet are not available either. Thus, considerable additional structure would be required simply to support the shield.

The use of Boral would present joining and support problems also, since Boral cannot be welded. Further, Boral has been shown to be quite inefficient as an absorber, due to self-shielding of the large B_4C particles used and streaming of neutrons between the particles.[37] Also, its dimensional stability at the service temperature is doubtful.

Pyrex glass sheets approximately 1/4 in. thick would provide sufficient shielding, but would also require a separate supporting structure. Data on the radiation stability of pyrex indicate that little damage would be expected.[38]

Canned B_4C powders or tiles were not seriously considered because of the settling and non-uniform density in the cans and because the materials and cans would likely be too costly. A shield of this type would be of a minimum weight and thickness, however.

After considering the various materials, the decision was made to use pyrex sheets supported by a structure of wrought steel. A significant reason for the choice was the data supporting its radiation stability, thus indicating that fragmentation of the pyrex and the containment of particles would not be a serious problem. Cost data which have been secured show that the cost of such a shield would be moderate.

---

[36] J. J. Lombardo, "Tensile and Impact Test Results on Irradiated Boron-Stainless Steels," WAPD-SFR-Fe-192 (June 28, 1955).

[37] W. R. Burrus, "How Channelling Between Chunks Raises Neutron Transmission Through Boral," Nucleonics, 16, No. 1, 91 (January, 1958).

[38] Private Communication from C. D. Bopp to G. Samuels, (November, 1957).

SECTION 4

FUEL ELEMENTS

4. FUEL ELEMENTS

CONTENTS

4.1 Internal Heat Transfer.....4.1
4.2 Fuel Element Configuration.....4.11
4.3 Fabrication and Costs of Fuel Element Assemblies.....4.14
4.3.1 Fuel Element Description.....4.14
4.3.2 Fuel Capsule Assembly Procedure.....4.20
4.3.3 Fuel Element Accessories.....4.20
4.3.4 Inspection of Fuel Capsules.....4.23

4. FUEL ELEMENTS

The fuel element is the point of origin of the thermal energy produced by the reactor and is therefore the point of highest temperature in the system. Once the size of the reactor is established by physics requirements the pro-rated reactor cost per unit of power output decreases with increasing power density or power output. The optimum power level is that which results in minimum cost net electric power. This rate is determined by power cycle economics and temperature limitations of the fuel element materials. The former considerations are discussed in Section 6 of this report. The latter will be considered here.

4.1 Internal Heat Transfer

For the purpose of this report, internal heat transfer is considered to be the process of transferring the heat from its point of origin in the uranium oxide slug to the gas-filled gap between the slug and the inside of the capsule, and finally through the capsule wall to the outer surface. The fuel element configuration must be such that this process can be carried out within the limits of temperature and thermal stress imposed by the materials.

Physics and economic considerations establish an active core 30 ft in diameter by 20 ft high containing approximately 330,000 lb of uranium oxide fuel distributed in 1597 channels on an 8-in. square lattice pitch.

Power plant economics indicate the power output should be approximately 700 Mw(T). With 1597 fuel channels 20 ft long, the average power output per foot of fuel channel length must be 22 kw/ft or about 75,000 Btu/hr-ft of length for 700 Mw of reactor output. Since the peak-to-average power density will be less than two, the maximum design power output per foot of fuel channel length is chosen to be 150,000 Btu/hr-ft of length. As will be shown later, the heat transfer coefficients which can be achieved with optimum gas pressure drops through the reactor are of the order of 275 Btu/hr-ft^2-°F. If the fuel capsule surface temperature is not to exceed 1200°F, the temperature drop between the gas and a metal fuel capsule sheath at the center of the reactor must not exceed about 400°F. The resulting heat flux is 110,000 Btu/hr-ft^2 and the surface area required for heat transfer is approximately 1.5 ft^2/ft of channel.

If the fuel is distributed equally per foot of channel throughout the reactor it will result in 10.4 lb or 0.0162 cu ft of uranium oxide per foot of channel. A single solid cylinder having this volume would be 1.73 in. in diameter, and its surface area excluding the ends would be 0.45 ft^2 compared to the 1.5 sq ft needed. Fins could be used to extend the capsule surface area, but there is little point in employing them with iron-base alloys because of their poor thermal conductivity and consequent low fin efficiency. Even more important, it is possible to obtain such high heat fluxes in the proposed design without fins that the radial temperature gradient within the fuel slugs and between the fuel slug and the capsule wall could become excessive if really effective fins were employed.

Preliminary calculations indicate that fins could be used to effect a reduction in pumping power of as much as 56%, but this would result in the introduction of additional nuclear poison in the core in the form of fin material. Serious consideration of extended surfaces must wait on the availability of materials having low-absorption cross sections and sufficient high-temperature strength.

For solid cylindrical slugs the temperature distribution within the uranium oxide depends upon the power density and the slug diameter according to the equation:

$$\Delta T \text{ (center to OD)} = \frac{W}{K}\frac{r^2}{4}$$

where W = power density

K = thermal conductivity

If a single large cylindrical slug of UO_2 were located at the peak power density region of the reactor its central temperature would theoretically be over 12,000°F. In determining a fuel element shape, it is therefore necessary not only to provide sufficient surface area; it is also necessary to shorten the path traveled by the heat in leaving the uranium oxide slug. The fuel element configuration must have a higher surface-to-volume ratio and smaller thickness than a single cylinder. Possible shapes include thin slabs or cruciforms, thin annuli with heat removal from both inner and outer surfaces, and bundles of small cylinders. Thin annuli have the advantage of structural stiffness and symmetry. The symmetry has an important effect on

the temperature structure in the coolant gas as will be discussed in Section 6. Unfortunately, present techniques for fabrication of uranium oxide forms do not permit dimensional tolerances which thin annuli would require to minimize the gap between the fuel slug and the capsule. Further, if internal pressures built up by the release of fission gases should exceed the coolant-gas pressure, buckling of the inner capsule wall could result. Thin slabs would encounter the same difficulties plus some additional ones. The choice of configuration is effectively narrowed to a bundle of small diameter cylinders. A pattern of seven cylinders with six located at the corners of a hexagon and one centrally located was arbitrarily chosen. While a larger number of smaller cylinders might be used, such an arrangement would be more expensive, less rugged for handling purposes, and more subject to hot-spot problems because of the reduced gap between adjacent cylinders. Figure 4.1 shows a full scale model of the proposed design which fits nicely into the cylindrical cooling channel. Its surface-to-area ratio permits the removal of 700 Mw(T) from the reactor with a maximum nominal capsule temperature of 1200°F and a coolant-outlet temperature of 1000°F. The uranium oxide slugs are 0.75 in. diameter and can readily be fabricated to tolerances which will permit their insertion in the capsules without further sizing operations after sintering.

Figure 4.2 shows the effects of slug diameter and heat flux on the temperature differences and thermal stress in solid uranium oxide slugs, while Fig. 4.3 presents similar information for hollow slugs in which the diameter of the hole is equal to one-half the outer diameter of the slug. In both instances the slugs are cooled by removing heat from the outer perimeter. These curves show that, to achieve the heat flux required from the capital investment standpoint, it will be necessary to employ power densities and slug diameters which will cause thermal stress cracking of the uranium oxide. This cracking does not constitute a serious problem.

The heat flux from the uranium oxide to the can wall is limited by the maximum allowable temperature in the center of the uranium oxide slug. The heat flux from the outside of the tube increases with gas velocity but is limited by the pumping power required. Although the melting temperature of the uranium oxide is 4800°F, the rate of release of the fission gases and the resulting high internal can pressures may impose a practical temperature

UNCLASSIFIED
PHOTO 42788

Fig. 4.1. Fuel Element Assembly.

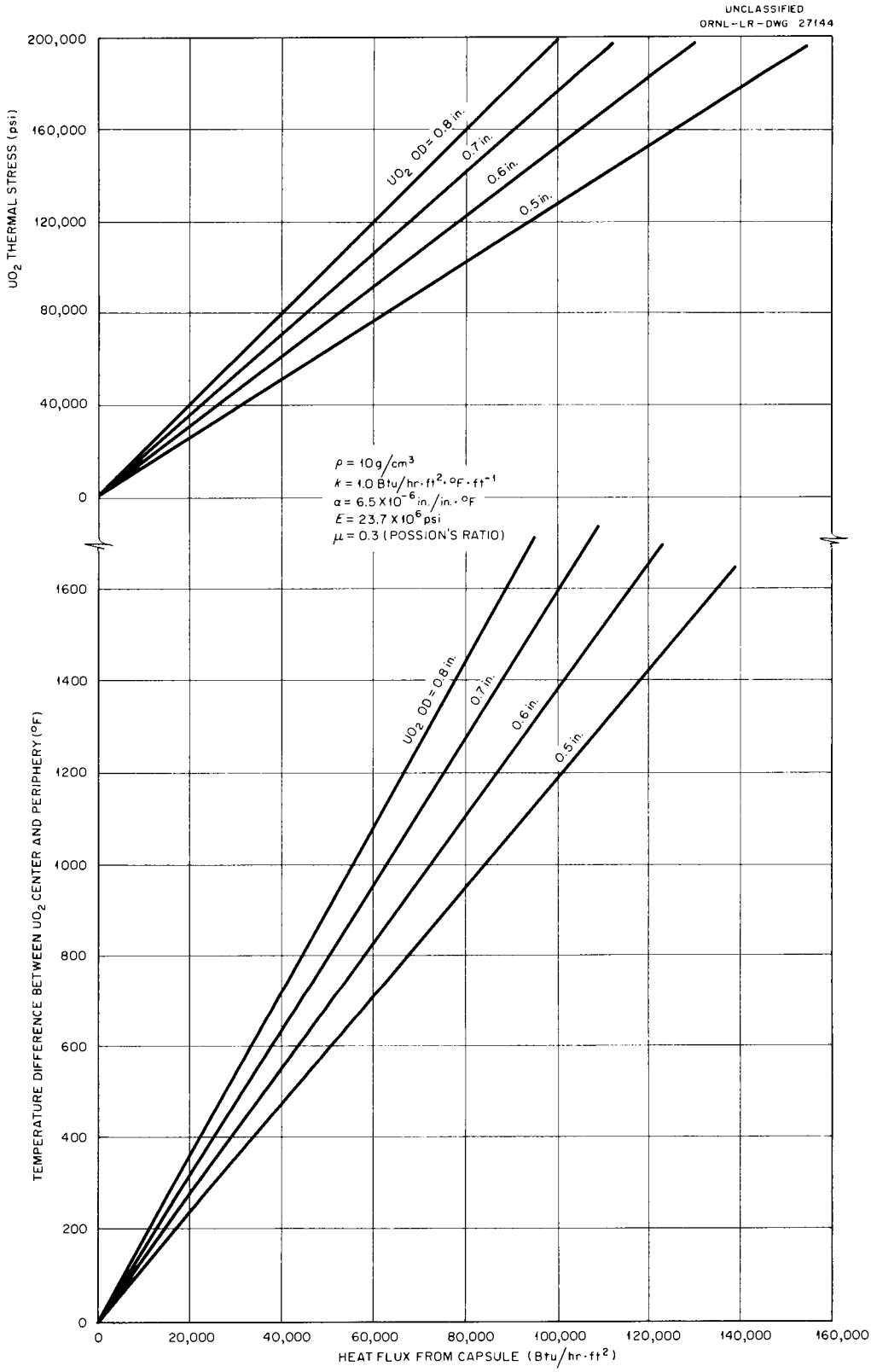

Fig. 4.2. Internal (Radial) Temperature Difference and Thermal Stress in Solid Cylindrical UO_2 Slugs as a Function of Slug Diameter and Heat Flux.

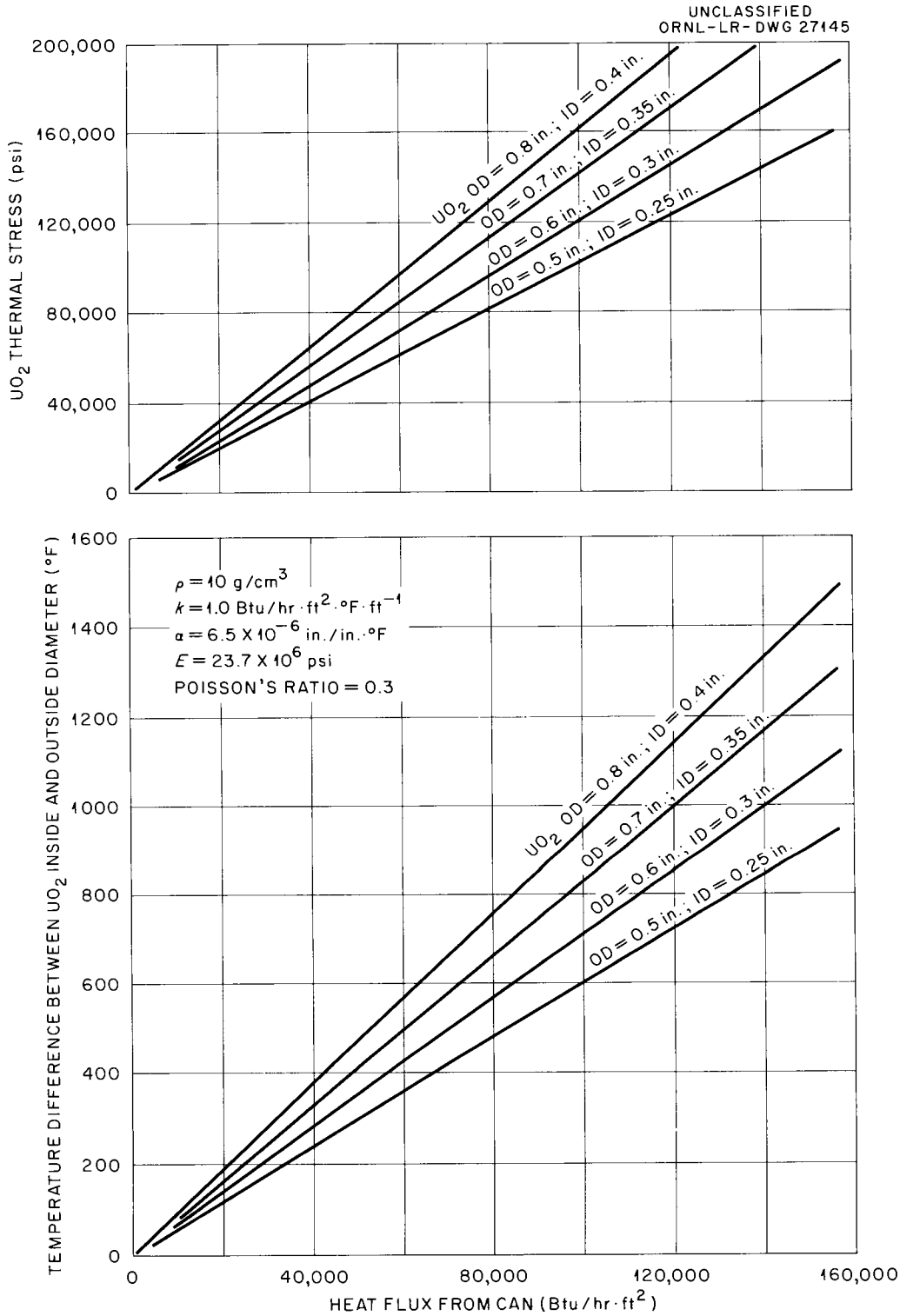

Fig. 4.3. Internal (Radial) Temperature Difference in Hollow, Cylindrical UO_2 Slugs as a Function of Slug Diameter and Heat Flux.

limit below the melting point. Thus the maximum internal heat flux depends primarily on the expected fuel element lifetime and on the clearance between the uranium and the can.

It is anticipated that production diametral tolerances will be ± 0.005 in. for the uranium oxide slugs if no post-firing sizing operation is performed and ± 0.001 in. for the tubing from which the capsule is made. For a nominal diametral clearance of 0.010 in. the maximum diametral clearance will be 0.016 in. and the minimum will be 0.004 in. Figure 4.4 shows the effect of radial clearance on the temperature difference between the uranium oxide and the can wall for a fresh fuel capsule; i.e., the gas volume contains only helium. Figure 4.5 shows the effect of dilution of the helium by fission gases for three clearances at the maximum heat flux. The effect of the release of the fission gases is to decrease the conductivity of the gas film and increase the temperature of the uranium oxide which in turn increases the rate of release of fission gases by as much as a factor of two. Fortunately, at fuel temperatures above 2000°F heat transfer by thermal radiation predominates so that the temperature of the uranium oxide becomes insensitive to either the composition of the gas within the capsule or the radial clearance between the uranium oxide and the capsule wall. Figure 4.6 shows the effects of fission product gas release as a function of operating time on the temperature of the uranium oxide and the resulting pressures. Note that the operating time given is in the region of maximum power density where 50,000 hr would correspond to a burnup of 17,000 Mwd/T.

One method of reducing the pressure built up by the fission gases is to provide a central hole in the uranium oxide. This hole reduces the final gas pressure in three ways, i.e., by providing a large volume to accumulate the gases, by reducing the temperature rise through the uranium oxide, and by reducing the degree of dilution of the helium. Of course, such a hole has the disadvantage that it might serve as a region into which fragments of uranium oxide could drop as a result of thermal stress cracking. If this were to occur, the temperature in these fragments might rise to the melting point in which case the fission product gases would be released and give a higher fission product gas concentration in the slugs than would otherwise

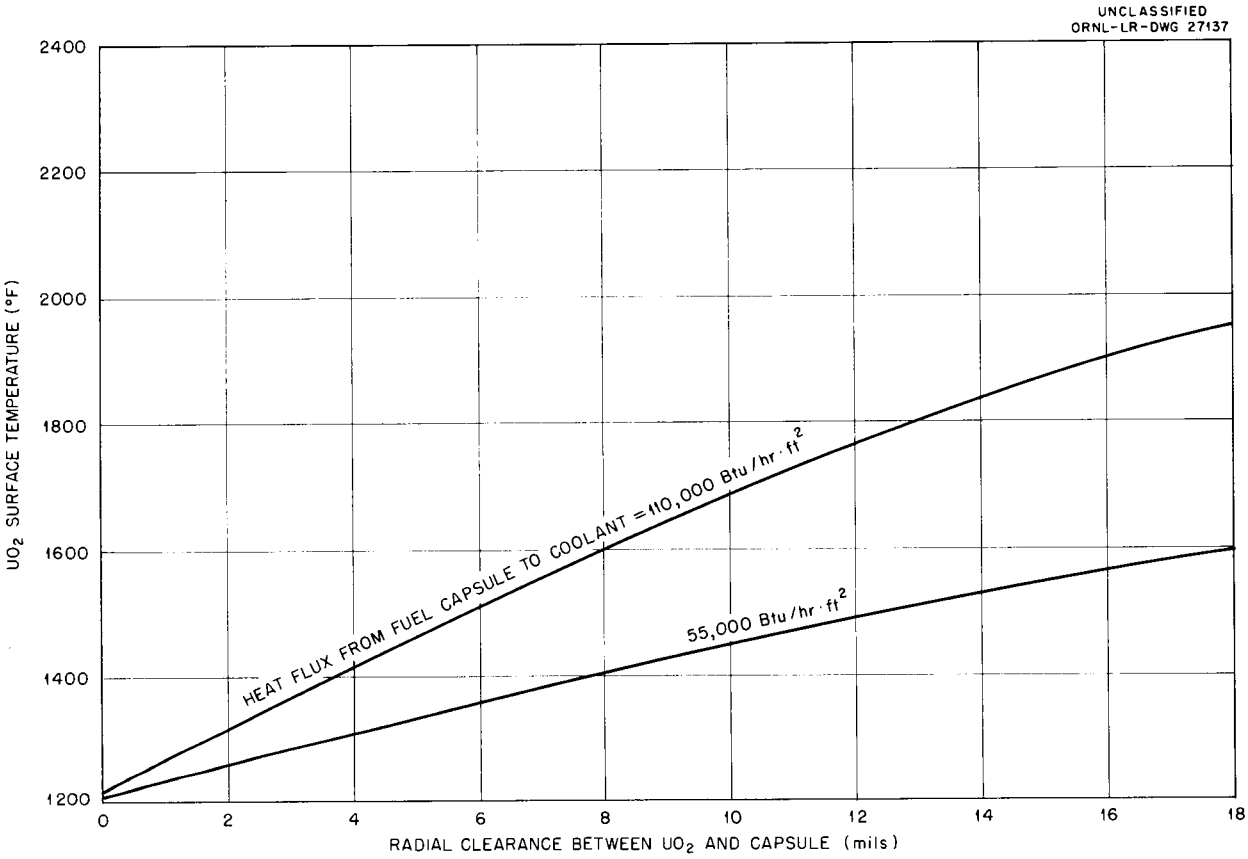

Fig. 4.4. Effect of Radial Clearance Between UO_2 and Capsule Wall on UO_2 Surface Temperature for a 1200°F Capsule Wall Temperature and a 100% Helium Atmosphere in the Capsule.

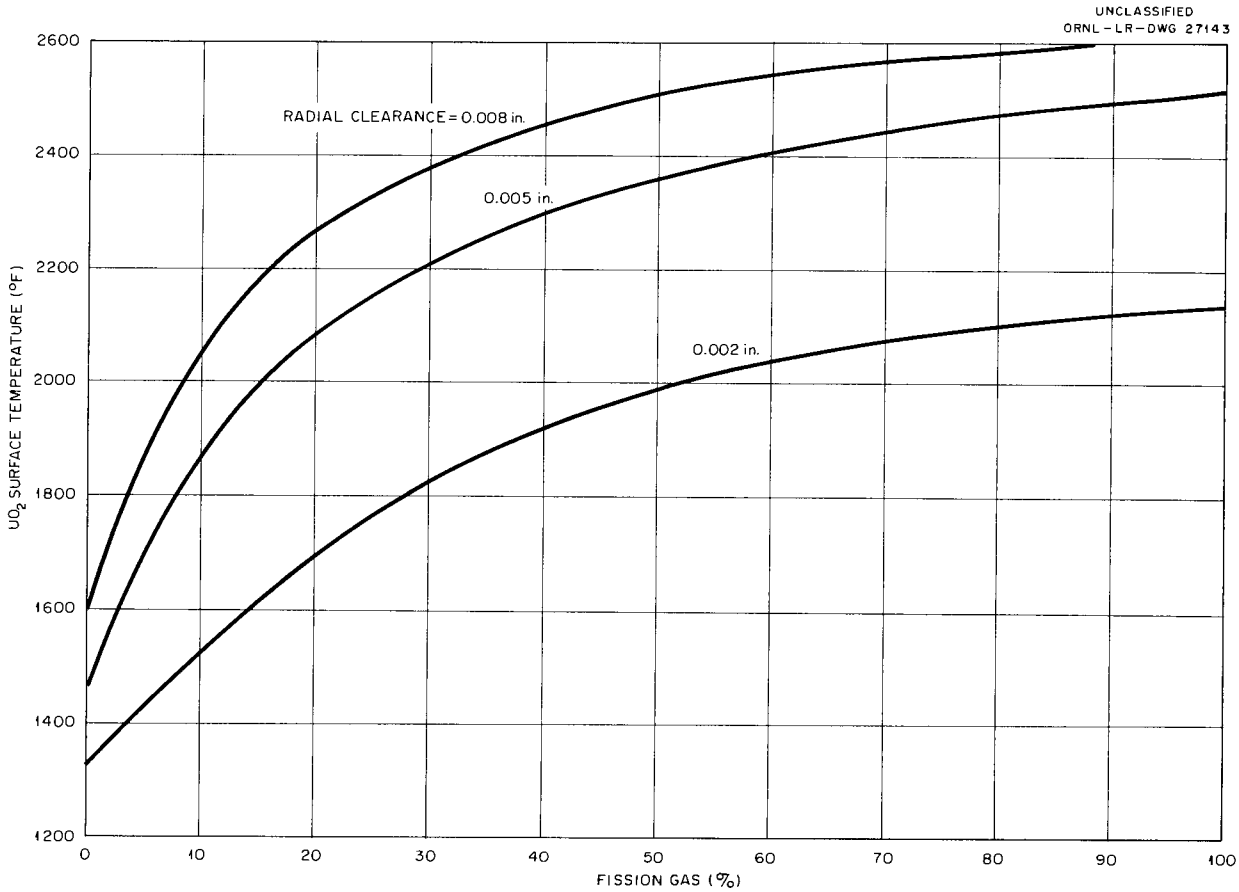

Fig. 4.5. UO_2 Slug Surface Temperature as a Function of the Dilution of Helium by Fission-Product Gasses.

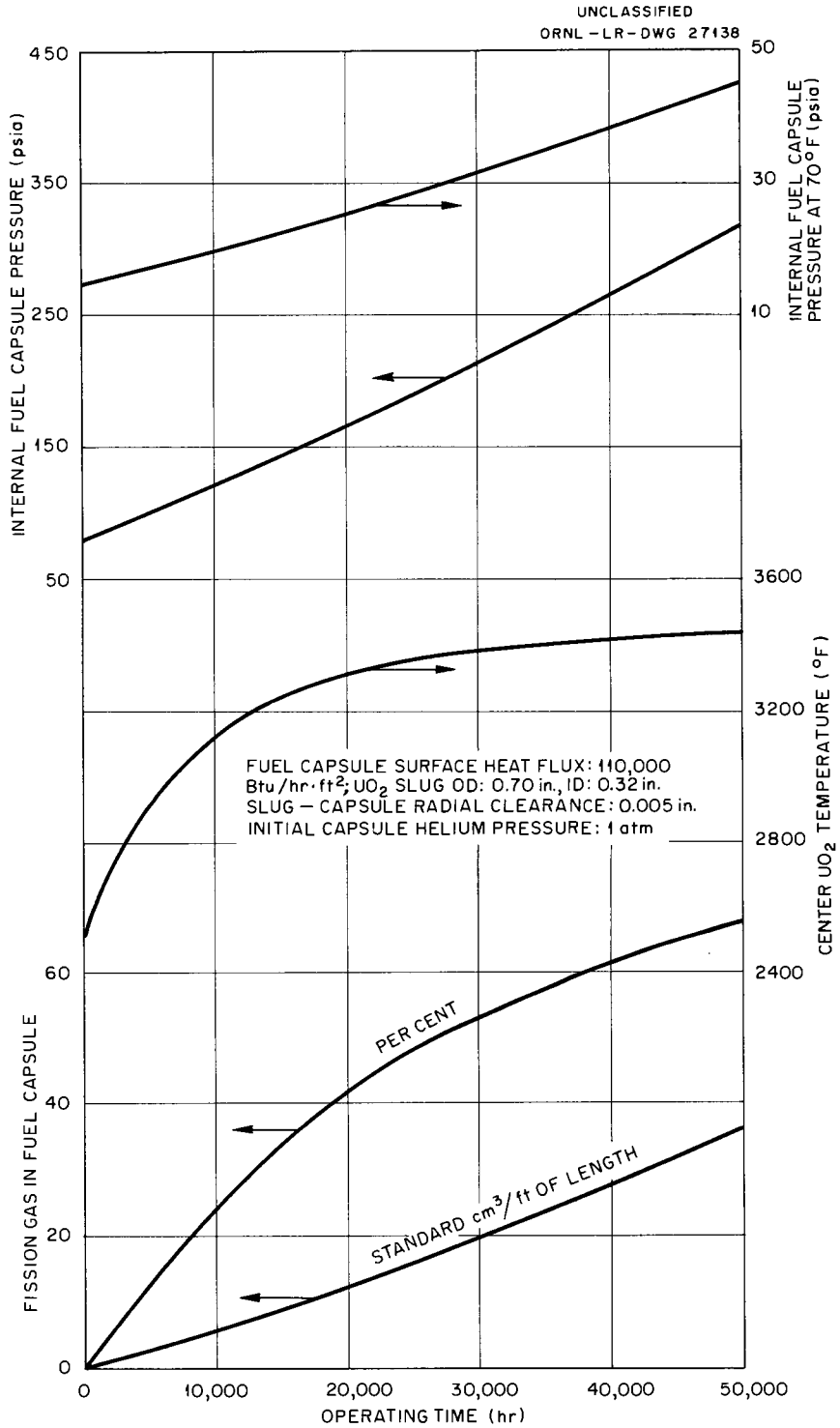

Fig. 4.6. Effects of Fission-Product Gas Release from UO_2 on the Pressure and Temperature Within the Fuel Capsule, as a Function of Operating Time at the Maximum Local Power Density in the Reactor.

be the case. As discussed elsewhere in this report, this problem will be investigated by in-pile tests to determine whether or not it is serious. Should tests show that it presents serious problems, a porous tube of graphite, magnesia, or alumina could be inserted to hold the fragments in place.

4.2 Fuel Element Configuration

The vertical cylindrical configuration for the graphite was selected partly because it represents the most desirable geometry for the support of the graphite and partly because it would be difficult to support long thin-walled capsules filled with heavy uranium oxide slugs in horizontal channels. The amount of support structure used to enclose and support the fuel slugs must be limited for the sake of neutron economy. Hence, the vertical fuel channels were selected as providing the best solution to the support problem for both graphite and fuel.

It was decided to hang the fuel elements in the coolant channels so that the capsule wall would be in tension. The principal advantage of this choice is the accessibility of the fuel element support structure to the fuel handling machine which approaches from the top of the channel. At operating temperatures, the helium pressure within the fuel capsule will vary from less than 50 psia to slightly less than the 300 psia external helium pressure, depending upon the power density, burn-up and temperature history of the fuel capsule. Collapsing tests under external pressure have been carried out for varying clearances between the fuel slugs and the inside wall of the metal capsule shell. No wrinkling of the metal sheath has been experienced for the specimens with 0.010 in. or less diametral clearance.

The fuel element, as shown in Fig. 4.7, is designed so that the seven capsules in each fuel element are in tension. A spacer located at the lower end of each fuel element serves to position the seven capsules in each element with respect to each other and the fuel element as a whole with respect to the graphite channel. The nominal length of the fuel element including the hanger and spacer is 40 in. The possibility exists that additional spacers may be required near the center of the element to control bowing of the individual capsules. Experimental and analytical work is in progress to determine how much bowing is to be expected, and its effect on coolant temperature distribution.

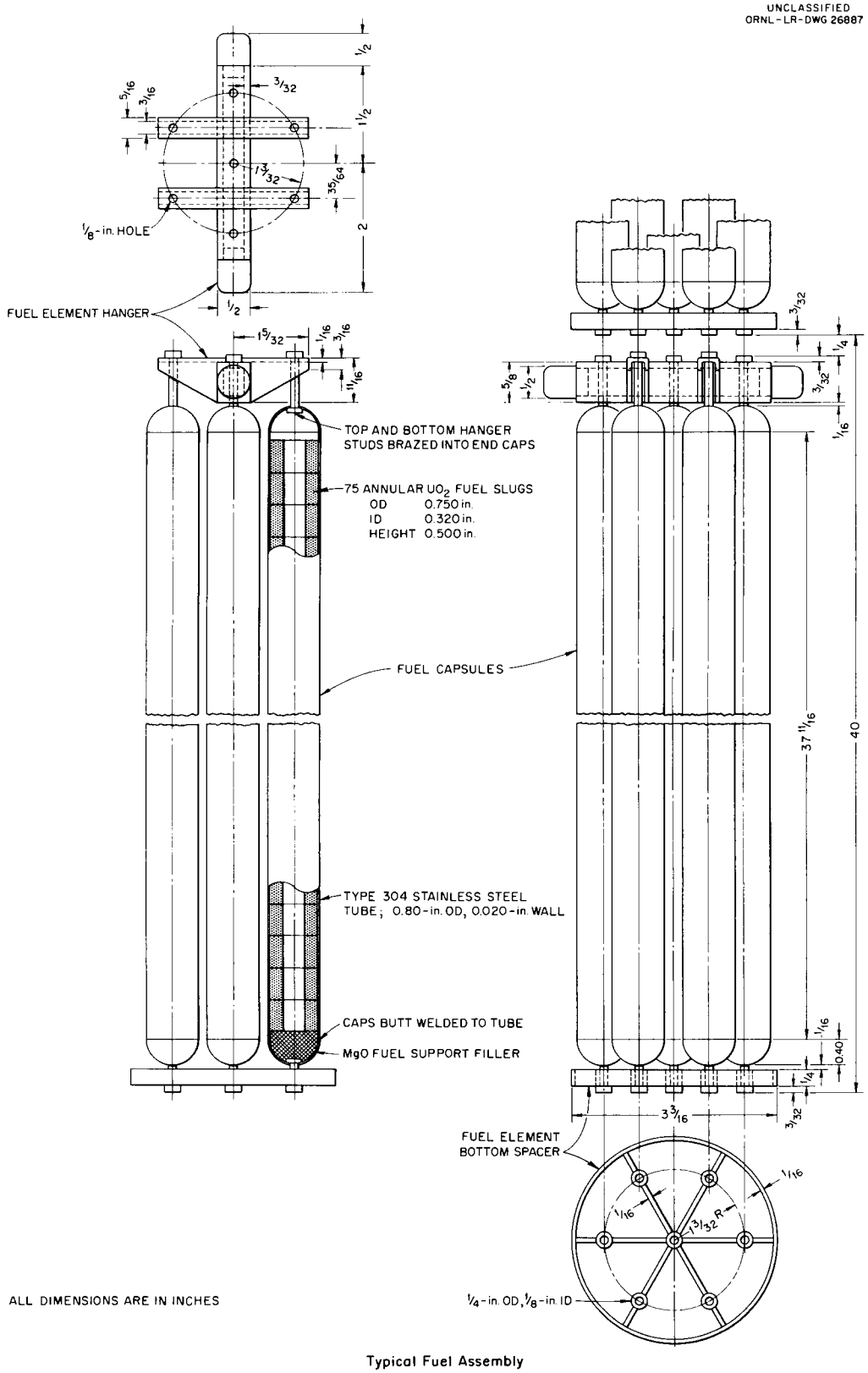

Fig. 4.7. Schematic Drawing of Fuel Element Assembly.

4.3 Fabrication and Costs of Fuel Element Assemblies

For economy in fabrication, an idealized fuel element would be one which utilizes manufacturing processes currently in use in industry. On this basis, the thirty companies listed in Table 4.1 were given the parameters listed in Appendix C, Tables C.1 and C.2, along with several suggested methods of manufacture and asked to submit estimates of fabrication costs commensurate with their facilities and capabilities. Each company was urged, also, to submit all design alternatives that they might have in order to accumulate the best thinking in the limited time available. During the period between issuing the request for estimates to the companies and preparation of this paper, fuel element parameters were changed to those listed in Appendix C, Table C.3. Therefore, a new estimate was made, based on vendors figures and adjusted to correspond to present thinking, and is shown in Table 4.2 as representative cost estimates for components, fabrication, etc., using the most applicable costs from each company. No significant change in cost per kilogram of fuel was noted between the fuel element cost for initial parameters and final parameters. The average estimated cost for the completed fuel element is $441.00.

4.3.1 Fuel Element Description: A fuel element assembly consists of one top hanger, seven fuel capsules, and one bottom spacer, as shown in Fig. 4.7. The top hanger is to be supported at two points 180 degrees apart in circumferential recesses in the graphite channel. Loading will consist of sliding the hanger into vertical grooves in the graphite channel and rotating the assembly to engage the hanger in the circumferential recesses.

The fuel capsule (Figs. 4.8 and 4.9) is type 304 stainless steel 0.80 in. OD x 0.020 in. wall x 38.5 in. long filled with UO_2 slugs and having hemispherical end caps with suitable attachments for hanging and positioning the capsule.

Components required for fabricating a fuel capsule are:

1. one tube
2. one top cap
3. one bottom cap
4. two MgO end spacers
5. 75 UO_2 fuel slugs

TABLE 4.1

COMPANIES CONTACTED FOR COST ESTIMATES

Westinghouse Electric Corporation
Babcock and Wilcox Company
Sylvania Electric Products Company
P. R. Mallory and Company, Inc.
The Electric Auto-Lite Company
Gulton Industries, Inc.
Wall Colmonoy
Thompson Products, Inc.
Clevite Corporation
Hydrocarbon Chemicals, Inc.
AiResearch Manufacturing Company
Atomic Power Development Associates
The Martin Company
Nuclear Development Corporation of America
Solar Aircraft Company
Bell Aircraft Company
General Electric Company
Griscom-Russell Company
Heintz Manufacturing Company
Allis-Chalmers Mfg. Company
Stewart-Warner Corporation
York Corporation
Loewy-Hydropress
Foster-Wheeler Corporation
General Motors Corporation
Radio Corporation of America
Koven Fabricators, Inc.
Austenal, Inc.
Superior Tube
Bantam Manufacturing

TABLE 4.2

ADJUSTED FUEL CAPSULE COST ESTIMATE (CURRENT PARAMETERS)

Item	Cost/kg UO_2 ($)	Cost/Capsule ($)	Total Cost/Reactor ($)
Fabrication of UO_2 Slugs	$ 7.55	$ 17.44	$ 1,170,224.00
Hangers	0.34	0.77	51,667.00
Spacers	0.07	0.16	10,736.00
Fabrication of Capsule	8.48[1]	19.59[1] 17.99[2]	1,314,489.00
Tooling Cost	0.26	0.61	40,931.00
Development Cost	1.32	3.06	205,326.00
Facilities	0.37	0.86	57,706.00
Other Related Costs	0.29	0.68	45,628.00
Total Fabrication Cost	$ 18.68	$ 43.17	$ 2,896,707.00
Conversion of UF_6 to UO_2	8.23	19.01	1,275,571.00
Transportation to Site	0.07	0.16	10,736.00
Assembly of Element at Site	0.20	0.46	30,866.00
TOTAL ESTIMATED COST	$ 27.18[1]	$ 62.80[1] 61.20[2]	$ 4,213,880.00[1]

Estimated Cost/kg U $30.89

Total Fuel Capsule Requirements:

UO_2 Slugs	2.31 kg ea.
67,100 Capsules	~ 155,000 kg UO_2
Uranium Inventory	~ 136,400 kg

[1] Seamless Tubing
[2] Weldrawn Tubing

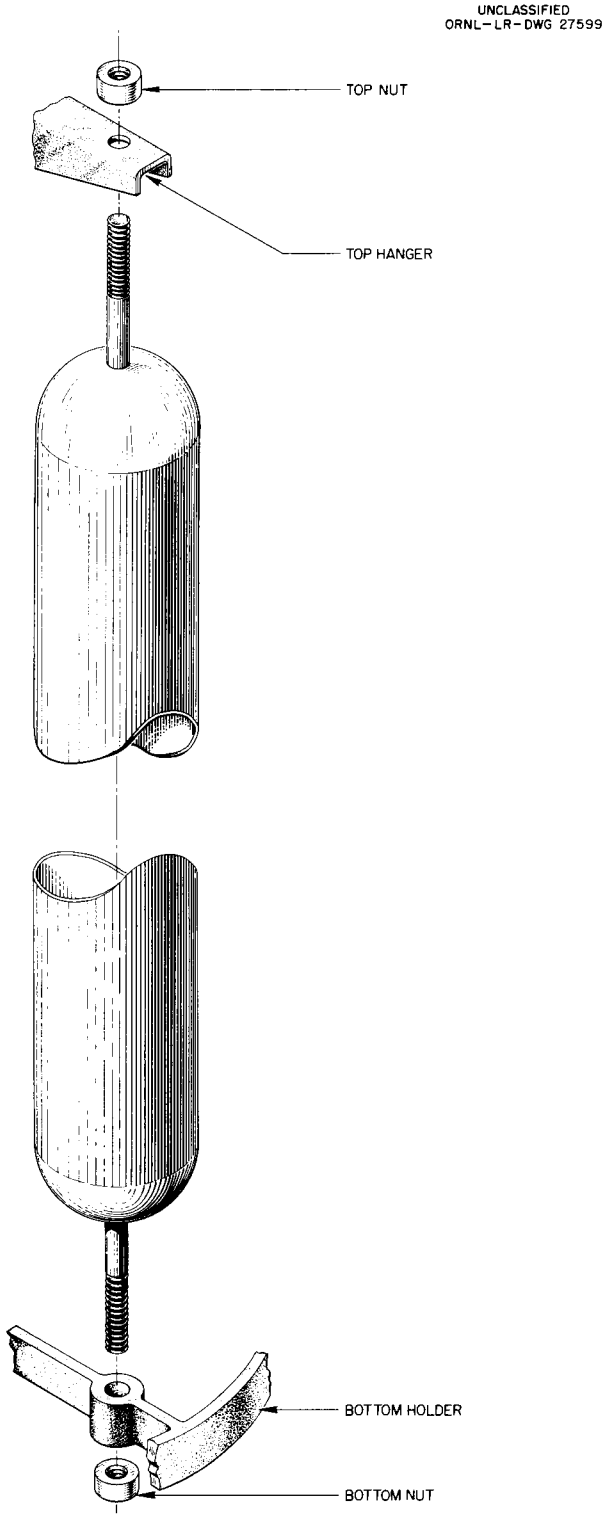

Fig. 4.8. Schematic Drawing of Fuel Capsule.

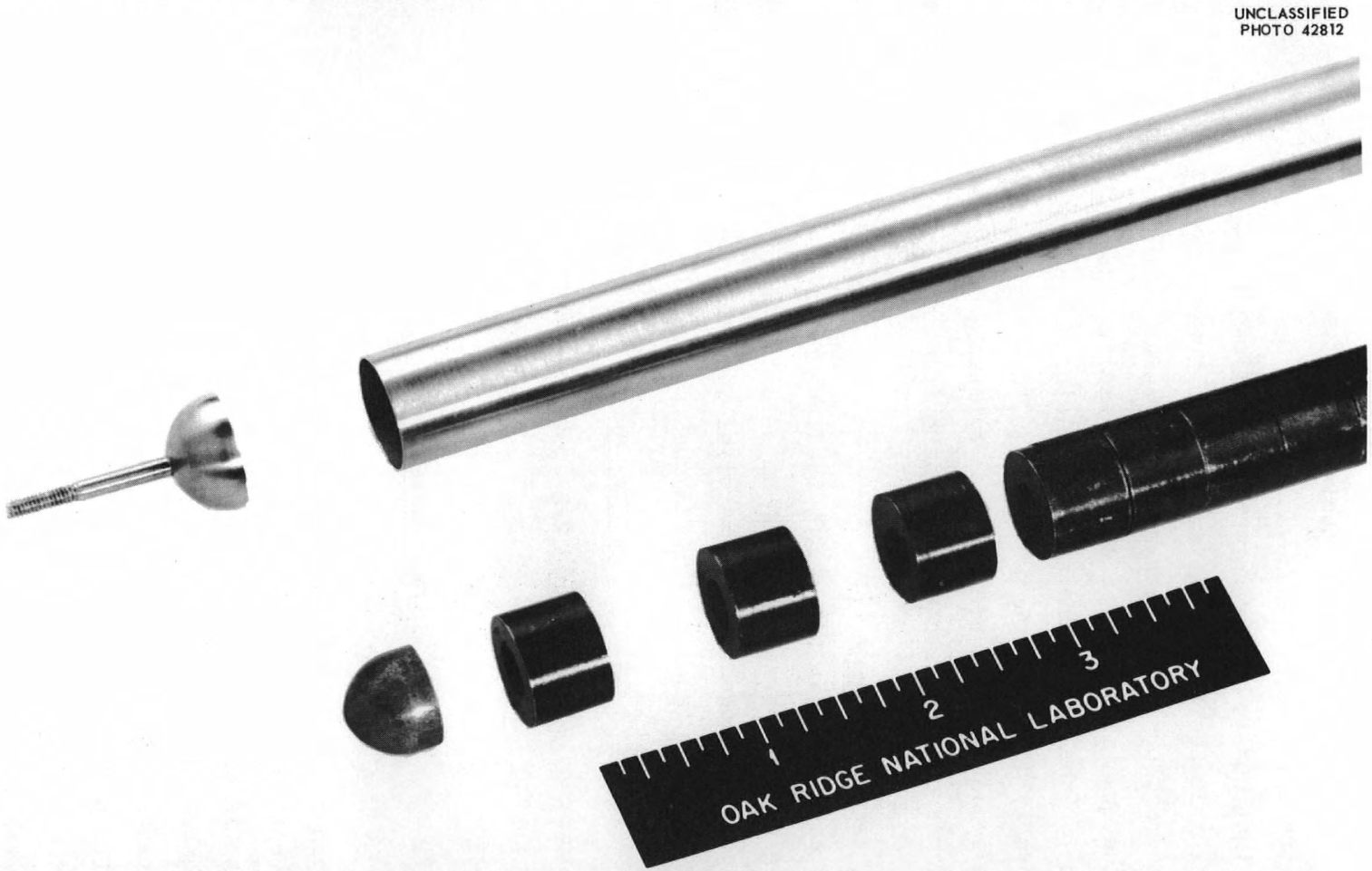

Fig. 4.9. Fuel Capsule Showing Fuel Slugs and MgO Spacer.

1. Tubing

The type 304 stainless steel tubing may be procured as seamless tubing or Weldrawn tubing. Table 4.2 shows costs for both types; however, it is believed that due to higher integrity and lower inspection costs, the seamless tubing is the better choice. Although the tubing is not of standard mill size, the difference between cost of special tubing and standard tubing for the quantity required should be small. Inspection methods and requirements for the tubing are described later. The cost of tubing will vary considerably depending on the amount of inspection required; for example, one vendor's costs are based on extremely rigid inspection while another vendor's costs are based on minimum inspection according to ASTM.

2. Top Cap

The top cap, shown in Fig. 4.10, shall be fabricated from 304 stainless steel forging-quality bar stock using an automatic screw machine. Ultrasonic testing will be used for raw material acceptance and dye penetrant will be used for acceptance of the finished product.

3. Bottom Cap

The bottom cap, also shown in Fig. 4.10, will be manufactured to the same requirements as the top cap but will be provided with an evacuation and filling hole for gas purge while welding and for leak detection.

4. MgO End Spacers

The use of MgO end spacers is desirable to protect the hangers and end caps from overheating and to distribute the weight of the column of fuel slugs on the bottom cap. Magnesium oxide was selected because it is easily fabricated and is compatible with both UO_2 and the capsule wall.

The spacers will be fabricated from refractory-grade magnesia by compacting and sintering to a density of 2.2 g/cc (60% dense). One end of the spacer will be hemispherical to fit the end cap. The diameter of the cylindrical part will be 0.060 in. smaller than the fuel slugs, so that the spacers will not interfere with the closure welds. The UO_2 fuel slugs have been discussed earlier in this report.

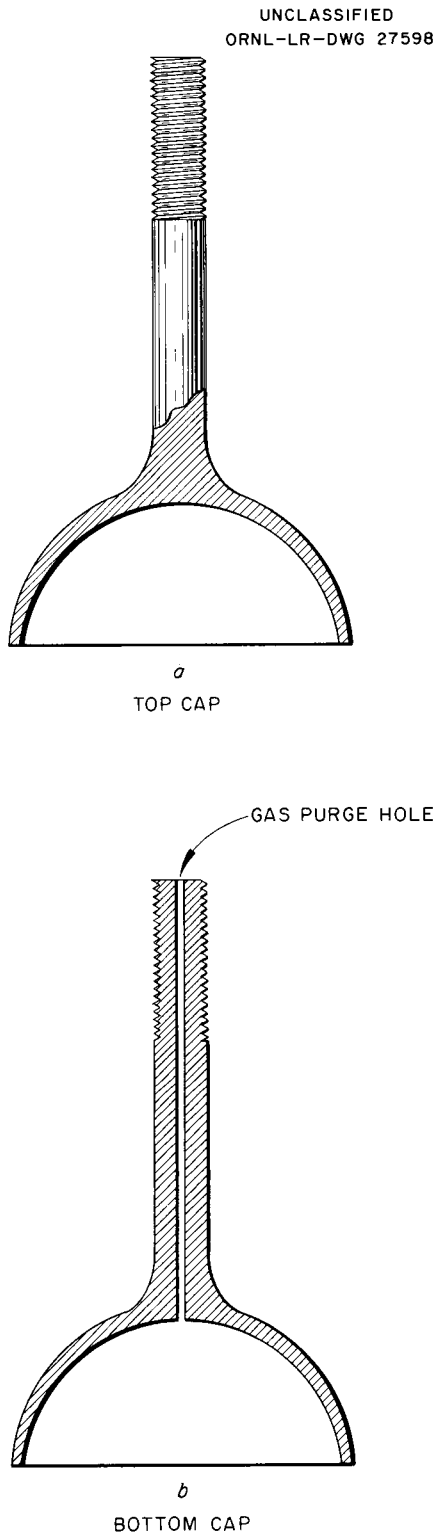

Fig. 4.10. Schematic Drawing of Fuel Capsule End Caps.

4.3.2 Fuel Capsule Assembly Procedure: A fuel capsule assembly sequence is shown in Table 4.3. Inspection of all components will be completed prior to assembly. In the first step, the bottom cap will be automatic fusion-heliarc welded to one end of the tube using a helium back-up atmosphere. This weld will then be inspected by x-ray, dye penetrant, and a helium mass spectrometer leak test. Defective welds at this stage may be repaired or cut out and replaced. After the bottom cap closure is complete, the assembly will be cut to length, cleaned and transferred to a controlled atmosphere chamber for placing the MgO end spacers and loading the UO_2 slugs. In order to avoid contamination hazards, the top cap will be welded in place in the controlled atmosphere chamber. After inspection of the top cap weld by dye penetrant and x-ray, the element will be evacuated and tested for leaks by use of the helium mass spectrometer. Upon acceptance, the capsule will be filled with helium and the bottom cap evacuation and filling hole will be welded shut. The final weld will also be examined by x-ray and dye penetrant.

At the completion of fabrication, the capsule will be packed for shipping. It is not anticipated that the capsules will be assembled into elements prior to shipping due to additional costs for adequate containers.

4.3.3 Fuel Element Accessories:

1. Fuel Capsule Hanger

Both stamping and casting techniques have been suggested for the fuel capsule hanger. The hanger design is based upon a maximum stress of 2,500 psi in the stainless steel. Note that the hanger temperature will be close to the gas temperature, i.e., a maximum of 1000°F. In addition to minimizing the metal volume and flow-obstructing area of the fuel hanger, it is desirable to limit the axial space within the channel made unavailable for fuel by the hanger and spacer. Due to the requirements for maximum strength over a long hanger life, casting techniques appear to be more favorable. Figure 4.11 illustrates one type of hanger.

2. Fuel Capsule Spacer

Figure 4.11 also illustrates the configuration of the bottom spacer. As structural requirements on this part are less rigid, manufacture may be either by casting or stamping.

TABLE 4.3

FUEL CAPSULE ASSEMBLY SEQUENCE

I. Components
   1. UO_2 slugs
   2. MgO slugs
   3. Tube
   4. End caps

II. Component Assembly
   1. UO_2 slugs
      a. UO_2 granulation
      b. Compacting
      c. Pre-sintering
      d. Sintering
      e. Grinding: (If necessary to meet tolerance requirements)
         Centerless
         Facing
      f. Testing and inspection
   2. MgO slugs
      a. Similar to those described for UO_2
   3. Tube (ASTM grade, cut to length at manufacturer)
      a. Unpack and visually inspect
      b. Inspect with Zyglo dye-penetrant
      c. X-ray
      d. Final visual
      e. Re-pack in storage container until ready for use
   4. End caps
      a. Inspect bar stock (ultrasound)
      b. Form parts on automatic screw machine
      c. Inspect visually and with dye-penetrant
      d. Pack for storage

III. Assembly
   1. Visual inspection of tube
   2. Weld on bottom cap
   3. Inspect bottom cap weld (x-ray and liquid dye-penetrant)
   4. Cut tube to length and weld allowing for weld shrinkage
   5. Load bottom MgO slug
   6. Load UO_2 slugs
   7. Load top MgO slug
   8. Weld on top cap
   9. Inspect weld on top cap (x-ray and liquid dye-penetrant)
   10. Visual inspection of fuel capsule assembly
   11. Leak test
   12. Fill with helium
   13. Weld end closure
   14. Pack element for storage

UNCLASSIFIED
PHOTO 42792

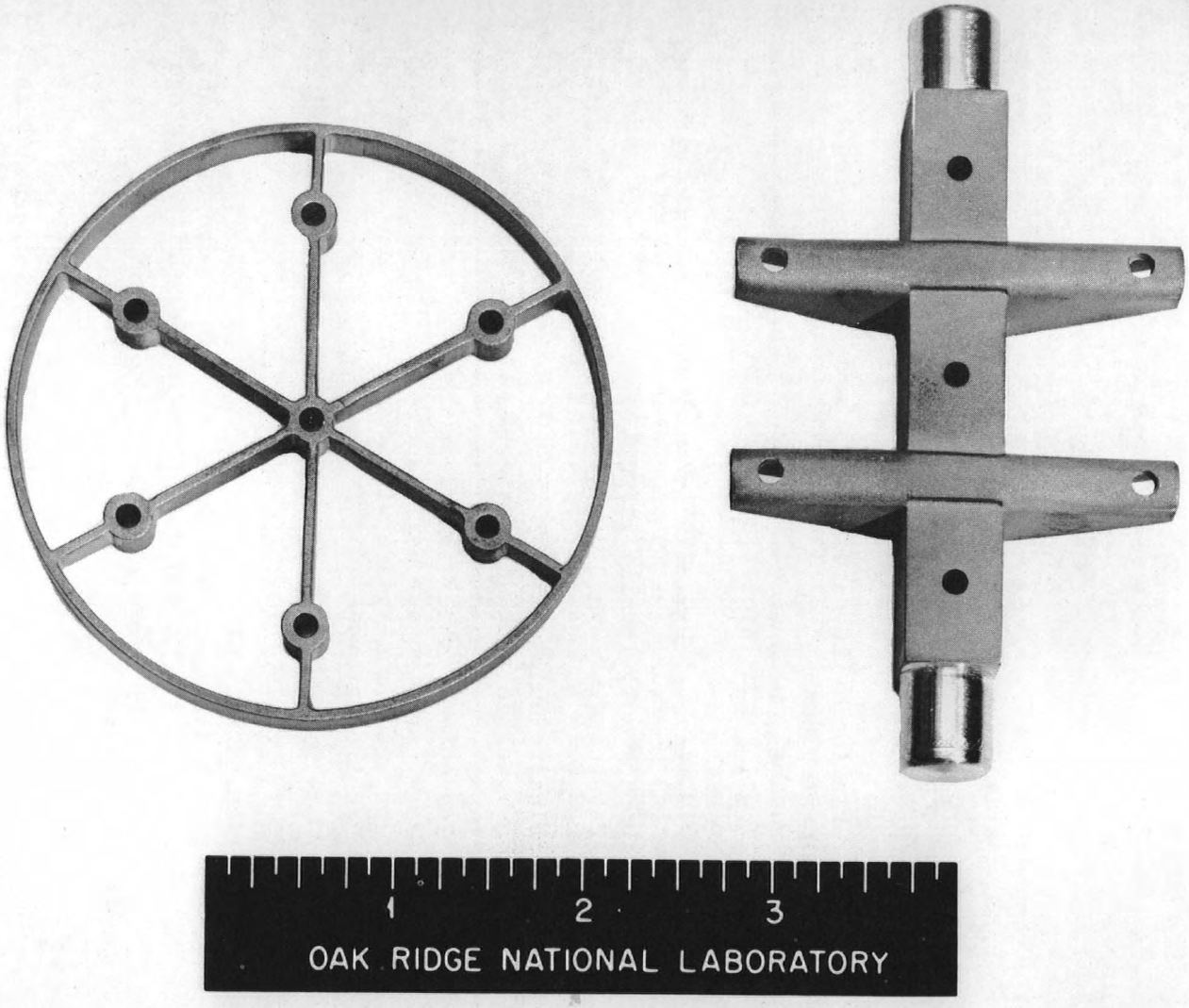

Fig. 4.11. Fuel Element Hanger and Spacer.

4.3.4 Inspection of Fuel Capsules: Tubing and end caps for the fuel capsules as well as the closure weld should be inspected. If defects between 1.5 and 2 mils can be tolerated in the tubing for the fuel capsules, inspection with fluorescent penetrants and with an encircling-coil eddy-current technique, followed by a visual inspection should be adequate.[1,2,3] This group of tests should cost less than ten cents per capsule.

A small amount of effort will be needed to modify existing eddy-current testing methods to eliminate the spurious signals caused by non-uniformity of the magnetic permeability that is always encountered in the austenitic stainless steels. If the tubing procured for fuel element fabrication is dimensionally uniform, and if the instrument eliminates the signals caused by variation in magnetic permeability, defects 1.5 to 2 mils deep and less than 0.065 in. long can be reliably detected in the 3/4-in. x 0.020-in. wall. This sensitivity should apply at both the inner and the outer surfaces of the tubing. The penetrant inspection is recommended since it will provide an evaluation of the quantity and distribution of pinhole-type defects. Pinholes, ranging from one to ten mils deep are frequently encountered in such tubing and the pinholes increase both in quantity and importance with decreasing tube-wall thickness. An excess of pinholes in the thin-walled tubing could constitute an expensive risk if used in manufacturing the fuel capsules. A fluorescent penetrant using post-emulsification cleaning and dry-powder developer is recommended for the evaluation of pinholes.

If, as proposed, the caps to form the end closures of the fuel capsules are made of bar stock on automatic screw machines, then the bar stock should be inspected prior to machining. By eliminating sections of the bar stock that contain excessive stringers, cracks and similar defects, considerable

---

[1] R. B. Oliver and J. W. Allen, "Inspection of Small-Diameter Tubing by Eddy-Current Methods," J. of Soc. for Nondestructive Testing, 15, No. 2, 104, (1957).

[2] R. B. Oliver, A. Taboada, and G. M. Tolson, "The Use of Penetrants in the Inspection of Small-Diameter Tubing," ASTM Book on the Symposium on Nondestructive Testing in the Field of Nuclear Energy, (In Publication).

[3] R. B. Oliver, J. W. Allen, and R. A. Nance, "Eddy-Current Measurement of Clad Thickness," ASTM Book on the Symposium on Nondestructive Testing in the Field of Nuclear Energy, (In Publication).

cost savings can be effected in machining operations. An immersed-ultrasonic inspection should be used on this bar stock since this method allows a high inspection speed.[4,5] The completed end caps should also be inspected using a fluorescent penetrant method. Since these are very small objects, they could be handled in bulk in baskets, and the inspection cost per end cap would be small. This group of inspections used on the materials for the fabrication of the fuel capsule should cost less than forty-five cents per capsule.

The weld joint between each end cap and the tubing used to form the capsule should be inspected by both radiographic and fluorescent penetrant methods. Radiography was selected as the method of inspection for the weld closure because very few installations are qualified to perform an ultrasonic inspection of this weld joint. Successful radiographic inspection of this joint will require that the end cap have a straight cylindrical section joining into the tubular container and that there be a radio-transparent plug that insures that the uranium oxide slugs are held at least 1/8 in. beyond the weld joint. The radiographic inspection should use precision techniques involving a small focal spot x-ray tube, a long film-to-focus distance, appropriate filtration, and a very fine-grained film of the Eastman Type M variety.[6] If it can be assumed that twenty to forty weld joints can be simulataneously radiographed and if it is assumed that three views are employed to inspect each closure, then the cost of radiographic inspection and fluorescent penetrant inspection should be less than ninety cents per fuel capsule. It would be good practice to complete the final closure weld of the fuel capsule with a slight positive pressure of

---

[4] Al Barath, "Applications of Ultrasonic Inspection," J. of Soc. for Nondestructive Testing, 11, No. 7, 27, (September, 1953).

[5] R. B. Oliver, R. W. McClung, and J. K. White, "Immersed Ultrasonic Inspection of Pipe and Tubing," J. of Soc. for Nondestructive Testing, 15, No. 3, 140, (May, June, 1957).

[6] "Radiography in Nuclear Industry," Eastman Kodak Book, 1957.

helium. These elements could then be put in a vacuum chamber and examined for the presence of leaks with a helium leak detector. The complete inspection of the fuel capsules would insure that all capsules put into service have a good chance of achieving satisfactory and safe operation for the duration of their anticipated service life.

SECTION 5

REACTOR

5. REACTOR

CONTENTS

5.1 Pressure Vessel 5.1

5.1.1 Design Basis and Choice of Material 5.1

5.1.2 Pressure Vessel Support Ring 5.2

5.1.3 Helium Pipe Penetrations 5.4

5.2 Reactor Support Platform 5.10

5.2.1 Design Basis 5.10

5.2.2 Truss Configuration 5.12

5.2.3 Graphite Support 5.13

5.2.4 Platform Weight 5.13

5.3 Reactor-Vessel Assembly Support 5.13

5.3.1 Possible Support Configurations 5.13

5.3.2 Thermal-Sleeve Support Method 5.14

5.4 Graphite 5.14

5.4.1 Thermal Expansion 5.16

5.4.2 Wigner Growth 5.16

5.4.3 Lateral Stability of the Pile 5.20

5.5 Fuel Loading 5.20

5.6 Thermal Neutron Curtain 5.38

5.7 Shield Cooling 5.40

5.7.1 Design Objectives 5.40

5.7.2 Nuclear Heating of Concrete 5.40

5.7.3 Heating of the Concrete by Thermal Radiation and Convection 5.42

5.7.4 Cooling Air Distribution System 5.48

5.8 Control Rods and Drives 5.50

5. REACTOR

5.1 Pressure Vessel

5.1.1 Design Basis and Choice of Material: Perhaps the most important structural element in the entire system is the reactor pressure vessel. The only serious accident that has been envisioned for this type of reactor is a pressure vessel failure. The prime consideration in the design of the pressure vessel is the achievement of the highest integrity obtainable.

The detailed design is complicated by the problems of support of the pressure vessel itself, support of the graphite, and provision for the various penetrations including the ducts, control rod drives and the fuel loading equipment. Another important consideration is the minimization of thermal deformations. A related problem is that of the costs for steels having good strength characteristics at temperatures 700°F to 1000°F. Both of these considerations have led to the conclusion that the pressure vessel should be designed in such a way that the entire inner surface is swept by the low temperature gas returning to the reactor so that its temperature will stay close to a uniform value of 460°F at all power levels. This necessitates the installation of a baffle in the outlet gas region to isolate the pressure vessel surface from the hot gas leaving the reactor. The vessel itself must be cooled by a continuous flow of incoming gas. Direct cooling by cold air circulated over the outer surface from an external ventilating system has the disadvantage that the heat losses would tend to be excessive and it would be difficult to maintain a uniform temperature distribution. The situation resulting in the least heat loss and the greatest assurance of a uniform temperature structure throughout the pressure vessel is that obtained with circulation of 460°F return gas over the inner surface of the vessel. The external surface is insulated to minimize heat losses and to help equalize pressure vessel temperatures. The junctions between the pressure vessel and outlet pipes carrying hot helium must be isolated thermally by means of sleeves and insulation to avoid the severe thermal deformations which would be associated with high temperature gradients in the vicinity of the junctions. Figure 5.1 gives the critical dimensions of

the spherical vessel, which is 50 ft in diameter having a 300 psia working pressure, with a cold zone temperature of 460°F.

The decision to maintain the temperature of the pressure vessel below 700°F has resulted in simplification of the problems associated not only with design but also material selection and fabrication. The detailed considerations involved in the selection of a suitable pressure vessel material have already been discussed in Section 3.

Because of the particular design selected for the vessel support (refer to Section 5.3), pneumatic testing at one and a quarter times the working pressure rather than hydro-testing is required to prevent excessive bending stresses from being induced in the shell. However, Chicago Bridge and Iron Company has suggested that hydro-testing could be performed with little additional cost increment by providing temporary supports at the equatorial periphery. Mass spectrometer leak testing has been specified to assure gas system tightness and cleanliness. Leak tightness problems are discussed in Sections 6 and 9. Although cleanliness can be obtained by extreme care during construction, low carbon steel does not lend itself readily to this procedure so that the most economical solution to the cleanliness problem appears to be by sand blast cleaning and protecting the vessel with a dry atmosphere.

5.1.2 Pressure Vessel Support Ring: In order to simplify the design, a structural configuration has been selected which provides combined support for the pressure vessel and the reactor. A preliminary study of the reactor support problem revealed that the support platform weight could be minimized by locating the foundation reactions on a circle having a diameter of approximately 22 ft (see Fig. 5.1, Detail 'a'). A support skirt of this diameter is therefore provided (see Section 5.3) which transmits the reactor loads through the pressure vessel directly to the foundation. Thus the internal components of the vessel do not produce additional stresses in the shell. The only stresses induced in the shell are those from its own weight and the internal pressure (including the discontinuities at the various penetrations).

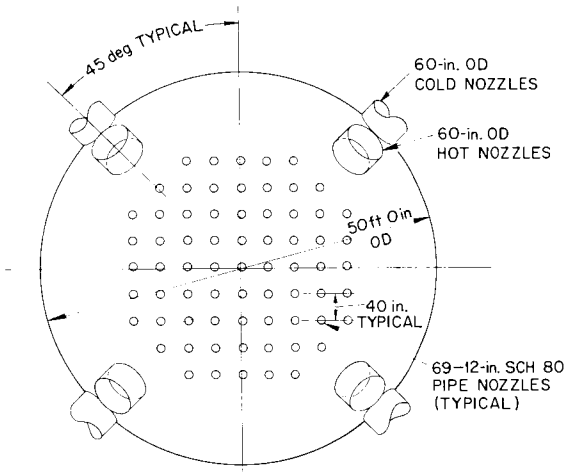

PLAN

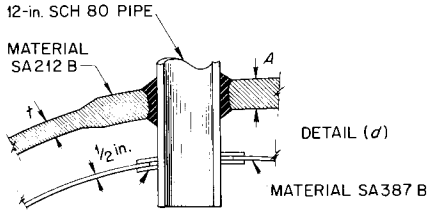

SLIP JOINT

t, PRESSURE VESSEL WALL THICKNESS (in.)	A, REINFORCED WALL THICKNESS (in.)
$3\frac{1}{4}$	$4\frac{1}{4}$
$4\frac{1}{4}$	$5\frac{3}{8}$

TYPICAL 12-in. NOZZLE DETAIL

NOTES:

1. VESSEL SHALL BE DESIGNED IN ACCORDANCE WITH SECTION VIII OF 1956 ASME BOILER AND PRESSURE VESSEL CODE AS A LETHAL VESSEL.
2. VESSEL SHALL HAVE ALL WELDS FULLY RADIOGRAPHED.
3. VESSEL SHALL BE STRESS-RELIEVED.
4. PRESSURE VESSEL SHELL SHALL BE CONSTRUCTED FROM SA212B

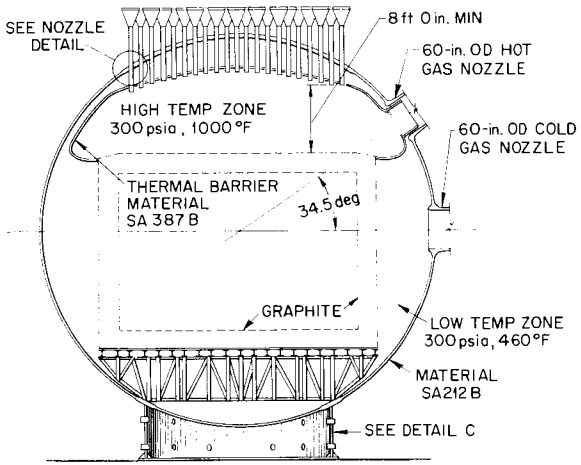

ELEVATION

DETAIL (a)

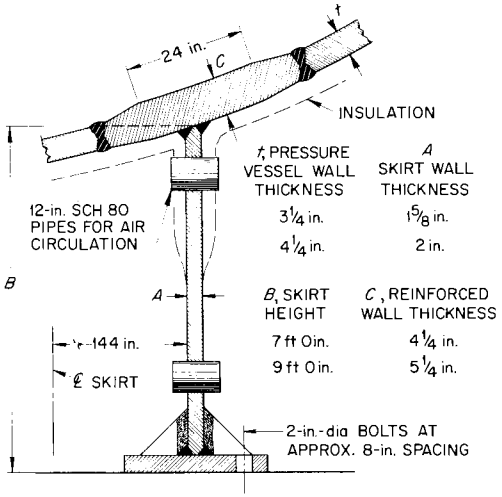

t, PRESSURE VESSEL WALL THICKNESS	A SKIRT WALL THICKNESS
$3\frac{1}{4}$ in.	$1\frac{5}{8}$ in.
$4\frac{1}{4}$ in.	2 in.

B, SKIRT HEIGHT	C, REINFORCED WALL THICKNESS
7 ft 0 in.	$4\frac{1}{4}$ in.
9 ft 0 in.	$5\frac{1}{4}$ in.

DETAIL (c)

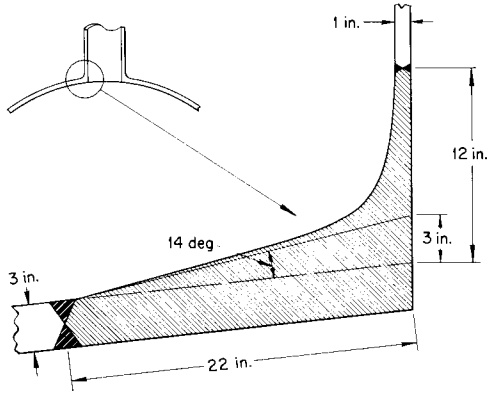

TYPICAL JUNCTION FORGING ACCEPTABLE FOR MAIN HELIUM PIPE PENETRATIONS.

DETAIL (b)

Fig. 5.1. Critical Dimensions of a Spherical Vessel.

The stress analysis of the vessel in the vicinity of the support reaction circle was based on the Esslinger method.[1] The idealized load diagram used for this purpose is shown in Fig. 5.2. These calculations were carried out for a variety of uniform thickness spherical shells each of which was subjected to a distributed line load equal to the vessel weight. The maximum meridional and circumferential stresses (weight reaction plus pressure) on the inside surface of the shell are shown in Fig. 5.2 as a function of shell thickness. It is seen that a 3-in. uniform thickness shell is subjected to stresses which exceed the 460°F limit. A 4-in. uniform shell, however, is able to support its own weight.

The selection of a 3-in. pressure vessel requires a reinforcing band 4 in. thick and approximately 24 in. wide at the reaction circle. An acceptable configuration is shown in Fig. 5.1, Detail 'c'.

5.1.3 Helium Pipe Penetrations: Two major structural problems are involved in the detailed design of the pressure vessel at the main helium pipe penetrations. These are: (1) the discontinuity stresses arising from the internal pressure in the vessel and the end thrusts from the pipes, and (2) the thermal deformations at the junction of the outlet pipe due to the difference in temperature between the pipe and the vessel.

Detailed analyses were carried out to determine the elastic stress distribution at the intersections of the pressure vessel and the main pipes. The analytical method[2] used for this purpose has been verified experimentally. Figure 5.3 shows representative membrane and bending stress distributions along the spherical surface as a function of angular displacement from the center of the pipe. This case was computed for a shell of uniform thickness with a ratio of shell thickness to pipe thickness of 2.5. Similar studies were undertaken to determine the local stress distributions around the control rod and fuel charging tube penetrations. The conclusions and recommendations drawn from these calculations are as follows:

---

[1] M. Esslinger, Static Calculation of Boiler Bottoms, (translation), ORNL CF 56-12-37.

[2] The method employed in these calculations is outlined by F. J. Stanek, in Spherical Segment with Circular Hole at Vertex Loaded Axisymmetrically Along the Edges, ORNL-2207, (December 19, 1956).

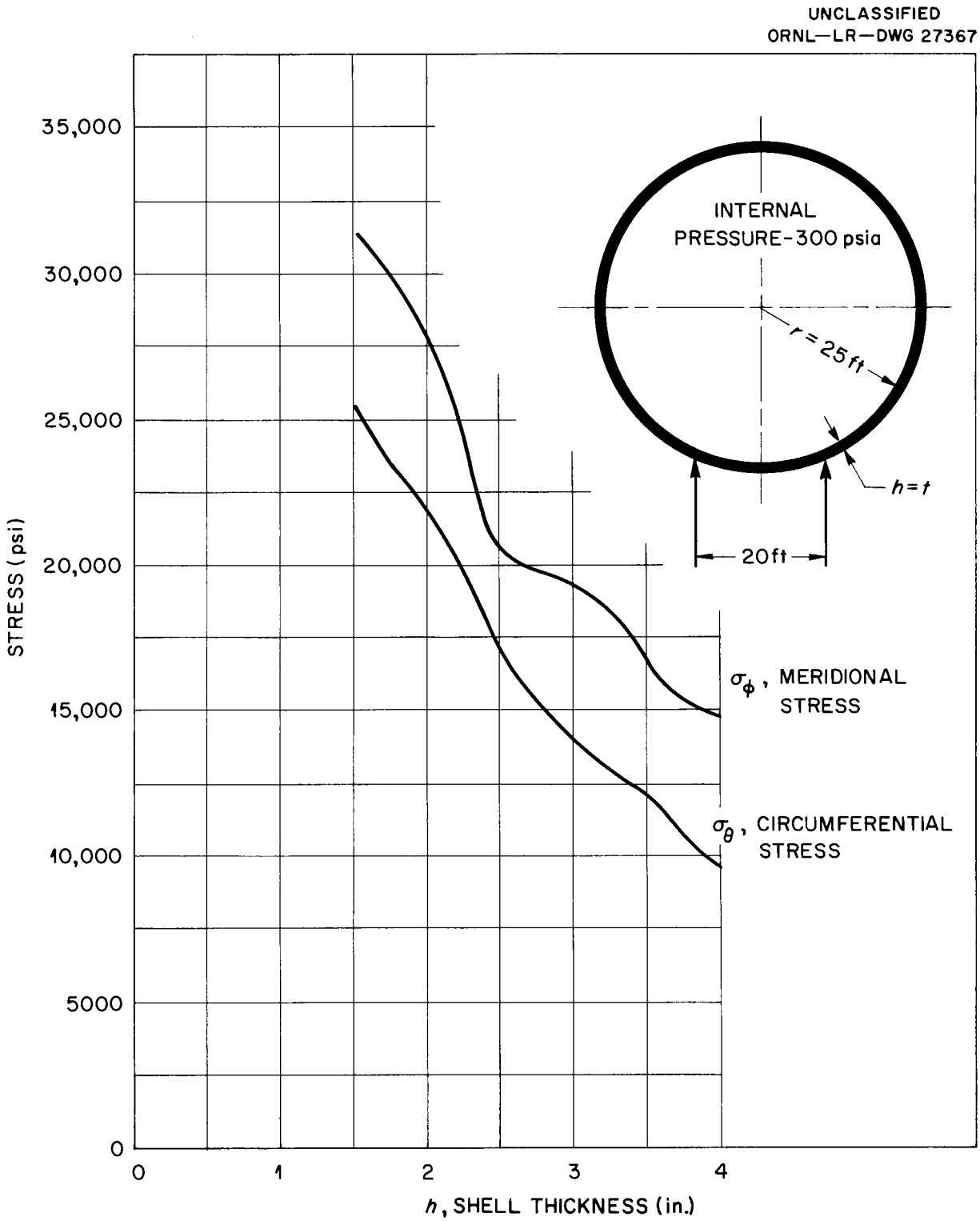

Fig. 5.2. Maximum Stresses in a Uniform Thickness Sphere Due to Support Load and Pressure.

UNCLASSIFIED
ORNL-LR-DWG 27369

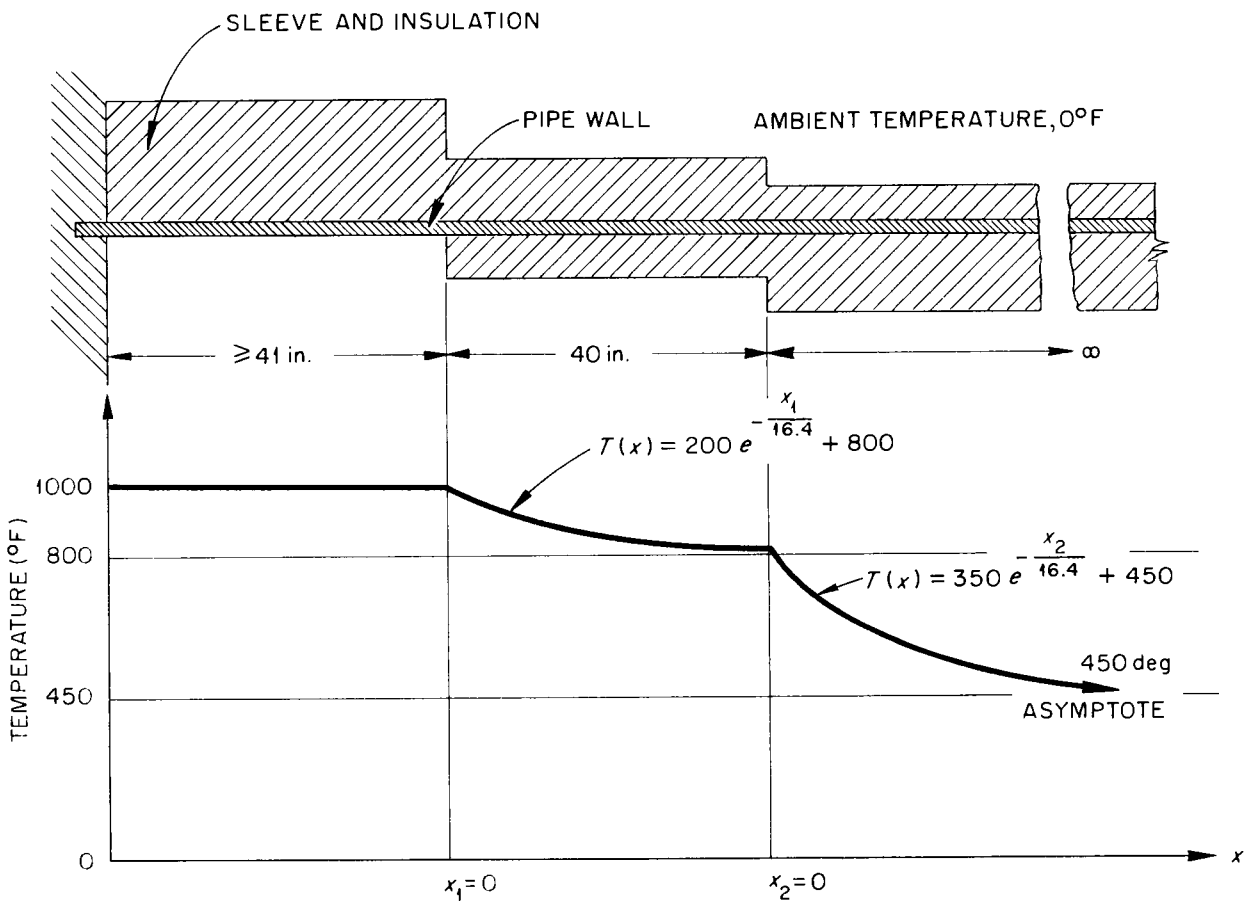

Fig. 5.3. Idealized Model of Thermal Sleeve and Temperature Distribution.

(A) Axial loads in the pipes due to internal pressure produce shell stresses of the same magnitude as those due to pressure in the vessel only. End thrusts in the pipes must therefore be supported externally so as to free the vessel of additional loads.

(B) Discontinuity stresses at the main pipe junctions are in the order of twice the usual spherical shell pressure stress (see Fig. 5.4). Hence, local reinforcement is required. Figure 5.1, Detail 'b', shows a structurally acceptable forging design.

(C) As the pipe diameter is decreased the shell stresses increase only slightly. Hence, in the area of the fuel charging tube penetrations, the shell thickness should be increased uniformly from 3 to 5 in. (see Fig. 5.1, Detail 'd'). This thickness will accommodate the overlapping of the stress distributions between adjacent holes.

Under full-power operating conditions, the temperature of the pressure vessel will be 460°F and that of the helium outlet pipe, 1000°F. This temperature difference gives rise to excessive thermal deformations around the junction. Tolerable values can be achieved, however, by controlling the radial heat flow rate out of the pipe through the addition of a suitable combination of inside and outside insulation.

Figure 5.3 shows an idealized model of the insulated sleeve arrangement and the resulting axial temperature profile. A two-break temperature distribution was selected when it was found that the thickness required for a single uniform layer of insulation was excessive if the thermal strains in the pipe were to remain within acceptable limits. The division indicated takes advantage of the greater strength of the metal in the colder section. The detailed temperature calculations were based on estimated thermal conductivities of asbestos in helium obtained from simple volume fraction corrections to the known conductivities of each material (see Fig. 5.5).

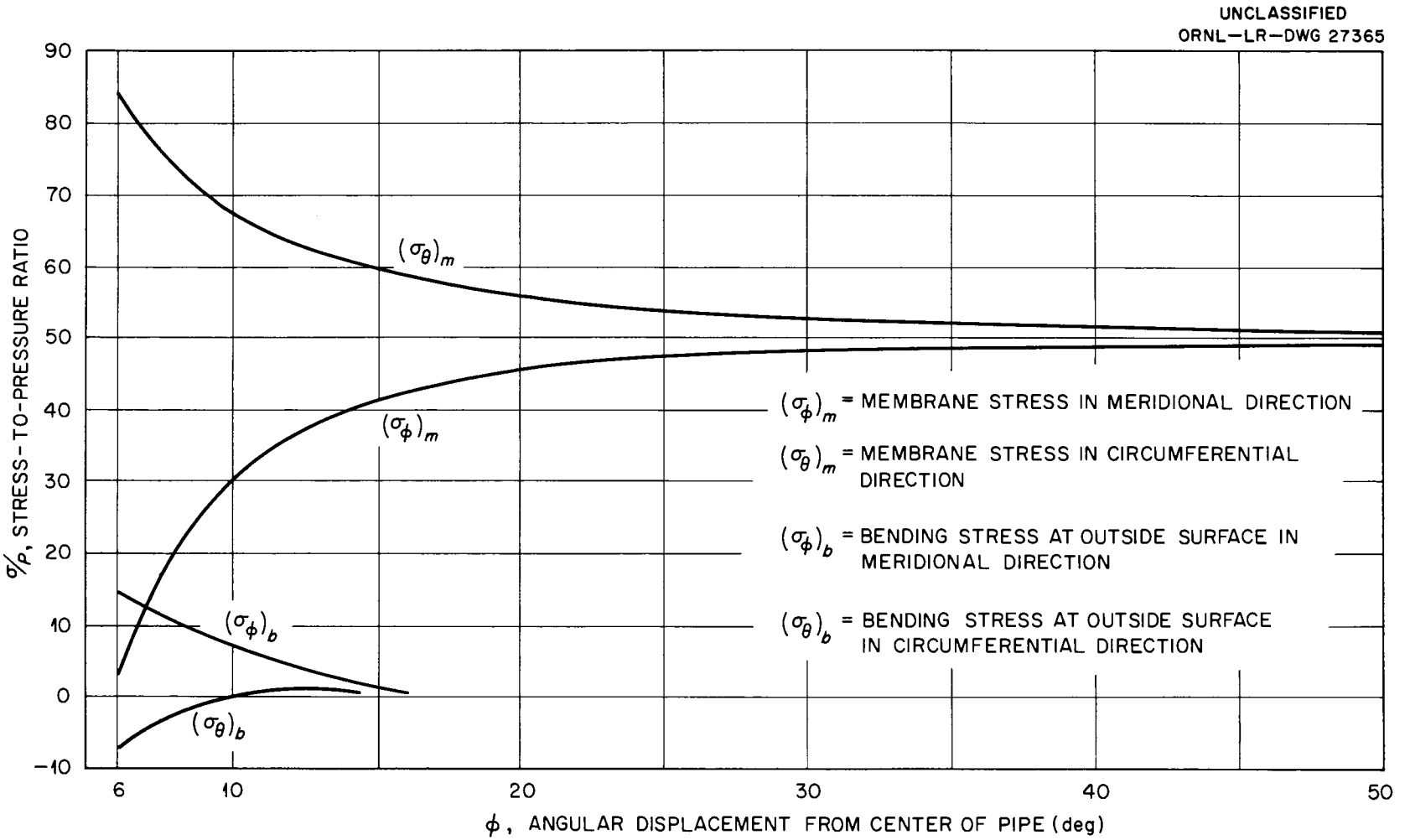

Fig. 5.4. Discontinuity Stresses in Spherical Shell Due to Internal Pressure Only.

UNCLASSIFIED
ORNL-LR-DWG 27370

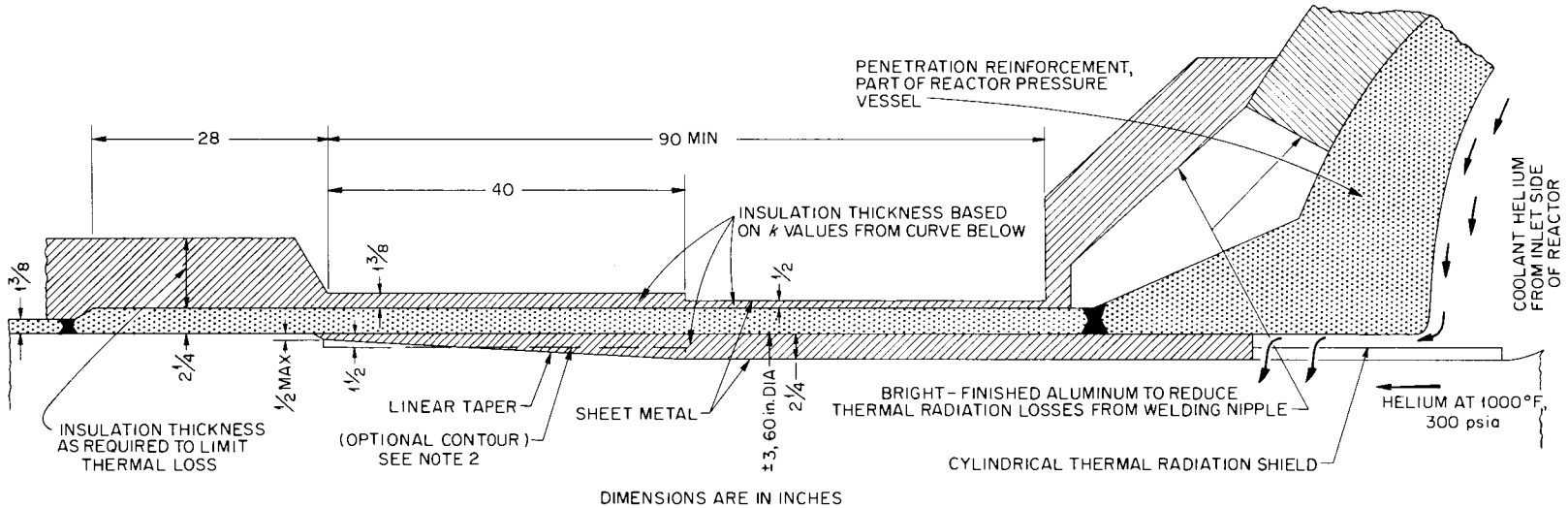

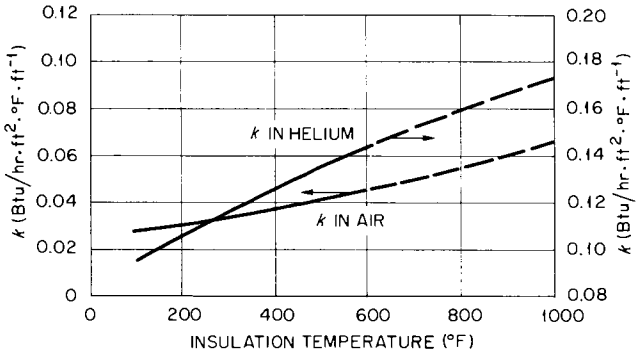

Thermal Conductivity of Asbestos vs. Temperature.

NOTE:

1. INSULATION IS ASSUMED TO BE ASBESTOS AT APPROXIMATELY 11 lb/ft^3
2. IT IS PERMISSIBLE TO REPLACE THE TAPERED SECTION WITH A CYLINDRICAL LAYER OF INSULATION AS SHOWN BY THE DASHED LINE. THE TAPERED SECTION IS BASED SOLELY ON FLOW CONSIDERATIONS.

Fig. 5.5. Thermal Sleeve Design for Main Helium Pipes.

The temperature profile in Fig. 5.3 was used in an elastic thermal stress analysis of the pipe-shell junction using the method of Cooper et al.[3] It is recognized that an accurate study of the problem should account properly for the plastic deformations and thermal fatigue developed during the operating life of the structure. In order that the present treatment suffice as a first approximation, the computed thermal stresses were kept well within the ASME allowable high-temperature elastic limits, viz., 7500 psi at 1000°F and 15,000 psi at $T \leq 750°F$.

5.2 Reactor Support Platform

5.2.1 Design Basis: The weight of the reactor assembly (core and reflector) is carried on a 35-ft diameter platform which is supported by a system of radial trusses (see Fig. 5.6). Directly under the reactor is a 2-in. thick floor plate which provides the bearing surface for the graphite. This plate is perforated by a system of circular holes located concentric with the fuel rod channels so as to allow the helium coolant to pass up through the floor. The plate itself bears directly upon a parallel array of 10-in. Junior beams placed on approximately 2 ft centers. This system of beams rests upon the radial array of trusses.

The truss configuration consists of three basic elements, viz., types I and II, type III and types IV and V. Types IV and V are full-length structures which extend across a diameter of the platform and divide the floor into 45° sectors. Type III and types I and II are short trusses which extend radially inward from the periphery of the platform and serve as intermediate supports for the beam grid. This complete system of trusses is supported on a 22-ft dia circle which transmits the reactor weight directly to the pressure vessel support skirt. The 22-ft dia circle was selected in an attempt to minimize the maximum moment in the through trusses (IV and V). About 40% of the total reactor weight, which is assumed to give a uniform pressure on the plate, is carried inside this load circle; the remaining 60% acts as an overhung load.

---

[3] W. E. Cooper, M. T. Roche, and J. L. Noble, Stresses in a Semi-Infinite Thin Walled Cylinder Caused by an Exponential Temperature Distribution, KAPL-973.

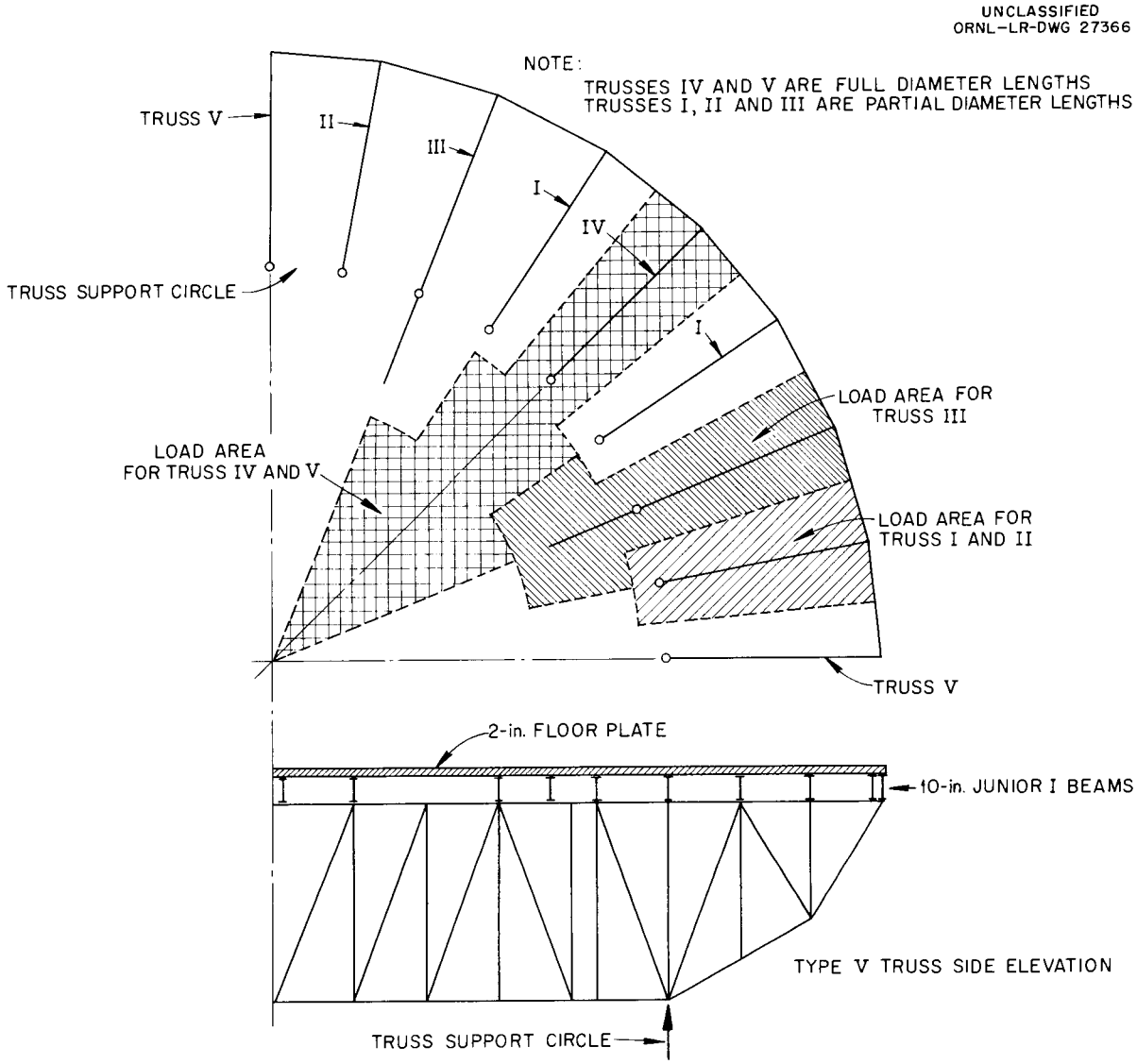

Fig. 5.6. Platform Load Distribution and Truss Support.

A uniform load of 4000 lb/ft^2 was used as the design condition for the platform. Figure 5.6 shows the horizontal distribution of this load for the three basic truss elements. The selection of the various struts in each truss was based on a 16,000 psi allowable stress. Since the platform weight is less than 10% of the supported load no attempt was made to include this weight in the design load.

The proposed platform configuration has not been optimized from the standpoint of minimum weight. However, it is believed that this design is a good approximation to an acceptable solution and will yield representative figures for cost estimates.

5.2.2 Truss Configuration: A planform of the radial arrangement of the trusses is shown in Appendix B, Fig. B.1. The through members (IV and V) are spaced at intervals of 45°, the intermediate trusses (III) at 45°, and the cantilevered trusses (I and II), at 22-1/2° intervals. Each of the three basic truss configurations is supported on the 22-ft dia circle. Whereas the major through trusses are maintained in equilibrium by a symmetric arrangement of reactions and loads, the partial trusses (I through III) require balancing moments at their inboard ends.

Appendix B, Figs. B.3–B.7, show side elevations of the 5 detailed truss designs required (note that only 3 basic configurations are involved). The location and magnitude of the floor loads from the Junior beams and from the support reactions are indicated in the figure. These correspond to the floor load distributions shown in Fig. 5.6. Note that this arrangement yields a fairly uniform loading on each truss. The balance moments at the inboard ends of the partial trusses appear principally as couples in the vertical plane which are transmitted to adjacent trusses by diagonal members located in the top and bottom horizontal planes of the platform (see Appendix B, Fig. B.1). Ultimately, each couple is resisted by the chords of a through truss where they appear as additional axial loads in the chords.

The chord and strut members in each truss consist of standard angle sections; acceptable sizes are indicated in each diagram. No attempt has been made to provide joint or gusset details.

5.2.3 Graphite Support: Appendix B, Fig. B.2, shows the platform for the parallel lattice of Junior beams which support the floor plate. A more or less circumferential arrangement has been selected in order to remain within the maximum beam span limitation of 2 ft. The 2-in. floor plate is a conservative choice for the selected beam spacing; however, it is expected to serve also as a thermal shield for the bottom of the reactor pressure vessel. The floor plate panels are to be attached to the trusses by tack welding after leveling with shims inserted over the panel points.

5.2.4 Platform Weight: The total weight of the platform shown in Appendix B, Figs. B.1–B.7, is 143,650 lb. The breakdown is as follows:

Truss	I : 8 at 1020 lb each	
	II : 8 at 1020 lb each	
	III : 8 at 2560 lb each	
	IV : 4 at 3360 lb each	
	V : 4 at 3680 lb each	
		65,000 lb
Laterals		3,700
Floor Plate (2 in. steel with holes)		68,200
Junior Beams		6,750
Total		143,650 lb

5.3 Reactor-Vessel Assembly Support

5.3.1 Possible Support Configurations: In an attempt to select the most practical and economical support configuration, three basically different designs were considered, namely, (1) roller bearing, (2) flexible column, and (3) thermal sleeve. Each method provides for the support of the complete reactor-pressure vessel assembly by means of suitable compression members located on a 22-ft dia circle beneath the vessel. Each method also allows for the free thermal expansion of the vessel (at 460°F) relative to the foundation (at ambient). All three methods were found to be feasible. The thermal-sleeve support, however, was judged to be the most practical and economical.

5.3.2 Thermal-Sleeve Support Method: The thermal-sleeve concept employs a continuous cylindrical skirt 2 in. thick, 22 ft in diameter and approximately 7 ft high (Fig. 5.1, Detail 'c'). The bottom of the skirt, which is embedded in the concrete foundation, rests directly upon a steel plate for improved bearing conditions, and the top is welded to the pressure vessel at the center of the 4 in. thick, 24 in. wide vessel support ring. This arrangement allows for the growth of the vessel in the same manner as a thermal sleeve in a pipe-vessel connection.

Calculations indicate that by providing complete insulation over the top 24 in. of the skirt and taking into account the heat losses by natural convection over the remaining exposed portion, the resulting temperature distribution takes the form shown in Fig. 5.7. The exponential decay indicated in the figure (with m = 0.9 ft) gives a first approximation to the actual distribution.

A stress analysis based on the assumption of a completely elastic system was carried out for this skirt design using the method[4] of KAPL-973. The choice of the final configuration was based on the requirement that the maximum shear stress due to the combined thermal and compression loads was within the allowable at the maximum temperature of 460°F. As indicated previously in connection with the design of the helium-pipe thermal sleeves, this approach is conservative.

An analysis of the buckling stability of the skirt indicates that the proposed design is satisfactory.

5.4 Graphite

The fuel elements for the gas-cooled reactor are located on an 8-in. square lattice. The core consists of rectangular graphite blocks 8 in. x 8 in. x 40 in., with the fuel channel bored through the center parallel to the long axis. Upper and lower reflector blocks are 8 in. x 8 in. x 30 in. Each channel comprises 6 core blocks stacked end to end, with a reflector block at each end of the stack; fueled length is 20 ft and over-all length is 25 ft. A pilot in the lower end of each block fits into a counter bored hole in the top of the block below, and assures alignment of the cooling hole

---

[4] W. E. Cooper, M. T. Roche, and J. L. Noble, op. cit., p. 5.10.

UNCLASSIFIED
ORNL-LR-DWG 27657

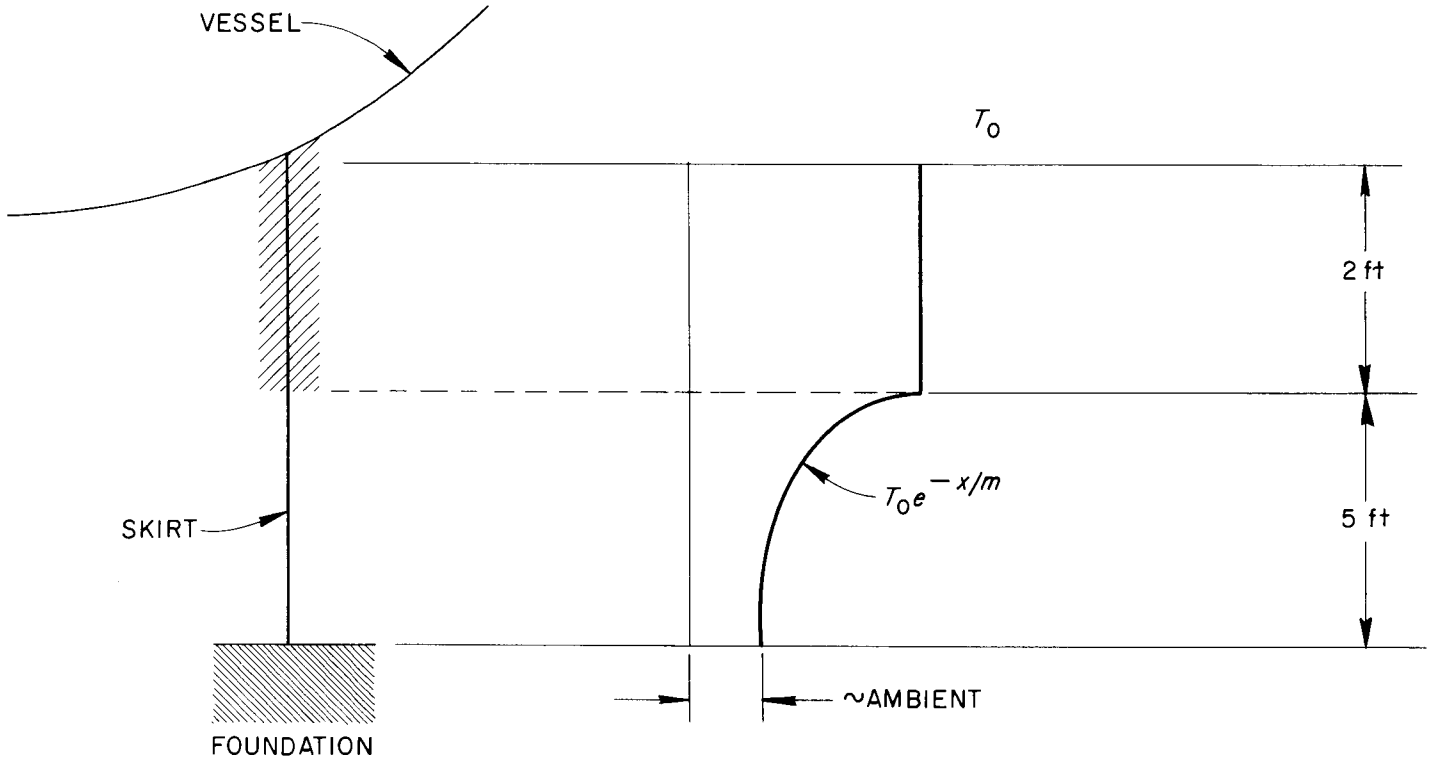

Fig. 5.7. Temperature Distribution in Pressure Vessel Support Skirt.

from block to block as shown in Figs. 5.8 and 5.17. Stability of the pile as a whole is provided by its own weight and by the lateral restraints discussed below. The principal problems associated with the graphite structure are discussed in the following paragraphs.

5.4.1 Thermal Expansion: No provision is made to allow the bottom course of graphite to move relative to the steel plate that supports it. Thermal expansion coefficients are about $6 \times 10^{-6}/°F$ for the steel and about $3.6 \times 10^{-6}/°F$ for the graphite. Since the bottom of the pile will normally be at 460°F, and the diameter of the pile is 420 in., the relative expansion of the support plate is about 0.4 in. on the diameter, or about 0.008 in. per graphite block. Thus, a gap of 0.008 in. will appear between adjacent blocks, at the bottom, as a result of thermal expansion. The bottom of the outermost fuel channel will move outward from the axis of the pile by 0.43 in. The top of the same channel, at 1000°F, will move out from the center by 0.62 in. The top of the lower reflector block of this channel will move out from the pile axis by 0.26 in. This will produce an angle in the channel of 0.4 degree, and an apparent 0.24 in. displacement of the bottom of the channel when viewed from the top. However, this break will occur at the lower reflector-core interface, and no harm will result. The ends of the lower reflector block will have a cylindrical surface, with 30-in. radius of curvature, and with the curvature in the plane containing the block and the axis of the pile. This curvature will accommodate the slight tilting of the second course of blocks relative to the bottom course. Bearing loads are still far below the allowable stresses for graphite.

The increase in the circumference of the pile is 3.0 in. at the bottom and 4.5 in. at the top. This expansion must be accommodated by the hoops that surround the reactor in tension at the parting planes between successive courses of blocks (see Section 5.4.3).

5.4.2 Wigner Growth: No allowance is made for dimensional changes in the graphite resulting from irradiation. It is well known that the change in linear dimensions of graphite, for a given exposure level, is a marked function of the graphite temperature during irradiation. Since the minimum graphite temperature in the reactor, during operation, will be greater than 460°F (238°C) a negligible change in graphite dimensions is expected to occur.

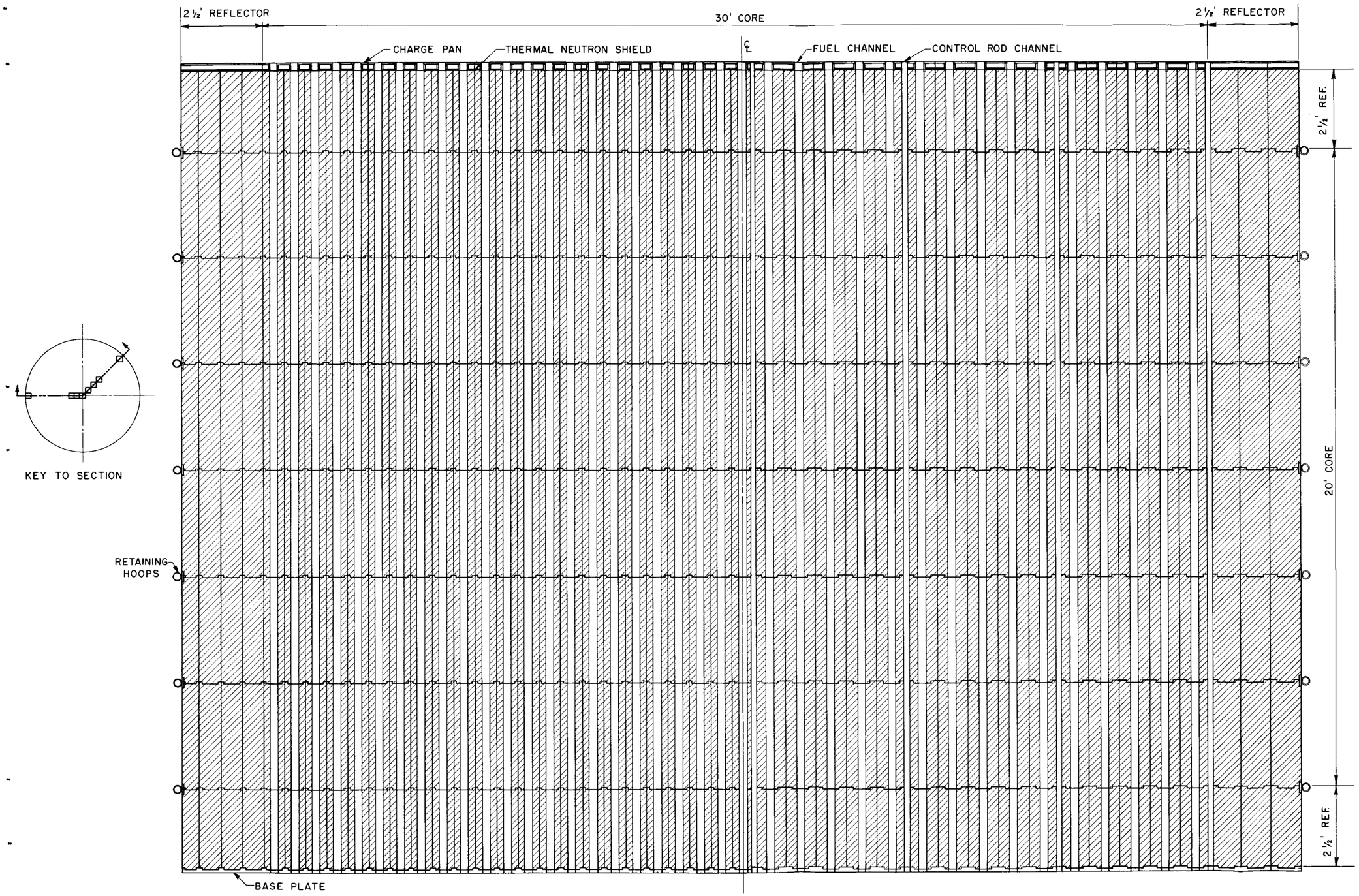

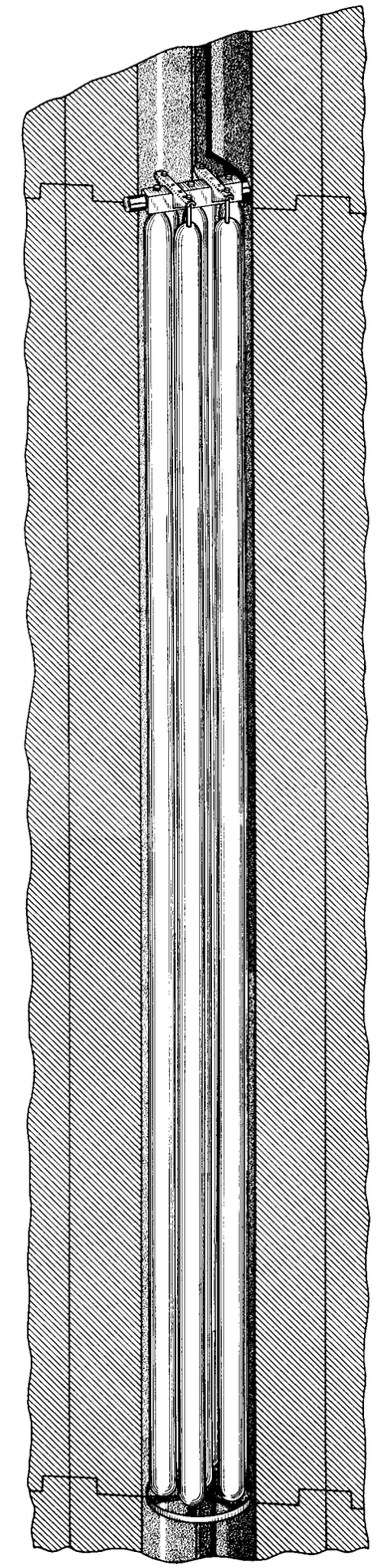

Fig. 5.8. Section of Graphite Core and Reflector.

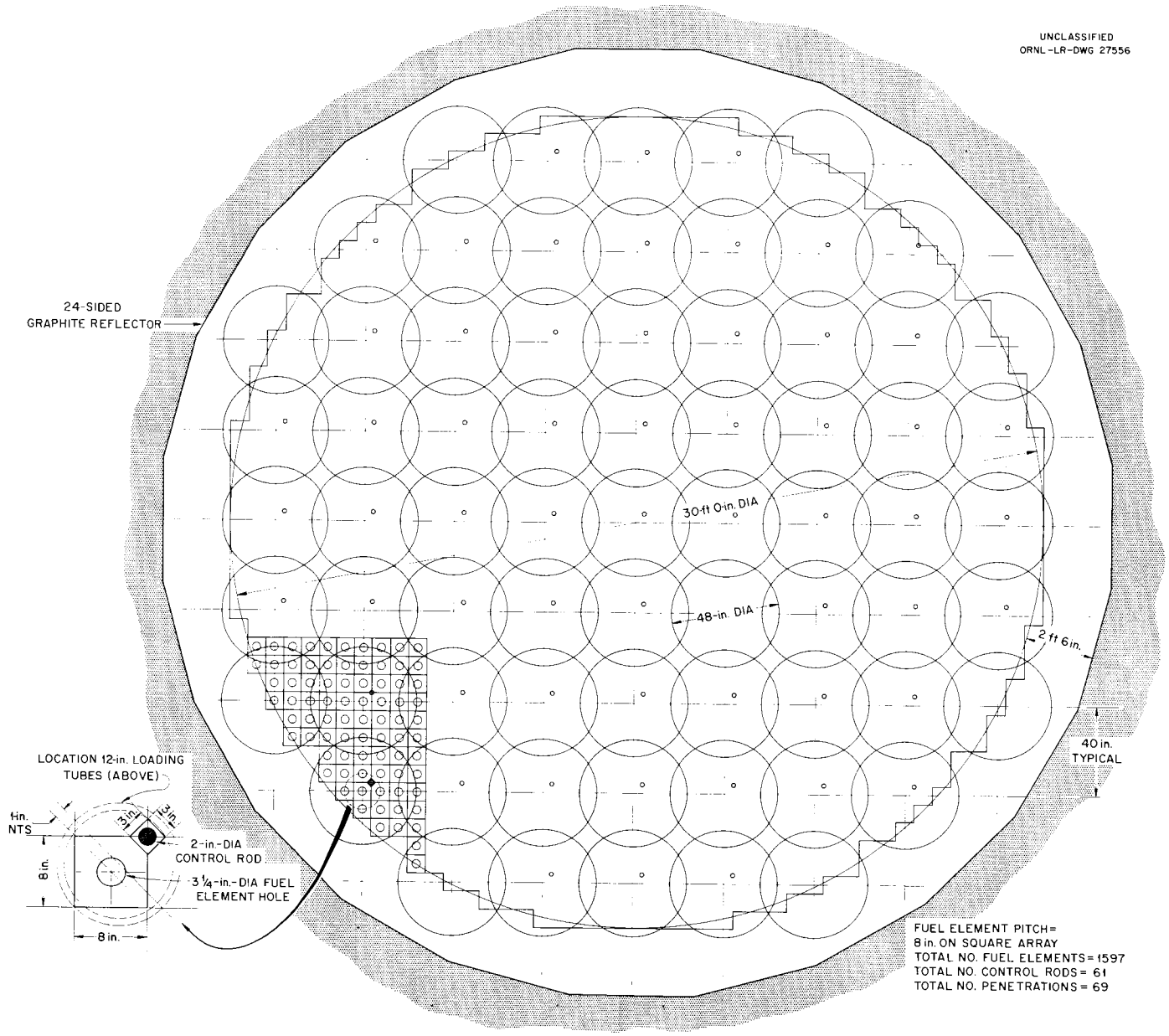

Fig. 5.9. Proposed Layout of Fuel Channel and Control Rod.

5.4.3 Lateral Stability of the Pile: The pile consists essentially of a collection of independent vertical articulated columns, each bearing on the steel support plate. Lateral support must be provided which will keep the pile from falling apart, either under normal conditions or under such unusual loads as might be imposed by an earthquake, and which will still accommodate the thermal expansion discussed above. The general solution to this problem that was adopted for the Calder Hall reactors seems like a very satisfactory one. At the parting planes between successive layers of graphite blocks, tubular hoops surround the reactor, bearing on flat steel plates which in turn bear on the graphite. (See Fig. 5.8). These hoops are of a unique multitube design which effectively increases, by a factor of 3 or 4, the elongation that steel can undergo without exceeding the elastic stress limit, and in addition can be made to approximate the thermal expansion characteristics of the graphite.

The entire pile will be prevented from moving laterally as a unit (as might occur during an earthquake) by a series of horizontal struts projecting outwards towards the pressure vessel. These would not normally touch the pressure vessel, but would limit any lateral displacement to about 1 in. Obviously, any event that would produce such a displacement would in any case require thorough inspection and possibly extensive repairs of the whole system.

5.5 Fuel Loading

The inherent characteristics of this reactor system require that fuel be introduced into and removed from the reactor fuel channels by means of remotely operated fuel handling equipment. The selection of the vertical cylindrical graphite core with round vertical fuel channels derived, in part, from a consideration of the effects upon the fuel handling system of a number of core and fuel channel configurations.

With the vertical cylindrical core, the fuel handling operations can in principle be carried out from either the top or bottom face, or charging can be done from one face and discharging from the other. Because cost provides a strong incentive to minimize both the size and number of penetrations through the reactor pressure vessel, fuel handling access was limited

to one face. The top face was selected because this area does not interfere with the support structure for the graphite and pressure vessel and because the decision to hang the fuel capsules in tension required that the fuel handling equipment approach the fuel elements from above. The outstanding advantage associated with bottom charging and discharging is the lower coolant temperature at the bottom of the core during operation. Since fuel charging and discharging will not be carried out during reactor operation, this advantage is not significant.

Section 2.4 presents the figures on expected fuel element reactivity lifetime and indicates that about 10% of the fuel elements would be replaced within the reactor per year. In consideration of the long anticipated fuel element service life, it was felt that shutdowns for inspection and maintenance of various plant equipment items would occur as frequently as refueling operations will be required.

A general review of the functions of the fuel charging system is helpful to an understanding of the proposed equipment. The 1,597 fuel channels through the graphite core must be loaded initially with fuel elements and thereafter any element must be capable of being removed and replaced. Once the reactor has operated at power, the radiation intensity at the surface of the spherical pressure vessel will be much above the usual tolerance dose level, and the closest approach to the system for fuel handling purposes will be on the fuel loading floor which is separated from the pressure vessel by a 9-ft-thick concrete biological shield. From this floor, the fuel must be placed in or removed from the reactor fuel channels by a remotely operated mechanical system. The first requirement of such a system obviously is some number of access openings through the concrete shield into the pressure vessel above the top face of the graphite. From the fuel handling point of view, one vertical pipe penetration or charge tube directly above each of the 1,597 fuel channels would be desirable. It is not reasonable to provide such an arrangement because the penetrations through the pressure vessel would be at least 6 in. pipes on the 8 in. square centers of the fuel channels. The solution selected is the division of the top face of the graphite into square groups of twenty-five fuel channels, as shown in Fig. 5.9 .

The use of a single charge tube above the center channel of each group or partial group of twenty-five channels reduces the shield and pressure vessel penetrations by a factor of twenty-five. However, the solution to one problem leads to another; twenty-four of the twenty-five fuel channels are not directly accessible to a fuel handling mechanism suspended through the charge tube. A device called the "charging chute" has been designed to overcome this problem. To accommodate this chute, and also a control rod, the charge tube is 12 in. in diameter and is arranged as shown in Fig. 5.10. Just above the top of the control rod actuator housing extension from the charge tube, a remotely operated slide valve is installed as shown in Fig. 5.11. This valve is provided to minimize displacement of helium from the reactor by air during periods when the charge tube is opened.

The distinction between the charge tubes and charging chute is emphasized for the sake of clarity. The 12-in. dia charge tubes extend from the fuel loading floor down through the shield and penetrate the pressure vessel. They are permanently installed extensions of the pressure confining system. Their upper ends are approximately flush with the fuel loading floor and are sealed by bolted flanges with double concentric gasket grooves fitted with soft aluminum gasket rings and solder sealed around their perimeter. These tubes also serve as the penetrations through which the control rods are installed and operated.

The charging chute is a long pipe which is inserted down through the charge tube after the reactor system has been shut down and reduced to approximately atmospheric pressure. The chute is removed after completion of the fuel charging and/or discharging operation. The bottom end of the chute registers in the central hole of any twenty-five hole group or partial group. Each of the twenty-four eccentric fuel channels lies on one of five circles around the central channel. Thus each of the twenty-four channels is specifically located by one polar and one radial coordinate with respect to the central channel. The charging chute provides access to these eccentric channels by means of a chute extension located at the bottom end of the chute and supported on a system of arms which position the chute extension radially. The arms form a linkage which maintains the chute extension parallel to the central column of the chute. The ends of

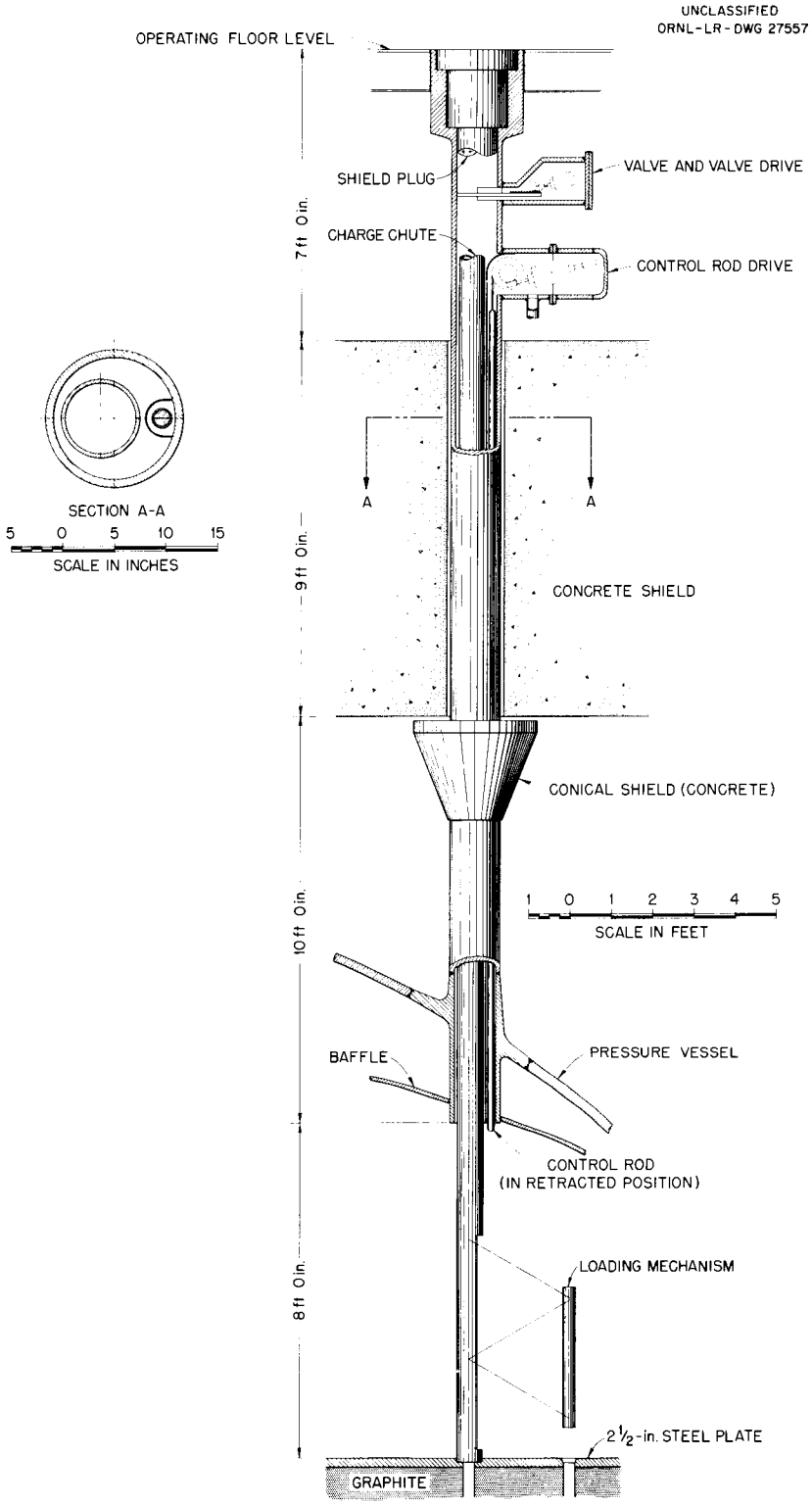

Fig. 5.10. Proposed Layout of Combined Control Rod and Fuel Loading Chute.

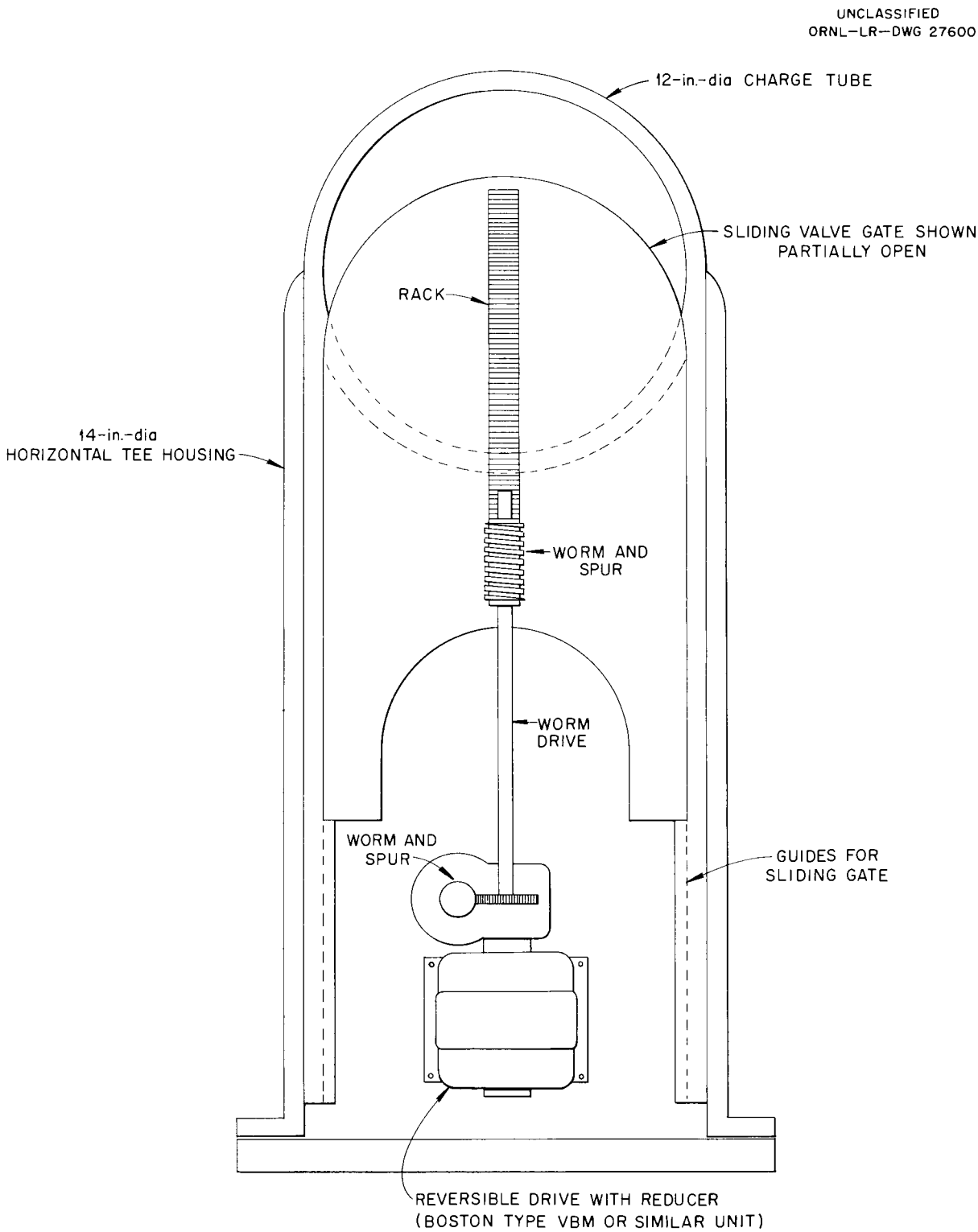

Fig. 5.11. Slide Valve in the Charge Tube at the Control Rod Drive Gallery Level.

the linkage arms are fixed to the main column of the charging chute through two slides which move vertically in a pair of tracks attached to the inside of the main column. The arms are positioned for a given radial displacement of the charging chute extension by moving the slides vertically. The radial displacement increases as the top and bottom slides move toward each other. The slides are driven by a pair of threaded drive screws which extend to the top of the charging chute where they are fitted to their drive mechanisms. The use of two drive screws permits vertical positioning of the chute extension. An alternate design using a single screw with right hand threads at the top and left hand threads at the bottom would be adequate to position the chute extension radially. This single screw, however, would not permit vertical positioning of the chute extension by means of the drive screw. Drawings of the top and bottom ends of the charging chute appear as Figs. B.8 and B.9, respectively, of Appendix B. Figures 5.12–5.15 are photographs of a model of the lower end of the charging chute. Figure 5.12 shows the charging chute extension in the central position, and Fig. 5.13 shows the chute extension positioned radially. Figure 5.14 affords a view of the central column of the charging chute and shows the drive screws, slides, and linkage arm attachments. The charging chute is shown positioned over a channel in Fig. 5.15 with the fuel element indexed into the circumferential hanger slot with the grab still in position.

The charge pan serves as the reference grid for positioning the charging chute. It is a steel plate placed over the top surface of the graphite and contains holes that register with the fuel and control-rod channels. It is designed in square sections, each of which covers one group of twenty-five fuel channels. These pans are keyed to the graphite to insure proper alignment with the graphite channels as thermal expansion takes place in the system. Each square section of the charge pan is designed to rest on the graphite around its perimeter, thus bridging the area under the pan to allow space for the 0.5-in.-thick pyrex-glass thermal-neutron curtain and the one-half inch diameter gas sampling tubes provided to monitor the effluent helium stream from each individual fuel channel for the detection of burst fuel capsules. These tubes will be grouped at one corner of the charge pan and rise vertically to avoid interference with the charging chute

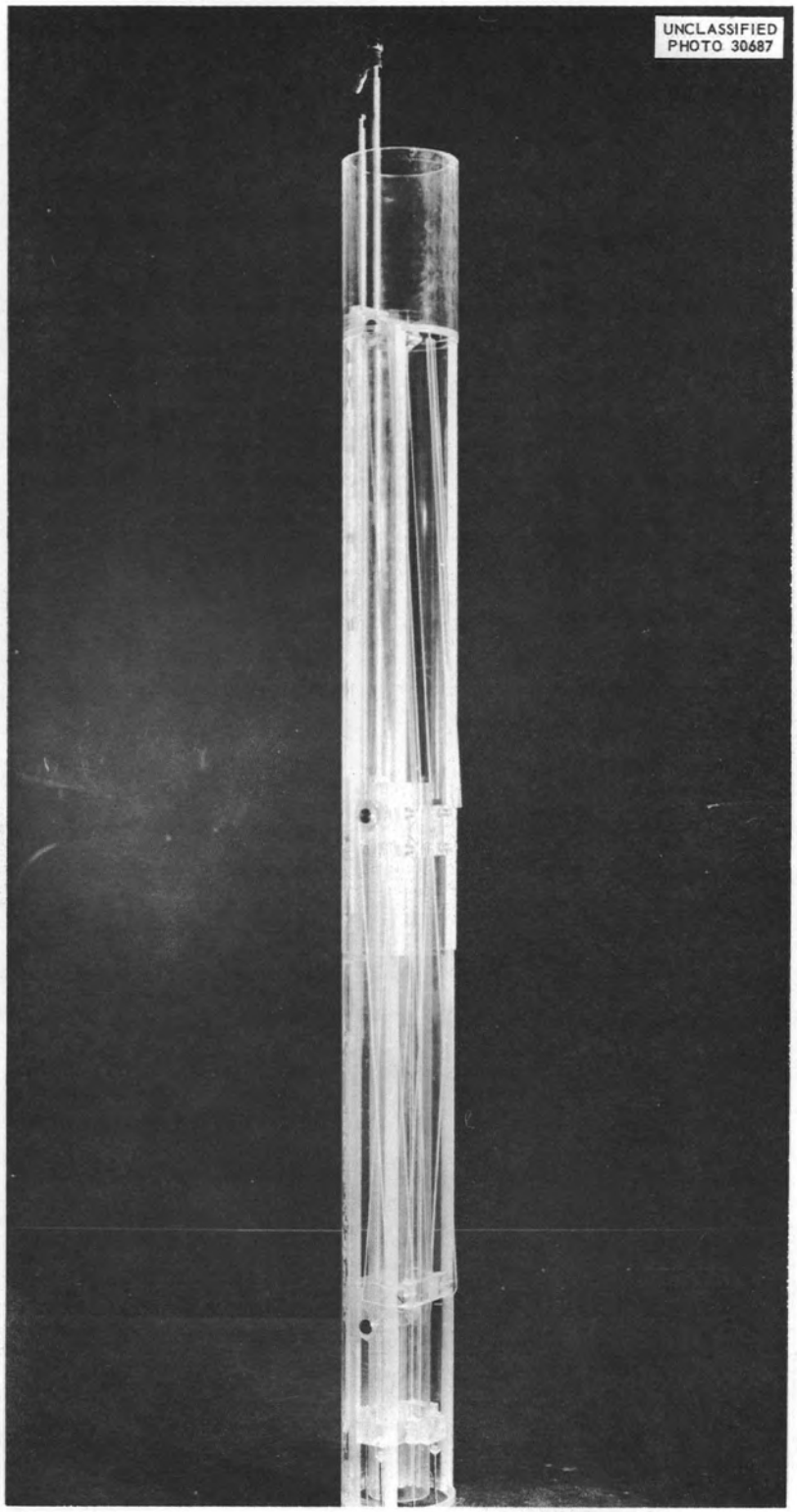

Fig. 5.12. Lower End of Fuel Charging Chute with Extension in Central Position.

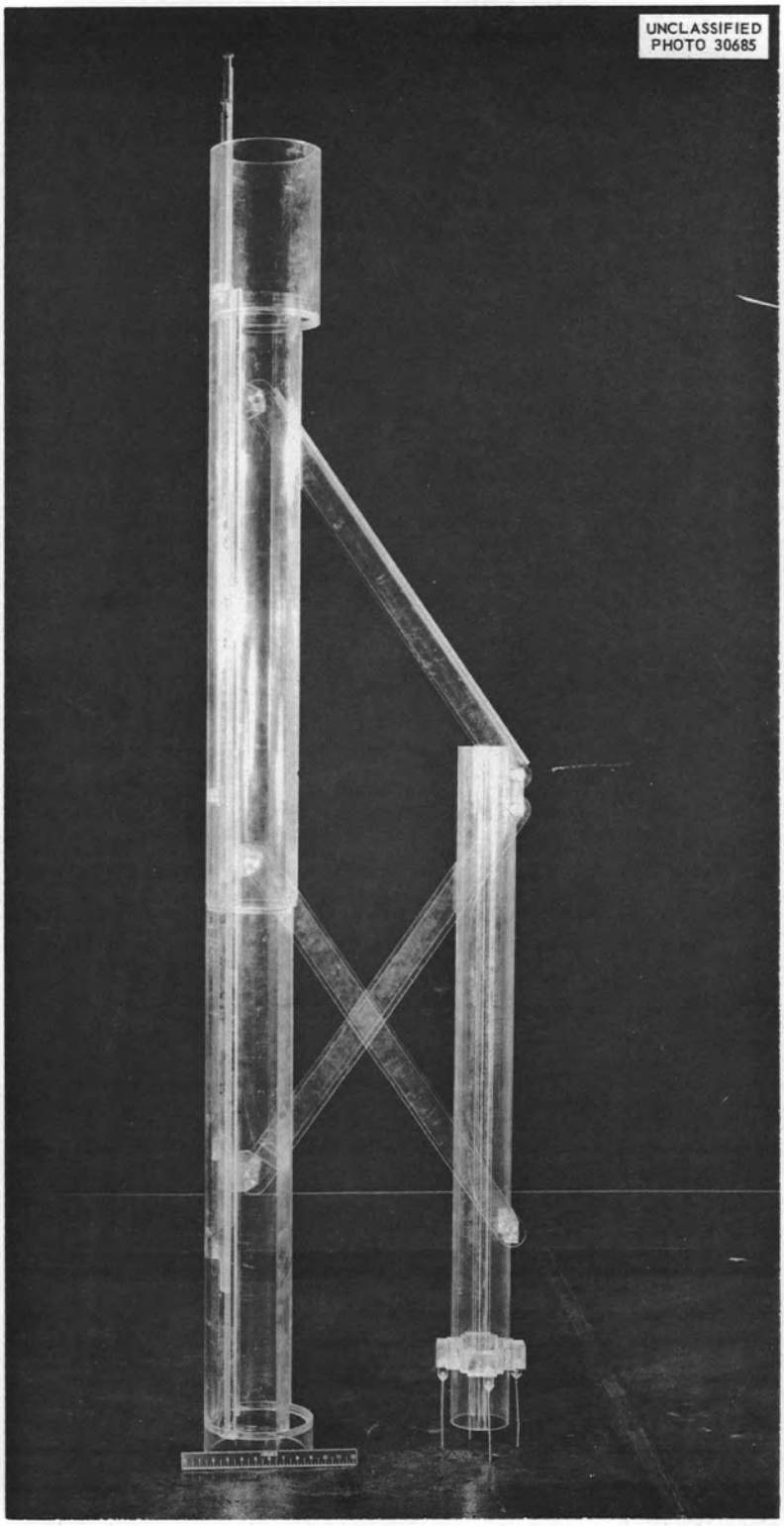

Fig. 5.13. Lower End of Fuel Charging Chute with Extension Positioned Radially.

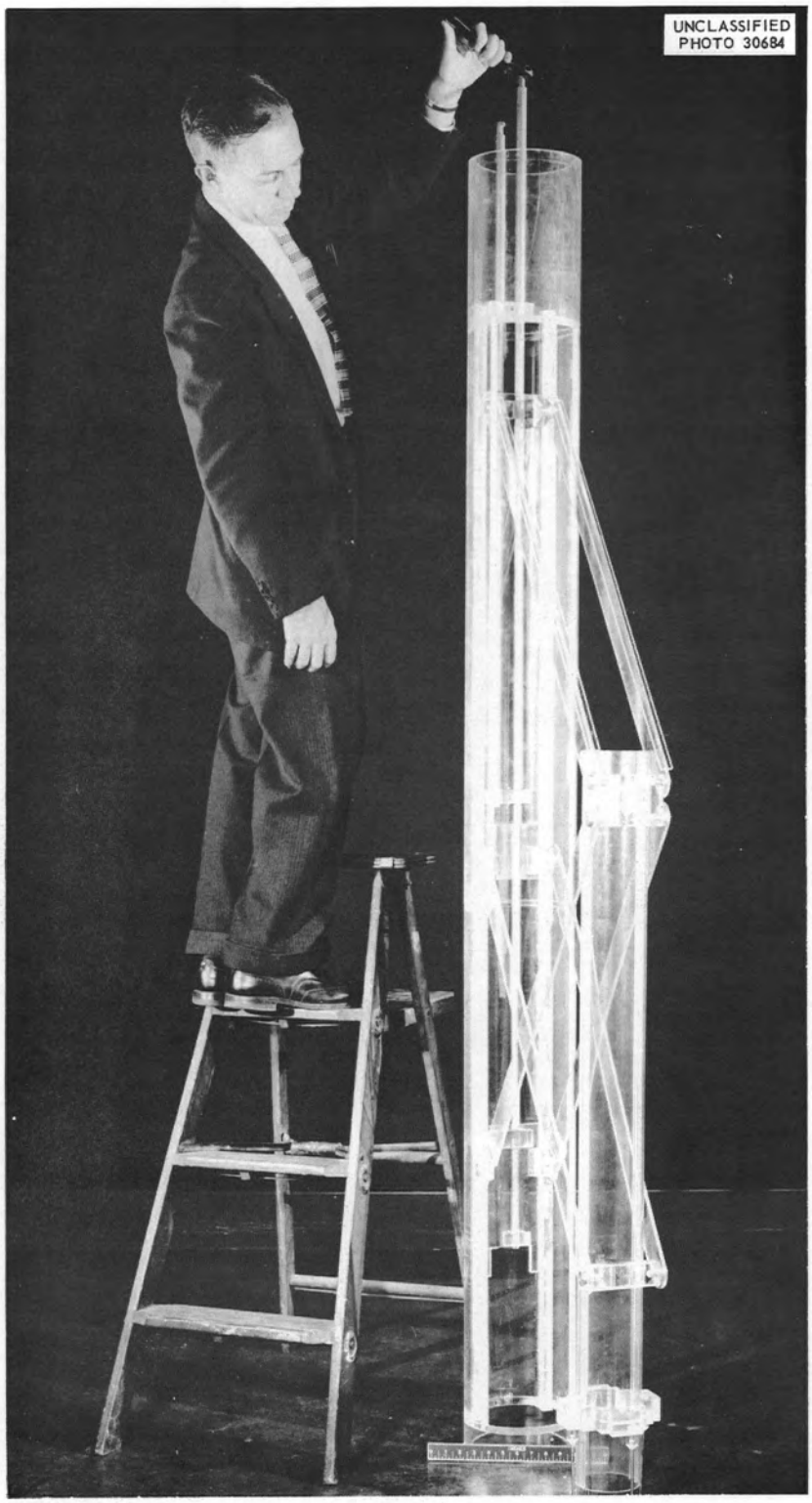

Fig. 5.14. View into Open Side of Fuel Charging Chute.

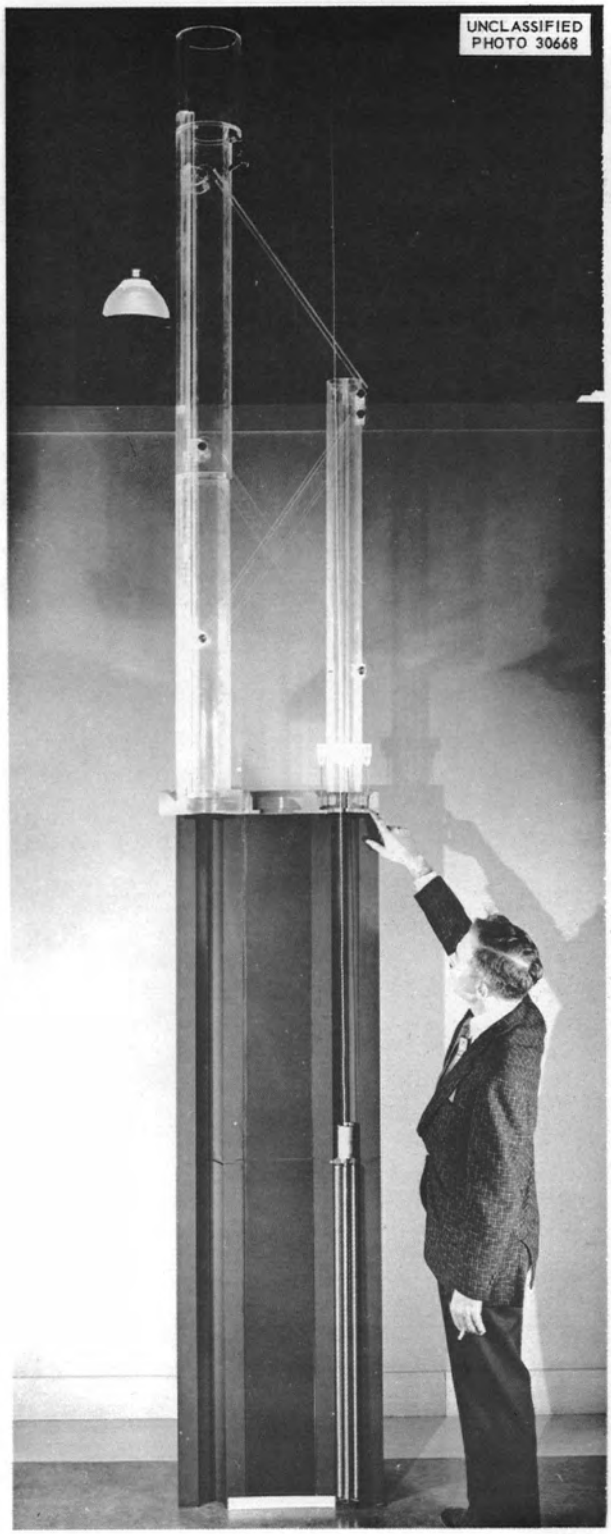

Fig. 5.15. Fuel Charging Chute Positioned Over Charge Pan and Graphite Channels.

extension. The top of the steel charge pan will be a smooth surface to which feeler switches on the bottom of the charging chute extension will be referenced to indicate through lights on the operating panel when the charging chute extension is properly positioned over a channel.

The holes in the charge pan will be shaped to guide the ends of the charging chute and chute extension into proper alignment with the graphite channels and to actuate the positioning feeler switches on the bottom of the chute extension, shown in Fig. 5.16, as a remote visual aid to the operator during the positioning operation.

An actual refueling sequence following a period of reactor operation would proceed as follows. After the reactor has been brought down to zero power, the temperature is reduced and the helium is evacuated into the helium storage system. When the pressure has been brought down to atmospheric level, the flange at the top of one or more charge tubes is unbolted, the solder seal is melted electrically, and the shield plug is withdrawn. As the shield plug clears the slide valve in the charge tube, this valve is closed and the plug completely removed. The overhead crane then lowers a charging chute into position with its lower end in the charge tube. The slide valve is opened and the charging chute lowered until the lower end engages the hole in the charge pan. This operation may be facilitated by suspending a television camera and light source either through an adjacent charge tube or through the charging chute being positioned. These cameras are described in Section 8. When the charging chute has properly engaged the charge pan, it is rotated to a specified alignment with respect to the flange on the top of the charge tube and lowered by the crane until the charging chute flange rests firmly on the charge tube flange and the flanges are bolted up.

A discharge machine, which is crane mounted to traverse the charge tube positions on the fuel loading floor, is then moved into position and attached. A section through a discharge machine is shown in Fig. B.10 of Appendix B. An empty fuel rack containing twelve fuel element positions will have been placed in the machine. With the charging chute extension drawn into the central position, the fuel element grab is lowered into it from the discharging machine. The chute extension is then positioned over a selected fuel channel by rotating the outer tube of the charging chute by

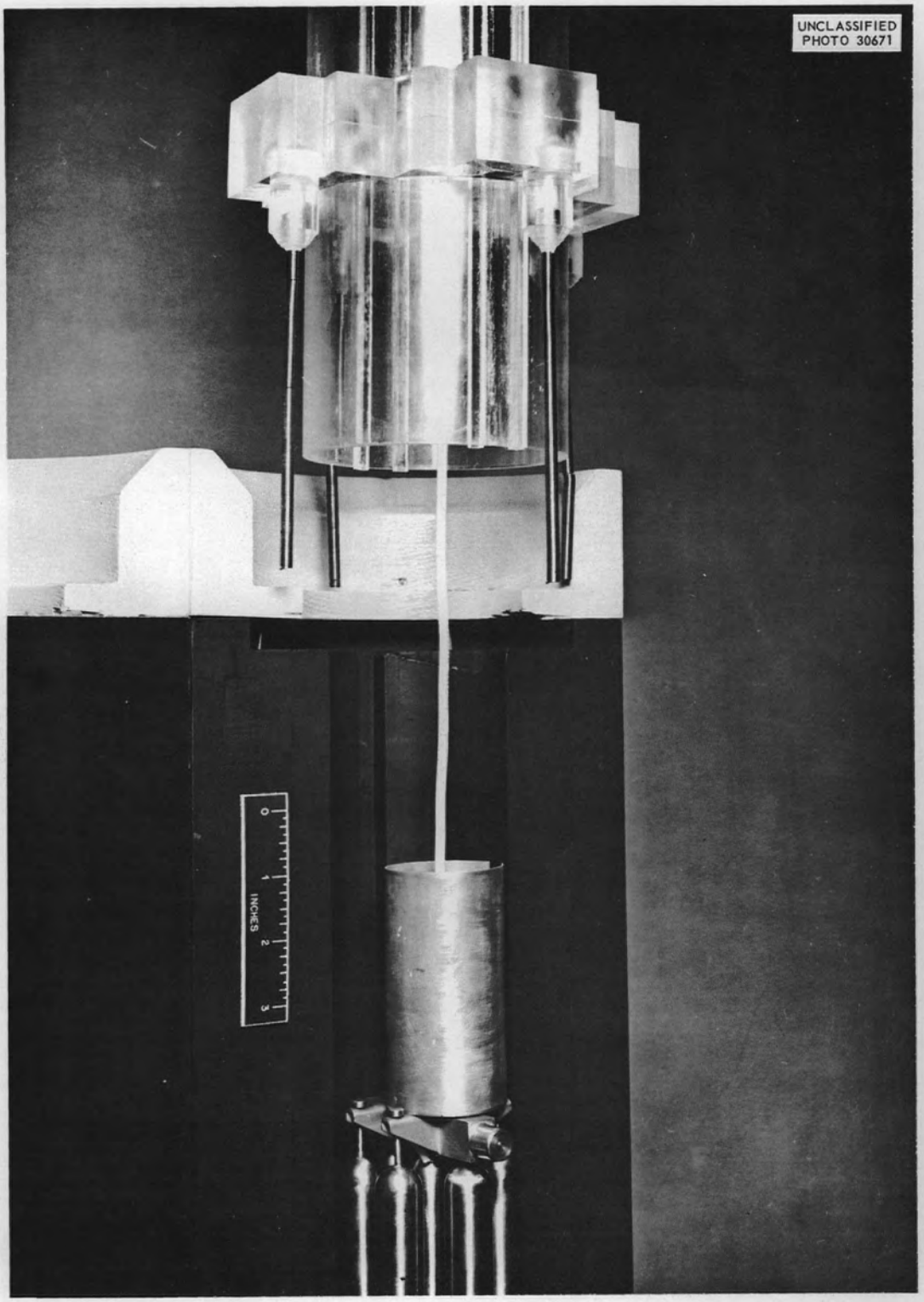

Fig. 5.16. Fuel Charging Chute Extension with Feeler Switches Registered in Charge Pan.

means of the drive mechanism at its upper end and then by positioning the extension radially until the feeler switches indicate that the extension is in alignment with the selected fuel channel. The fuel element grab is then lowered and the top fuel element withdrawn into the charging chute extension, the extension is drawn into the central position, and the fuel elment is withdrawn into the discharging machine, transferred into a vacant position in the rack, and the operation repeated until all six fuel elements have been removed. This machine is then moved to another fuel channel in which a chute has been installed and six more spent fuel elements are removed. The full rack of twelve elements is then transferred by the machine to the fuel discharge well and lowered onto a dolly for transport to the storage pond.

The discharge machine is followed by the charging machine which is identical except that the heavy lead shielding around the fuel rack is not required. The twelve positions in the fuel element rack are occupied by fresh fuel elements which are placed in the fuel channels by reversing the procedure described above for discharging a channel.

The support of the six fuel elements within a channel is provided by six pairs of circumferential hanger slots spaced at equal vertical intervals along the pair of vertical and diametrically opposite guide slots which extend down the length of each fuel channel. The two ends of the fuel elment hanger engage and slide vertically in the two guide slots and are indexed into the hanger support slots in the manner of a bayonet lock. This arrangement is represented in Fig. 5.17. Figure 5.18 is a photograph with the upper portion of the graphite channel removed to show the fuel element fully indexed into the bayonet-type fuel hanger slot. Figure 5.19 shows the bottom of the graphite section which was removed to expose the fuel element as shown in Fig. 5.18. Also shown are the upper half of the hanger slot and the circular matching end that keys the vertical channel sections together and maintains channel alignment. In the reactor these channels would be bored through a single square graphite piece without the diametral partition shown in these photographs. The two rectangular guide slots and the hanger slots are clearly visible in these two figures. The hanger slots are sloped downward away from the guide slots as a precaution against the possibility that a fuel element might work out into the guide slots and drop.

UNCLASSIFIED
ORNL-LR-DWG 27452

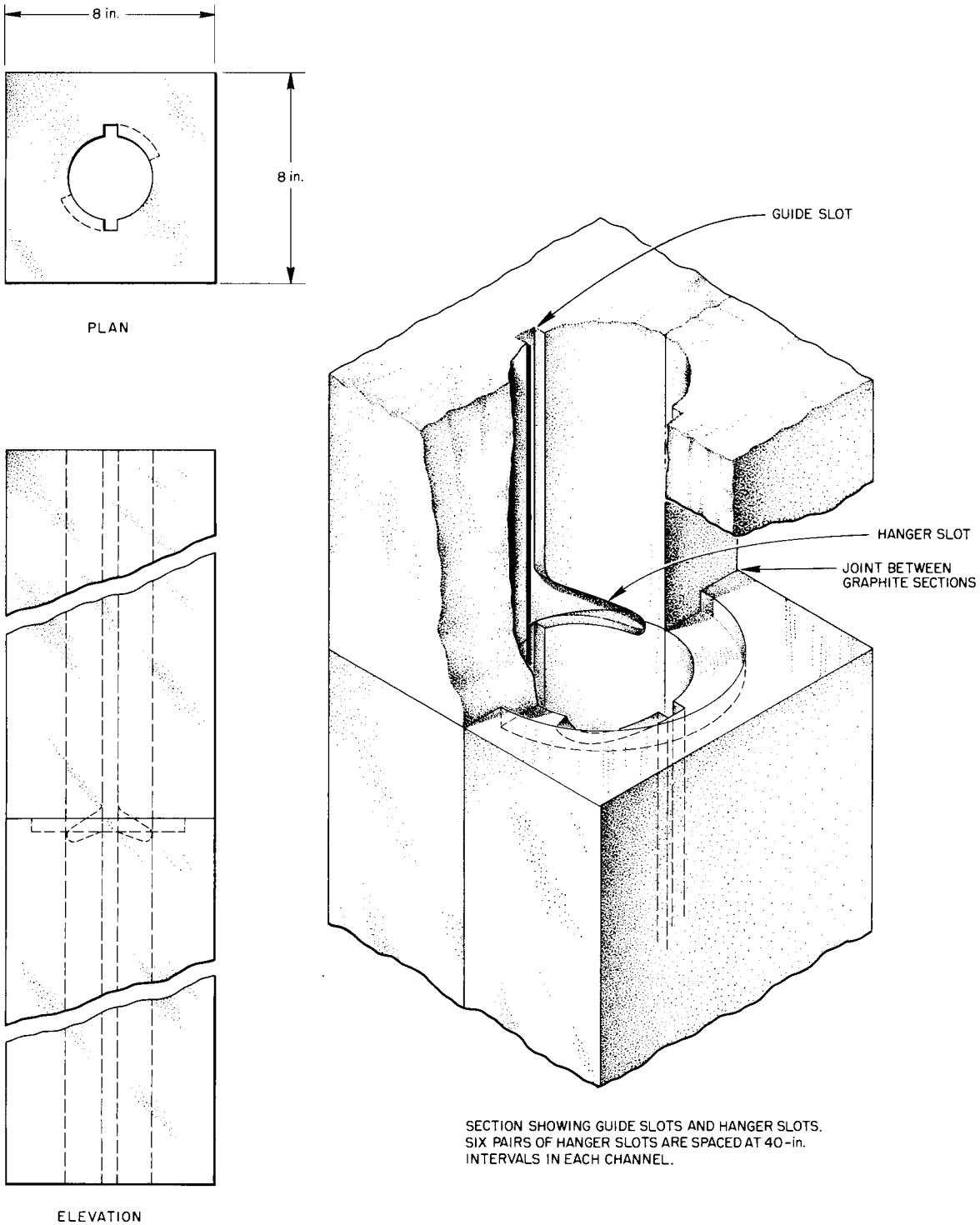

Fig. 5.17. Graphite Fuel Channel Showing Guide Slots and Fuel Element Hanger Slots.

UNCLASSIFIED
PHOTO 30669

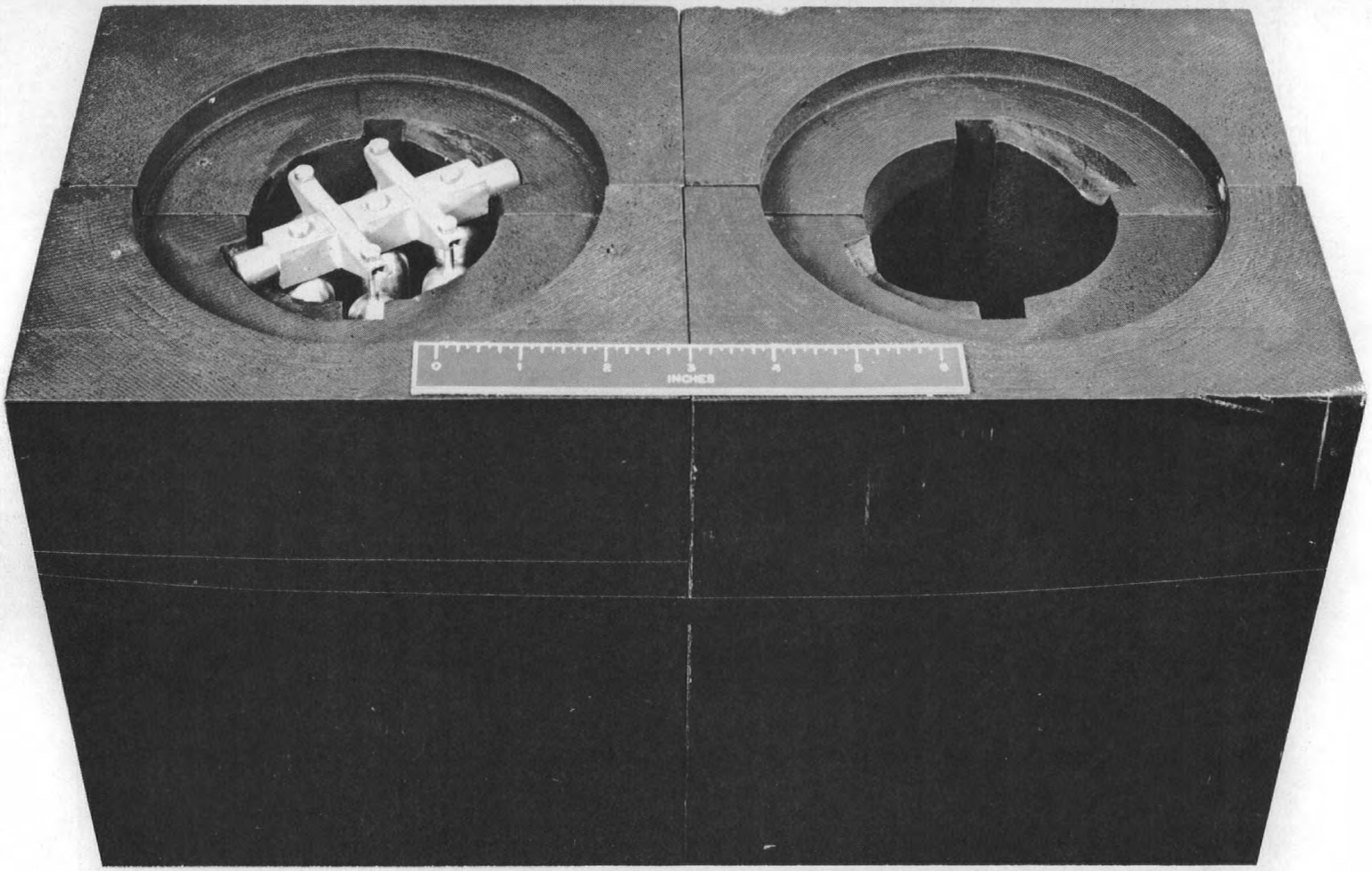

Fig. 5.18. View into Graphite Channel with Mating Graphite Removed Showing Fuel Element Hanger Properly Positioned in Hanger Slot.

UNCLASSIFIED
PHOTO 30670

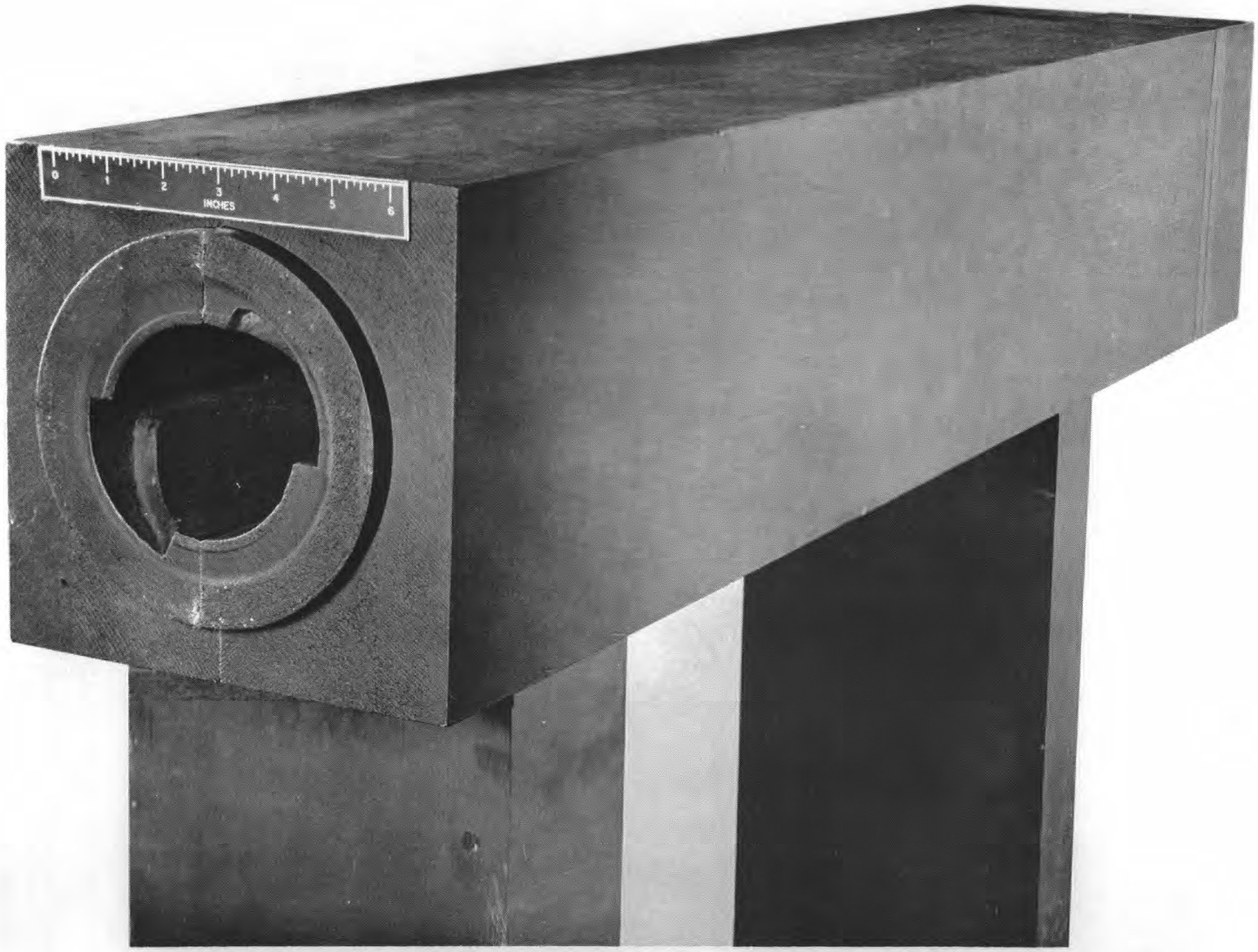

Fig. 5.19. View Looking into Bottom of the Graphite Channel Section Removed to Obtain the View in Fig. 5.18.

To insure that the fuel element and grab slide freely between the charging chute extension and the graphite channel, a pair of matching slots are provided in the chute extension. The fuel element hanger and grab guides are led into these slots in the chute by ramps as they are lowered. These slots are on a diameter transverse to the direction of extending motion and hold the fuel element centered even as the chute extends and the supporting cable departs from its vertical position. The guide slots down each graphite channel are positioned to register with those in the charging chute extension which places them on the diameter of each channel that is normal to the radius connecting that channel to the central channel in the group.

Part of the refueling operations will consist of transferring fuel elements from one reactor location to another. In this case, the shielded discharge machine transfers fuel elements between channels as the schedule requires.

The basic components of the fuel charging machine are the crane system on which it moves over the fuel loading floor, the chamber in which the fuel element rack is carried, the fuel rack winch and cable, the fuel rack indexing mechanism, and the fuel element grab and winch. The fuel discharging machine is identical with the charging machine except that it is fitted with the required lead shielding and a combined cooling and venting system to dispose of the decay heat from spent fuel elements.

The fuel element grab must be capable of two mechanical actions; the opening and closing action of the jaws, and the rotating action required to index a fuel element into or out of the hanger slot in the graphite channels. A section through the grab showing its general arrangement is shown in Fig. 5.20. Three solenoids are arranged to deliver the required motions. The power may be delivered to them through rheostats to avoid snap action.

The fuel handling system that has been described involves a sequence of mechanical operations for the refueling of a given channel. In the operation of a power station, the refueling operation must be carried out in a reasonable time. An annual refueling shutdown would require fuel loading operations involving about 20% of the 1,597 fuel channels. One charging and one discharging machine and five charging chutes should be provided. With this equipment in twenty-four hour service, about two weeks would be required to complete such a refueling operation.

UNCLASSIFIED
ORNL-LR-DWG 27559

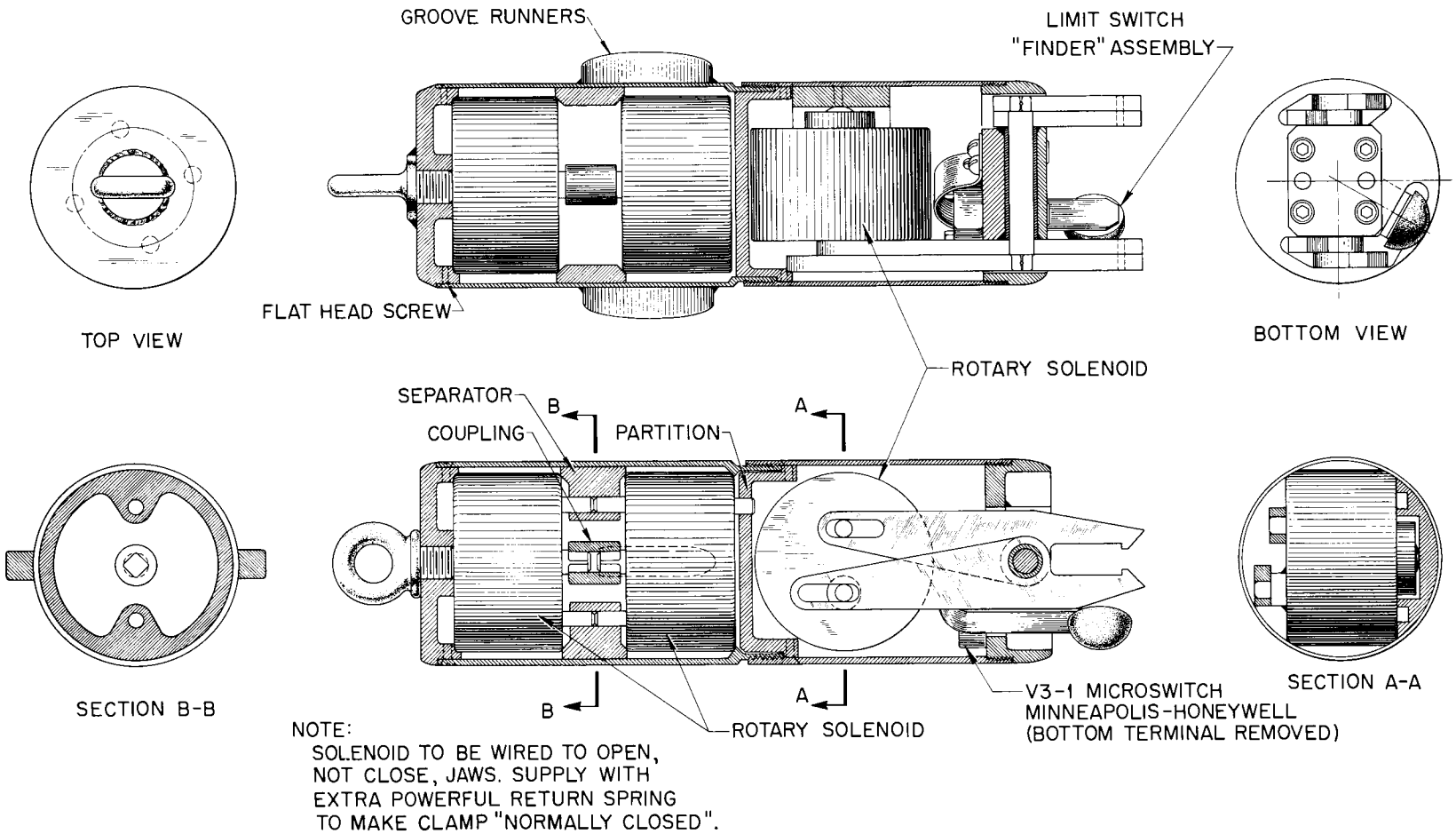

Fig. 5.20. Grab Assembly for Charging Machine.

5.6 Thermal Neutron Curtain

The only unconventional feature of the shield design is the use of a boron curtain placed around the outside of the graphite reflector to absorb a high percentage of the thermal neutrons escaping from the graphite so that they will not be absorbed in the pressure vessel. This will reduce both the radiation damage to the pressure vessel and the pressure vessel activation. It will also reduce heating in both the pressure vessel and the concrete, thus reducing the temperature gradient which would otherwise be induced and the resulting thermal stresses. It further has the advantage that it will reduce the thickness of the concrete required and will be particularly helpful in reducing the problem of shielding around the penetrations for the gas ducts and for the fuel loading and control rod drive equipment. While the cost of the boron curtain will not be high, it will not be entirely offset by the reduced cost of the concrete shield. It is believed that the advantages mentioned above more than justify its use.

The construction of the boron curtain is indicated in Fig. 5.21. Sheets of pyrex glass will be placed in pockets provided by welding hot rolled steel sheets together. The panels prepared in this fashion will be hung around the outer perimeter of the graphite in such a way that the return cooling gas for the reactor circulates over both surfaces. The heat flux from the pyrex will be 100 to 200 Btu/hr-ft^2 and will result in a temperature rise of 10°F to 20°F above the 460°F helium. The top surface of the reflector is to be covered with pyrex tiles placed inside sheet steel cans. The heat generated in these tiles will be transferred to the graphite. These cans would be stamped out in the form of large pans to yield assemblies to cover the area around the twenty-five channels under one charge pan. The cans provided for both the tiles at the top and for the sides are intended primarily to minimize the dispersal of particles of pyrex glass which might be chipped off during mechanical handling operations. Radiation damage data indicate that, while some cracking of the pyrex might occur as a result of thermal stresses, the pyrex should be able to take approximately ten times the radiation damage to be expected in this application over a twenty-year period.[5,6] The pressure shell at the bottom of the reactor will be protected from radiation by the 2 in. thick steel plate which supports the graphite blocks.

---

[5] Solid State Semiann. Prog. Rep., August 30, 1956, ORNL-2188 (December, 1956).

[6] Solid State Semiann. Prog. Rep., August 31, 1957, ORNL-2413 (November, 1957).

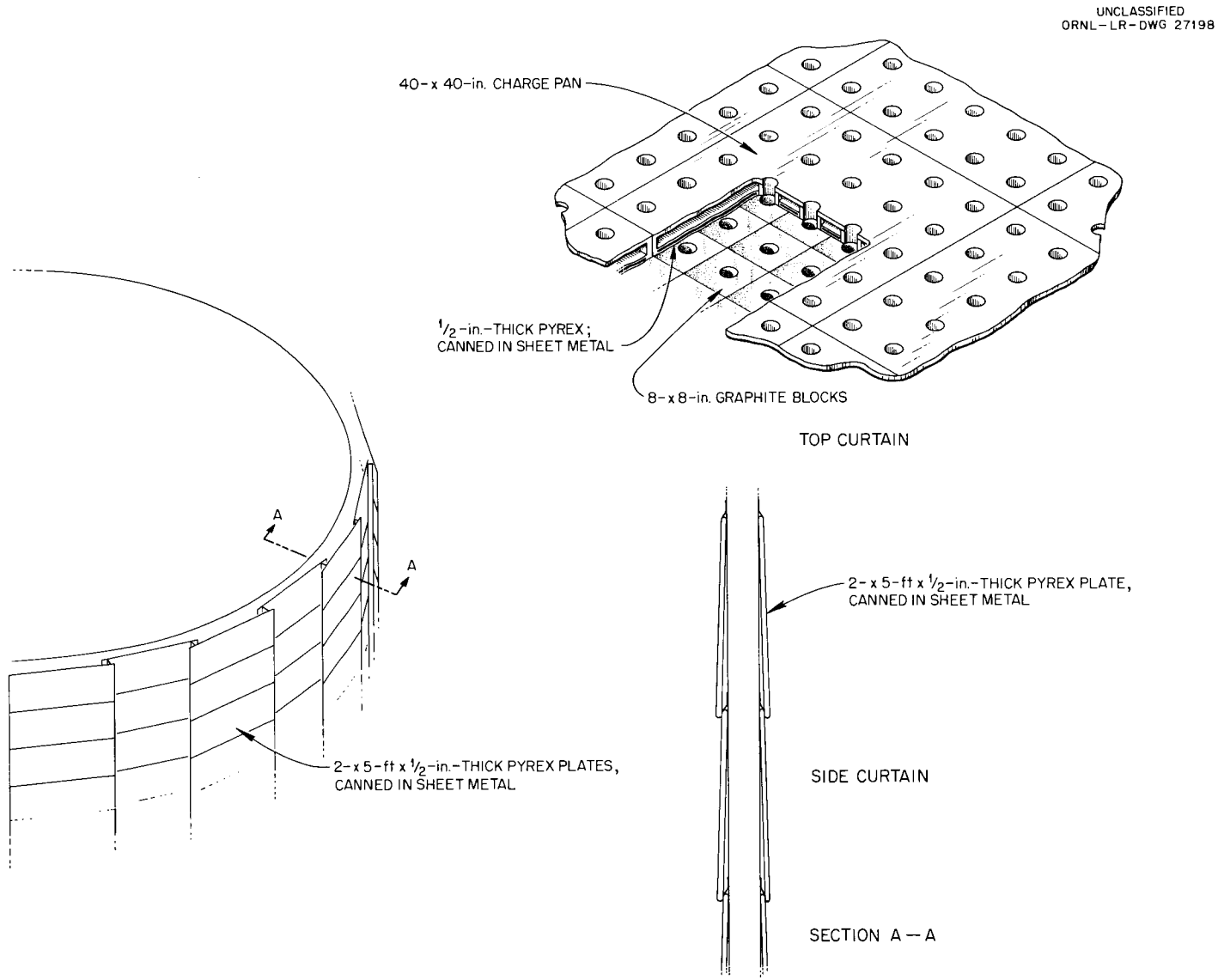

Fig. 5.21. Neutron Shield.

5.7 Shield Cooling

5.7.1 Design Objectives: The design objectives for the cooling system were established as: maximum concrete temperature 212°F; minimum temperature differential across the concrete consistent with economical design; optimum insulation thickness on vessels, and heat removal from the concrete by forced air circulation. Air cooling for the concrete biological shield surrounding the reactor and gas piping system was selected because (1) the concrete shielding could serve to duct the air flow, (2) an air system poses fewer construction problems than an embedded piping system utilizing cooling water, and, in the event of a helium leak, (3) any radioactive material leaking out would be exhausted to the stack since the cooling passages in the shield are to be on the suction side of the fan and thus will be maintained slightly below atmospheric pressure. The cost estimate for the shield cooling system is given in Table 5.1.

The effect of a thermal neutron curtain around the graphite reflector in reducing the heating in the concrete shield is discussed in Section 5.6. With the boron curtain installed the total gamma ray and neutron energy deposition in the concrete adjacent to the reactor is approximately 11.4 x 10^{-5} w/cc or 11 Btu/ft^3-hr. (See Section 2.8).

5.7.2 Nuclear Heating of Concrete:[7] For the determination of the nuclear heating in the concrete the following assumptions were made:

Rate of energy absorption in concrete = Q_o = 7.1 Btu/ft^3-hr

Shield thickness, L, 8 ft

Inside concrete temperature, t_1, 180°F

Energy absorption coefficient for concrete, μ_e, 0.05 cm^{-1} or 1.53 ft^{-1}

Concrete thermal conductivity, k, 0.54 Btu/hr ft^2/°F/ft

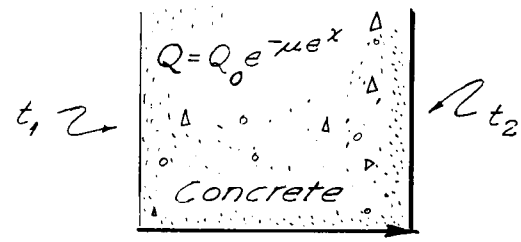

[7] Glasstone, Principles of Nuclear Reactor Engineering, First Ed. p. 666.

TABLE 5.1

COST ESTIMATE FOR SHIELD COOLING SYSTEM

	Unit	Size	Installed Cost
1.	Blowers	32,000 cfm	$ 6,830 (*)
2.	Filters	900 sq ft of face area	10,000
3.	Duct work	Table 5.3	6,150 (+)
4.	Air baffles	Fig. 12.4	7,500
5.	Stack	10 ft dia x 92 ft high	15,000
6.	Insulation(Reactor vessel, hot and cold helium piping)	86,280 board ft	45,000 (++)
		TOTAL	$ 90,480

(*) Cecil H. Chilton, Chemical Engineering, 56, (McGraw Hill Pub. Co.), 97 (June, 1949).

(+) Robert Snow Means, Building Construction Cost Data, TH11-M4, No. 2, Duxberry, Mass., (1956).

(++) Brooks-Fisher Insulating Company to V. J. Kelleghan, Private Communitcations, (January 7, 1958).

The location of the maximum temperature in the concrete is given by:

$$(X)_{t\ max} = -\frac{1}{\mu_e} \ln\left[(t_1 - t_2)\frac{k\mu_e}{Q_o L} + \frac{1 - e^{-\mu_e L}}{\mu_e L}\right]$$

$$(X)_{t\ max} = -\frac{1}{1.53} \ln\left[(180 - 100)\frac{0.54(1.53)}{15.5(8)} + \frac{1 - e^{-1.53(8)}}{1.53(8)}\right]$$

$$= 0.318 \text{ ft} = 3.81 \text{ in.}$$

NOTE: For rate of energy absorption in concrete, 15.5 Btu/ft^3-hr was used in calculation but 11 Btu/ft^3 is the latest accepted value.

The maximum temperature is then represented by:

$$t_{max} - t_1 = (t_2 - t_1)\frac{x}{L} + \frac{Q_o}{k\mu_e^2}\left[(e^{-\mu_e L} - 1)\frac{x}{L} - e^{-\mu_e x} + 1\right]$$

$$t_{max} - 180 = (100 - 180)\frac{0.318}{8} + \frac{15.5}{0.54(1.53)^2} \times$$

$$\left[(e^{-1.53(8)} - 1)\frac{0.318}{8} - e^{-1.53(0.318)} + 1\right]$$

$$t_{max} - 180 = 1.05$$

$$t_{max} = 181°F$$

This indicates that the thermal stresses in the concrete induced by nuclear radiation heating will not be significant.

5.7.3 Heating of the Concrete by Thermal Radiation and Convection: The determination of the required insulation thickness on the reactor vessel and pipes was based on a series of approximations with the following assumptions: 80°F still air outside the insulation; heat cost in dollars per million Btu 0.88; varying thickness of insulation; cold pipe insulation 85% magnesia; k = 0.47 Btu/ft^2 °F/in.; hot pipe insulation J/M thermobestos, k = 0.55 Btu/ft^2 °F/in.

It was possible[8] to determine the most economical insulation thickness. This thickness was then used for still air and heat loss was compared to that for the air flow conditions assumed. The heat loss was then adjusted to determine if the thickness for still air was still the optimum insulation thickness.

Table 5.2 shows the economical insulation thickness for 1000°F and 450°F pipe wall temperatures. The calculated thicknesses were rounded off upward in every case. These principal thicknesses are 6 in. for the piping at 1000°F and 4 in. for the piping and pressure vessel at 450°F.

Using the above thicknesses of insulation, and air flows which provide adequate air changes for the concrete enclosures, the temperature of the surface of the shield concrete will be 145°F opposite the hot piping and 128°F opposite the pressure vessel and the cold piping.

The surface areas were computed from the geometry of the concrete shield and piping layout as given in Section 12.

A, surface of pressure shell = $4\pi(25^2)$ = 7850 sq ft

A, surface of pipes = $\pi(5) \times 48$ = 755 sq ft

A, concrete surface = 24 x 8 x 58 = 11,120 sq ft

$$\frac{11,120}{8600} = 1.293$$

$$\frac{8600}{11,120} = 0.774$$

Assuming that all of the heat transferred through the 4 in. insulation passes into the air by convection from the surface of the insulation and the concrete, the concrete, insulation surface, and air temperatures may be determined for 8600 ft^2 insulated steel surface at 450°F with 25,000 cfm air flow.

$$\frac{A_1(t_{i_1} - t_{i_2})}{\frac{Y}{k}} = h_1 A_1 (t_{i_2} - t_a) + h_2 A_2 (t_c - t_a)$$

---

[8] Chemical Processing, 17, 198 (June, 1954).

TABLE 5.2

ECONOMIC THICKNESS OF INSULATION

Hot Surface Temperature	Insulation Thickness	Annual Cost of Heat Loss $/ft^2	Annual Saving Over 1 in. Thickness $/ft^2	Installed Insulation Cost $/ft^2 Mat.	Labor	Total	x2.8 = 14% 20 yrs	Value of Heat Saved 20 yrs	Additional Cost to Save This Heat Over 1 in. Thickness
1000°F	1	3.45		0.41	1.81	2.22	6.21		
JM	2	2.05	1.40	0.83	2.22	3.05	8.55	28.00	2.34
Thermobestos	3	1.42	2.03	1.24	2.70	3.94	11.03	12.60	2.48
Insulation	4	1.10	2.35	1.65	3.34	4.99	13.98	6.40	2.95
	5	0.88	2.57	2.07	3.99	6.06	16.98	4.40	3.00
Economic	6	0.75	2.70	2.50	4.83	7.33	20.50	2.60	3.52
Thickness	7	0.63	2.82	2.91	5.75	8.66	24.20	2.40	
450°F	1	1.08		0.40	1.15	1.55	4.34		
JM	2	0.60	0.48	0.80	1.15	1.95	5.46	9.60	1.12
85% Magnesia	3	0.42	0.66	1.20	1.17	2.37	6.64	3.60	2.30
Economic	4	0.31	0.77	1.60	1.27	2.87	8.04	2.20	3.70
Thickness									

Notes:
1. 80°F ambient still air.
2. Scaffolding charges not included since they will be constant for 1 in. thickness and over.
3. 15% added to labor charge for working at high elevations.
4. Heat cost 0.88 $/million Btu.

where

A_1 = 1.0 sq ft

Y = insulation thickness, in.

k = thermal conductivity

h_1 = film heat transfer coefficient at insulation

h_2 = film heat transfer coefficient at concrete

t_{i_1} = insulation inside surface temperature

t_{i_2} = insulation outside surface temperature

t_a = air temperature

t_c = concrete temperature

and

$$h_1 = 0.19(t_{i_2} - t_a)^{0.3}$$

$$h_2 = 0.19(t_c - t_a)^{0.3}$$

$$A_2 = \frac{\text{Concrete surface area}}{\text{Pressure shell surface area + pipe surface area}}$$

$$\frac{1(450 - t_{i_2})}{\frac{4}{0.47}} = 0.19(t_{i_2} - t_a)^{0.3}\ (1)\ (t_{i_2} - t_a) + 0.19(t_c - t_a)^{0.3}\ 1.293(t_c - t_a)$$

Based upon a heat loss of 37 Btu/hr ft^2 for still air, the total heat loss is 8600 x 37 = $\frac{\text{Btu}}{\text{hr}} \div 60$ = 5300 Btu/min.

The air weight flow is 1775 lb/min (for a volume flow of 25,000 cfm).

The associated air temperature rise then is: $5300 = 1775(0.24)(\Delta t)$

$\Delta t = 12.4°F \therefore t_{in} = 100°F,\ t_{out} = 112.4°F,\ t_{avg} = 106°F$

Assuming that the temperature of the surface of the insulation is 140°F and the temperature of the surface of the concrete is 128°F then by substitution in the above equation

$$\frac{450 - 140}{\frac{4}{0.47}} = 0.19(34)^{0.3}(1)(34) + 0.19(22)^{0.3}(1.293)(22)$$

$$36.4 = 20.3 + 15.15 = 35.45 \text{ Btu/ft}^2 \text{ hr}$$

The heat radiated to the concrete must equal the heat convected away from the concrete.

$$15.5 = F_E F_A (A) 0.173 \left[\left(\frac{T_{i_2}}{100} \right)^4 - \left(\frac{T_c}{100} \right)^4 \right]$$

$$F_E = \text{Emissity factor} = \frac{1}{e_i} + \frac{A_1}{A_2} \left(\frac{1}{e_c} - 1 \right) = \frac{1}{\frac{1}{0.94} + 0.774 \left(\frac{1}{0.91} - 1 \right)} = 0.877$$

e_i = emissity of insulation

e_c = emissity of concrete

F_A = geometry factor = 1

T_{i_2} = insulation temperature, °R = 460 + 140 = 600

T_c = concrete temperature, °R = 460 + 128 = 588

$$15.15 = 0.877(1)(1)(0.173) \left[(6)^4 - (5.88)^4 \right] = 15.32$$

Using the computed heat loss the assumed air temperature differential can be verified.

$$QA = wc_p \Delta T$$

$$\frac{36 \times 8600}{60} = 1775(0.24)(\Delta t)$$

$$\Delta t = 12.1°F$$

Since the calculated heat loss is somewhat lower than assumed in the economic evaluation, a thinner application of insulation might be slightly more economical. It is felt that the selection of 4 in. insulation is judicious in that it will permit some flexibility in allowing greater heat loss at critical locations such as thermal sleeves.

The temperatures prevailing in the concrete enclosures surrounding the hot piping were determined as follows:

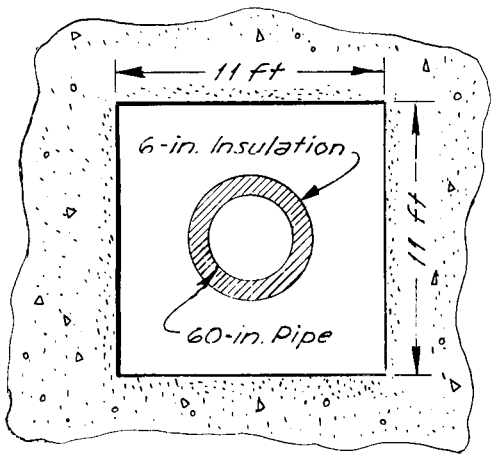

Cross Section of Concrete Enclosure

Assume an air flow of 1600 cfm at 120°F average temperature, with 100°F inlet and 140°F outlet air for each enclosure. Flow area = 11 x 11 - $\frac{\pi(6)^2}{4}$ = 92.8 ft^2

Air velocity = $\frac{Q}{A} = \frac{1600}{92.8}$ = 17.25 ft/min

Area for heat conduction through insulation assumed at 5.5 ft diameter. The same diameter was used for convection calculations.

$\pi(5.5)$ = 17.25 sq ft/ft for insulation

11 x 4 = 44 sq ft/ft for concrete

$\frac{44}{17.25}$ = 2.55; reciprocal = 0.392

air weight flow $\frac{1600(60)(14.7)(144)}{(53.3)(560)}$ = 6830 lb./hr

$$\frac{1000 - t_{i_2}}{\frac{6}{0.55}} = h_1(t_{i_2} - 120) + h_2(2.55)(t_c - 120)$$

assume t_{i_2} = 170 $\qquad h_1 = 0.78$

t_c = 145 $\qquad h_2 = 0.555$

$$\frac{1000 - 170}{\frac{6}{0.55}} = 0.78(50) + 0.555(2.55)(25)$$

76 = 39 + 35.4 = 74.4

The heat radiated to concrete must equal the heat convected away from the concrete

$$35.4 = F_E F_A (A)(0.173)\left[\left(\frac{T_{i_2}}{100}\right)^4 - \left(\frac{T_c}{100}\right)^4\right]$$

$$35.4 = 0.902(1)(1)(0.173)\left[(6.3)^4 - (6.05)^4\right]$$

$$35.4 = 0.156(235.7) = 36.8$$

where

$$F_A = 1$$

$$F_E = \frac{1}{\frac{1}{0.94} + 0.392\left(\frac{1}{0.9} - 1\right)} = 0.902$$

Using the computed heat loss the assumed air temperature differential of 40°F can be verified for the hot pipe length which is 55 ft.

$$76(55 \times 17.25) = 6830(0.24)(\Delta t)$$
$$\Delta t = 44°F$$

Even though this higher temperature air is mixed with the air in the reactor enclosure, it will have small effect upon the previously assumed air temperature rise within the reactor enclosure. This is substantiated by the following

$$6830(140) = 950{,}000$$
$$60(1775)(106) = \underline{11{,}289{,}000}$$
$$\frac{12{,}239{,}000}{113{,}330} = 109°F \text{ average reactor enclosure air temperature.}$$

5.7.4 Cooling Air Distribution System: The concrete enclosures surrounding the reactor and the pipes will be cooled and ventilated by 32,000 cfm exhaust blowers. A filter bank which prevents venting of any solid contaminated material to the atmosphere is placed between the blowers and the air outlet from the reactor enclosure. It is estimated[9] that approximately 900 ft^2 of face area is required for the filters. The filters consist of 1/2 in. of type FG-50 filter material backed up with 1/2 in. of type FG-25 material. The filters as manufactured by the American Air Filter Company would be changed every two years and it is anticipated that the air pressure drop through the filters at change time would be 4.9 in. of water. Allowing a Δp of 1 in. H_2O for control louvers and 1 in. H_2O for duct losses a blower rated at 32,000 cfm at 7 in. water would be satisfactory.

The inlet to each external duct is filtered and an inlet register is provided for balancing the system air flow. Air flow is directed into the reactor enclosure which is held at a negative pressure. Air flows also into the reactor enclosure from the hot and cold helium pipe enclosures and through the annular space between the fuel loading channels, the control rods, and the upper shield (see Section 12). Table 5.3 shows the flow and duct sizes selected.

---

[9] Reactor Handbook, 2, 501.

TABLE 5.3

SHIELD COOLING AIR FLOW DISTRIBUTION

Flow Path	Volume of Flow (cfm)	Duct Size (in.)
1. From atmosphere, through hot duct room, and into reactor room.	6,400	4 - 12 x 12
2. From atmosphere, through cold duct room, and into reactor room.	6,400	4 - 12 x 12
3. From atmosphere through duct into gallery. From gallery, around control rods and fuel channels into reactor room.	6,700	4 - 12 x 24
4. From atmosphere through duct into reactor room at bottom.	12,500	4 - 24 x 24
5. Outlet from reactor room into filter room.	32,000	8 grills in 36 x 24 duct leading to a 48 x 48 duct to filter room

The baffles at the top and bottom of the reactor enclosure direct the air flow across the pressure vessel and ensure more efficient cooling. The blowers discharge to a stack which extends to 60 ft above the roof of the building. This requirement is discussed in greater detail in the section on hazards.

5.8 Control Rods and Drives

The general construction of a control rod is illustrated in Fig. 5.22. A hollow silver cylinder, 18 ft long, 2 in. OD, and 1-1/4 in. ID forms the neutron absorbing section. In order to provide adequate strength in the event of a large temperature overshoot the silver is sheathed with type 304 stainless steel, 0.065 in. thick on the outside surface and 0.035 in. thick on the inside surface.

The rod is hung by a stainless steel stranded cable, the cable being suspended from a drum located above the pressure vessel but immediately below the loading floor. The construction of the rod actuating mechanism is also illustrated in Fig. 5.22 . Each rod is positioned by a separate actuator. The total weight supported by the cable is estimated to be 215 lb.

In addition to the neutron absorbing silver, there is to be a shock absorbing device installed at the bottom of each rod. Should the rod fall freely the motion will be arrested by the steel plate supporting the graphite. The silver would mushroom, and probably become jammed in the channel if the energy of the free fall were not absorbed gradually. A possible shock absorber consists of corrugated pieces of stainless steel which are compressed by the deceleration of the rod mass. This crushing of the corrugations would absorb the energy of only one free fall. The rod must be removed for inspection and repair in the event of such an incident.

The cable drum is driven by a polyphase 60-cycle reversible electric motor during normal rod withdrawal and insertion. Synchronization of rod positions, will be performed manually as required. The rod position indication will be achieved by means of a synchro system which revolves approximately 300 degrees during a full rod stroke. Limit switches will operate at the fully withdrawn and inserted positions. In addition, a

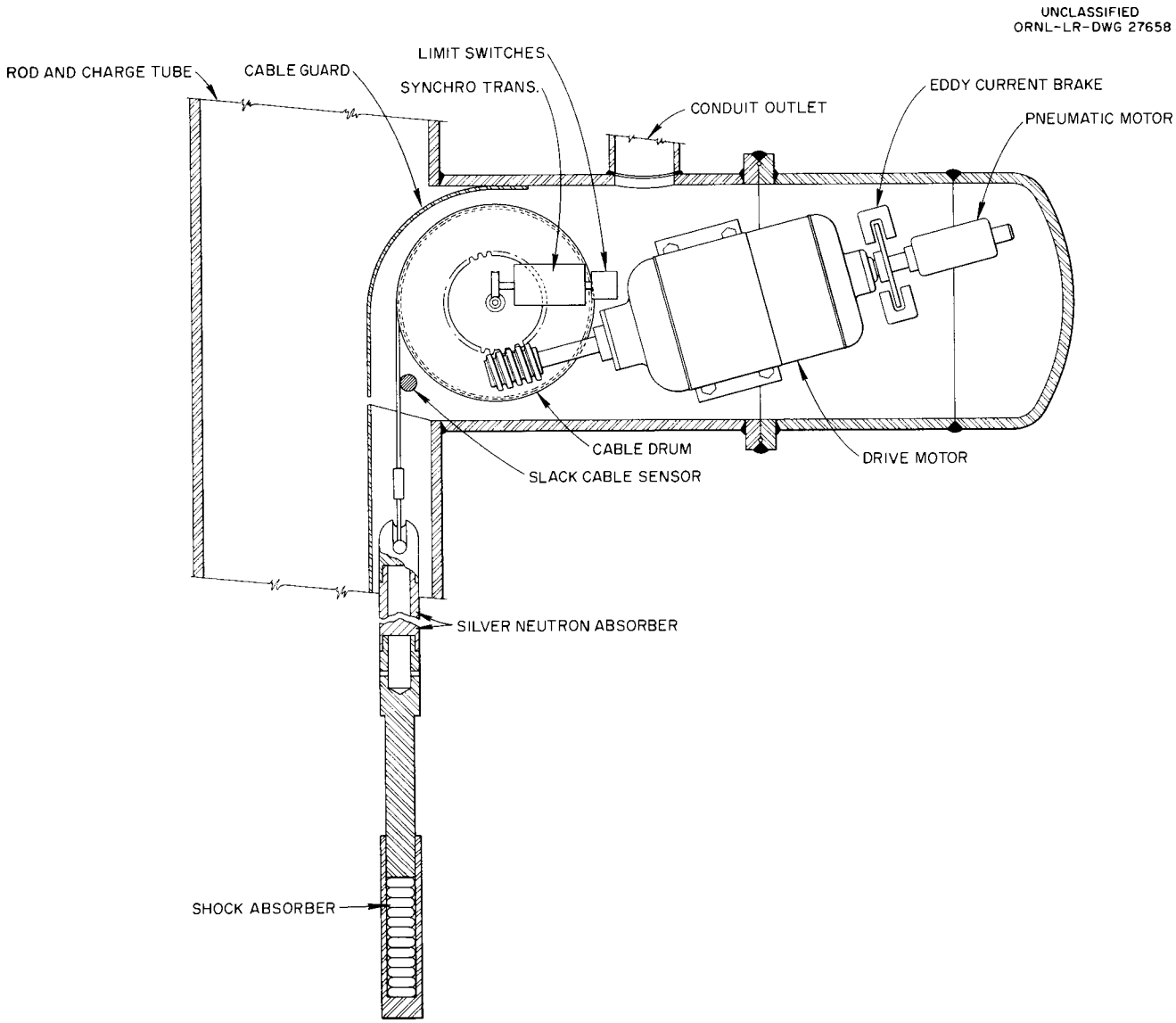

Fig. 5.22. Control Rod Actuator.

slack cable indication is obtained from a limit switch which is closed by the pressure of the taut cable against a roller. Should the cable become slack, it will tend to spiral away from the drum and allow the slack cable sensing roller to move, thus actuating the slack cable alarm.

A pneumatic motor will provide an emergency insert speed approximately ten times that of the electric motor. This emergency motor will rotate the shaft of the electric motor and drive the cable drum through the normal gearing. Thus, no clutches or gear shifts are necessary. The gas to drive the pneumatic motor will be obtained from high pressure bottles of helium, the helium being admitted through electrically operated valves. The helium will be exhausted into the reactor pressure vessel. The station battery will supply the control power for the helium valves. A lower limit switch will cause these valves to close before overrunning of the cable drum occurs at the fully inserted position.

It is necessary to provide a nearly constant speed of insertion when the helium is applied to the pneumatic motor. The torque of the motor is almost entirely a function of the gas pressure applied, and the speed is proportional to the gas flow. Thus, a pressure regulator together with a flow restricting orifice is employed. In addition, an eddy-current brake using permanent magnets is provided to load the motor shaft. The load torque demanded by this brake is proportional to the speed, which should limit the motor speed in case the gear friction loading happens to be low at any time. The eddy-current brake will produce only a small load on the electric motor because of the relatively low speed of the electric motor compared to that of the pneumatic motor.

To protect against a malfunction in the actuator system, a physical means must be provided to prevent overrunning of the drum as the rod reaches the bottom of the stroke. This overrunning would be followed by withdrawal of the rod as the cable would wind back on the drum with the drum rotating in the direction which normally lowers the rod. One method of preventing this overrunning is to attach the cable to the drum in a manner that allows the end of the cable to fall freely away from this attachment and become disconnected from the drum. The end of the cable is held captive by the protecting shield; thus, the cable cannot fall onto the top of the

reactor where it might become entangled in other rod drives.

All of the rod actuating mechanism is enclosed within the reactor pressure system. The high speed shaft bearings and gears on the actuator will be sealed in a gear box and grease lubricated. The slow speed worm and gear driving the cable drum is to be supplied with a dry lubricant such as molybdenum disulphide, or run unlubricated. The slow speed worm and gear driving the position indicating synchro transmitter are to be unlubricated.